# NATURE INSPIRED TECHNOLOGY: A NEW PROCESS FOR SILICIFICATION BASED ON MARINE SPONGES

by

AMI ATUL SHAH

Presented to the Faculty of the Graduate School of

The University of Texas at Arlington in Partial Fulfillment

of the Requirements

for the Degree of

DOCTOR OF PHILOSOPHY

THE UNIVERSITY OF TEXAS AT ARLINGTON

May 2018

Supervising Committee:
Dr. Pranesh Aswath (Research Advisor)
Dr. Venu Varanasi
Dr. Antonella Motta
Dr. Efstathios “Stathis” I.Meletis
Dr. Kyung Suk Yum
Dr. Harry Tibbals

Acknowledgements

I sincerely express my gratitude to Dr Aswath and Dr Varanasi for guiding me throughout my research. Their guidance helped induce independent thinking and logical reasoning that a good researcher must imbibe in the most interesting way.

I would especially like to thank Dr. Antonella Motta, for giving me the opportunity to work with her in the Biotech Lab, Trento at University of Trento for a good semester of 5 months. Her guidance and knowledge of understanding of biology was greatly instrumental to my learning curve and expanding my horizons in that new field.

I would also like to thank my committee members Dr Efstathios Meletis, Dr Harry Tibbals and Dr Kyung Suk Yum for their intuitive comments and words of encouragement that helped shape a good focused perspective towards the research.

I am also thankful to my colleagues, Dr. Vibhu Sharma, Dr. Vinay Sharma, Dr. Felipe Monte, Dr. Azhar Ilyas,Kamal Awad and Kimaya Vyavhare for being supportive and sharing their experienced knowledge throughout my research as well as keeping me motivated throughout the 4 years. I am also grateful to all my colleagues in Trento, Silvia Chiera, Rosasilivia Raggio, Cristiano Carlomagno, Susan Young, Lorenzo Moschini, Lorena Maines and Dr. Walter Bonani for being wonderfully accepting and helpful in getting acquainted with the laboratory and teaching new techniques they had to offer.

My sincere acknowledgment to Dr Jeichao Jiang and David Yen for the all the support and training at CCMB facility. My deepest words of appreciation to Jennifer, Beth and Natalie for helping through all the official matters and for their good wishes through all the four years of my graduation.

I would like to thank the most important, my family, my parents Atul Shah and Chetana Shah, my sister Aditi Shah and my brother-in- law Rushikesh Shah for continuously encouraging me to continue seeing the end through all the hardships in 4 years and for their non-exhausting support till the end.

Last but not the least I thank all my friends here at UTA especially Pari Patel, Kaustubh Shinde, Yuvraj Kashyap, Seshikanth Sudarshanam, Dheeral Bhole and Sujay Bagi who have forced me to continue at my lowest points and celebrated the smallest achievements to help me see through the whole graduation, without whom, I would still be writing my thesis.

May 07, 2018

DEDICATION

This work is dedicated to the memory

of my grandfather,

Mr. Rameshchandra. B. Shah

and uncle

Mr Ramesh. Jain

# ABSTRACT

NATURE INSPIRED TECHNOLOGY: A NEW PROCESS FOR SILICIFICATION BASED ON MARINE SPONGES

Ami Shah, PhD

The University of Texas at Arlington, 2018

Supervising Professor: Pranesh B. Aswath

Silica is used in various industries, ranging from automobile industry for tires to semiconductor industry, paints and coatings, biomedical devices & applications to food & drug industry. The current processing techniques for precipitated silica involve harsh conditions like high temperature and extreme pH conditions. Nature already has highly evolved production techniques for silica. They run at physiological conditions and exhibit intricate control over the synthesis, leading to very pure and ornate siliceous structures. These structures exhibit organized architecture at scales as small as nano-dimensions.

The proposed research work is a step, towards development of new techniques that bio-mimic the silica production where they can be scaled up for industrial productions. Also the products obtained can be easily integrated into its potential applications, specifically bone tissue engineering has been targeted in this study. For this the investigators have first gone through an extensive and defined literature study. On basis of this they select the best material alternatives to mimic the biosilica silicification process. These techniques replace the need to use raw materials harvested from the natural marine species and thus avoid

disturbing the marine ecology. They optimize the parameters to achieve steady state nucleation, growth and precipitation. These precipitates are extensively analysed for understanding mechanism of the process and the effect of the parameters on the final precipitate. Techniques like SEM, EDX, IR spectroscopy methods, crystalline-amorphous phase studies with XRD, and chemical environment at molecular level via XANES are employed. Applicability of the product in biomedical applications is tested by exploring its potential as composite material in scaffolds for bone tissue engineering. The basic biocompatibility of the material is tested using them as composites with fibroin and making 2D test structures viz. films. The material and biological properties of these created particles are compared with natural spicules obtained from Tethya aurantia, which were primarily characterized to gather the knowledge of the material that is bio-mimicked.

This study is pursued with view that successful generation of silica particles will contribute to greener, smarter and faster technique of production of silica and other alkoxides that have similar precipitation techniques currently being employed. It will also present us with a potential replacement biomaterial for bone tissue engineering.

Table of Contents

List of Illustrations

List of Tables

# Chapter 1. General Introduction

## 1. Background:

### Silica and Biosilica

Silicon as a member of metalloid family is one of the few elements having both metallic and non-metallic properties. It is one of the most abundant elements in the universe and also the second most dominant component of the earth's crust. It is an important part of our lives from glass windows, bricks and mortars in the construction industry to semiconductors, optical data transmission fibres and also healthcare devices. Silica ($SiO_2$), an oxidized form of silicon, is synthesized at high temperature or extreme pH conditions in current industries.[1,2] The industrial capacity in 2010 for silica production is around 1 x $10^6$ tonnes per annum while silica based materials form ~£2 billion industry. [3] The industry covers a wide range of applications in catalysis separations food and drug technology biomedical materials and paints. Observing the tremendous use in many industries, modifying the processing conditions to moderate conditions can offer advantages in cost, energy and safety perspectives.

Interestingly, a wide variety of marine organisms produce biosilica with various morphologies at moderate physiological conditions to maintain life. Biology produces through bio mineralization inorganic materials like silica at scales > 6.7 × $10^9$ tonnes of silicon per year.[4,5] The scales at which biology produces silica is orders of magnitude greater than the industrial capacity. It appears that biology has identified a greener and smarter way to produce ornate structures of nanomaterials. Elucidating the secrets of biological silica production could lead to materials with novel applications / new technologies for material production.

Sponges and diatoms are one of the most commonly known organism forming biosilica. The uptake silicic acid from the environment and build external biosilica

structure to protect themselves from incoming threats. They use different type of biomolecules the precipitate silica ions. In addition to forming biosilica at physiological conditions these organisms demonstrate strong points in control of particle sizes and pore sizes from nano to micro scales, in construction of structures and morphologies and in control of silica condensation rates. [6–8]

*Marine Sponges and Silicification Process*

Sponges, the oldest animals on earth, can form both calcareous and siliceous spicules.[9] It does so enzymatically. The sponge spicules have been studied widely for the morphology, chemistry and nanostructure for their superior optical and interesting mechanical properties.[10,11] Research in sponge biosilicification is not a new field, but dates back to early 1800s when it was found that it has siliceous structures.[12] Recently it was demonstrated that this axial filament is proteinaceous and has templating as well as catalytic activity in directing the polymerization if silica.[13,14,9]

The silicatein filament was isolated from the spicule and found that it has three isoforms (silicatein α, β & γ).[7,12] Silicatein plays two roles in silicification process. The first, catalytic activity is suggested from the study followed by Cha J.N et al where the axial filaments separated from the spicule showed catalysed hydrolysis of various silicon precursors at physiological conditions.[15] The activity was reproduced by silicatein monomers separated from the filament as well as by the recombinant form synthesized in genetically engineered Escherichia coli. The site Ser (26) and /or Histidine (165) of silicatein α in the mutant protein were replaced by alanine, and the silica formation significantly decreased.[16] This indicated the active groups involved in the catalysis were hydroxyl side chain at Serine and imidazole side group at Histidine site in silicatein. Based on this and the catalytic hydrolysis of the peptide bond by serine proteases following explanation of the reaction was theorized:[17]

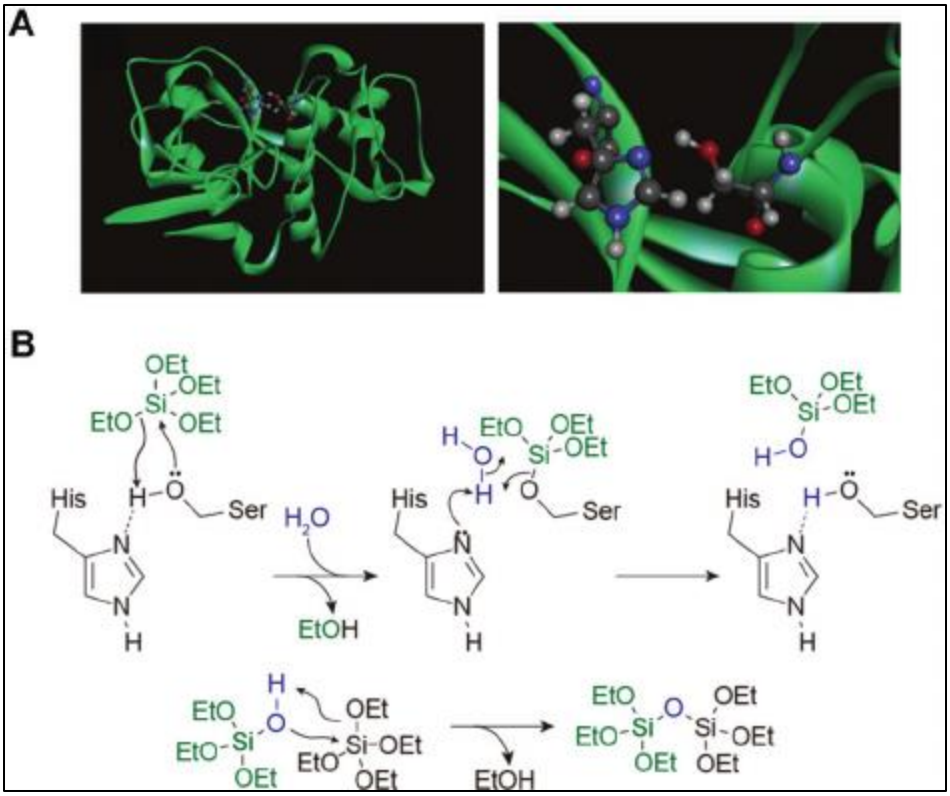


Figure 1-1:[A] Silicatein a protein. (right) enlarged serine hydrolase catalytic site. [B]: The hydroxyl bond from the Ser site initiates a nucleophilic attack on the Si ion in the precursor, causing hydrolysis of TEOS, leading to condensation of TEOS and formation of Si-O-Si bond.

The second role is that of templating agent and constructing the axial filament. Self-assembly of silicatein to form a filamentous structure maybe mediated by interaction with the hydrophobic patches on surfaces on silicatein isoforms.[14] This was tested by treatment with heat and detergent that led to inhibited activity. The isoforms guide the condensation to occur over the length of filament.[15]

Continued efforts for deeper understanding of the mechanism and the process of biosilicification are being pursued by researches and still on-going work. Summarized information about the study on different levels of molecular, biological and structural hierarchy controlling the fabrication of intricately architectured spicules has been

obtained from Wang et al [18] to have a clear understanding of how the knowledge can be used towards the fabrication of new technology/applications.

Genetic Hierarchy – describes the function of silicatein, silintaphin-1 and silintaphin-2 as the pillars of the enzymatic machinery involved in the silicification process. Silicatein is the only pillar involved in enzymatic silica polymerization activity. Silintaphin-1 is silicatein interacting protein that enhanced the biosilica formation activity of silicatein when added in 4:1 ratio [Silicatein: silintaphin-1].[7] Silintaphin-2 is another interacting protein that provides $Ca^{2+}$ required for formation between galectin and silicatein, main components of organic spectrum of growing spicules.[19] The pH of the reaction decides the type of aggregate formation due to the change in charge on the silica particles where at pH<7, the particles are weakly ionized allowing fibrillar structure and at pH>7 the charge particle promote Ostwald ripening process, enlarging the particle size but decreasing the particle number.[18]

Biological Hierarchy – identifies the cellular pillars involved in the synthesis as sclerocytes, archaeocytes, chromocytes and lophocytes. Sclerocytes are cells that provide silicatein, silintaphin-1 and premature silintaphin-2.[20,18] Archaeocytes produce galectin, and important component that forms the organic cylinder with silicatein.[21,22,18] Chromocytes induced by silicates, release BMP-1 , that allows silintaphin-2 to mature and deliver $Ca^{2+}$ ions to extraspicular space where the organic shell is produced.[18] Lophocytes contribute in collagen production.[23] The growth of spicule occurs in two directions, axially via elongation of the filament and appositional layering of the silica lamellae. The soft silica ages during biosintering and hardens.[24,25]

Structural Hierarchy – Involves the process of “precision biosilica moulding” where the soft amorphous silica gets injected into the organic cast and hardens and the spicule achieves the final shape.[18]

These studies reveal that the biosilica is potentially an intelligent material, since main component involves protein, it could exhibit self-repair properties.[26] It can show adaptive capabilities to the level of polycondensation required via genetic and biological control. Most biological reactions being reversible, this system could also have a feedback control (quality of the silica produced) formed.[26] The anabolically driven silicatein reaction is countered by the catabolically acting enzyme silicase.[27] Dynamic feedback mechanisms are crucial in adjusting the dynamic homeostasis of internal environment of living systems[28,18] and very difficult to adapt in synthetic processes. These works provide with strategies to fabricate hybrid particles based glass materials that can be used as potential biomaterials for bone repair processes.[29]

*Biosilica Applications:*

Silicon is seen to accumulate in mammal, in tissues adjoining bone forming regions.[30] It has been demonstrated that silicon, and biosilica prepared with silicatein as well, have shown upregulation of osteoblasts[31] and adverse effects on osteoclasts.[32] It was seen in SaOS-cell line that presence of biosilica displayed differential gene expression, with increasing steady state level of osteoprotegerin (OPG) transcripts without changing the transcript level of the osteoclasto-genic ligand, receptor activator of nuclear factor-kB (NF-kB) ligand (RANKL).[31] Thus making biosilica a potential replacement biomaterial for osteogenic applications.

It is also considered for other biomedical applications like surface coatings, scaffolds and biomolecules delivery.[33]

Based on all this gathered knowledge regarding the silicification mechanism in sponges and diatoms, studies have been pursued to understand the polymer based processes with alkoxides as precursors. Polymerization of these precursors to form sol gels involves three steps (a) Formation of particles (b) Growth of particles (c) Formation of the network.[34] If the process can be stopped at step (b) then it can help achieve fine

particles of nano/micro size. The use of catalytically charged synthetic polymer for the same is proposed. It is also suggested this polymer may function in similar mechanism as silicatein in facilitating Si structures. The results of this study proved that it was not only proteins that could catalyse the synthesis of silica at neutral pH and support as template.[35]

In the proposed research, study has been pursued to reproduce silica synthesis of TEOS precursor by following the silicatein mechanism but replacing the enzyme with functionally similar polymers to achieve silica particles at room temperature and pressure and natural pH conditions.

*Scientific Merit and Socio-Economic importance of proposed research work:*

Silica ($SiO_2$) being one of the most abundant materials on earth's crust has found its way into the maximum applications in human life. It is used in various industry from construction industry to biomedical and health applications and still finding use in many new areas and fields.

The Global Precipitated Silica Market Report 2017- 2021 published by Technavio for next 5 years predicts steady growth in market and a CAGR of >6% during the time.[36] According to report published by Future Market Insights on Specialty Silica Market, precipitated silica is expected to dominate the market for forecast period of 2016-2026 besides the fumed, fused and colloidal silica. Global demand for specialty silica in terms of volume stands at 3188.1KT (thousand tonnes) at the end of 2016 again with precipitate silica being the dominant in the market.[37]

Being able to develop alternative greener, faster and smarter production technique to this US$ 5.6Bn industry[37] will definitely help environment by replacing the harsh synthesis conditions and resulting by-products.

By using biosilica synthesis within sponge as inspiration we are learning from the most optimized and well tested techniques used and developed by nature over millions

of years. In this approach core scientific understanding of natural process has been studied before proposing the man-made/synthetic approach that will lead to similar results. The entire approach has been mimicked at molecular level allowing to understand the exact chemical mechanism of synthesis reaction as well as test the theory. The results of these tests will help understand fundamentals of catalytic activity involved and elucidate the templating function of enzymes in natural sponges and gain knowledge to controlled synthesis and morphology of silica particles, that form a major part of today's industry and applications.

## 2. Aims and Objectives:

The main aim of the proposed research is to elucidate the mechanism for biosilicification and achieve potentially a greener technique for synthesizing amorphous silica that will be beneficial for novel applications and/or new technologies for nanomaterials production. The second half of the research will be focusing on its application in biomedicine/biotechnology as a potential material for osteogenic applications. Complete chemical pathway for synthesis of silica will be explored in detail as well as the contribution of silicon in osteogenesis via biological study will be done. This will contribute to valuable knowledge to fields of biotechnology and biology/chemistry.

The study focuses on biomimicking the theoretically observed mechanism of silicification in sponges via silicatein by replacing the natural protein silicatein with functionally similar chemicals. The aim is to generate amorphous silicon particles at low temperature, pressure and natural pH conditions at rate as fast as 30 min. The product will be further tested for its biological compatibility and its applicability for osteogenic applications as a scaffold material will be explored.

A combinatorial package including both material and biological characterisation tests will be used to investigate the details of chemical synthesis of the amorphous Si and its contribution as the Silicon donor for biomineralization process of bone.

Hypothesis:

It is seen in literature that Si based materials have improved bone regeneration rate.[38,39,9] Silicon is involved in biomineralization process, though the exact pathway is unknown. The use of biosilica based materials like diatoms have shown improved rate of bone regeneration.[40,41] The understanding of silicification process in these natural sources has been well documented.[42,43,44] Researchers have narrowed down the process to catalytic involvement of enzymes like silicatein present in sponges and sillafins present in diatoms, that help generate $SiO_2$ at low temperature, pressure and neutral pH conditions. Cha et al further has further tested silicatein in detail to conclude that the serine and histidine moieties in the protein are the active sites contributing to silica generation.[15]

Biotechnologists, have used this knowledge to further enhance its applicability as biomaterial in bone regeneration applications. They have incorporated silicatein, as encapsulated nanomaterials loaded at the defect site, to improve regeneration by supplying the catalyst at the defect site and relying on Si ions from the natural system as a source to create silica.[45]

This research work focuses on mimicking the role of the active sites by using structurally similar chemicals imidazole and glucose in presence of Si precursor to create the amorphous Si that can then be used as a direct source for regeneration. Since it is bio-mimicked the properties of generated Si will be similar to biosilica helping in increased improvement.

The knowledge acquired from these experiments will help have a detailed control on creation of Si particles in terms of morphology, activity and functionality. This can be further used for exploring different applications such as coatings or patterned surfaces. Also the chemical synthesis approach can be extended to other materials, to enable their generation at low temperature, pressure, neutral pH conditions at a quick rate.

The study of these methods are aimed such that scale up processes are easier to achieve and industrial manufacturing of these materials is a viable option in near future (within 5 years).

### 2.1. Aim 1: Synthesis of the Si particles via biomimicking

The first step will be to select the catalysts to mimic the role of silicatein. The most identical chemistries seemed to be that of imidazole and glucose. Complex polymers are not selected at first to keep the mechanistic understanding simpler. The other chemical involved would be the precursor, TEOS and TMOS being the preferred two in literatures. To recreate the synthesis, understanding of the different affecting parameters like concentrations of the chemicals involved, reaction time, reaction pH, reaction stopping, particle separation. The variables are optimised to achieve particle nucleation and growth enough to be able to separate them from the liquid phase. These particle reactions are studied using SEM and EDX for basic formations. FTIR/Raman, XRD and XANES studies will be further pursued to get detailed analysis of the achieved chemical composition and structure of the material. These characteristics shall also be compared with the natural siliceous spicules obtained from the sponge Tethya aurantia to be able to compare the design to its original.

### 2.2. Aim 2:Understanding the mechanism of the bio mimicked process

Different experiments will be designed to conduct the evaluation of each functional group involved in the synthesis and understand its functionality. Different

concentrations of the catalysts will be tested to know the minimum limits at which their presence becomes effective and also be able to understand the efficiency of the reaction. Elucidate the parameters affecting particle morphology and size, by varying the catalyst from monomers to polymers.

Study the parameters affecting silicification process of precursor TEOS by comparing with behaviour of TMOS when used as precursor as noted in literature. Also analyse whether the mechanism is precursor specific and thus contribute to knowledge of precursor hydrolysis and condensation process acquired till now.

The results of these tests will be again characterized by material characterization techniques such as SEM, EDX, FTIR/Raman, XRD and XANES.

These experimental details will contribute to the currently understood mechanism of silicification while cementing the fundamentals of science of silicification.

### 2.3. Aim 3:

Applicability of the particles in biotechnology/osteogenic applications.

The particles will be first evaluated for basic biocompatibility such as cytotoxicity, proliferation and metabolism. To do so the particles will be embedded with Fibroin obtained from Bombyx Mori Silk cocoons to make a controlled 2D structure. Again, their performance will be compared to natural particles. Further complex studies will be done with 3D structures. Designs to make scaffold using the material will be explored. The mechanical strength of these particles on their own may not be sufficient and hence and the other material to make composite scaffold will be required to be selected as well. Studies involving, different particle weight compositions, placement of particles (bulk or as coating) will also be conducted besides its dissolution characteristics to further enable understanding to the role of Si played in biomineralization. Biological tests like cytotoxicity, cell proliferation and metabolism and osteogenic activation will be conducted to test the scaffold made using generated Silica.

3. Dissertation Structure:

The following paragraphs provide an overview and summary of the five chapters of this dissertation. In addition, the relevance and contribution of each chapter to the central theme of the dissertation will be highlighted.

Chapter 1, General Introduction: This chapter starts with the background and significance of study pursued divided in three parts. First part deals with the general information about silica and its production rates and signifies why studying synthesis mechanism of biosilica is important. Second part deals with what is known and understood about biosilica silicification mechanism already and what knowledge can be taken from this while forming the hypothesis. Third part deals with the applications of biosilica in biomedical field and potential uses for the product resulting as an outcome of the pursued research. Then it moves on to describe the specific aims of this research work. Overall this chapters contains the important scientific information that forms the backbone of the information derived and explained in the remaining chapters.

Chapter 2 includes previously published papers in which, the work that has been contributed, was used to develop the background for the remaining thesis. The paper on “Role of Hydrogen and Nitrogen on the Surface Chemical Structure of Bioactive Amorphous Silicon Oxynitride Films” discusses the effects of nitrogen incorporation in SiO films via PECVD processes on surface chemical structures. The chemistries are studied using different characterisation methods to analyse the chemical make-up and the type of bonding models, random bonding vs random mixing followed as N incorporation increases. The main layout of the work was developed and done by authors Venu Varanasi, Pranesh Aswath, Megen Velten and Azhar Ilyas. The RMM and RBM modelling and partial charge calculations based on RBS, XANES and EDS data found and its theory was contributed by authors Ami Shah and Venu Varanasi. This

modelling study has been further used in this thesis to understand the chemical structural formation of bio mimicked particles. Chapter 2 also includes the paper on “Amorphous Silica, a New Antioxidant Role for Rapid Critical-Sized Bone Defect Healing”. This paper discusses the effects of Si ion release on the SOD 1 and hence enhanced osteogenesis offered by the amorphous SiON coatings. In-vitro studies and exclusive Si ion release studies were performed to understand the effect and underlying mechanism in which Si ions function. Positive effects of the ions also warranted in-vivo studies which further confirmed beneficial incorporation of N which affected the Si ion release. This study is combined contribution of biological and material analysis work of many authors, Azhar Ilyas, Tetsuro Odatsu, Ami Shah, Felipe Monte, Harry K.W. Kim, Philip Kramer, Pranesh B. Aswath and Venu G. Varanasi, each lending expertise in their fields. The individual contribution of thesis author Ami Shah was in particular in material characterisation of samples from in-vivo study using Raman spectroscopy, to study the chemical changes in the surface structure and formation of new bone, XANES analysis and SEM EDX study of the surfaces at the end of in-vivo studies. The results of this study further were used as a background to validate potential of the bio mimicked particles in bone tissue engineering and hence pursue in-vitro studies on these particles. The dissolution study from this paper also led to need of understanding the various different parameters that affected the Si ion release besides the chemistry and hence became one of the main goals of this thesis study.

Chapter 3 includes the study pursued to synthesize nanosized silica structures following method stated in hypothesis. This chapter provides the exact experimental procedure followed to successfully synthesize the particles. It discusses the results of the detailed characterisations performed on the obtained materials to accurately understand it morphology, chemical composition and structure. It also discusses the study to elucidate the synthesis mechanism of these particles. Experimental design to

realise the functional contribution of each reactant and XPS and XANES characterisations used to study the effect of these contributions in the molecular structure are reported herein. Overall this chapter deals with the specific aims 1 and 2, showing that the hypothesis regarding the synthesis mechanism is true and also to unfold that the reactants have more functions than covered in the hypothesis.

Chapter 4 explores the applicability of the synthesized material as potential bioactive material in bone tissue engineering application. The particles are loaded onto silk fibroin films and tested for various bioactivity factors. The activity of these particles is also compared with the natural material  Tethya aurantia spicules. The fabrication process of the test films and their morphological characterisation are stated in this chapter. They are further tests for cytotoxicity, adhesion, morphology, cell proliferation and metabolic activity using a set of various assays. The results show that the particles are non-cytotoxic, and cells prefer to grow in their environments. They show comparable performance with the natural material and improved performance than bare silk fibroin control.

Chapter 5 deals with the different fabrication models for 3D scaffolds incorporating the synthesized particles to create potential test platforms for the complex in-vitro studies. Silk fibroin scaffolds and bTCP scaffolds are chosen as the base scaffolds on which materials were loaded in different ways. These scaffolds are characterised to observe their architecture and morphology. They are tested with FTIR to look at effect of particle incorporation on the chemical bonding nature of the base material. Other important parameters of scaffolds that affects its applicability in tissue engineering such as pore size, porosity, hydrophilicity are also tested in these chapters. In-vitro dissolution experiments to study the effects of various parameters on the kinetics of $Si^{4+}$ ions release rate from the particles is also studied. This study can provide with

data for tuneable properties of silica based scaffolds that in turn can be used appropriately to enhance the SOD1 activity and hence the osteogenesis process.

Chapter 6 presents the final conclusions of this dissertation work. This chapter summarizes the major findings of this research and also provides an insight into how the results of each chapter are interconnected to each other and to the central idea of the dissertation.

References:


1. Rahman IA, Padavettan V. Synthesis of Silica Nanoparticles by Sol-Gel: Size-Dependent Properties, Surface Modification, and Applications in Silica-Polymer Nanocomposites—A Review. *J Nanomater*. 2012;2012:1-15. doi:10.1155/2012/132424.
2. Wong Po Foo C, Patwardhan S V., Belton DJ, et al. Novel nanocomposites from spider silk-silica fusion (chimeric) proteins. *Proc Natl Acad Sci*. 2006;103(25):9428-9433. doi:10.1073/pnas.0601096103.
3. World Markets for Precipitated Silica 2006. 2006. http://www.notchconsulting.com/pdf/Silica_Contents06.pdf. Accessed August 27, 2017.
4. Tacke. Milestones in the Biochemistry of Silicon: From Basic Research to Biotechnological Applications. *Angew Chem Int Ed Engl*. 1999;38(20):3015-3018. http://www.ncbi.nlm.nih.gov/pubmed/10540406. Accessed August 27, 2017.
5. Tréguer P, Nelson DM, Bennekom AJ Van, et al. The Silica Balance in the World Ocean: A Reestimate. *Source Sci*. 1995;268(21):375-379. http://www.jstor.org/stable/2886587. Accessed August 27, 2017.
6. Belton DJ, Deschaume O, Perry CC. An overview of the fundamentals of the chemistry of silica with relevance to biosilicification and technological advances. *FEBS J*. 2012;279(10):1710-1720. doi:10.1111/j.1742-4658.2012.08531.x.
7. Schloßmacher U, Wiens M, Schröder HC, Wang X, Jochum KP, Müller WEG. Silintaphin-1 - interaction with silicatein during structure-guiding bio-silica formation. *FEBS J*. 2011;278(7):1145-1155. doi:10.1111/j.1742-4658.2011.08040.x.
8. Patwardhan S V., Lee KB, Kim DJ, et al. Biomimetic and bioinspired silica: recent developments and applications. *Chem Commun*. 2011;47(27):7567. doi:10.1039/c0cc05648k.
9. Wang X, Schröder HC, Müller WEG. Enzyme-based biosilica and biocalcite: Biomaterials for the future in regenerative medicine. *Trends Biotechnol*. 2014;32(9):441-447. doi:10.1016/j.tibtech.2014.05.004.
10. Weaver JC, Pietrasanta LI, Hedin N, Chmelka BF, Hansma PK, Morse DE. Nanostructural features of demosponge biosilica. *J Struct Biol*. 2003;144(3):271-281. doi:10.1016/j.jsb.2003.09.031.

11. Polini A, Pagliara S, Camposeo A, et al. Optical properties of in-vitro biomineralised silica. *Sci Rep*. 2012;2:0-5. doi:10.1038/srep00607.

12. Imsiecke G, Steffen R, Custodio M, Borojevic R, G MiLLER WE. FORMATION OF SPICULES BY SCLEROCYTES FROM THE FRESHWATER SPONGE EPHYDATIA MUELLERI IN SHORT-TERM CULTURES IN VITRO. *Vitr Cell Dev Biol--Animal*. 1995;31:528-535. https://link.springer.com/content/pdf/10.1007/BF02634030.pdf. Accessed August 27, 2017.

13. Arakaki A, Shimizu K, Oda M, Sakamoto T, Nishimura T, Kato T. Biomineralization-inspired synthesis of functional organic/inorganic hybrid materials: Organic molecular control of self-organization of hybrids. *Org Biomol Chem*. 2015;13(4):974-989. doi:10.1039/C4OB01796J.

14. Murr MM, Morse DE. Fractal intermediates in the self-assembly of silicatein filaments. http://www.pnas.org/content/102/33/11657.full.pdf. Accessed August 27, 2017.

15. Cha JN, Shimizu K, Zhou Y, et al. Silicatein filaments and subunits from a marine sponge direct the polymerization of silica and silicones in vitro. *Proc Natl Acad Sci U S A*. 1999;96(2):361-365. doi:10.1073/PNAS.96.2.361.

16. Zhou Y, Shimizu K, Cha J, Stucky G. Efficient catalysis of polysiloxane synthesis by silicatein α requires specific hydroxy and imidazole functionalities. *Angew Chemie*. 1999. http://onlinelibrary.wiley.com/doi/10.1002/(SICI)1521-3773(19990315)38:6%3C779::AID-ANIE779%3E3.0.CO;2-%23/full. Accessed August 27, 2017.

17. Arakaki A, Shimizu K, Oda M, Sakamoto T, Nishimura T, Kato T. Biomineralization-inspired synthesis of functional organic/inorganic hybrid materials: organic molecular control of self-organization of hybrids. *Org Biomol Chem*. 2015;13(4):974-989. doi:10.1039/C4OB01796J.

18. Wang X, Schröder HC, Wang K, et al. Genetic, biological and structural hierarchies during sponge spicule formation: from soft sol–gels to solid 3D silica composite structures. *Soft Matter*. 2012;8(37):9501. doi:10.1039/c2sm25889g.

19. Müller WEG, Binder M, von Lintig J, et al. Interaction of the retinoic acid signaling pathway with spicule formation in the marine sponge Suberites domuncula through activation of bone morphogenetic protein-1. *Biochim Biophys Acta - Gen Subj*. 2011;1810(12):1178-1194. doi:10.1016/j.bbagen.2011.09.006.

20. Simpson TL. *The Cell Biology of Sponges*. New York, NY: Springer New York; 1984. doi:10.1007/978-1-4612-5214-6.

21. Müller WEG, Blumbach B, Wagner-Hülsmann C, Lessel U, 淳平林. Galectins in the Phylogenetically Oldest Metazoa, the Sponges (Porifera). *Trends Glycosci Glycotechnol*. 1997;9(45):123-130. doi:10.4052/tigg.9.123.

22. Schütze J, Krasko A, Diehl-Seifert B, Müller WEG. Cloning and expression of the putative aggregation factor from the marine sponge Geodia cydonium. *J Cell Sci*. 2001;114(17). http://jcs.biologists.org/content/114/17/3189.short. Accessed August 28, 2017.

23. Harrison F, Davis D. Morphological and cytochemical patterns during early stages of

reduction body formation in Spongilla lacustris (Porifera: Spongillidae). *Trans Am Microsc Soc*. 1982. http://www.jstor.org/stable/3225749. Accessed August 28, 2017.

24. Müller W, Rothenberger M, Boreiko A. Formation of siliceous spicules in the marine demosponge Suberites domuncula. *Cell tissue*. 2005. http://link.springer.com/article/10.1007/s00441-005-1141-5. Accessed August 28, 2017.

25. Schröder HC, Boreiko A, Korzhev M, et al. Co-expression and Functional Interaction of Silicatein with Galectin. *J Biol Chem*. 2006;281(17):12001-12009. doi:10.1074/jbc.M512677200.

26. Müller WEG, Schloßmacher U, Wang X, et al. Poly(silicate)-metabolizing silicatein in siliceous spicules and silicasomes of demosponges comprises dual enzymatic activities (silica polymerase and silica esterase). *FEBS J*. 2008;275(2):362-370. doi:10.1111/j.1742-4658.2007.06206.x.

27. Silicase, an enzyme which degrades biogenous amorphous silica: contribution to the metabolism of silica deposition in the demosponge Suberites domuncula. *Prog Mol Subcell*. 2003. http://link.springer.com/content/pdf/10.1007/978-3-642-55486-5.pdf#page=252. Accessed August 28, 2017.

28. Bernard C. *Introduction à l'étude de La Médecine Expérimentale Par m. Claude Bernard*.; 1865. https://books.google.com/books?hl=en&lr=&id=iBdSKwntgUAC&oi=fnd&pg=PA5&dq=C+bernard+1865+introduction+a+l%27Etude&ots=xW586PKZEE&sig=amCMOH0qSlxoTYVZ4BALTOOGT84. Accessed August 28, 2017.

29. Wang X, Schröder H, Wiens M, Ushijima H. Bio-silica and bio-polyphosphate: applications in biomedicine (bone formation). *Curr Opin*. 2012. http://www.sciencedirect.com/science/article/pii/S095816691200033X. Accessed August 28, 2017.

30. Jugdaohsingh R. Silicon and bone health. *J Nutr Health Aging*. 2007. https://www.ncbi.nlm.nih.gov/pmc/articles/PMC2658806/. Accessed August 28, 2017.

31. Wiens M, Wang X, Schröder H, Kolb U. The role of biosilica in the osteoprotegerin/RANKL ratio in human osteoblast-like cells. *Biomaterials*. 2010. http://www.sciencedirect.com/science/article/pii/S0142961210008434. Accessed August 28, 2017.

32. Schröder H, Wang X, Wiens M. Silicate modulates the cross-talk between osteoblasts (SaOS-2) and osteoclasts (RAW 264.7 cells): Inhibition of osteoclast growth and differentiation. *J Cell*. 2012. http://onlinelibrary.wiley.com/doi/10.1002/jcb.24196/full. Accessed August 28, 2017.

33. Jo BH, Kim CS, Jo YK, Cheong H, Cha HJ. Recent developments and applications of bioinspired silicification. *Korean J Chem Eng*. 2016;33(4):1125-1133. doi:10.1007/s11814-016-0003-z.

34. Boehm H. The chemistry of silica. Solubility, polymerization, colloid and surface properties, and biochemistry. Von RK Iler. John Wiley and Sons, Chichester 1979. XXIV, 886 S.,. *Angew Chemie*. 1980.

http://onlinelibrary.wiley.com/doi/10.1002/ange.19800920433/full. Accessed August 28, 2017.

35. Patwardhan S V, Mukherjee N, Clarson SJ. Effect of process parameters on the polymer mediated synthesis of silica at neutral pH. *Silicon Chem*. 2002;1(1):47-54. doi:10.1023/A:1016026927401.

36. Global Precipitated Silica Market 2017-2021 | Market Research Reports - Industry Analysis Size & Trends - Technavio. Technavio. https://www.technavio.com/report/global-specialty-chemicals-global-precipitated-silica-market-2017-2021. Published 2017. Accessed August 27, 2017.

37. Specialty Silica Market - Global Industry Analysis, Size and Forecast, 2016 to 2026. Future Market Insights. doi:2016-05-24.

38. Odatsu T, Azimaie T, Velten MF, et al. Human periosteum cell osteogenic differentiation enhanced by ionic silicon release from porous amorphous silica fibrous scaffolds. *J Biomed Mater Res - Part A*. 2015;103(8):2797-2806. doi:10.1002/jbm.a.35412.

39. Ilyas A, Lavrik N V., Kim HKW, Aswath PB, Varanasi VG. Enhanced Interfacial Adhesion and Osteogenesis for Rapid “bone-like” Biomineralization by PECVD-Based Silicon Oxynitride Overlays. *ACS Appl Mater Interfaces*. 2015;7(28):15368-15379. doi:10.1021/acsami.5b03319.

40. Cicco SR, Vona D, De Giglio E, et al. Chemically Modified Diatoms Biosilica for Bone Cell Growth with Combined Drug-Delivery and Antioxidant Properties. *Chempluschem*. 2015;80(7):1104-1112. doi:10.1002/cplu.201402398.

41. Le TDH, Bonani W, Speranza G, et al. Processing and characterization of diatom nanoparticles and microparticles as potential source of silicon for bone tissue engineering. *Mater Sci Eng C*. 2016;59:471-479. doi:10.1016/j.msec.2015.10.040.

42. Likhoshway Y V., Sorokovikova EG, Belykh OI, et al. Visualization of the silicon biomineralization in cyanobacteria, sponges and diatoms. *Biosph Orig Evol*. 2008;(Table 1):219-230. doi:10.1007/978-0-387-68656-1_16.

43. M??ller WEG, Wang X, Cui FZ, et al. Sponge spicules as blueprints for the biofabrication of inorganic-organic composites and biomaterials. *Appl Microbiol Biotechnol*. 2009;83(3):397-413. doi:10.1007/s00253-009-2014-8.

44. Müller WEG, Wang X, Belikov SI, et al. Formation of Siliceous Spicules in Demosponges: Example Suberites domuncula. *Handb Biomin Biol Asp Struct Form*. 2008;1:59-82. doi:10.1002/9783527619443.ch4.

45. Wang S, Wang X, Draenert FG, et al. Bioactive and biodegradable silica biomaterial for bone regeneration. *Bone*. 2014;67:292-304. doi:10.1016/j.bone.2014.07.025.

46. Iler RK. *The Chemistry of Silica : Solubility, Polymerization, Colloid and Surface Properties, and Biochemistry*. Wiley; 1979. https://www.wiley.com/en-us/The+Chemistry+of+Silica%3A+Solubility%2C+Polymerization%2C+Colloid+and+Surface+Properties+and+Biochemistry+of+Silica-p-9780471024040. Accessed May 6, 2018.

47. Healy TW. Stability of Aqueous Silica Sols. In: ; 1994:147-159. doi:10.1021/ba-1994-

0234.ch007.

48. Chen* S-L, Peng Dong, Guang-Hua Yang and, Yang J-J. Kinetics of Formation of Monodisperse Colloidal Silica Particles through the Hydrolysis and Condensation of Tetraethylorthosilicate. 1996. doi:10.1021/IE9602217.

49. Coltrain BK, Kelts LW. The Chemistry of Hydrolysis and Condensation of Silica Sol—Gel Precursors. In: ; 1994:403-418. doi:10.1021/ba-1994-0234.ch019.

50. Patwardhan S V., Clarson SJ. Silicification and biosilicification. *Polym Bull*. 2002;48(4-5):367-371. doi:10.1007/s00289-002-0043-x.

51. Brinker CJ, Scherer GW. *Sol-Gel Science : The Physics and Chemistry of Sol-Gel Processing*. Academic Press; 1990.

52. Stöber W, Fink A, Bohn E. Controlled growth of monodisperse silica spheres in the micron size range. *J Colloid Interface Sci*. 1968;26(1):62-69. doi:10.1016/0021-9797(68)90272-5.

53. Kröger N, Deutzmann R, Sumper M. Polycationic peptides from diatom biosilica that direct silica nanosphere formation. *Science*. 1999;286(5442):1129-1132. http://www.ncbi.nlm.nih.gov/pubmed/10550045. Accessed May 6, 2018.

54. Patwardhan S V, Clarson SJ. Silicifacation and biosilicification Part 6. Poly-L-histidine mediated synthesis of silica at neutral pH. *J Inorg Organomet Polym*. 2003;13(1):49-53. doi:10.1023/A:1022952931063.

55. Cha JN, Stucky GD, Morse DE, Deming TJ. Biomimetic synthesis of ordered silica structures mediated by block copolypeptides. *Nature*. 2000;403(6767):289-292. doi:10.1038/35002038.

56. Tahir MN, Théato P, Müller WEG, et al. Monitoring the formation of biosilica catalysed by histidine-tagged silicatein. *Chem Commun*. 2004;0(24):2848-2849. doi:10.1039/B410283E.

57. Tahir MN, Théato P, Müller WEG, et al. Formation of layered titania and zirconia catalysed by surface-bound silicatein. *Chem Commun*. 2005;0(44):5533. doi:10.1039/b510113a.

58. Tahir MN, Eberhardt M, Therese HA, et al. From Single Molecules to Nanoscopically Structured Functional Materials: Au Nanocrystal Growth on TiO2 Nanowires Controlled by Surface-Bound Silicatein. *Angew Chemie Int Ed*. 2006;45(29):4803-4809. doi:10.1002/anie.200503770.

59. Jan L. Sumerel, Wenjun Yang, David Kisailus, James C. Weaver, Joon Hwan Choi and, Morse* DE. Biocatalytically Templated Synthesis of Titanium Dioxide. 2003. doi:10.1021/CM030254U.

60. Kisailus D, Choi JH, Weaver JC, Yang W, Morse DE. Enzymatic Synthesis and Nanostructural Control of Gallium Oxide at Low Temperature. *Adv Mater*. 2005;17(3):314-318. doi:10.1002/adma.200400815.

61. Gritsenko VA, Kwok RWM, Wong H, Xu JB. Short-range order in non-stoichiometric amorphous silicon oxynitride and silicon-rich nitride. *J Non Cryst Solids*. 2002;297(1):96-

101. doi:10.1016/S0022-3093(01)00910-3.

62. Bruggeman DAG, G. DA. Berechnung verschiedener physikalischer Konstanten von heterogenen Substanzen. I. Dielektrizitätskonstanten und Leitfähigkeiten der Mischkörper aus isotropen Substanzen. *Ann Phys*. 1935;416(7):636-664. doi:10.1002/andp.19354160705.

63. Kuiper AET. Deposition and composition of silicon oxynitride films. *J Vac Sci Technol B Microelectron Nanom Struct*. 1983;1(1):62. doi:10.1116/1.582543.

64. Snyder PG, Xiong Y-M, Woollam JA, et al. Graded refractive index silicon oxynitride thin film characterized by spectroscopic ellipsometry. 1992. http://digitalcommons.unl.edu/electricalengineeringfacpub. Accessed May 19, 2018.

65. Varanasi VG, Ilyas A, Velten MF, Shah A, Lanford WA, Aswath PB. Role of Hydrogen and Nitrogen on the Surface Chemical Structure of Bioactive Amorphous Silicon Oxynitride Films. *J Phys Chem B*. 2017;121(38):8991-9005. doi:10.1021/acs.jpcb.7b05885.

66. XANES: Theory - Chemistry LibreTexts. https://chem.libretexts.org/Core/Physical_and_Theoretical_Chemistry/Spectroscopy/X-ray_Spectroscopy/XANES%3A_Theory. Accessed May 5, 2018.

67. Wang S-F, Wang X-H, Gan L, Wiens M, Schröder HC, Müller WEG. Biosilica-glass formation using enzymes from sponges [silicatein]: Basic aspects and application in biomedicine [bone reconstitution material and osteoporosis]. *Front Mater Sci*. 2011;5(3):266-281. doi:10.1007/s11706-011-0145-1.

68. Kim S. *Marine Biomaterials Characterization, Isolation and Applications.* CRC Pr I Llc; 2017.

69. Silva TH, Alves A, Ferreira BM, et al. Materials of marine origin: a review on polymers and ceramics of biomedical interest. *Int Mater Rev*. 2012;57(5):276-306. doi:10.1179/1743280412Y.0000000002.

70. Sowjanya JA, Singh J, Mohita T, et al. Biocomposite scaffolds containing chitosan/alginate/nano-silica for bone tissue engineering. *Colloids Surfaces B Biointerfaces*. 2013;109:294-300. doi:10.1016/j.colsurfb.2013.04.006.

71. Ravichandran R, Sundaramurthi D, Gandhi S, Sethuraman S, Krishnan UM. Bioinspired hybrid mesoporous silica–gelatin sandwich construct for bone tissue engineering. *Microporous Mesoporous Mater*. 2014;187:53-62. doi:10.1016/J.MICROMESO.2013.12.018.

72. Wang X, Schröder HC, Grebenjuk V, et al. The marine sponge-derived inorganic polymers, biosilica and polyphosphate, as morphogenetically active matrices/scaffolds for the differentiation of human multipotent stromal cells: potential application in 3D printing and distraction osteogenesis. *Mar Drugs*. 2014;12(2):1131-1147. doi:10.3390/md12021131.

73. Wang X, Schröder HC, Wiens M, Ushijima H, Müller WE. Bio-silica and bio-polyphosphate: applications in biomedicine (bone formation). *Curr Opin Biotechnol*. 2012;23(4):570-578. doi:10.1016/j.copbio.2012.01.018.

74. Patwardhan S V, Mukherjee N, Steinitz-Kannan M, Clarson SJ. Bioinspired synthesis of new silica structures. doi:10.1039/b302056h.

75. Le TDH, Liaudanskaya V, Bonani W, Migliaresi C, Motta A. Enhancing bioactive properties of silk fibroin with diatom particles for bone tissue engineering applications. *J Tissue Eng Regen Med*. 2018;12(1):89-97. doi:10.1002/term.2373.

76. Rezwan K, Chen QZ, Blaker JJ, Boccaccini AR. Biodegradable and bioactive porous polymer/inorganic composite scaffolds for bone tissue engineering. *Biomaterials*. 2006;27:3413-3431. doi:10.1016/j.biomaterials.2006.01.039.

77. Wu X, Liu Y, Li X, et al. Preparation of aligned porous gelatin scaffolds by unidirectional freeze-drying method. *Acta Biomater*. 2010;6(3):1167-1177. doi:10.1016/j.actbio.2009.08.041.

78. Liu C, Xia Z, Czernuszka JT. Design and Development of Three-Dimensional Scaffolds for Tissue Engineering. *Chem Eng Res Des*. 2007;85(7):1051-1064. doi:10.1205/cherd06196.

79. Holzwarth JM, Ma PX. Biomimetic nanofibrous scaffolds for bone tissue engineering. *Biomaterials*. 2011;32(36):9622-9629. doi:10.1016/j.biomaterials.2011.09.009.

80. Guarino V, Causa F, Ambrosio L. Bioactive scaffolds for bone and ligament tissue. *Expert Rev Med Devices*. 2007;4(3):405-418. doi:10.1586/17434440.4.3.405.

81. Descamps M, Richart O, Hardouin P, Hornez JC, Leriche A. Synthesis of macroporous β-tricalcium phosphate with controlled porous architectural. *Ceram Int*. 2008;34(5):1131-1137. doi:10.1016/j.ceramint.2007.01.004.

82. Ko E, Cho S-W. Biomimetic Polymer Scaffolds to Promote Stem Cell-Mediated Osteogenesis. *Int J Stem Cells*. 2013;6(2):87-91. doi:10.15283/ijsc.2013.6.2.87.

83. Mieszawska AJ, Llamas JG, Vaiana CA, Kadakia MP, Naik RR, Kaplan DL. Clay enriched silk biomaterials for bone formation. *Acta Biomater*. 2011;7(8):3036-3041. doi:10.1016/j.actbio.2011.04.016.

84. Ilyas A, Odatsu T, Shah A, et al. Amorphous Silica: A New Antioxidant Role for Rapid Critical-Sized Bone Defect Healing. *Adv Healthc Mater*. 2016;5(17):2199-2213. doi:10.1002/adhm.201600203.

Chapter 2. Background Studies



## A. Role of Hydrogen and Nitrogen on the Surface Chemical Structure of Bioactive Amorphous Silicon Oxynitride Films

Venu G. Varanasi,[a,*] Azhar Ilyas,[b] Megen F. Velten,[c] Ami Shah,[c] William A. Lanford,[d] and Pranesh B. Aswath [c]

[a] Department of Biomedical Sciences, Texas A&M Health Science Center, College of Dentistry, Dallas, TX 75246.

[b] Department of Electrical and Computer Engineering, New York Institute of Technology, Old Westbury, NY, 11568.

[c] Materials Science and Engineering Department, University of Texas at Arlington, Arlington, TX 76019.

[d] Physics Department, University at Albany SUNY, 1400 Washington Avenue, Albany, NY 12222.

[*] To whom correspondence should be addressed:
Venu G. Varanasi, Ph.D.
3302 Gaston Avenue, Texas A&M Health Science Center, Dallas, TX 75246, USA
Phone: +1-214-370-7006
Fax: +1-214-874-4538
E-mail: varanasi@tamhsc.edu

Abstract

Silicon oxynitride (Si-O-N) is a new biomaterial in which its O/N ratio is tunable for variable Si release and its subsequent endocytotic incorporation into native hydroxyapatite for enhanced bone healing. Yet, the effect of nitrogen and hydrogen bonding on the formation and structure of hydroxyapatite is unclear. This study aims to uncover the roles of H and N in tuning Si-O-N surface bioactivity for hydroxyapatite formation. Conformal Si-O-N films were fabricated by plasma-enhanced chemical vapor deposition (PECVD) onto Ti/Si substrates. Fourier transform infrared spectroscopy (FTIR) and Rutherford backscattering spectrometry (RBS) analysis indicated increased Si-H and N-H bonding with increased N content. Surface energy decreased with increased N content. X-ray absorbance near edge structure (XANES) analysis showed tetrahedral coordination in O-rich films and trigonal coordination in N-rich films. O-rich films exhibited a 1:1 ratio of 2p3/2 to 2p1/2 electron absorbance while this ratio was 1.73:1 for N-rich films. Both Si and N had a reduced partial charge for both O- and N-rich films whereas O maintained its partial charge for either film. O-rich films were found to exhibit random bonding SizOxNy while N-rich films exhibited random mixing: [Si-Si]–[Si-O]–[Si-N]. Thus, hydrogen bonding limits random nitrogen bonding in Si-O-N films via surface Si-H and N-H bonding. Moreover, increased nitrogen content reduces the partial charge of constituent elements and changes the bonding structure from random bonding to random mixing.

## 1. Introduction

Amorphous silicon oxynitride (Si-O-N) thin films have been extensively studied as a result of their use in microelectronic and optical devices. Plasma enhanced chemical vapor deposition (PECVD) has been established for fabricating these types of films because of its tunability and reproducibility.[1] These features of Si-O-N films make them a potential attractive coating for biomedical devices used in fracture healing. In particular, these materials can be used for sustained release of ionic Si ($Si^{4+}$) which enhances the mineralization process and up-regulates several important physiological processes that occur in bone mineralization.[2-7] While Si-O-N films used in optoelectronics require process optimization to reduce hydrogen bonding (N-H and Si-H) and subsequent hydrolysis, hydrogen bonding may prove favorable for hydrolysis within physiological environments. Thus, PECVD films for applications in improving bone-implant bonding may actually benefit from significant levels of N-H and Si-H bonding when local delivery of $Si^{4+}$ ions is desired.

The long-term stability of PECVD films for bone healing applications prompted an investigation into the chemical structure of such films; and two distinct theoretical models have been proposed: the Random Mixing Model (RMM) and the Random Bonding Model (RBM) represented in Figure 1. The RMM states that a non-stoichiometric silicon oxynitride (Si-O-N) can be treated as a simple mixture of Si-O, Si-N, and Si-Si polyhedra.[8-14] In the RBM, silicon, oxygen, and nitrogen incorporate into the basic silicon dioxide tetrahedral network to form $Si_zO_xN_y$, where $x+y=4$[15] and account for multiple ringed structures composed of 3 to 8 tetrahedra.[16] The basic structure of $Si_3N_4$ (Si-N bonding) is a trigonal planar space group in which a N atom bonds with 3 Si atoms to form a 3D network while Si-Si bonding is constrained to either 4-fold or 6-fold coordination and is denoted for the excess Si structure within the RMM.

Both models have been used to examine $SiO_2$, $Si_3N_4$, and Si-O-N thin films produced using PECVD, LPCVD (low pressure CVD), and other deposition methods under a variety of reaction conditions.[15, 17-19] On one hand, these films have been generally described by random bonding in which Si bonds to O or N as a substituted species (i.e. $Si_zO_xN_y$).[15, 18] On the other hand, these films have also been described by random mixing in which Si-Si, Si-O, and Si-N bonds exist in a simple mixture with no clustering of these structures.[20] These research groups have used a variety of methods including X-ray Photoelectron Spectroscopy (XPS), XANES, FTIR, and ellipsometry to verify the composition and model fit. XANES analysis is optimized to detect singly or multiply coordinated surface structures. For example, for PECVD-based Si-O-N material Si K-edge analysis, researchers have found the $SiO_4$ tetrahedron to describe the structure of Si-O-N.[21] However, unless there is fabrication of Si nanostructures within a silicon nitride or Si-O-N materials, such as those fabricated by Wilson et al.,[21] the Si K-edge cannot discern such clusters within PECVD Si-O-N film. Si-Si structures in Si K-edge analysis may be observed when the beam energy shifts to lower energies.[21] Yet, follow up of this spectra with Si L-edge is still needed to discern the multiply coordinated structures more definitively. Such examination has been lacking from previous research into examining PECVD amorphous silicon oxynitride surface structures.

This need for more detailed XANES analysis is further indicated by our previous work on biomineralization using Si-O-N thin films. In that work, it was found that trigonally coordinated carbonate species, tetrahedrally coordinated phosphate species, and calcium species formed on the surface within a few hours of *in-vitro* immersion.[22] This was determined using x-ray absorbance near edge structure (XANES) spectroscopy (Ca L-edge, P L-edge, O K-edge). This “configurational match” of the Si-O-N surface would be desired to elicit similarly epitaxially grown biomineral of like coordination to maximize the density of grown film.[23] Thus, this combination of our

previous results and the presence of enhanced hydrogen bonding in these films along with their bioactive effects warranted an examination of the surface chemical structure in terms of the applicability of either the RMM or the RBM. An improved understanding of these models with respect to the structure of silicon oxynitride may aid in production of osteogenic materials having enhanced and reproducible bone healing capabilities.

In the present study, Si-O-N films with various oxygen and nitrogen ratios were fabricated via a PECVD process designed to yield a potentially bioactive coating for biomedical devices. The model material surface was commercially pure Ti. It was applied to a Si wafer using electron-beam physical vapor deposition (EBPVD). Process validity and repeatability measures were obtained via Transmission electron microscopy (TEM), XPS, ellipsometry, and refractometry. Scanning electron microscopy (SEM) with energy dispersive spectroscopy (EDS) was used to evaluate coating composition. Fourier transform infrared spectroscopy (FTIR) was used to investigate N-H and Si-H bonding. Nuclear reaction analysis (NRA) was used to measure the absolute concentration of H, C, N and O (atoms/$cm^2$) in these films and Rutherford backscattering spectrometry (RBS) was used to measure the Si content. XANES spectroscopy evaluated the chemical structure of the Si-O-N films for their fit with the RBM or RMM. The low energy Si $L_{2,3}$ absorption edge resolved with a high resolution $3^{rd}$ generation synchrotron provided insight into the coordination of Si and its binding with either oxygen or nitrogen. We concluded that surface hydrogen bonding with nitrogen (N-H) influenced the substitution of N in amorphous Si-O-N films prepared by PECVD. The presence of a high concentration of Si-H bonding combined with N-H bonding contributed to the formation of a random mixture of Si-Si, Si-O, and Si-N bonds within high N-content films. The presence of N-H surface bonding contributed to the formation of randomly bonded N-substitution within the amorphous silica network (i.e., $Si_zO_xN_y$) for high O-content films.

## 2. Experimental and/or Theoretical Methods

### *2.1. Device Fabrication*

To create the Ti/$TiO_2$-$SiO_x$ devices and Si-O-N overlays, processes were tailored around rapid prototyping of various deposition, and analysis techniques. The procedure described below was modified from previous work.[22] The fabrication process started with standard cleaning of single crystal Si wafers; these were used as the base substrate. Ti layers were deposited using electron-beam physical vapor deposition (EB-PVD). Thermal oxidation was then employed to create a sufficient layer of $TiO_2$ to anchor overlays. PECVD of amorphous silica-based overlays was then conducted to build $SiO_x$/Si-O-N onto structured Ti/$TiO_2$ surfaces. All materials were fabricated at the University of Texas in the Arlington Nanotechnology Center.

### 2.2. Electron Beam Physical Vapor Deposition (EBPVD) of Ti films

P-type Si wafers with <100> orientation (Nova Electronic Materials, Flower Mound, TX) were employed as substrates for deposition of a uniform layer of Ti using electron beam physical vapor deposition (EB-PVD). Columnar Ti grains were deposited to a depth of 300 nm at a rate of 1 $A^o$/sec using an emission current of 3.1 mA and a chamber pressure of 5 x $10^{-8}$ Torr.

### 2.3. Plasma-Enhanced Chemical Vapor Deposition (PECVD) of Si-O-N Films

A TRION ORION II PECVD/LPECVD system (Trion Technology, Clearwater, FL) was used to deposit a uniform (non-uniformity < 1%) 100 nm $SiO_x$ layer followed by 100-1000 nm deposition of a Si-O-N amorphous film. All coatings were fabricated at a substrate temperature of 400°C, chamber pressure of 900 mTorr, an ICP power of 30 W, and an applied excitation frequency of 13.56 MHz. Source gases included silane ($SiH_4$) carried by argon (Ar) (15%/85%), nitrous oxide ($N_2O$), nitrogen ($N_2$), and ammonia ($NH_3$). The silane flow rate was kept low at 24 standard cubic centimeters per minute (sccm) to prevent undesirable gas-phase reactions. The nitrogen and ammonia flow rates were

kept high at 225 and 50 sccm, respectively, to increase N-H as well as Si-H bonding within the thin films. Five different types of films were prepared by varying the $N_2O$ flow rate as shown in Table 1. The refractive indices and the thickness of the films were measured using ellipsometry at a wavelength of 632.8 nm (Gaertner LS300). The results were confirmed through the use of a reflectometer (Ocean Optics NC-UV-VIS TF Reflectometer) and a scanning electron microscope (Hitachi S-3000N VP SEM). Deposition rates were determined from thickness measurements and plasma-on times.

### 2.4. Transmission electron microscopy (TEM)

TEM facilities were provided by the Center for Nanophase Materials Sciences (CNMS) at Oak Ridge National Laboratory, Oak Ridge, TN (ORNL). After fabrication, samples were sectioned using a Hitachi NB5000 dual-beam scanning electron microscope focused ion beam (SEM-FIB) onto Cu grids prior to imaging by TEM. TEM imaging was carried out using a Hitachi HF-3300 300kV FEG TEM/STEM with electron energy loss spectroscopy (EELS).

### 2.5. X-ray Photoelectron Spectroscopy (XPS)

XPS facilities were also provided by CNMS at ORNL. XPS analysis was conducted using a Thermo Scientific K-Alpha XPS with capabilities for sample through-thickness milling. Monochromatic Al-K alpha source with an energy of 1486.6 eV and $Ar^+$ beam sputtering operated at an energy of 4.2 keV was used for XPS analysis. This type of analysis aids in measuring surface and interfacial elementals.

### 2.6. X-Ray Diffraction (XRD)

X-ray diffraction was used to investigate films for the formation of crystalline phases. A Bruker D8 Advance diffractometer was used to collect $\theta$ - $2\theta$ (Bragg-Brentano) scans using Cu kα radiation (λ=1.5418 Å) at room temperature. Data were recorded over the $2\theta$ range of 20-80˚ with a 0.02˚ step size and a dwell time of 1 second.

XRD was carried out at the Center for Characterization in Materials and Biology at the University of Texas at Arlington.

### 2.7. Fourier Transform Infrared (FTIR) Spectroscopy

A FTIR spectrometer (Nicolet 6700, Thermo-Nicolet Corp., Madison, WI) in attenuated total reflectance (ATR) mode was used to collect FTIR spectra. Each spectrum was recorded using 32 scans from 650-4000 $cm^{-1}$ with a resolution of 4 $cm^{-1}$. An uncoated Si wafer was used to perform background subtraction before each measurement. Quantitation of N-H bond concentration was developed by Lanford and Rand[11, 12, 24, 25] and they determined the absorption cross-section of the N-H bond to be 5.3 x $10^{-18}$ $cm^2$.[11] The FTIR-ATR results should be held in relative context and represent semi-quantitative analysis. Therefore, the area under the curve was normalized to an oxide wafer reference to estimate the relative N-H bond concentration. A similar process was used to evaluate normalized Si-H bonding. Its reported absorption cross-section is 7.4 x $10^{-18}$ $cm^2$.[11] The FTIR-ATR results were normalized relative to pure amorphous silica ($SiO_x$) since this compound's FTIR-ATR results correspond well with FTIR transmission results. ATR technique accounts only for the relative shifts in band intensity and absolute shifts in the frequency. The relative intensity shift is well described and can be easily corrected, whereby the absolute shift in frequency domain is more difficult to correct. Therefore, the frequency shift is often neglected. The ATR correction algorithm in the FTIR software corrects the relative shifts. ATR correction also accounts for the variations in effective path-length by scaling the ATR spectrum accordingly.

### 2.8. Contact Angle Measurement and Surface Energy Evaluation

A sessile drop technique was used to determine contact angles of distilled, deionized water and diiodomethane (> 99%, Sigma-Aldrich, St. Louis, MO, USA) on the coated wafers. For each liquid, 9 repeat drops were measured at 25 ˚C. Each coating was tested in triplicate. The surface tension of the testing fluids, including the polar and

dispersive components, were taken from literature values under the same experimental conditions. The surface energy ($\gamma_{LV}$) and its corresponding dispersive ($\gamma^d$) and polar ($\gamma^p$) component values for water are 72.8, 21.8, and 51.0 mJ/m$^2$, respectively, and 50.8, 50.4, and 0.4 mJ/m$^2$, respectively, for diiodomethane.[26, 27] Surface hydrophilicities were inferred from contact angle measurements; surface energy values were obtained by relating the probing liquid contact angles ($\theta$) to solid surface energy dispersive and polar components using the Owens-Wendt-Kaeble relation. Wetting characteristics of a solid strongly depend on the roughness of its surface and preparation of a smooth solid surface is essential for obtaining accurate and reproducible contact angle measurement.[28-30] Surface roughness measured via Scanning Probe Microscopy (SPM) imaging indicated that the as-deposited roughness for all sample groups was very small (Ra < 1 nm) so the sample surface roughness will have no effect on the measurement of equilibrium contact angles.[12-14]

### 2.9. Scanning Electron Microscopy (SEM) and Electron Dispersive Spectroscopy (EDS)

Surface morphology, film composition, and film thickness were investigated using a scanning electron microscope (Hitachi S-3000N Variable Pressure SEM) equipped with an energy dispersive X-ray spectroscopy system (EDS). SEM micrographs were captured at an acceleration voltage of 20 keV and a working distance of 15 mm.

### 2.10. X-ray Absorbance Near Edge Structure (XANES) Spectroscopy

XANES spectroscopy was carried out on $SiO_2$ and $Si_3N_4$ model compounds and four Si-O-N samples — two high nitrogen content samples (1 and 2) and two high oxygen content samples (4 and 5). The acquired XANES spectra were compared with the model compounds for silicon (Si), oxygen (O), and nitrogen (N). The Si-$L_{2,3}$ edge and Si-, O-, and N-K edges were used to characterize the chemical nature and structural environment in the amorphous films. The spectra were obtained at the Canadian Light Source (CLS, Saskatoon, Canada) using the Variable Line Spacing Plane Grating

Monochromator (VLS-PGM, 11ID-2) for Si L-edge and the High Resolution Spherical Grating Monochromator (SGM, 11ID-1) beam lines for Si K-edge, O K-edge, and N K-edge. The total electron yield (TEY) data for these edges is considered to be collected from the near-surface (~25 nm for O K-edge, ~70 nm for Si K-edge, and ~20 nm for N K-edge) while the fluorescence yield (FY) data contains information from a relatively higher depth of penetration (~150 nm for O K-edge, ~70 nm for Si L-edge, and ~125 nm for N K-edge).[31, 32]

Sample sections of 12 mm × 12 mm × 0.5 mm were attached to the stage with carbon tape and examined under vacuum with the beam normal to the sample surface. For the Si- $L_{2,3}$ edge acquired on the VLS-PGM beam line, the fluorescence yield (FY) signal was recorded. For the Si-K, O-K and N-K edges acquired on the SGM beam line, total electron yield (TEY) and partial fluorescence yield (PFY) data was recorded. All sample edges were acquired with a 1 sec dwell time and a step size of 0.5/0.1/0.25 eV for the pre-edge/edge/post-edge spectral features. At least two spectra were acquired per sample per edge. Spectra were energy shifted using reference compounds collected during the same session using established peak positions, $Si_3N_4$ nanopowder (Nanostructured & Amorphous Materials Inc, Houston, TX, USA) and $SiO_2$ (>99.5%, Sigma-Aldrich, St. Louis, MO, USA). Linear background subtraction was performed using the spectral pre-edge for peak area calculations; however, spectra without background subtraction are presented for clarity.

### 2.11. Nuclear Reaction Analysis and Rutherford Backscattering Spectroscopy

Nuclear reaction analysis (NRA) and Rutherford backscattering spectroscopy (RBS) were used to measure the elemental content of the films. Films were prepared as described above using PECVD, with the exception that they were deposited onto Si wafers (001, p-type) for the NRA and RBS analysis. These MeV ion beam analysis techniques have the major advantage that they give absolute concentration in atoms/cm$^2$

without the need for measurements relative to “standard samples.” These methods are described in detail in references.[25, 33] Briefly, the H content is determined by bombarding the films with ~6.5 MeV $^{15}N$ ions, which can induce a nuclear reaction with protons (hydrogen) in the target emitting a characteristic gamma-ray. By varying the bombarding energy and measuring the number of characteristic gamma-rays emitted, the H content vs. depth can be determined. The other light elements in the target (C, N, and O) were determined by bombarding with 1.2 MeV deuteron beam and measuring the counts from nuclear reactions. The C, N, and O contents were determined by the yields from the $^{12}C(d,po)^{13}C$, $^{14}N(d,\alpha 1)^{12}C$ and $^{16}O(d,po)^{17}O$, respectively.[25, 33] The Si content was determined by conventional 2 MeV $^{4}He$ RBS. All three techniques rely on nuclear reaction or scattering cross-sections. They are independent of chemical bonding resulting in determination of absolute elemental concentrations (atoms/cm$^2$). Once a film composition was determined as outlined above, it was used to predict the complete RBS energy spectrum with no adjustable parameters. The comparison of its predicted spectrum with its measured spectrum provided a robust check and ensured that there were no large errors or omission in the film’s analysis.

2.12. RBM, RMM and Partial Charge Theory

The RMM calculations were based on the theory that the model is a simple mixture of $Si_3N_4$, Si-Si and $SiO_2$ phases. The Bruggeman approximation equation helps associate the refractive index to the volume fractions of the phases.[16, 34] It is given by;

$$vSiO_{2.}\cdot\frac{n_{SiO_2}^2-<n>^2}{n_{SiO_2}^2+2<n>^2}+vSi_3N_{4.}\cdot\frac{n_{Si_3N_4}^2-<n>^2}{n_{Si_3N_4}^2+2<n>^2}+vSi\cdot\frac{n_{Si}^2-<n>^2}{n_{Si}^2+2<n>^2}=0 \quad (1)$$

where,$v_x$ is the volume fraction of that phase and $n_x$ is the refractive index of the phase and $n$ is refractive index of the film.

The Bruggeman effective medium approximation (EMA) methodassumes that the grains of each phase in the composite are randomly mixed, and that their

dimensions are much smaller than the wavelength of light but large enough for each grain to be characterized by its bulk optical response.[35] For our model we considered excess Si, $Si_3N_4$ and $SiO_2$ (i.e. Si-Si, Si-N and Si-O bonds) phases.

We assumed that all the oxygen and nitrogen were found in the form of bonded $Si_3N_4$ and $SiO_2$ states. Thus, using mass balance equations:

$$n[Si] + 2n[O] \rightarrow n[SiO_2]$$

$$3n[Si] + 4n[N] \rightarrow n[Si_3N_4]$$

One can derive,

$$\frac{[O]}{[O]+[N]} = \left[1 + \cdot 2 \cdot 1.3 \cdot \frac{v[Si_3N_4]}{v[SiO_2]}\right]^{-1} \qquad (2)$$

The factor of 1.3 stems from the ratio of the atomic concentration of oxygen in $SiO_2$ ($4.64 \times 10^{22}$ cm $^{-3}$) and that of nitrogen in $Si_3N_4$ ($5.88 \times 10^{22}$ cm$^{-3}$).[34]

The volume fractions of all the phases should sum to one,

$$\sum v_f = 1 \qquad (3)$$

Using equations 1, 2 & 3 we modelled the expected phase mixture ratios of SiO2, Si3N4 and Si-Si phases. This was denoted as the RMM fit and the results are shown in Table 3.

For the RBM, there are five distinct stoichiometric tetrahedrons possible: SizOxNy where x+y=4. By convention, these tetrahedrons are referred to as Siz where z is equal to the number of silicon atoms in a given tetrahedron. A relation for the distribution of these Siz tetrahedrons as a function of oxygen (x) and nitrogen (y) contents has been developed by Phillips and is given in Equation 4.17

$$\mathrm{W}_v(\mathrm{x},\mathrm{y}) = \left(\frac{2\mathrm{x}}{2\mathrm{x}+3\mathrm{y}}\right)^v \left(\frac{3\mathrm{y}}{2\mathrm{x}+3\mathrm{y}}\right)^{4-v} \frac{4!}{\mathrm{v}!(4-\mathrm{v})!} \qquad (4)$$

where, W(x,y) is the work function associated with the random bonding model. The ratios of O/Si (x) and N/Si (y) are used along with the coordination number (v) for

finding the random distribution of the five potential tetrahedrons that represent the $SiO_vN_{4-v}$ models.

Partial charge calculations were conducted to observe the trend in the shift of the Si $2p_{3/2}$ peaks as compared to partial charge on Si. In addition, when the net charge (summation of partial charges on Si, O and N) was considered equal to zero, the mathematical model used to find the different O and N stoichiometry in each film composition was completely satisfied.[9] The equations used for partial charge calculations were as follows:

$$P_j(v) = (S_{SiON} - S_j)/(2.08S_j^{1/2}), \qquad (5)$$

where $S_{SiON}=(S_{Si}{}^{k}S_O{}^{m}S_N{}^{n})^{1/(k+m+n)}$

$$P_{Si}(x,y) = \sum_{v=0}^{4}[P_{Si}(v)W(v,x,y]\Big/\sum_{v=0}^{4}[W(v,x,y)] \quad (6)$$

$$P_O(x,y) = \sum_{v=0}^{4}[P_O(v)W(v,x,y]\Big/\sum_{v=0}^{4}[W(v,x,y)] \quad (7)$$

$$P_N(x,y) = \sum_{v=0}^{4}[P_N(v)W(v,x,y]\Big/\sum_{v=0}^{4}[W(v,x,y)] \quad (8)$$

## 3. Results

### 3.1. Device Fabrication and Characterization

Three regions were fabricated on top of the Si-wafer (Figure 2a and b). Region C is the EB-PVD Ti layer, Region B is the thermally grown $TiO_2$ layer, and Region A is the PECVD-based $SiO_x$ layer. Ti layers were found to have a columnar structure and within the Ti layer, columnar planes of Ti atoms were clearly observed. The thermally grown $TiO_2$ was then overlaid with a PECVD silica layer. PECVD overlays were found to be conformal with the underlying columnar Ti layer surface. The interface between the PECVD overlay and underlying Ti/$TiO_2$ was observed to have a gradual transition with structural features distinct for each region and a less distinctive structure between

regions (Figure 2b). EDS analysis showed low levels of contaminant elements for high-nitrogen and high-oxygen samples (Figure 2c and d).

3.2. XPS Analysis

Results from the XPS analysis (Fig. 3a) were obtained by milling through the thickness of the device. These data present the changes in elemental composition for the entire coating (overlays) as a function of deposition depth, including Regions A, B, and C. The binding energy of individual elements observed in these regions is given in Figure 3b for each region. The XPS results confirmed the coating thickness to be approximately 100 nm of PECVD $SiO_x$, 300 nm of Ti layer, and a graded interface between the $SiO_x$ overlay and $TiO_2$ layers. This graded interface exhibits near stoichiometric concentrations of $SiO_2$ and $TiO_2$ at the interface indicating that the silica and titania layers formed direct ionic bonding between the two layers. The $TiO_2$ layer was distinct and had a thickness of approximately 10 nm. However, data for oxygen within the Ti layer (O-Ti) showed oxygen diffused into the Ti layer, likely along the columnar grain boundaries.[36]

3.3. Refractive Index of the Films

From this point forward, the study of the various film compositions was conducted using a Si wafer as the substrate for PECVD-based Si-O-N films. This was done to allow for further characterization without interference from the Ti surface. Moreover, the methods used below were calibrated to the Si wafer substrate which was subtracted from all analyses presented herein.

The refractive indices and deposition rates for each set of gas flow conditions was determined using ellipsometry (Table 1). The refractive index inhomogeneity was determined to be less than 0.005 and the thickness non-uniformity as measured at 15 points on each 4” wafer was in the range of 1.2-2.4%. The refractive indices ranged from near that of silicon nitride (Si3N4 n≈2.0)37, 38 to near that of silicon dioxide (SiO2

n≈1.46).39 Deposition rates decreased and refractive indices increased as the flow of nitrous oxide decreased. This was expected as N2O was the primary source of oxygen incorporated into the film. Table 1 also shows the refractive index of the samples as a function of the ratio of the flow rates for the primary reactive gases, N2O and SiH4.

### 3.4. X-ray Diffraction (XRD) Analysis

X-ray diffraction was used to confirm the amorphous nature of the films. Figure 4a shows representative XRD spectra from the highest nitrogen and oxygen content samples. Although X-ray spectra do not show the two broad 2θ peaks typical to amorphous Si-O-N films,[40] (i.e., 20-30˚ and 60-80˚), it can be assumed that the $SiO_x$ sub-layer dominates the spectra resulting in one amorphous silica peak. All collected XRD spectra were found to have a similar broad peak between 20-40˚.

### 3.5. FTIR Characterization and Nuclear Reaction Analysis (NRA)

A thicker coating (1.0 μm) of Si-O-N was deposited for FTIR and NRA characterization. Figure 4b shows the absorption spectra of the Si-O-N films. Strong Si-O bending and Si-O stretching peaks near 790 $cm^{-1}$ and 1140 $cm^{-1}$, respectively, were seen in all spectra indicating that information from the oxide sub-layer was most likely also being observed. It should be noted that the region from 2100 to 4000 $cm^{-1}$ was magnified fivefold to highlight the contribution of both the 2270 $cm^{-1}$ Si-H and 3385 $cm^{-1}$ N-H stretching bands. The position of the Si-H band shifts from about 2270 $cm^{-1}$ in the high refractive index samples to about 2252 $cm^{-1}$ in the lower index samples, while the N-H peak position remains constant. The hydrogen concentration was calculated by deconvolution of the Si-H and N-H bands and fitting them to Gaussian distributions. The observed H concentration from Si-H bonds gradually increased as a function of refractive index, ranging from 1.32-1.65 x $10^{21}$ atoms/$cm^3$ while the N-H bond concentration showed only a modest increase from the low to the high refractive index

samples. The Si-H and N-H bond concentrations (normalized to pure amorphous silica, $SiO_x$) are shown in Figure 4c.

Table 2 shows the results of nuclear reaction analysis of the as-deposited PECVD overlays. Samples are arranged from the highest N-rich overlays (sample 1) to the highest O-rich overlays (sample 5). The increased presence of H with increasing N content appears to limit the random mixing of N in the Si-N structure. This is indicated by the lower concentration of Si and N in the high N-rich structure as compared to their stoichiometric values given in Table 2 for $Si_3N_4$. This is likely due to under-coordinated Si and N within the Si-N overlay.

### 3.6. Surface Energy Evaluation

Water contact angles (Figure 4d) increased with increasing nitrogen content. High oxygen content samples (4 and 5) were more hydrophilic than the high nitrogen content samples (1 and 2). For this sample set, the diiodomethane contact angle was relatively constant, indicating that the dispersive component was relatively constant for these surfaces. Differences observed in the contact angle with water can be primarily attributed to a change in the polar component of the surface energy. Figure 4e shows the polar ($\gamma^p$), dispersive ($\gamma^d$) and the total surface energy ($\gamma$) values calculated from the Owens-Wendt-Kaeble equation in $mJ/m^2$. The dispersive component for all samples ranged from 23.1 to 24.9 $mJ/m^2$ while the polar component varied with nitrogen content. The highest oxygen content sample (5) had a polar component of 32.1 $mJ/m^2$ while the highest nitrogen content sample (1) was nearly half at around 16.1 $mJ/m^2$. The variation of oxygen and nitrogen in these coatings allowed for tunability of the polar component of the surface energy. This may provide a limited method for control over protein adhesion and cell attachment.[41] The tunability of the surface energy of these coatings makes them attractive for use in biomedical applications. This stems from the fact that the O/N ratio in

these films influences the contact angle, the surface energy and in turn the attachment, migration, and growth of cells on the Si-O-N surface.[41]

### 3.7. XANES Analysis

The Silicon Si-L2,3 edge42, 43 and Si-K42 edge can be used to investigate both the chemical species that give rise to changes in binding energies as well as to distinguish between four-fold and six-fold coordination of Si while O K-edge44 and N K-edge can be used to investigate local oxygen and nitrogen structure.

#### *3.7.1. Silicon K-edge*

Figure 5b shows the Si K-edge TEY data for 4 sample chemistries and the $SiO_2$ and $Si_3N_4$ standards. There are two main peaks of interest in these spectra: peak **a**, the main Si K-edge peak around 1847± 0.3 eV and a post edge peak **b** feature common to all spectra around 1864.8 ± 0.2eV. Peak **a** can be thought of as the sum total contribution of Si-Si bonding (~1841 eV), Si-N bonding (~1844.5 eV) and Si-O bonding (1847 eV) resonances.[21] In the $Si_3N_4$ standard, some oxygen contamination was observed and the peak was split between Si-N and Si-O resonant energies. On the other hand, the high-N content samples showed evidence of all three bonding forms with a leading edge around 1841 eV and a broad absorption peak encompassing both Si-N and Si-O resonant energies. The high-O content samples primarily showed Si-O bonding, with a small spectral contribution around 1841 eV, suggesting Si-Si bonding. In contrast, the $SiO_2$ standard peak **a** was centered at 1847± 0.3 eV and had a leading edge at 1843 ± 0.3 eV, which was well above the energy level suggesting Si-Si bonding.

From the Si-K edge data above, [4]Si and [6]Si coordination in O- and N-containing samples was difficult to resolve. The main 1847 eV Si-O peak is attributed to [4]Si coordination, [6]Si coordination peaks occur around 1848.5 eV (main line) and 1853 eV (post-edge resonance). Whereas the higher O-content samples and SiO2 standard show no evidence of either peak, these spectral features overlap with broad

high-N content main edge peak, which both have a post-edge shoulder that extends to energies higher than 1853 eV making it difficult to draw a conclusion about any [6]Si content in these samples. Also of note is the shift towards lower energy of peak a as the N content increases in the samples. This was also observed by Wilson et al.,21 in which was suggested to manifest as a result of multiple coordinated structures. Further investigation of the Si L-edge was therefore, needed to ascertain if such coordination structures could be observed.

*3.7.2. Silicon $L_{2,3}$-edge*

Figure 5a shows the FY data for 4 sample chemistries and the $SiO_2$ and $Si_3N_4$ standards. Six peaks of interest were identified and labeled a-f. Peaks **a** and **b** at 105.5±0.1eV and 106.1±0.1eV, respectively, arise from the transition of 2p electrons to unoccupied 3d orbitals that have been split by ~0.6 eV by spin-orbital splitting.[42, 43] Table 3 shows the calculated **a:b** peak area ratio for the two model compounds and the four sample films investigated. The **a:b** peak area ratio data suggest that while the silica tetrahedron-based RBM may provide a useful approximation of the Si-O-N bonding in the higher oxygen containing samples, the high nitrogen content samples may form a structure better approximated by that of the β-$Si_3N_4$ standard. The ratio of these peaks has been used to differentiate the contribution from disparately substituted $SiO_4$ tetrahedra.[31] That is, the **a:b** integrated peak area ratio can be used as a semi-quantitative measure of nitrogen substitution into a $SiO_4$ tetrahedron, which aligns well with the RBM view of Si-O-N structure.

The highest intensity peak **c** that was found in both standards and all samples is the main Si $L_{2,3}$-edge peak. Its position can be used to distinguish between fourfold ($^{[4]}$Si) and six fold ($^{[6]}$Si) coordinated silicon in silicate glasses.[42, 45] For $^{[4]}$Si, the main peak is centered at 107.9 ± 0.2eV while in $^{[6]}$Si an additional main edge peak is observed at 106.7 ± 0.2 eV.[43] In Figure 5a, the peak **c** line was centered at 108.0 ± 0.2eV indicating

that $^{[4]}$Si was in all samples and standards. However, second order derivative fitting of samples 1 and 2 indicates that there may be a peak centered near 106.8 eV, which may be an indication that a mix of $^{[4]}$Si and $^{[6]}$Si was present in these chemistries. Peak **d** centered at 115.3 ± 0.2eV was a resonance Si-peak found in both $Si_3N_4$ and $SiO_2$ and therefore cannot be used to distinguish between the chemical fingerprints of either structure. Peak **e** is characteristic of Si-N resonance bonding[21] and was found centered at 103.2 ± 0.2eV for the $Si_3N_4$ standard. This peak was observed to shift to higher energies in high-N content Samples 1 (104.0 ± 0.2eV) and 2 (104.7± 0.2eV) which indicates a distortion of the Si-N bond in a nitride matrix.[21] Peak **f** at 99.7 ± 0.2eV was found in all samples, though the intensity of the main edge peak makes it difficult to ascertain in Samples 4 and 5. This peak has previously been observed in other Si-O-N films with excess Si and is attributed to Si-Si bonding in silicon nanoclusters (Si-nc) found within the coating.[21]

Silicon L-edge data support the theory that the high-oxygen content Si-O-N sample coating chemistries can be described as N-substituted silica tetrahedrons ($^{[4]}$Si) with small amounts of Si-nc to account for excess Si according to the RBM view of the structure. However, the high-nitrogen content samples show inconclusive evidence of both $^{[4]}$Si and $^{[6]}$Si coordination with oxygen substituted into a β-$Si_3N_4$-like matrix that becomes increasingly distorted with additional oxygen content.

*3.7.3. Oxygen K-edge*

Figure 6 shows the O K-edge TEY and FY data for four sample chemistries and the $SiO_2$ standard. All data have been scaled to the signal intensity of the $SiO_2$ standard. There were three main peaks observed in these spectra: peak **a**, a pre-edge peak around 529.9 ± 0.2 eV, the main O-K edge peak **b** around 535.2 ± 0.2 eV, and a post edge peak **c** feature around 558.5 ± 0.2 eV. Peak **a**, which was observed as a distinct peak in all sample chemistries in the TEY data and as a pre-edge shoulder in the $SiO_2$

standard in both the TEY and FY data suggest the presence of silanol (Si-OH) bonding at the near surface while the absence of this peak in the FY data suggests that the primary oxygen bonding in the bulk of the films for all samples can be attributed to Si-O-Si bridges, as evidenced by the main peak **b** and post-edge resonance peak **c**.[15]

*3.7.4. Nitrogen K-edge*

Figure 7 shows the N K-edge TEY and FY data for four samples chemistries and the $Si_3N_4$ standard. All data have been scaled to the signal intensity of the $Si_3N_4$ standard. There were three main peaks observed in these spectra: peak **a**, around 398.6 ± 0.2 eV, the main peak **b** around 402.6 ± 0.2 eV, and a post edge peak **c** feature around 421.4 ± 0.2 eV. Peak **a** has been attributed to the presence of under-coordinated (i.e. two-fold coordinated) or hydrogen-bound nitrogen which indicates either the presence of N-H bonding or the substitution of a nitrogen atom for an oxygen atom into a Si-O-Si bridge.[15, 46]

While this peak was particularly prominent in the TEY spectra of the lowest-N containing sample, it was also observed as a pre-edge shoulder in the other TEY spectra. The apparent increased intensity of the peak in the low-N Sample 5 chemistry suggests that a proportionately larger amount of N in this sample was 2-fold coordinated, or, conversely, that the Si-O-Si bridge network remains relatively undisturbed by the limited amount of N incorporation into the coating. The main edge peak was similar for all samples and the $Si_3N_4$ standard, suggesting that the bulk of the spectral contribution was due to Si-N bonding. However, the post-edge peak **c** resonance appears distorted in the lower-N content sample FY data. The peaks observed between 425 eV – 435 eV in these spectra may be due to a higher order spectral contribution from silicon, which overwhelmed the N signal in these relatively Si-rich and N-poor films. Also of note was the apparent shift of the N K-edge spectra (TEY) as a function of increasing N content,

which was similarly found in the Si K-edge spectra and associated with a change in bond coordination as explained above.

*3.8. RMM and RBM Calculations*

Calculations for the RMM and RBM are presented in Table 3, and Figures 8 and 9. For the random mixing model, the calculations were performed using the RBS compositional data and Eqs. 1-3. The calculated RMM values are given in Table 3. For the RMM, the calculated values for the O-rich samples (refractive index of 1.45 and 1.57) are not in agreement with the XANES spectra, because the Si L- and K- edges do not indicate the presence of Si-Si or $Si_3N_4$ bonding. Thus, the RMM fit for the O-rich films is not applicable. For the RBM based on calculation from Eq. 4 and represented in Figure 8, it can be observed that the $SiO_4$ tetrahedron has a higher ratio (in the higher O content samples) indicating tetrahedral coordination for Si. This was further confirmed by the XANES Silicon L-edge results showing the a:b peak ratio closer to unity for the higher O content (1.45 and 1.57 refractive index) samples. Figure 8 shows the calculated work function based on the RBM view of the structure using the measured RBS data in which several types of silica tetrahedra were compared for fit. According to the RBM, it was found that even the high N content samples have Si in tetrahedral coordination as opposed to the trigonal coordination observed from the XANES data. So, the RBM is applicable only for high O content samples.

The results of partial charge calculations are given in Figure 9. Reflecting on these results, decreased N content results in an increase in the partial charge on each atom, an increase in the electronegativity between the Si-N and Si-O bonds, and a decrease in the a:b peak ratio resulting in higher surface polarity. This was also observed in surface energy evaluation, where lowering N content was shown to have increased surface energy, and decreased contact angle, indicating the surface was more wettable. Improved biological activity, protein adhesion and cell-attachment has been

reported for relatively more hydrophilic (lower contact angle) surfaces.[22, 47, 48] Thus, the lower a:b: peak ratio observed in the XANES data can be related to the lower contact angle measurements; these results help predict the potential ability of a material to facilitate cell growth and migration.

## 4. Discussion

Five distinct Si-O-N chemistries were fabricated via a repeatable PECVD process designed to create potentially bioactive Si-O-N films on commercially pure Ti surfaces. These films ranged from nitrogen rich Si-O-N (for films produced at low $N_2O$ flow rates between 0-16 sccm) to oxygen rich Si-O-N (for films produced at high $N_2O$ flow rates 155 and 160 sccm). XRD spectra indicated that the films were amorphous. XPS results demonstrated formation of a Ti-O-Si interface between the PECVD films and the underlying $Ti/TiO_2$.

The relatively high N-H and Si-H bond concentrations calculated from the FTIR spectra suggest that these films may be partially soluble under physiological conditions because readily available surface silanols by PECVD process[49, 50] and low nitrogen content (high N-H and Si-H bonding) allow immediate dissolution/degradation *in vitro* as explained in our previous work.[5, 22] The highest concentration of Si-N and Si-H bonding was observed in the highest nitrogen content samples. Comparing the N-H bond concentration to the nitrogen concentration in the samples revealed that a greater percentage of the nitrogen in the low-nitrogen content samples was bound to hydrogen. Thus, hydrogen bonding may limit nitrogen substitution within the Si-O network as a byproduct of the PECVD process and it prevents alterations of the Si-O tetrahedral structure. This change in relative under-coordinated nitrogen in the films may have implications for *in vitro* dissolution.[51]

Based on surface energy and contact angle measurement, the high O containing samples were generally more wettable than the high N containing samples. Reduced

wettability has been linked to the decreased O-H density with increased N doping.[50, 52] Our results further indicate that poorer wettability (higher contact angle) and decreased surface energy was associated with increased surface H bonding with increasing N doping. In previous work, these trends were observed to promote more osteoblast migration on Si-O surfaces as compared to Si-O-N or Si-N surfaces.[22] Yet, Si-O-N surfaces promoted rapid human periosteum cell formation of collagen-like ECM and enhanced their osteogenic response as compared with Si-O or Si-N surfaces.[22] These results and discussion suggest that surface polarization, contact angle, and surface energy associated with hydrogen bonding are likely reliable predictors of cell migration whereas other factors, such as surface chemical coordination associated with surface nitrogen bonding, surface N-H bonding, and ion dissolution play more of a role during osteoblast differentiation, collagen ECM bonding, and mineralization.

From the XANES spectral features in these elemental edges, it is apparent that increased N content alters the bonding environment of the Si-O-N films. For the higher nitrogen content films, the Si L-edge **a:b** peak ratio remains close to that of $Si_3N_4$ for these samples which suggests that the Si-N bonding environment is similar to the nitride standard, which would be expected in a random mixture of silica and silicon nitride. The broad main peak **a** in the Si-K edge spectra for these samples also suggests that Si-O and Si-N bonding both exist in forms similar to the silica Si-O bonding and the nitride Si-N bonding structures simultaneously since the broad peak overlaps with both of the standards. For the higher oxygen content films, the Si L-edge **a:b** peak ratio remains close to that of $SiO_2$ for these samples which suggests that Si-O bonding environment is similar to that of silica. The narrow main peak **a** in the Si K-edge spectra for these samples also suggests that silica-like Si-O bonding dominates the structure. The presence of the sharp resonance peak in the N K-edge data also suggests that nitrogen

is substituted into the place of a bridging oxygen atom, which would occur in systems where the silica tetrahedra is the basic structural unit.

The a:b peak ratio has been used to differentiate the contribution from disparately substituted SiO4 tetrahedra.31 As applied in this work, this ratio could be used as a semi-quantitative measure of nitrogen substitution into a SiO4 tetrahedron and would align with the RBM view of Si-O-N structure. However, this association does not hold for higher N-rich Si-O-N films. On one hand, Criado et al.15 showed that increasing N content did not induce a change in the absorption edge for Si-N as compared to Si-O. They found them to be of random bonding model, which aligns more with the topological constraint theory that generally associates the coordination structure of amorphous films to the average coordination number of the constitutive atoms. On the other hand, Rahman et al.20 viewed the structure from a random mixing model in which the individual structures of Si-Si, Si-O, and Si-N simply mix and do not phase segregate or cluster based on compositional analysis. These 2 opposing viewpoints have been shared fairly equally amongst a number of research groups, hence, added computational analysis was needed to ascertain the appropriate model for the XANES, RBS, and refractive index data.

Computational analysis of the compositions coupled with surface characterization found that the high O-containing films conformed to the RBM evidence by the work function (W(x,y)) showing a value of unity for higher O content sample (n=1.45). Meanwhile, partial charge calculations showed that O maintained a partial charge close to that of the pure oxide, which indicated that Si-O bonding governed O incorporation in high N containing films. Coupled with this was a loss in the partial charge of N with increasing N content. These results indicate Si-O, Si-N, and Si-Si bonding when coupled with XANES analysis. This illustrates that the RMM is suitable for high N-containing films. Table 3 was revised to reflect the application of RBM and RMM models to the

samples based on composition, XANES a:b peak ratios, and our calculations using the RBM view of the electronic structure.

The change in the a:b peak ratio with a change in the nitrogen content in the films was of note. Pure silicon will always have an a:b peak area ratio equal to 2 since this represents 4 2p electrons with $3/2$ energy (2p3/2) vs. 2 2p electrons with ½ energy (2p1/2). These 2p core shell electron binding energies can shift depending on the amount of N and O added to Si. This is due to a charge transfer that occurs between Si and O or N.53 In the case of oxygen, this highly electronegative atom shifts the 2p core electrons toward higher energy, as indicated by a shift in the a:b peak ratio from 2:1 to 1:1. As the nitrogen concentration increased, the binding energy of the Si 2p core shell electrons shifts towards a lower value because of the higher surrounding electron density.51 This effect of increasing N content is accompanied by a shift of the N 1s line (N K-edge spectra), which is connected with the increased number of next-nearest and further far-neighbor N atoms (induction effect).53 Thus, the decrease in partial charge on Si with increasing N content suggests that the 2p core shell electron shifts to lower energy, thereby, resulting in an increased a:b peak ratio.

In previous work,22 we found that these films promote different types of biomineral. High O containing Si-O-N and pure Si-O films promoted the formation of calcium phosphate while a mixture of phosphate and carbonate was observed for higher N-containing Si-O-N and pure Si-N samples as shown by the O K-edge XANES analysis of Si-O-N samples (Figure 10a). The coupled formation of carbonate and phosphate near edge structures indicates the presence of hydroxycarbonate apatite with increasing carbonate to phosphate ratio as the N/O ratio increases in the Si-O-N film. Given that calcium carbonate and calcium phosphate can exhibit trigonal and tetrahedral bonding structures, respectively, it may be likely that formation of these different mineral types depends on random bonding or random mixing within the Si-O-N films. Random bonding

within tetrahedrally coordinated Si-O-N likely promoted the surface formation of tetrahedrally coordinated phosphate-containing mineral while the random mixing of Si-O (tetrahedral) and Si-N (trigonal) likely promoted the formation of phosphate- and carbonate-containing (trigonal) biomineral. This carbonate to phosphate ratio of resultant biomineral is vital to the healing rate of different physiological biomineral structures. Thus, the ability for Si-O-N films to be tuned to elicit varying resultant carbonate-to-phosphate ratios allows for tailored design of osseointegratable implants for a range of bone implant applications with predictable healing rates.

The effect of the a:b peak ratio on the biomineral carbonate to phosphate peak ratio may be explained as follows. In our previous work, a shift in the O K-edge to lower binding energy was observed with increased N content resulting in formation of the carbonate structure for mineralized tissue that formed by human periosteum cells on the surface of Si-O-N films (Figure 10). The shift towards lower energy in the 2p core electron shell of Si in Si-O-N films coincides with a similar shift in the O-K edge in the biomineral. This associated effect may induce the formation of calcium carbonate via the lower binding energy of electrons in the oxygen within the biomineral bound to the Si atoms in the Si-O-N films. The incorporation of N into silica network promoted the rapid formation of collagen ECM by human periosteum cells. This could be due to the increased surface N-H groups (Figure 4c) that can bind and substitute for amide groups within collagen (Figure 10d) as it forms prior to mineralization. From an application point of view, this means that fabrication of biomaterials for targeted bone formation and bone chemistry can be influenced by the fabrication of the material by targeting the a:b peak ratio. This suggests that the a:b peak ratio could be potentially used as a predictive tool for targeting various types of bone formation; in turn, this a:b peak ratio can be targeted based on the input conditions of the PECVD process.

## 5. Conclusions

The aim of this study was to investigate the role that nitrogen and hydrogen play on the surface chemical structure of PECVD-based amorphous Si-O-N films for future bone implant applications. A range of Si-O-N compositions were used for these studies. XANES analysis revealed that high O-containing Si-O-N films and pure silica exhibited Si-O bonding with 2p3/2:2p1/2 (a:b peak ratio is Si L-edge) to be close to unity while high N-containing Si-O-N films and pure silicon nitride films exhibited Si-Si, Si-O, and Si-N bonding with 2p3/2:2p1/2, which increased with increasing N content. Ellipsometry, and RBS analysis combined with computational analysis showed that high O-containing Si-O-N and pure silica films are described by the RBM, hence denoting their tetrahedral structure as SizOxNy. High N-containing Si-O-N and pure silicon nitride films are described by the RMM, hence denoting their structure as [Si-Si]–[Si-O]–[Si-N]. The change in the electron configuration and bonding structure of Si-O-N films with increasing N content was attributed to changes in the partial charge on Si, N, and O based on the combined analyses. FTIR analysis and NRA-RBS data showed that Si-H and N-H bonding increased with increasing N content. In low N-containing Si-O-N samples, the small amount of N that was present was likely bound to surface hydrogen as a consequence of the PECVD process. Thus, the density of hydrogen to nitrogen bonding influences the coordination of N in amorphous Si-O-N prepared by PECVD.

## Acknowledgments

The authors would like to thank Drs. Nickolay Lavrick, Harry Meyer, and Karen Moore for their assistance with characterization of materials in the HTML at ORNL via the CNMS and SHARE program. The authors would like to thank Drs. Lucia Zuin, Tom Regier, and Youngfeng Hu at the Canadian Light Source Inc. for their assistance with XANES analysis. The XANES experiments were performed at the Canadian Light Source, which is supported by NSERC, NRC, CIHR, and the University of

Saskatchewan. We also thank Kamal Awad from for his help with data analysis. Si-O-N thin films were deposited at the Nanofabrication Facility at UT Arlington. FTIR experiments were conducted at Center for Characterizations for Materials and Biology at The University of Texas at Arlington. The work was supported by a grant from National Institutes of Health/National Institute for Dental and Craniofacial Research (1R03DE023872-01A1, Varanasi PI).

**References**

(1) Ay, F.; Aydinli, A., Comparative Investigation of Hydrogen Bonding in Silicon Based Pecvd Grown Dielectrics for Optical Waveguides. *Opt. Mater.* **2004**, *26*, 33-46.

(2) Tousi, N. S.; Velten, M. F.; Bishop, T. J.; Leong, K. K.; Barkhordar, N. S.; Marshall, G. W.; Loomer, P. M.; Aswath, P. B.; Varanasi, V. G., Combinatorial Effect of Si 4+, Ca 2+, and Mg 2+ Released from Bioactive Glasses on Osteoblast Osteocalcin Expression and Biomineralization. *Mater. Sci. Eng., C* **2013**, *33*, 2757-2765.

(3) Varanasi, V. G.; Owyoung, J. B.; Saiz, E.; Marshall, S. J.; Marshall, G. W.; Loomer, P. M., The Ionic Products of Bioactive Glass Particle Dissolution Enhance Periodontal Ligament Fibroblast Osteocalcin Expression and Enhance Early Mineralized Tissue Development. *J. Biomed. Mater. Res. Part A* **2011**, *98A*, 177–184.

(4) Varanasi, V.; Saiz, E.; Loomer, P.; Ancheta, B.; Uritani, N.; Ho, S.; Tomsia, A.; Marshall, S.; Marshall, G., Enhanced Osteocalcin Expression by Osteoblast-Like Cells (Mc3t3-E1) Exposed to Bioactive Coating Glass (Sio 2–Cao–P 2 O 5–Mgo–K 2 O–Na 2 O System) Ions. *Acta Biomater.* **2009**, *5*, 3536-3547.

(5) Ilyas, A.; Odatsu, T.; Shah, A.; Monte, F.; Kim, H. K.; Kramer, P.; Aswath, P. B.; Varanasi, V. G., Amorphous Silica: A New Antioxidant Role for Rapid Critical-Sized Bone Defect Healing. *Adv. Healthcare Mater.* **2016**, *5*, 2199-2213.

(6) Varanasi, V.; Leong, K. K.; Jue, S. M.; Dominia, L. M.; Loomer, P. M.; Marshall, G. W., Si and Ca Combinatorially Target and Enhance Early Mc3t3-E1 Osteoblast Expression of Osteocalcin. *J. Oral Implantol.* **2012**, *38*, 325-336.

(7) Varanasi, V.; Velten, M.; Odatsu, T.; Ilyas, A.; Iqbal, S.; Aswath, P., Surface Modifications and Surface Characterization of Biomaterials Used in Bone Healing. *Mater. Dev. Bone Disord.* **2016**, 405.

(8) Sivaram, S., *Chemical Vapor Deposition: Thermal and Plasma Deposition of Electronic Materials*. Springer Sci. Bus. Media: **2013**.

(9) Gritsenko, V.; Kwok, R.; Wong, H.; Xu, J., Short-Range Order in Non-Stoichiometric Amorphous Silicon Oxynitride and Silicon-Rich Nitride. *J. Non-Cryst. Solids* **2002**, *297*, 96-101.

(10) Jehanathan, N.; Liu, Y.; Walmsley, B.; Dell, J.; Saunders, M., Effect of Oxidation on the Chemical Bonding Structure of Pecvd Sin X Thin Films. *J. Appl. Phys.* **2006**, *100*, 123516.

(11) Lanford, W.; Rand, M., The Hydrogen Content of Plasma-Deposited Silicon Nitride. *J. Appl. Phys.* **1978**, *49*, 2473-2477.

(12) Feng, B.; Chen, J.; Qi, S.; He, L.; Zhao, J.; Zhang, X., Characterization of Surface Oxide Films on Titanium and Bioactivity. *J. Mater. Sci. : Mater. Med.* **2002**, *13*, 457-464.

(13) Kaelble, D., Dispersion-Polar Surface Tension Properties of Organic Solids. *J. Adhes.* **1970**, *2*, 66-81.

(14) Owens, D. K.; Wendt, R., Estimation of the Surface Free Energy of Polymers. *J. Appl. Polym. Sci.* **1969**, *13*, 1741-1747.

(15) Criado, D.; Alayo, M.; Pereyra, I.; Fantini, M., Structural Analysis of Silicon Oxynitride Films Deposited by Pecvd. *Mater. Sci. Eng., B* **2004**, *112*, 123-127.

(16) Bruggeman, V. D., Berechnung Verschiedener Physikalischer Konstanten Von Heterogenen Substanzen. I. Dielektrizitätskonstanten Und Leitfähigkeiten Der Mischkörper Aus Isotropen Substanzen. *Ann. der Phys.* **1935**, *416*, 636-664.

(17) Philipp, H., Optical Properties of Non-Crystalline Si, Sio, Siox and Sio2. *J. Phys. Chem. Solids* **1971**, *32*, 1935-1945.

(18) Scopel, W.; Fantini, M.; Alayo, M.; Pereyra, I., Local Structure and Bonds of Amorphous Silicon Oxynitride Thin Films. *Thin Solid Films* **2002**, *413*, 59-64.

(19) Criado, D.; Zúñiga, A.; Pereyra, I., Structural and Morphological Studies on Sioxny Thin Films. *J. Non-Cryst. Solids* **2008**, *354*, 2809-2815.

(20) Rahman, H. U.; Gentle, A.; Gauja, E.; Ramer, R. In *Characterisation of Dielectric Properties of Pecvd Silicon Nitride for Rf Mems Applications*, Multitopic Conference, 2008. INMIC 2008. IEEE International, IEEE: **2008**; pp 91-96.

(21) Wilson, P. R.; Roschuk, T.; Dunn, K.; Normand, E. N.; Chelomentsev, E.; Zalloum, O. H.; Wojcik, J.; Mascher, P., Effect of Thermal Treatment on the Growth, Structure and Luminescence of Nitride-Passivated Silicon Nanoclusters. *Nanoscale Res. Lett.* **2011**, *6*, 168.

(22) Ilyas, A.; Lavrik, N. V.; Kim, H. K.; Aswath, P. B.; Varanasi, V. G., Enhanced Interfacial Adhesion and Osteogenesis for Rapid “Bone-Like” Biomineralization by Pecvd-Based Silicon Oxynitride Overlays. *ACS Appl. Mater. Interfaces* **2015**, *7*, 15368-15379.

(23) Pauleau, Y., *Materials and Processes for Surface and Interface Engineering*. Springer Sci. Bus. Media: **2012**; *Vol. 290*.

(24) Lanford, W., Analysis for Hydrogen by Nuclear Reaction and Energy Recoil Detection. *Nucl. Instrum. Methods Phys. Res., Sect. B* **1992**, *66*, 65-82.

(25) Lanford, W.; Tesmer, J.; Nastasi, M., Handbook of Modern Ion Beam Materials Analysis. *Mater. Res. Soc. Symp. Proc.* **1995**, 193.

(26) Amaral, M.; Lopes, M.; Santos, J.; Silva, R., Wettability and Surface Charge of Si 3 N 4–Bioglass Composites in Contact with Simulated Physiological Liquids. *Biomaterials* **2002**, *23*, 4123-4129.

(27) Correia, N. T.; Ramos, J. J. M.; Saramago, B. J.; Calado, J. C., Estimation of the Surface Tension of a Solid: Application to a Liquid Crystalline Polymer. *J. Colloid Interface Sci.* **1997**, *189*, 361-369.

(28) Wenzel, R. N., Resistance of Solid Surfaces to Wetting by Water. *Ind. Eng. Chem.* **1936**, *28*, 988-994.

(29) Bikerman, J. J., The Surface Roughness and Contact Angle. *J. Phys. Colloid Chem.* **1950**, *54*, 653-658.

(30) Morrow, N. R., The Effects of Surface Roughness on Contact: Angle with Special Reference to Petroleum Recovery. *J. Can. Pet. Technol.* **1975**, *14*.

(31) Kasrai, M.; Lennard, W.; Brunner, R.; Bancroft, G.; Bardwell, J.; Tan, K., Sampling Depth of Total Electron and Fluorescence Measurements in Si L-and K-Edge Absorption Spectroscopy. *Appl. Surf. Sci.* **1996**, *99*, 303-312.

(32) Leinweber, P.; Kruse, J.; Walley, F. L.; Gillespie, A.; Eckhardt, K.-U.; Blyth, R. I.; Regier, T., Nitrogen K-Edge Xanes–an Overview of Reference Compounds Used to Identifyunknown'organic Nitrogen in Environmental Samples. *J. Synchrotron Radiat.* **2007**, *14*, 500-511.

(33) Wang, Y.; Pan, Z.; Ho, Y.; Xu, Y.; Du, A., Nuclear Instruments and Methods in Physics Research Section B: Beam Interactions with Materials and Atoms. *Nucl. Instrum. Methods Phys. Res., Sect. B* **2001**, *180*, 251-256.

(34) Kuiper, A.; Koo, S.; Habraken, F.; Tamminga, Y., Deposition and Composition of Silicon Oxynitride Films. *J. Vac. Sci. Technol., B: Microelectron. Process. Phenom.* **1983**, *1*, 62-66.

(35) Xiong, Y.-M.; Snyder, P. G.; Woollam, J. A.; Al-Jumaily, G.; Gagliardi, F.; Krosche, E. R., Controlled Index of Refraction Silicon Oxynitride Films Characterized by Variable Angle Spectroscopic Ellipsometry. *Thin Solid Films* **1991**, *206*, 248-253.

(36) Golightly, F.; Stott, F.; Wood, G., The Influence of Yttrium Additions on the Oxide-Scale Adhesion to an Iron-Chromium-Aluminum Alloy. *Oxid. Met.* **1976**, *10*, 163-187.

(37) Kuo, Y., Plasma Enhanced Chemical Vapor Deposited Silicon Nitride as a Gate Dielectric Film for Amorphous Silicon Thin Film Transistors—a Critical Review. *Vacuum* **1998**, *51*, 741-745.

(38) Subramanian, A., et al., Low-Loss Singlemode Pecvd Silicon Nitride Photonic Wire Waveguides for 532–900 Nm Wavelength Window Fabricated within a Cmos Pilot Line. *IEEE Photonics J.* **2013**, *5*, 2202809-2202809.

(39) Idris, I.; Sugiura, O., Film Characteristics of Low-Temperature Plasma-Enhanced Chemical Vapor Deposition Silicon Dioxide Using Tetraisocyanatesilane and Oxygen. *Jpn. J. Appl. Phys.* **1998**, *37*, 6562.

(40) Gaind, A.; Hearn, E., Physicochemical Properties of Chemical Vapor-Deposited Silicon Oxynitride from a Sih4-Co 2-Nh 3-H 2 System. *J. Electrochem. Soc.* **1978**, *125*, 139-145.

(41) Redey, S.; Razzouk, S.; Rey, C.; Bernache-Assollant, D.; Leroy, G.; Nardin, M.; Cournot, G., Osteoclast Adhesion and Activity on Synthetic Hydroxyapatite, Carbonated Hydroxyapatite, and Natural Calcium Carbonate: Relationship to Surface Energies. *J. Biomed. Mater. Res. Part A* **1999**, *45*, 140-147.

(42) Li, D.; Bancroft, G.; Kasrai, M.; Fleet, M.; Secco, R.; Feng, X.; Tan, K.; Yang, B., X-Ray Absorption Spectroscopy of Silicon Dioxide (Sio 2) Polymorphs; the Structural Characterization of Opal. *Am. Mineral.* **1994**, *79*, 622-632.

(43) Demirkiran, H.; Hu, Y.; Zuin, L.; Appathurai, N.; Aswath, P. B., Xanes Analysis of Calcium and Sodium Phosphates and Silicates and Hydroxyapatite–Bioglass® 45s5 Co-Sintered Bioceramics. *Mater. Sci. Eng., B* **2011**, *31*, 134-143.

(44) Rajendran, J.; Gialanella, S.; Aswath, P. B., Xanes Analysis of Dried and Calcined Bones. *Mater. Sci. Eng., B* **2013**, *33*, 3968-3979.

(45) Li, D.; Bancroft, G.; Kasrai, M.; Fleet, M.; Feng, X.; Tan, K.; Yang, B., High-Resolution Si K-and L2, 3-Edge Xanes of A-Quartz and Stishovite. *Solid State Commun.* **1993**, *87*, 613-617.

(46) Pinakidou, F.; Katsikini, M.; Paloura, E., Xafs Characterization of Buried Si X N Y O Z Samples. *Nucl. Instrum. Methods Phys. Res., Sect. B* **2003**, *200*, 66-72.

(47) Grinnell, F.; Feld, M., Fibronectin Adsorption on Hydrophilic and Hydrophobic Surfaces Detected by Antibody Binding and Analyzed During Cell Adhesion in Serum-Containing Medium. *J. Biol. Chem.* **1982**, *257*, 4888-4893.

(48) Giovambattista, N.; Debenedetti, P. G.; Rossky, P. J., Effect of Surface Polarity on Water Contact Angle and Interfacial Hydration Structure. *J. Phys. Chem. B* **2007**, *111*, 9581-9587.

(49) Szili, E. J.; Kumar, S.; Smart, R. S. C.; Lowe, R.; Saiz, E.; Voelcker, N. H., Plasma Enhanced Chemical Vapour Deposition of Silica onto Titanium: Analysis of Surface Chemistry, Morphology and Hydroxylation. *Surf. Sci.* **2008**, *602*, 2402-2411.

(50) Ceiler, M.; Kohl, P.; Bidstrup, S., Plasma-Enhanced Chemical Vapor Deposition of Silicon Dioxide Deposited at Low Temperatures. *J. Electrochem. Soc.* **1995**, *142*, 2067-2071.

(51) Poon, M.; Kok, C.; Wong, H.; Chan, P., Bonding Structures of Silicon Oxynitride Prepared by Oxidation of Si-Rich Silicon Nitride. *Thin Solid Films* **2004**, *462*, 42-45.

(52) Sakai, N.; Fujishima, A.; Watanabe, T.; Hashimoto, K., Quantitative Evaluation of the Photoinduced Hydrophilic Conversion Properties of Tio2 Thin Film Surfaces by the Reciprocal of Contact Angle. *J. Phys. Chem. B* **2003**, *107*, 1028-1035.

(53) Hasegawa, S.; He, L.; Inokuma, T.; Kurata, Y., Analysis of Photoemission in Amorphous Sio X and Sin X Alloys in Terms of a Charge-Transfer Model. *Phys. Rev. B* **1992**, *46*, 12478.

Table 2-1:Gas flow rates for silicon oxynitride (Si-O-N) layer deposition as they relate to their measured index of refraction by ellipsometry.

| Sample | Refractive Index | Deposition Rate (Angstroms/min) | Gas Flow Rates (sccm) $N_2O$ /$SiH_4$ | 15% $SiH_4$/Ar | $N_2O$ | $N_2$ | $NH_3$ |
|---|---|---|---|---|---|---|---|
| 1 | 2.0 | 320 | 0 | 24 | 0 | 225 | 50 |
| 2 | 1.82 | 360 | 0.13 | 24 | 3 | 225 | 50 |
| 3 | 1.65 | 390 | 0.67 | 24 | 16 | 225 | 50 |
| 4 | 1.57 | 520 | 6.46 | 24 | 155 | 225 | 50 |
| 5 | 1.45 | 550 | 6.67 | 24 | 160 | 225 | 50 |

Table 2-2:. Atomic Concentration of elements in Si-O-N overlays measured by Nuclear Reaction Analysis

| Sample | Element Surface Concentration ($10^{15}$ atoms/$cm^2$) C | N | O | Si | H | Areal Density mg/$cm^2$ |
|---|---|---|---|---|---|---|
| 1 | 8.337 | 562.7 | 29.65 | 410.7 | 238.0 | 0.03372 |
| (at. %) | 0.6673 | 45.04 | 2.373 | 32.88 | 19.05 | |
| 2 | 8.187 | 589.0 | 122.7 | 420.1 | 256.0 | 0.03729 |
| (at. %) | 0.5865 | 42.19 | 8.811 | 30.09 | 18.33 | |
| 3 | 7.159 | 333.3 | 225.2 | 356.0 | 175.0 | 0.03089 |
| (at. %) | 0.6526 | 30.38 | 20.51 | 32.45 | 15.99 | |
| 4 | 6.031 | 44.95 | 710.7 | 424.7 | 44.9 | 0.04009 |
| (at. %) | 0.4899 | 3.652 | 57.76 | 34.50 | 3.646 | |
| 5 | 5.726 | 0 | 814.7 | 408.8 | 22.10 | 0.04104 |
| (at. %) | 0.4577 | 0 | 65.15 | 32.68 | 1.767 | |

The areal density was determined from the sum of the elemental concentration and multiplying by the average molecular weight.
This method is very sensitive to carbon and the carbon results above are likely a surface contamination (almost universally present on surfaces.

Table 2-3:Calculations for the RMM and RBM mathematical models for Si-O-N films.

| Sample | | RMM [Si-Si] – [Si-O] – [Si-N]) | | | RBM $Si_zO_xN_y$ | | | Partial Charge ($P_i$) | | | $\sum P_i$ |
|---|---|---|---|---|---|---|---|---|---|---|---|
| | a:b | Si-Si | Si-O | Si-N | z | x | y | Si | O | N | |
| $Si_3N_4$ | 1.73 | 0.02 | 0.04 | 0.94 | 1.00 | 0.00 | 1.33 | 0.24 | 0.00 | -0.18 | 0.00 |
| 1 | 1.72 | 0.05 | 0.11 | 0.83 | 1.00 | 0.14 | 3.86 | 0.36 | -0.21 | -0.09 | 0.00 |
| 2 | 1.7 | 0.01 | 0.35 | 0.64 | 1.00 | 0.49 | 3.51 | 0.38 | -0.20 | -0.08 | 0.00 |
| 3 | | 0.01 | 0.63 | 0.36 | 1.00 | 1.24 | 2.76 | 0.40 | -0.18 | -0.06 | 0.00 |
| 4 | 1.2 | 0.08 | 0.90 | 0.02 | 1.00 | 3.65 | 0.35 | 0.49 | -0.13 | -0.01 | 0.00 |
| 5 | 1.15 | 0.00 | 1.00 | 0.00 | 1.00 | 4.00 | 0.00 | 0.51 | -0.13 | 0.00 | 0.00 |
| $SiO_2$ | 1.02 | 0.01 | 0.99 | 0.00 | 1.00 | 2.00 | 0.00 | 0.40 | -0.20 | 0.00 | 0.00 |

a:b represents peak area ratio based on XANES analysis of the Silicon L-edge
Partial charge calculations assert the validity of RBM model ($\sum P_i=0$)

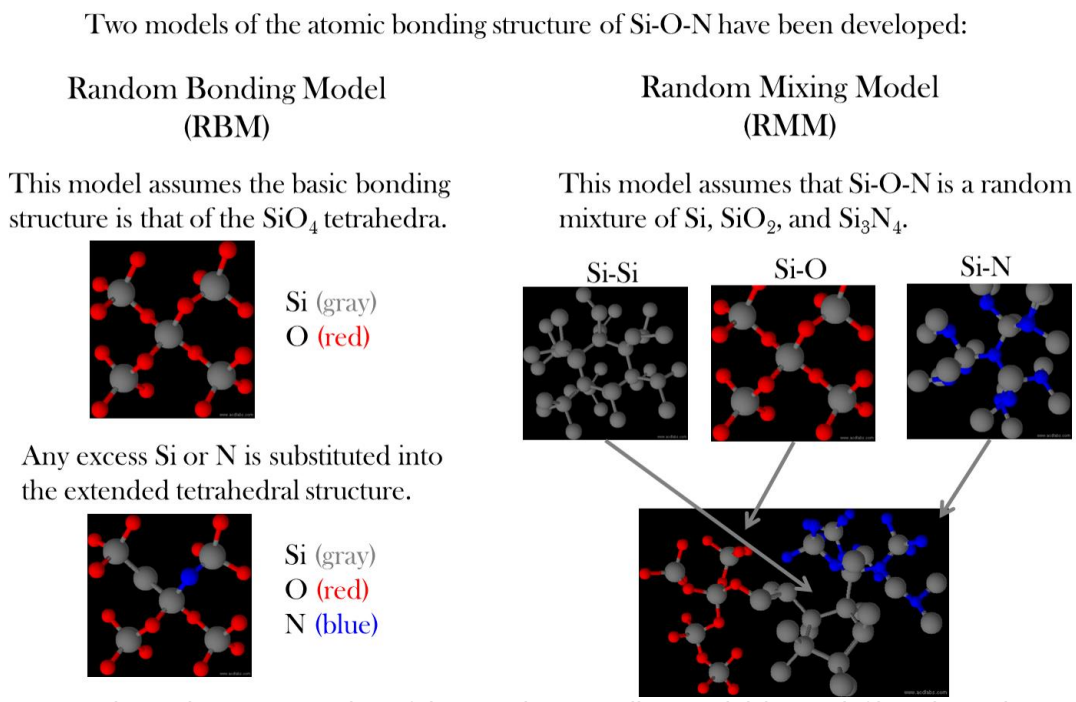


Figure 2-1:Schematic representation of the Random Bonding Model (RBM, left) and Random Mixing Model (RMM) of the amorphous Si-O-N elemental system.

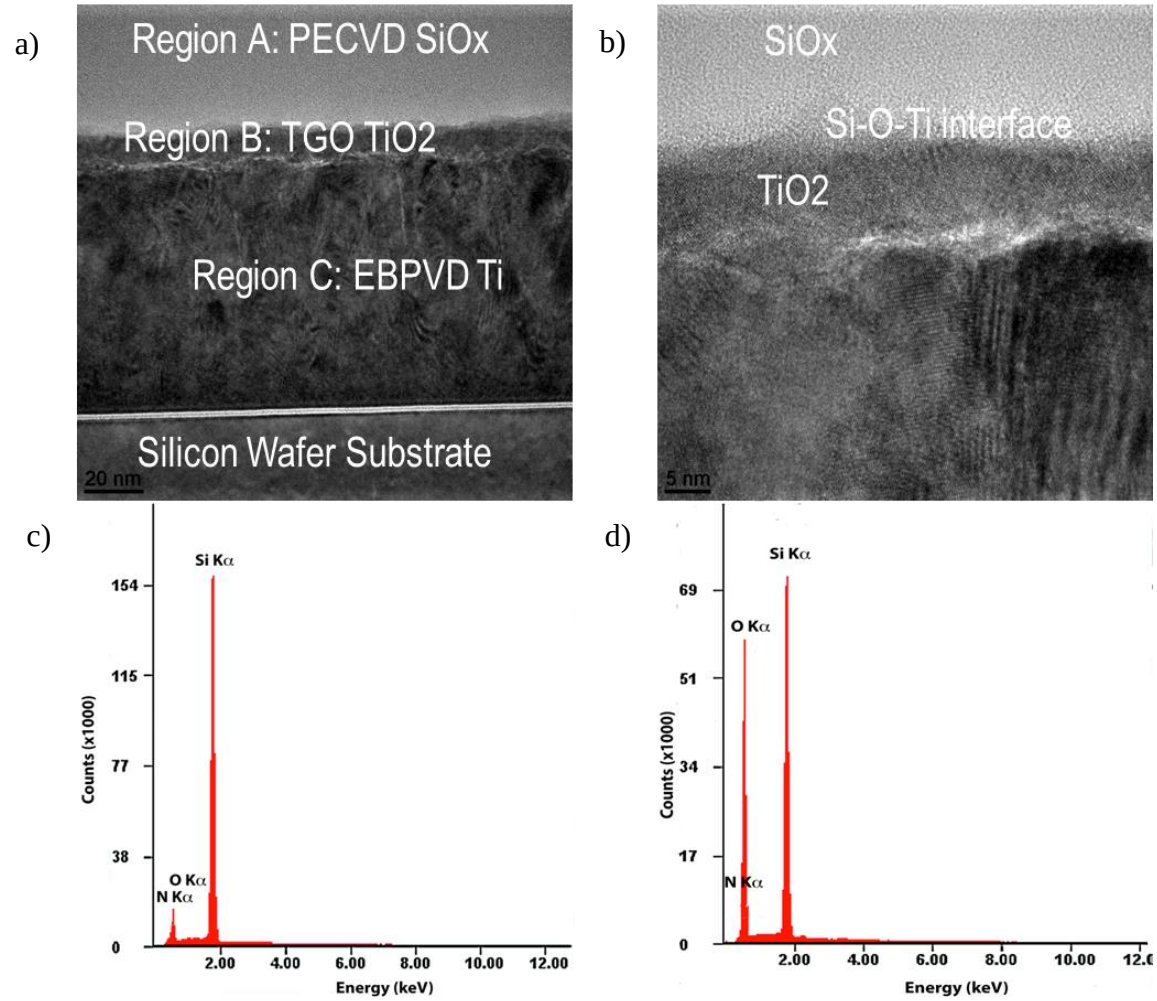


Figure 2-2:Transmission electron micrographs and EDX spectra of (a) the fabricated Ti-TiO2-SiOx based biomedical device and (b) the magnified view of Ti-O-Si interface. EDS spectra showing low contaminant element levels for a (c) high-nitrogen and (d) high-oxygen Si-O-N sample.

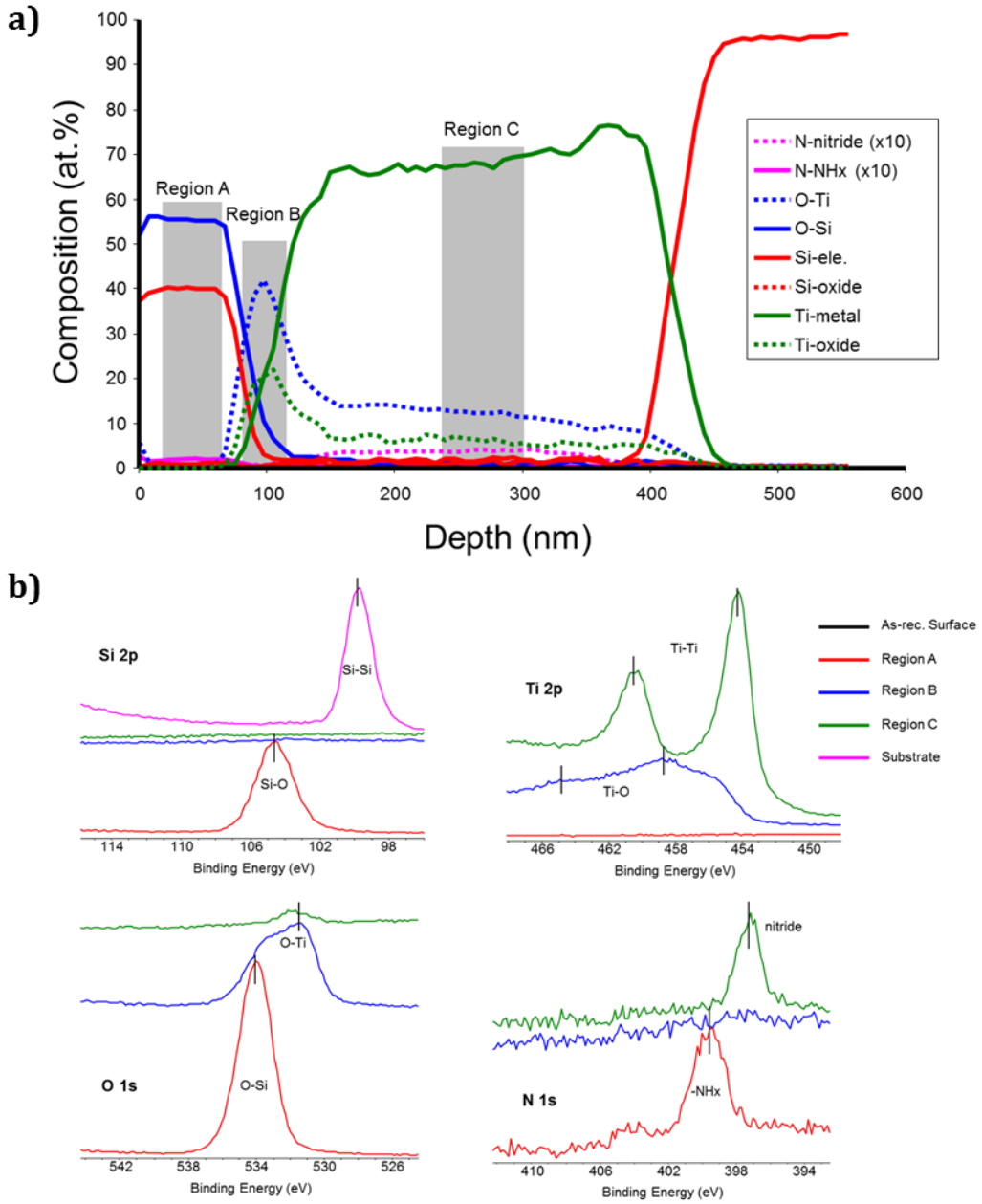


Figure 2-3:XPS analysis of biomedical devices elemental composition through the thickness of the device from

Figure 3a. (a) Depth scale determined by sputter rate of 15 nm/min. Sputter cycles were 30 sec. Shaded areas show particular region that had different chemical signals, i.e. N

was present in the $SiO_2$ layer in one chemical form and was present in a different chemical form in the Ti layer. (b) Individual spectra from these regions are compared for Si, O, Ti, and N. Note that the N ($NH_x$ and nitride) signals are all plotted magnified by a factor of 10.

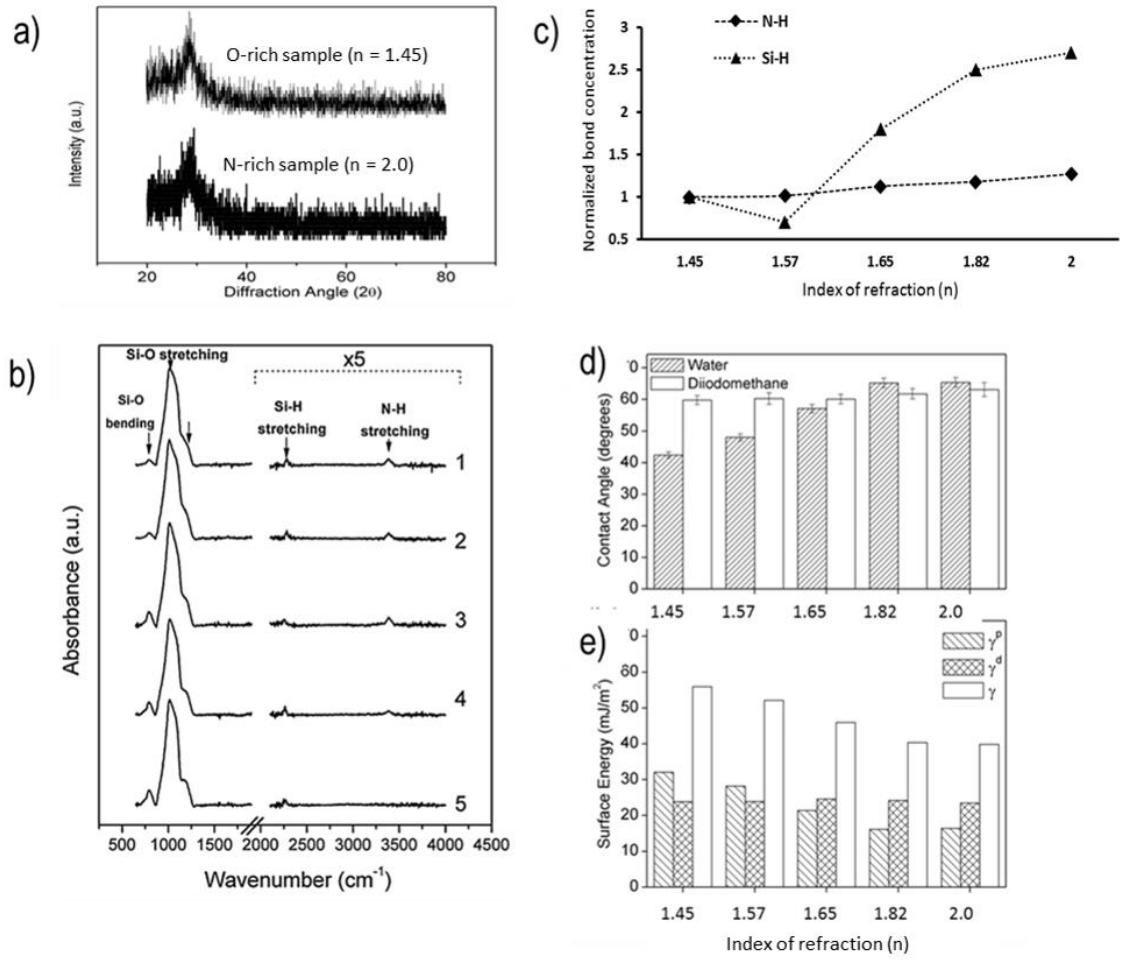


Figure 2-4: Surface characterization of PECVD Si-O-N films.

(a) X-ray diffraction results indicating the presence of amorphous silica-based films. (b) FTIR spectra of Si-O-N films with Si-H and N-H spectral contribution magnified and (c) Plot of normalized N-H and Si-H bond concentration as a function of refractive index. The concentrations of N-H ($0.128 \times 10^{22}$ atoms $cm^{-3}$) and Si-H ($1.8 \times 10^{22}$ atoms $cm^{-3}$) on amorphous silica surfaces (n=1.45) evaluated by FTIR-ATR in this work were used to illustrate the relative change in these bond concentrations for higher refractive index samples. (d) Sessile drop contact angle of water and diiodomethane and (e) calculated

surface energy of samples, broken into polar $\gamma^p$ and dispersive $\gamma^d$ components. The dispersive component is relatively constant while the polar component increases with increasing nitrogen content.

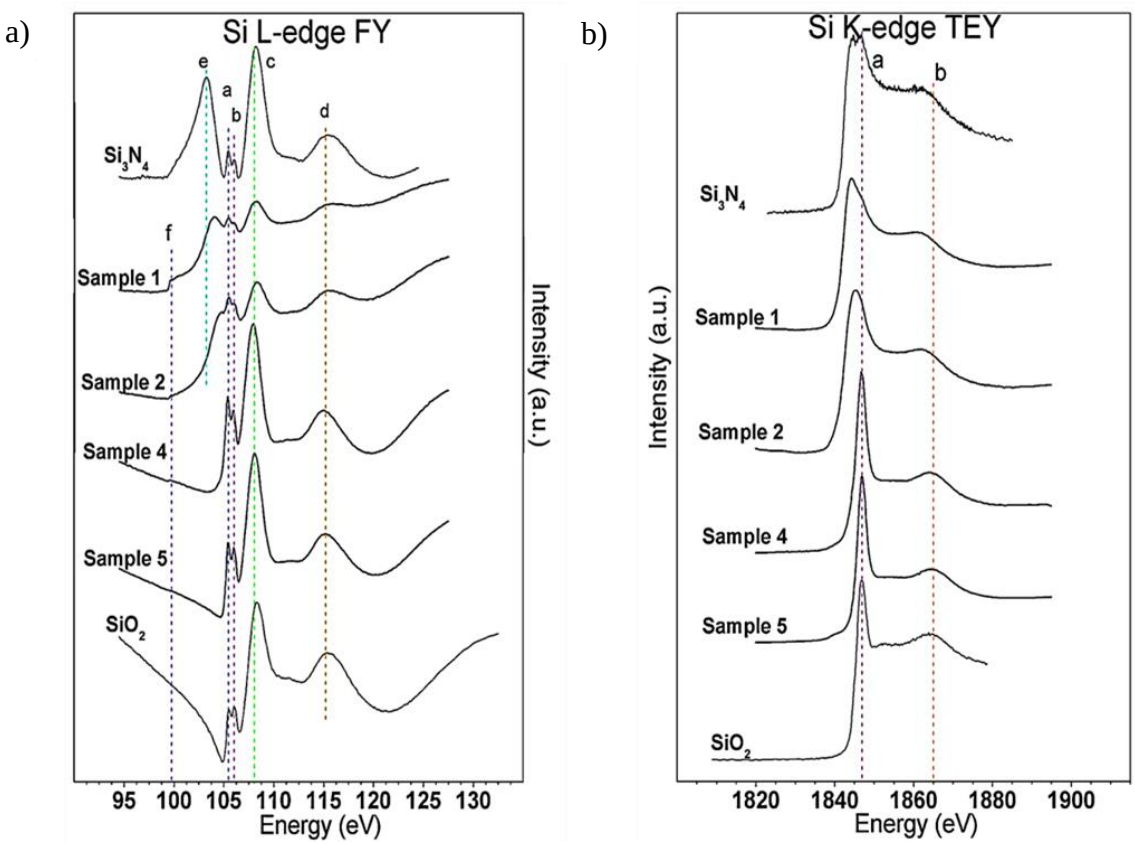


Figure 2-5: (a) Silicon L2,3-edge XANES spectra and (b) Silicon K-edge XANES spectra of four Si-O-N coating chemistries with Si3N4 and SiO2 standards for comparison.

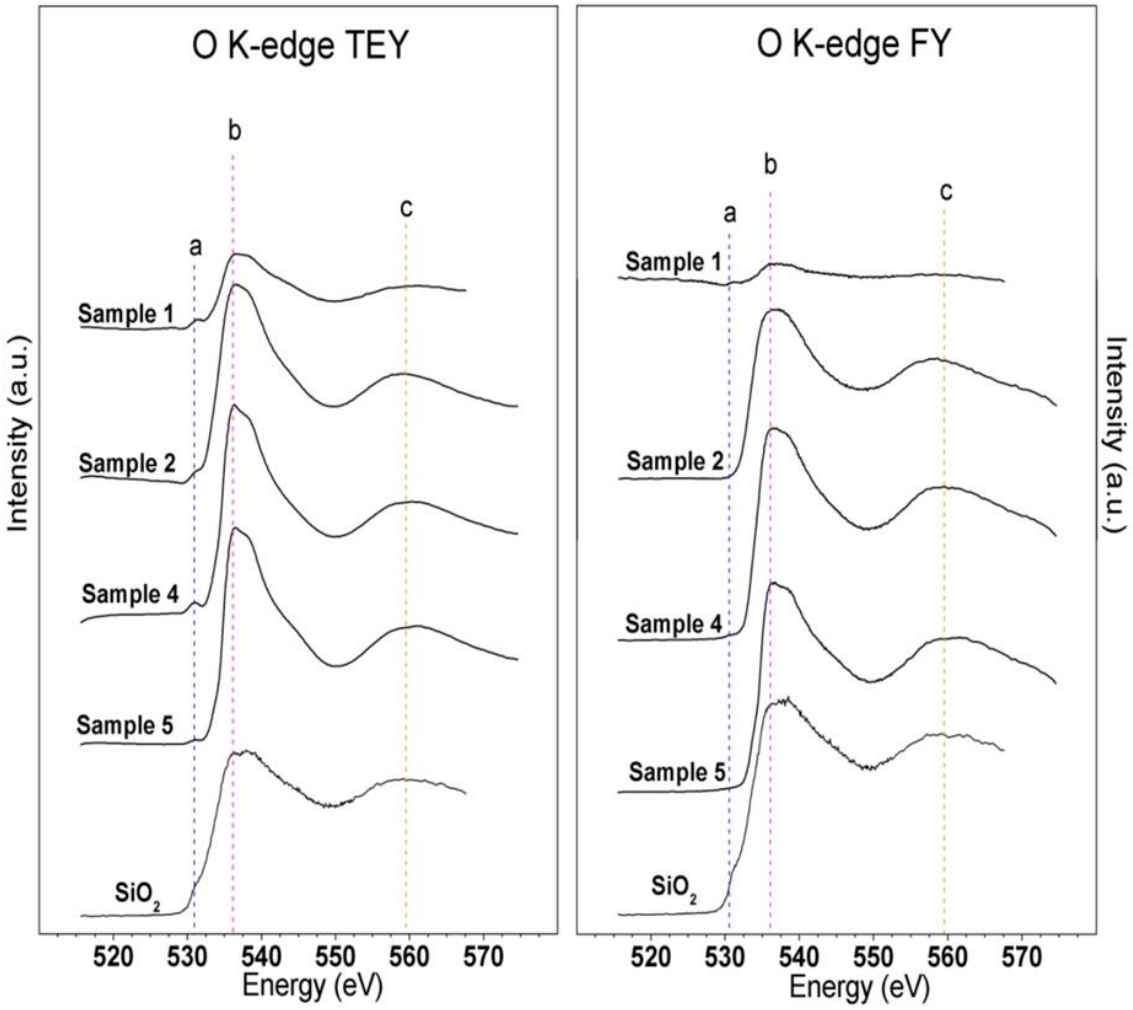


Figure 2-6: Oxygen K-edge XANES TEY and FY spectra of four Si-O-N coating chemistries with an SiO2 standard for comparison.

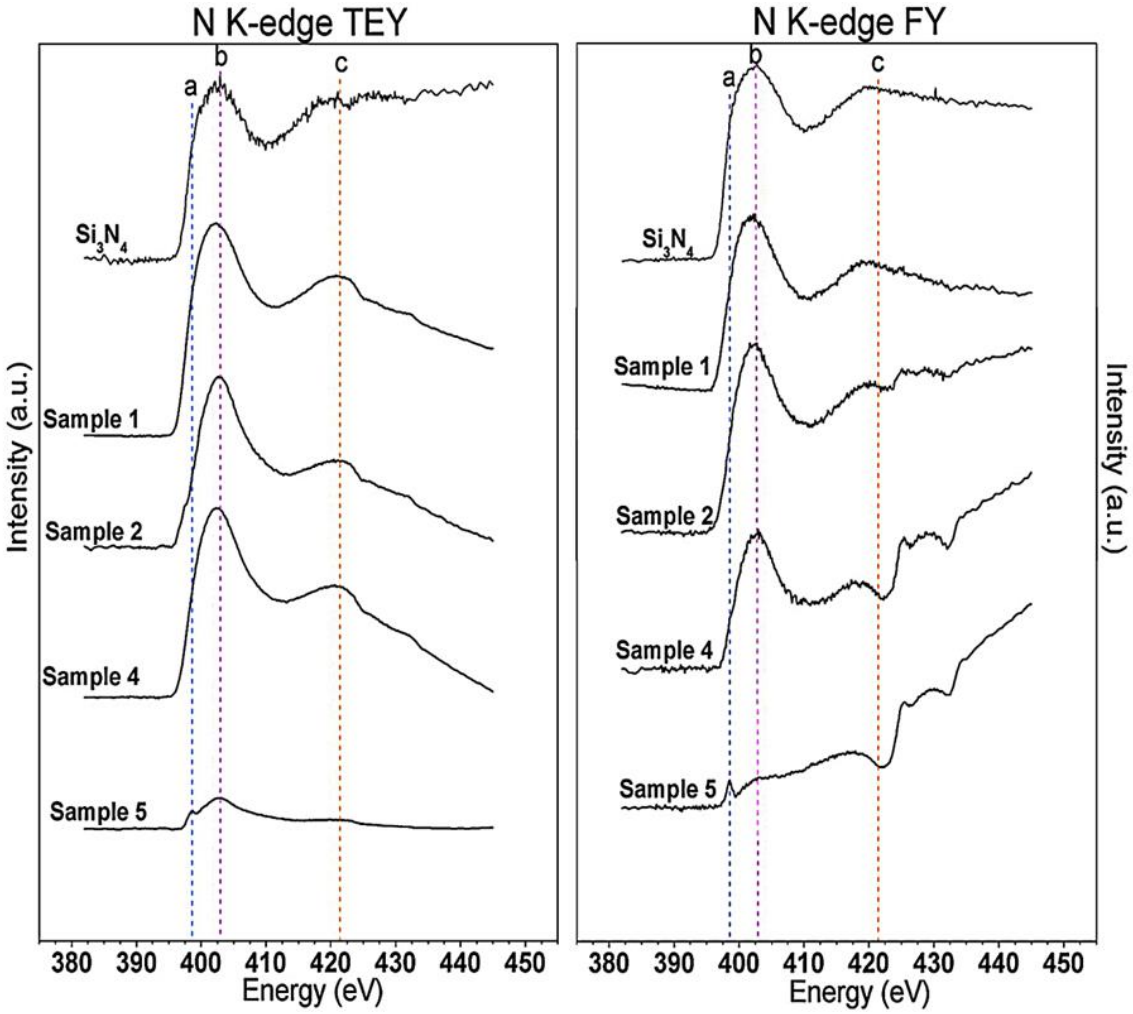


Figure 2-7 Nitrogen K-edge XANES TEY and FY spectra of four Si-O-N coating chemistries with a Si3N4 standard.

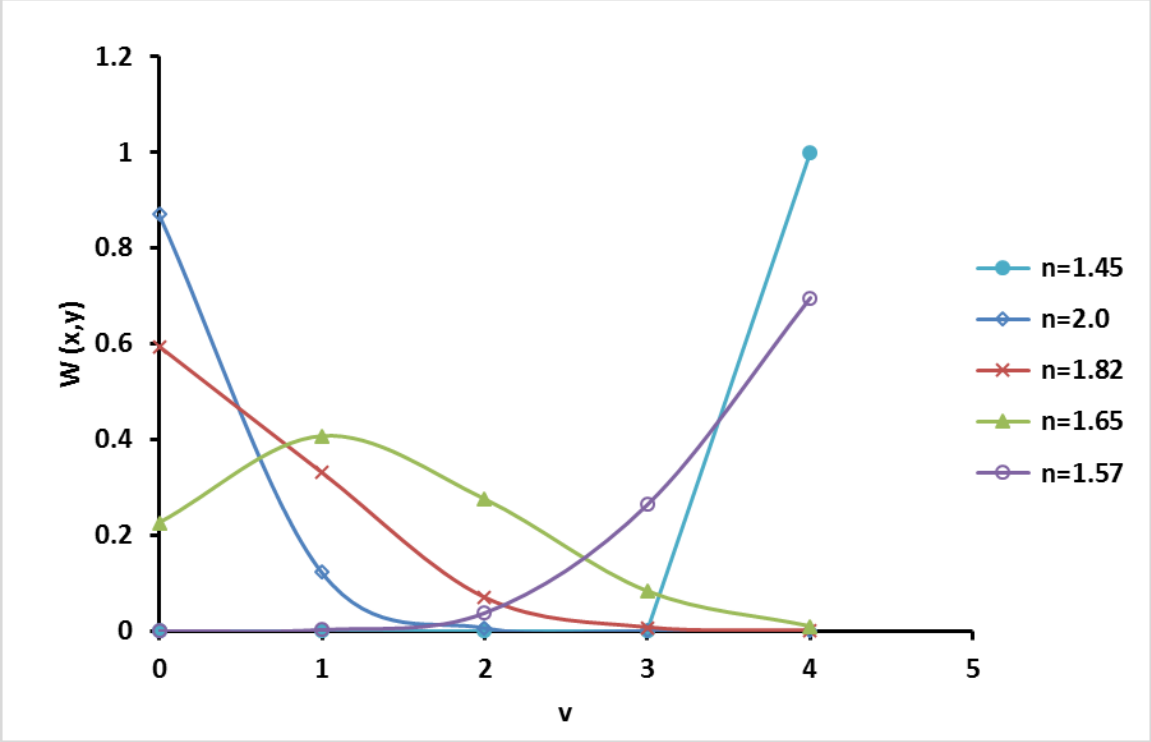


Figure 2-8: Work function distribution plotted against oxygen coordination number v

The results of calculations using the data from RBS for the Si-O-N samples in Table 2. For the O-rich samples (n=1.45, 1.57), W(x,y) was estimated to be close to unity indicating their fit with the $SiO_4$ tetrahedron while the samples with increased N content (n=1.65, 1.82, 2.0) exhibited coordination that is not reflected in the tetrahedral model.

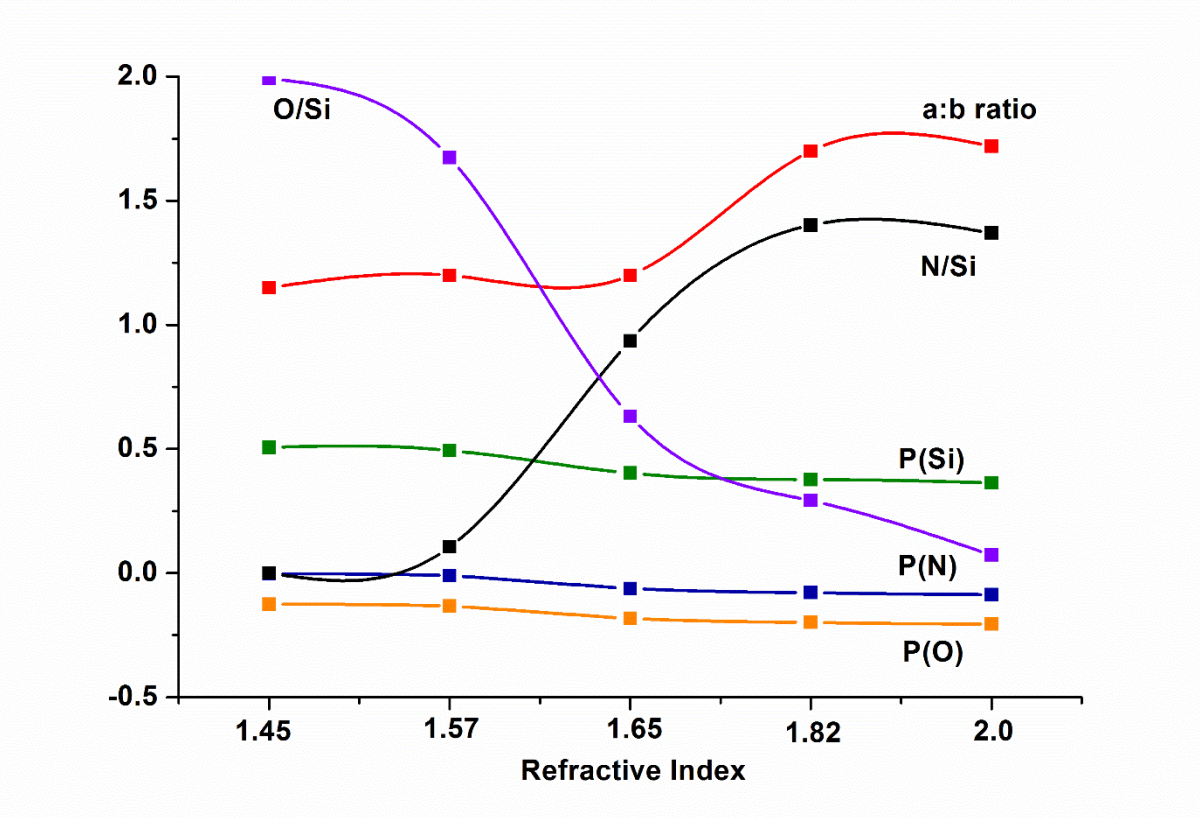


Figure 2-9: The calculated partial charge of silicon P(Si), oxygen P(O), and nitrogen P(N) as a function of Si-O-N film refractive index.

Also plotted in this figure are the experimentally determined O/Si ratio (x) and N/Si ratio (y) and the a:b peak area ratio based on XANES analysis of the Silicon L-edge.

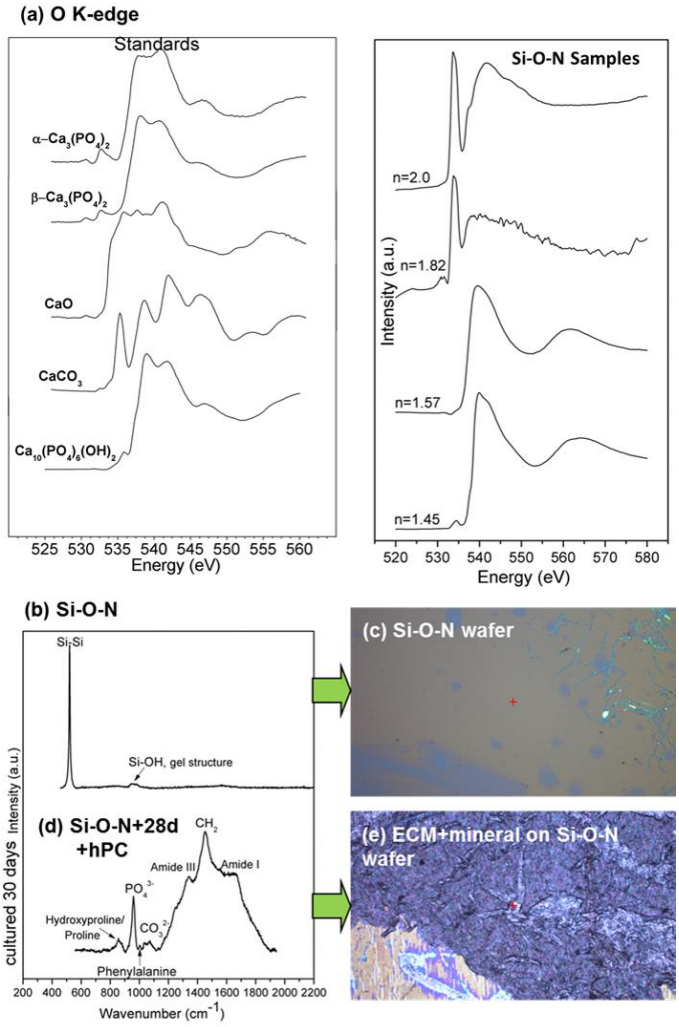


Figure 2-10:Figure 10. (a) XANES analysis of O K-edge data shows that as the N content increases, the presence of O peaks coordinated in a carbonate structure appears with increasing intensity relative to the peak showing O coordinated into a phosphate structure (b) Raman spectroscopy showed the initial layers of silica on Si-O-N surfaces. (c) Similarly, the optical micrograph showed no minerals present on the surfaces initially. (d) After 4 weeks of *in vitro* cell culture, Si-O-N surfaces exhibited the formation of carbonate, phosphate, and amide peaks associated with

mineralized tissue to indicate the presence of collagenous matrices. (e) Optical micrograph showed the presence of hydroxycarbonate apatite biomineral on the Si-O-N surface, indicated by the formation of white nodules on the surface Reprinted with permission from American Chemical Society: ACS Applied Materials and Interfaces,[22] copyright (2015).

## TOC Figure

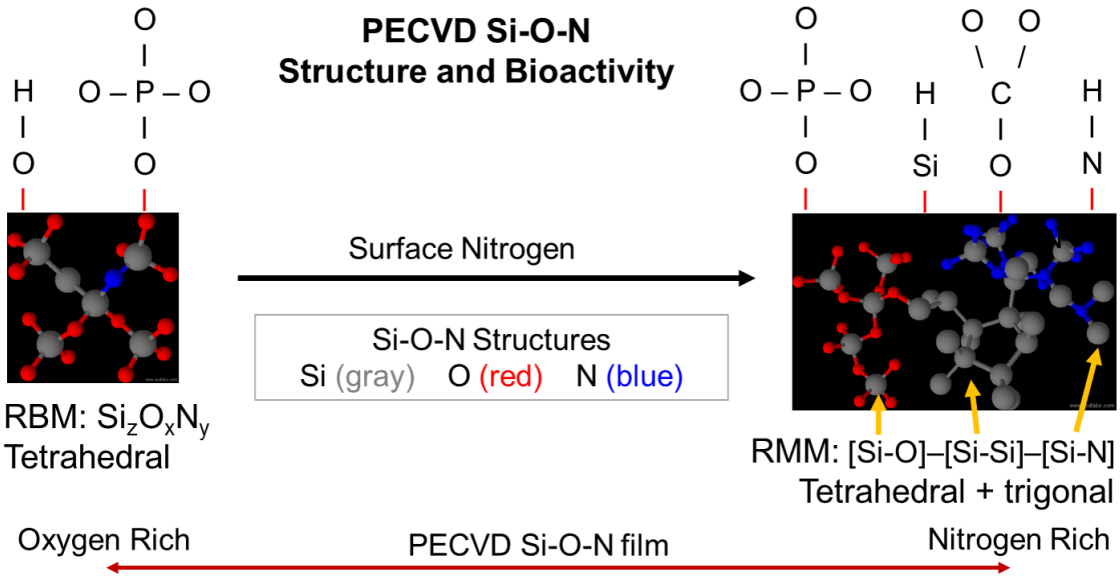
PECVD Si-O-N
Structure and Bioactivity
Surface Nitrogen
Si-O-N Structures
Si (gray) O (red) N (blue)
RBM: $Si_zO_xN_y$
Tetrahedral
RMM: [Si-O]–[Si-Si]–[Si-N]
Tetrahedral + trigonal
Oxygen Rich
PECVD Si-O-N film
Nitrogen Rich

## B. Amorphous Silica, a New Antioxidant Role for Rapid Critical-Sized Bone Defect Healing

Azhar Ilyas,[a] Tetsuro Odatsu,[a,b] Ami Shah,[c] Felipe Monte,[d,e] Harry K.W. Kim,[e,f] Philip Kramer,[a] Pranesh B. Aswath[c] and Venu G. Varanasi,[a,*]

[a] Department of Biomedical Sciences, Texas A&M University, Baylor College of Dentistry, Dallas, TX 75246, USA

[b] Department of Applied Prosthodontics, Graduate School of Biomedical Sciences, Nagasaki University, 1-7-1, Sakamoto, Nagasaki 852-8588, Japan

[c] Department of Materials Science and Engineering, University of Texas at Arlington, Arlington Texas 76019, USA

[d] Department of Bioengineering, University of Texas at Arlington, Arlington Texas 76019, USA

[e] Center for Excellence in Hip Disorders, Texas Scottish Rite Hospital, Dallas, TX 75219, USA

[f] Department of Orthopaedic Surgery, University of Texas Southwestern Medical Center at Dallas, Dallas, TX 75390, USA

[*] To whom correspondence should be addressed:
Venu G. Varanasi, Ph.D.

3302 Gaston Avenue, Texas A&M Health Science Center, Dallas, TX 75246, USA
Phone: +1-214-370-7006
Fax: +1-214-874-4538
E-mail: varanasi@bcd.tamhsc.edu

Abstract

Traumatic fractures cause structurally unstable sites due to severe bone loss. Such fractures generate a high yield of reactive oxygen species (ROS) that can lead to oxidative stress. Excessive and prolonged ROS activity impedes osteoblast differentiation, and instigates long healing times. Stimulation of antioxidants such as superoxide dismutase (SOD1), are crucial to reduce ROS, stimulate osteogenesis, and strengthen collagen and mineral formation. Yet, no current fixative devices have shown an ability to enhance collagen matrix formation through antioxidant expression. Here, we report plasma-enhanced chemical vapor deposition (PECVD)-based amorphous silicon oxynitride (Si(ON)x) as a potential new fracture healing biomaterial that adheres well to the implant surface, releases $Si^{+4}$ to enhance osteogenesis, and forms a surface hydroxyapatite for collagen mineral attachment. These materials provide a sustained release of $Si^{+4}$ in physiological environment for extended times. The dissolution rate partially depends on the film chemistry and can be controlled by varying O/N ratio. The presence of $Si^{+4}$ enhances SOD1, which stimulates other osteogenic markers downstream and leads to rapid mineral formation. *In-vivo* testing using a rat critical-sized calvarial defect model shows a more rapid bone-regeneration for these biomaterials as compared to control groups, that implies the clinical significance of the presented biomaterial.

**Keywords:** Superoxide dismutase, bone formation, antioxidant, blood vessel formation, PECVD

## 1. Introduction

Bone fracture incidence from trauma, age-related fragility or disorders is estimated to rise 400% by 2050 as life expectancy increases. This contributes to ~$8 billion in morbidity/mortality costs and ~800,000 procedures annually.[1-3] Upon fracture, the site is structurally unstable and hypoxic due to severe bone loss and ischemia. Inflammation ensues after site re-vascularization and oxygen metabolites accumulate as reactive oxygen species (ROS: $O_2^-$, $H_2O_2$). During normal healing, osteoblasts express antioxidant enzymes (e.g., superoxide dismutase [SOD1]) to convert ROS into oxygen and water and induce osteoblast differentiation. This promotes collagen synthesis, cross-linking, strength, and osteogenic marker expression [osterix (OSX), osteocalcin (OCN), collagen (COL(I)), and lysil oxidase (LOX)] for bone formation.

However, in the case of substantial bone defects, structural instability persists and the high ROS activity leads to oxidative stress, which inhibits osteogenesis and lowers bone regenerative capacity.[4] Cells express antioxidant markers, including endogenous genes and exogenous enzymes that eradicate ROS in order to protect themselves against DNA damage.[5] An imbalance between excessive ROS generation and insufficient antioxidant defense mechanism makes these fractures difficult to heal.[6,7] ROS reduction requires enhanced enzymatic antioxidant production (e.g., SOD1, glutathione reductase, catalase).[8,9] SOD1 is also important because its deficiency reduces LOX-induced collagen cross-linking, and bone strength by 25%.[10] Patients suffering

with such fractures given dietary antioxidants (Vitamin C/E) had higher SOD1 activity (1.5-3-fold), which down-regulated ROS (3-fold), increased OCN (3-fold),[6,11] and showed the potential to cut health care costs by reducing hospital stays by 2 days.[12] Thus, antioxidants for enhanced expression of SOD1 are critical to pursue normal bone healing in such fractures.

Despite their benefits, dietary antioxidants cannot heal fractures on their own and require structural support for bony union.[13] Metal implants (e.g., titanium [Ti]) are used as structural materials because of their strength, however, they have long healing times, do not resorb, and have not shown any antioxidant effect.[14] Previous attempts to coat the metal implants with bioglass show that ionic products like $Si^{+4}$ from the dissolution of bioglass enhance osteogenic markers expression and provide high production of collagen by osteoblast cells.[15,16] Similarly, strontium-doped bioactive glass coatings onto metal implants showed an improved anti-oxidative defense against ROS[4] yet, bioactive glass coatings lack interfacial adhesion and face delamination issues due to thermal expansion mismatch.[17] Bioglass with added MgO for improved thermal expansion matching, have shown a drawback to down-regulate important osteogenic markers associated with bone formation due to $Mg^{2+}$ release.[18] Thus, there is a great clinical need for novel biomedical device materials/designs that provide structural and antioxidant support to accelerate bone healing.

Alternatively, amorphous silica (SiOx) integration onto metal implants can provide structural support along with enhanced osteogenesis by inducing rapid hydroxyapatite (HA) formation needed for bone attachment. Moreover, SiOx

network releases $Si^{+4}$ that stimulates biomineral synthesis, thus, eliminates the need for drugs. Yet, sustaining $Si^{+4}$ release, hastening surface HA formation, and understanding its osteoinductive role are needed to form SiOx-modified devices that support and improve fracture healing. In this study, we proposed PECVD-based nitrogen-incorporated amorphous silica (Si(ON)x) overlays, to modify biomedical devices for rapid fracture healing. We hypothesized that these devices would provide sustained $Si^{+4}$ release to stimulate SOD1 expression and enhance osteogenesis while rapid formation of carbonated HA improves osseointegration and helps rapid fracture healing. Bio-inspired surface features at micro/nanometer scales are known to influence cellular behaviors such as cell adhesion, growth, migration and differentiation.[19-23] Micrograting structures (regular ridge and groove pattern) have gained maximum interest due to its simplicity.[19] Moderately rough surfaces (1-2 μm) exhibit stronger bone responses than smoother or rougher surfaces.[22] Recently marketed oral implants are moderately rough and allow bone ingrowth into minor surface irregularities, promoting osseointegration.[22] Therefore, in this study, we will integrate micrograting patterns to make the surface moderately rough for enhanced cellular responses.

Thus, our central hypothesis was that Si(ON)x-modified devices would provide dual antioxidant and structural support for rapid bone regeneration and fracture healing. In order to study the antioxidant role of ionic Si, two treatment conditions (control, ionic Si) were prepared and tested with MC3T3 cell. Wild type and SOD1 knockdown cells (using siRNA) were tested with each treatment.

Amorphous silica-based biomaterials were fabricated to develop an ionic Si delivery device. The amorphous silicon oxynitride Si(ON)x thin films were overlaid onto sample surfaces using plasma enhanced chemical vapor deposition (PECVD) process while 3-dimensional surface nano-features were formed by lithography and etching processes as described in our previous work.[24] The samples were tested *in-vitro* to study cell-surface interactions and *in-vivo* evaluation of the optimized Si(ON)x chemistry was performed using a rat critical size calvarial defect model. Studies show that the implants are typically harvested 4 to 6 weeks postoperatively to analyze the bone healing effect.[25-27] For that reason, we chose 5 weeks to look at the defect healing over the course of healing period. The results of this study demonstrated that Si(ON)x-modified devices provided sustained $Si^{+4}$ release to stimulate osteogenesis and accelerated biomineralization via rapid bioactive HA formation. The ionic Si up-regulated SOD1 and several other osteogenic markers for wild type cells whereas SOD1 knockdown inhibits $Si^{+4}$ enhancement of osteoblast differentiation. *In-vivo* testing of the optimized Si(ON)x chemistry showed rapid bone-regeneration in a rat critical size calvarial defect model whereas such a speedy bone healing was not observed in the absence of ionic Si.

## 2. Results

Results of testing the effect of ionic Si on osteogenic differentiation are shown in **Figure 1**. Ionic Si was observed to enhance superoxide dismutase SOD1 (more than 3-fold) and several genes associated with osteogenesis including osterix (more than 2-fold), lysil oxidase (more than 2.5-fold) and

collagen type 1 (nearly 2.5-fold) for the wild type MC3T3 cells. SOD1 knockdown cells were prepared by siRNA transfection over 6 days. Cell viability test verified that the transfecting vehicle did not impact cell viability, also evidenced by control siRNA and control treatments having similar effect on ECM formation (data not shown). As compared to wild type control treated cells, SOD1 knockdown cells (45% knockdown) were observed to decrease SOD1, osterix, lysil oxidase and collagen type 1 expression and the presence of $Si^{+4}$ didn't show any improvement in expression of these osteogenic markers for SOD1 knockdown cells. Results from optical microscopy of ECM samples (Figure 1B) also showed an absence of elongated collagen fiber matrices after 6 days for SOD1 knockdown cells. Whereas, the presence of ionic Si was observed to enhance the density of elongated collagen fibers in resultant extracellular matrices for wild type cells, evidenced by Picrosirius red stained tissue with yellow-orange elongated collagen fibers indicated by yellow dotted circles. Quantitative analysis confirms one order of magnitude higher collagen formation for wild type cells in the presence of ionic silicon (Figure 1C). Therefore, these results show that ionic Si enhanced osteogenic expression and elongated collagen matrix formation during osteoblast differentiation that was observed for wild type cells but not for SOD1 knockdown cells. It shows that the enhanced osteogenic gene expression and collagen matrix formation by ionic Si depends on SOD1 enhancement.

For ionic Si to be useful in applications of bone healing, delivery devices must be fabricated that can sustain the release of $Si^{+4}$ to attached cells. **Figure 2a** shows a schematic diagram to illustrate the cross section view of the device

fabrication process whereas Figure 2b shows the SEM micrograph for the actual device after fabrication. Plasma-enhanced chemical vapor deposition (PECVD) gave highly conformal, adherent and uniform thin film overlays onto ridge and groove patterned (micrograting) surfaces.[24] PECVD-based amorphous silicon oxynitride (Si(ON)x) surfaces showed a sustained release of ionic silicon ($Si^{+4}$) when immersed in physiological environment. **Figure 3a** shows the ICP-OES data to demonstrate the release of $Si^{+4}$ from 12 mm x 12 mm sample sections immersed in 4 mL of αMEM and incubated for 0, 6, 12, 24, 48, 96, and 192 hours. According to manufacturer's specifications, αMEM contained little to no silicon (<0.01 ppm). Initially in the soaking experiment, there was little silicon in solution, however, after 12 hours sample 1 (n= 1.80) showed some evidence of dissolution. For the other Si(ON)x chemistries studied, Si release was observed after 24 hours of dissolution. The data showed a sustained release of $Si^{+4}$ over a period of 8 days and the degradation kinetics depending on the surface chemistry (incorporation of N). Comparison of surface topographies before and after *in-vitro* immersion (Figure 3b, 3c) exhibited the formation of hydroxyapatite (HA) on the surface, facilitated by the hydroxyl groups readily available on the surface by PECVD process as explained in our previous work.[24] Table 2-4 lists coating thickness dissolved for each of the four Si(ON)x sample chemistries as a function of time in dissolution. The starting coating thickness on all of these samples was 100 nm (with 3-5% variance based on manufacturer's specifications).

Table 2-4: Coating thickness dissolved after immersion in αMEM (determined by Si release)

| Sample | Thickness (nm) with an estimated error of ≤5% | | | | | | |
|---|---|---|---|---|---|---|---|
| | 0h | 6h | 12h | 24h | 48h | 96h | 192h |
| 1 (n=1.80) | 0 | 0.2 | 34.2 | 50.5 | 58.9 | 69.6 | 83 |
| 2 (n=1.68) | 0 | 1.6 | 4.1 | 56.5 | 71.8 | 82.8 | 102.5 |
| 3 (n=1.58) | 0 | 0.6 | 2.2 | 54.9 | 61.1 | 91.5 | 98.1 |
| 4 (n=1.45) | 0 | 1.7 | 3.2 | 56.0 | 63.8 | 81.9 | 102.3 |

After 12 hours in solution, less than 5% of the coating dissolved for all chemistries except Sample 1. In this sample, about 35% of the coating was dissolved after 12 hours, and after 8 days (192 hours), approximately 20% of the coating still remained. For the other samples, release of Si was not observed until 24 hours in solution, where approximately 50% of the coating was left. However, after 8 days in solution, these coatings appeared to have completely dissolved. The thickness values were calculated by using the ionic silicon ($Si^{+4}$) release data measured by ICP-OES analysis. The variance in the ICP measurements and the simplifying assumptions involved in thickness calculations could lead to inaccurate results with an estimated error of ≤5%. However, this data suggests that Si release kinetics is partially dependent on the coating chemistry, which can be altered and fine-tuned to get the desired $Si^{+4}$ release whereas the coating thickness accounts for the length of release period.

Moreover, it was also desired to determine if there was an effect of the surface chemistry on osteogenic markers expression. Therefore, relative expression of several genes associated with osteoblast differentiation was

studied using MC3T3 cells and the human periosteum cells. The results for MC3T3 cells (**Figure 4**) showed that expression of SOD1 was significantly increased at 6 hours after induction of differentiation (Figure 4a, 3 to 12 times relative to control glass cover slip group), and settled down to same level at 24 hours. The transcription factors Runx2 and Sp7, were chosen for measurement due to their vital role in stimulating osteoblast differentiation and mineralization. The transcription factors Runx2 and Sp7 showed the same trend as SOD1 gene expression, but their reduction was moderate compared to SOD1. The gene expression of OCN on wafer sample was remarkably increased at 6 hours, and continued until 48 hours after induction of differentiation. The gene expression of Col(I)-α1 up-regulated and down-regulated alternately at these time points. Similarly, human periosteum cells also showed (**Figure 5**) an enhanced expression of SOD1 on Si(ON)x surfaces at 24 hours after induction of differentiation. The up-regulated expression of SOD1 induced downstream expression of the osteoblast differentiation markers including Runx2 and collagen type 1, maximally enhanced at 48 hours time point.

*In-vivo* evaluation of these biomaterials was performed using a rat critical-sized calvarial defect model. The Si(ON)x test samples were implanted in the rat calvaria as shown in **Figure 6**. The implanted sample was extracted after allowing 5 weeks of recovery. The extracted bone-implant sample showed a strong fixation of the implant with the surrounding bone whereas micro-level computerized tomography (μCT) scan confirmed the presence of hard mineralized newly formed bone that filled almost all space around the Si(ON)x

coated implant (**Figure 7a**). On the other hand, controls samples (substrate only) were found mobile and loosely connected to surrounding bone via soft tissue when extracted after 5 weeks. The micro-CT data revealed that no ample regeneration of new bone occurred to fill the interfacial gaps for control samples during the same recovery time (Figure 7b). Similarly, negative control (empty defect) showed no signs of sufficient healing and confirmed that the defect remained critical size and would not heal on its own (Figure 7c). The bone mineral density and the ratio of bone volume (BV) to total volume (TV) was determined using microCT data to give more quantitative insight into bone regeneration (Figure 7d). The results showed that Si(ON)x surfaces which were able to fill the interfacial gap with newly generated bone after 5 weeks of recovery had about 5 times higher BV/TV as compared to control samples. Higher BV/TV indicates larger volume of mineralized bone regenerated for the Si(ON)x surfaces. Similarly, histology analysis using Stevenel's Blue stain and Van Gieson Picro-Fuchsin counterstain also verified the formation of fully mineralized bone at the bone-implant interface for Si(ON)x test samples whereas the control samples showed less mineral formation with mostly collagenous fiber as shown in **Figure 8**. Histology data also indicated the presence of blood vessels in the newly generated bone and well-oriented collagenous fibers with osteoblasts sitting along the bone edges, which designates the healing impact of the implanted material.

Raman spectroscopy data was analyzed to study the composition and the maturity (mineralization) of the newly formed bone after 5 weeks of recovery

time. Intensity of $PO_4^{3-}$ peak at 950$cm^{-1}$ is proportional to mineralized content of the bone. Peaks at 955$cm^{-1}$ and 957$cm^{-1}$ indicate transient bone mineral phase from the immature bone. Peak at 853$cm^{-1}$ and 872$cm^{-1}$ indicate presence of collagen proline and hydroxyproline respectively. Peaks at 1242 and 1272$cm^{-1}$ represent Amide III protein β sheet and protein α helix respectively. Peak at 1446$cm^{-1}$ corresponds to protein $CH_2$ deformation and 1660$cm^{-1}$ is the strongest Amide I peak with high polarisation sensitivity. Prominent shoulder at 1690$cm^{-1}$ are indicative of immature cross links, β sheets and disordered secondary structure. The results (**Figure 9**) demonstrated that the surrounding bone (A), non-defected original bone, showed all the peaks expected to be present in a mature rat bone. The newly formed bone (B), at the boundaries of the initially created defect (adjoining surrounding bone), showed the peaks very similar to the surrounding bone and appeared fully mineralized indicated by the $v_1PO_4^{3-}$ peak intensity. The full width half maximum of $v_1PO_4^{3-}$ is proportional to c-axis length of crystal and hence proportional to maturity of the crystal. The content of mineralization decreased as we moved towards the center of the defect, indicated by drop in the intensity of $v_1PO_4^{3-}$ band indicating less phosphate present. At the far end of the newly formed bone towards Si(ON)x surface (C), we observed distinct peaks for collagen presence as well as Amide III and Amide I formation and $CH_2$ deformation. This indicates protein presence and some immature mineralized content. Whereas in the middle of the Si(ON)x sample (D), peaks for Amide III, Amide I and $CH_2$ deformation were seen but there was no collagen or phosphate-carbonate presence indicating no

mineralization occurred. In addition a distinct peak showing Si-Si bond was recorded, which might have stemmed from the underlying silicon substrate.

The results from the XANES data (**Figure 10**) were analyzed to study the coordination chemistry of the newly grown bone as compared to the surrounding bone. The Ca K-edge data showed that Ca was present in large abundance on the newly formed bone surface and the overall dominant chemistry was similar to hydroxyapatite (HA). This was evident by the peaks specific to HA (Ca K-pre edge peak at 4039.1 eV, pre edge shoulder at 4044.4 eV, main peak b at 4048.27 eV and the post edge shoulder). The P L-edge data indicated that surrounding bone was more like stable hydroxyapatite whereas the new bone formed on Si(ON)x surface was also largely HA but was not mature as evidenced by the smaller peak d (phosphate specific peak at 146.7eV) which was indicative of smaller phosphate content. The shoulder after peak c (137.8 eV) is characteristic of Ca-phosphates and arises from transitions from 2p of P to empty 3d orbitals of Ca. The presence of this shoulder clearly illustrates that the phosphates present on the surface are in the form of calcium phosphates/HA. Moreover, the new bone spectra had a weak post edge shoulder indicating that the Ca was not all coordinated in the form of HA and may have some soluble phosphates, that was also evident from the smaller peak a. Similarly, the P K-edge (Figure 10c) also confirmed the presence of HA on the surface, evident by the post edge peak b around 2155 eV, which is unique for HA and corresponds to transition of 1s P electron to 3d Ca orbital. The O K-edge data showed that the newly formed bone on the Si(ON)x surface was a mixture of calcium carbonates

and phosphates. Peak a (Figure 10d) represents carbonate ions substituted into bone mineral structure. It is shifted from $CaCO_3$ structure due to second nearest neighbor effects of mineral lattice on electron density.[28] Peak between b and c match the higher energy peaks in phosphate-containing compounds suggesting beginning of formation of b-TCP or HA like structure that is relatively ordered and matrix is starting to mineralize whereas the peak d represents resonant feature. XANES data also verified that the composition of the newly formed bone was exactly the same as that of the surrounding bone. SEM micrographs (**Figure 11**) showed that the newly generated bone grew over the implant surface indicated by the dotted circle whereas arrow points out the implanted sample. EDS mapping showed the presence of Ca-P based bone formation over the implant coating surface. This was evident by the appearance of a small area that was not covered yet, indicated by excessive silicon presence. This reveals nearly complete bony union over the implant surface and indicates that rapid HA formation on the surface led to early collagen synthesis followed by mineralization to make the collagenous matrix into mature bone. Such rapid bone healing by Si(ON)x surface demonstrated the osteoinductive nature of our material that induced osteogenesis leading to early formation of HA and biomineralization.

## 3. Discussion

In this study, we tested the hypothesis that ionic silicon and PECVD-based amorphous silica enhance osteogenesis via enhancement of superoxide dismutase 1 (SOD1), a known antioxidant. In the first part of this study, we found

that ionic Si enhanced SOD1 expression and osteogenic markers (LOX, OSX, Col(I)) for wild type osteoprogenitor (MC3T3) cells. But such enhancement was not observed for SOD1 knockdown cells, indicating that SOD1 is required for $Si^{+4}$ to enhance osteogenesis. This result is the first evidence showing this mechanism. SOD1 is dependent on the activity of local cations for its expression and activity. Since $Si^{+4}$ is a cation with +4 valence state, it was hypothesized that ionic Si enhanced osteogenesis through this pathway. Previous evidence illustrating this effect was observed in plants where ionic Si was observed to enhance the immune response by plants under biotic or abiotic stresses such as drought, salinity, and nutrient toxicity or deficiency in which SOD1 was stimulated by the presence of $Si^{+4}$ to maintain viability under these conditions.[29,30]

PECVD-based amorphous silica thin film coatings were assessed for sustained delivery of $Si^{+4}$ in physiological environments. We observed that amorphous silica with nitrogen incorporation Si(ON)x gave continual release of $Si^{+4}$ when immersed in cell-free *in-vitro* settings. The ionic release was controlled by the surface chemistry (O/N ratio) formulated by PECVD process under optimized conditions and the release period depended upon the thickness of the film. A 100 nm thick layer of Si(ON)x gave a sustained release of $Si^{+4}$ over 8 days of time period as shown in Table I above. Though more silicon was released than the theoretical maximum after 8 days immersion for sample chemistries 2 and 4 resulting in dissolved thickness higher than 100 nm, this was likely due to the simplifying assumption that the system consisted of a predominantly $Si_3N_4$ or $SiO_2$ system while in reality, there was ~10-20% excess Si in the coatings.

Moreover, in order to estimate the percentage thickness of the coating dissolved, some simplifying assumptions were made. First of all, the coatings were assumed to be chemically and structurally uniform in the direction normal to the surface. Secondly, since the exact densities of the coatings were unknown, a reasonable approximation was to use the density of similar low-temperature fabricated PECVD coatings. According to MIT's material property database, low-temperature PECVD deposited silicon nitride has a density of about 2.5 $gcm^{-3}$ while similarly fabricated silicon dioxide has a density of about 2.3 $gcm^{-3}$.[3] Since the Si(ON)x coatings composition were intermediate to these two extremes, these values were used to calculate the total amount of silicon that was able to dissolve as a function of time. Despite its limitations, this simplified model of dissolution coating thickness allowed for the observation of interesting trends in the data and relative release rates of $Si^{+4}$ with varying O/N ratio in surface chemistries.

*In-vitro* cell culture studies using amorphous silica-based materials showed that these materials up-regulated the expression of SOD1, which induced downstream expression of Runx2 and collagen type 1. Though both the cell types (MC3T3 and human periosteum cells) showed enhanced expression of osteogenic markers on Si(ON)x surfaces but slight differences in time and expression levels were observed. It might have stemmed from the differences in their osteoblast differentiation kinetics including cell proliferation, cell migration–aggregation and cell differentiation. Osteogenic markers expression was maximally enhanced at an optimal Si(ON)x composition in which O/N was nearly

unity (refractive index =1.58) . The amorphous silica-based $Si^{+4}$ delivery device showed even higher impact on osteogenesis enhancement via SOD1 expression as compared to ionic Si. This enhanced effect was likely owed to surface effects from the amorphous silica samples. These materials were patterned and thus had different surface energy than flat samples. Moreover, bio-inspired surface morphology amplified cell-surface interactions to have better cell-attachment, cell-growth and differentiation. Therefore, the cells appeared to adhere at a high density on the amorphous silica Si(ON)x surfaces as compared to control glass surfaces. These results indicate that PECVD process can be tuned to acquire amorphous silica-based biomaterial for an optimized release of $Si^{+4}$ that enhances osteogenesis via SOD1 expression while surface morphology integrates bio-mechanical bonding to bio-chemical attachment of such coated implants. Cerium oxide coatings have also been previously tested with fibroblasts to study the antioxidant capacity of cerium oxide nanocrystals toward $H_2O_2$-induced oxidative stress.[31,32] However, these nanoparticles did not induce any effect on antioxidant enzymes or genes rather, they were shown to only electrochemically reduce hydrogen peroxide. Such reduction is not specific to the reduction of the key anion associated with oxidative stress, superoxide anion. The up-regulated effect of Si(ON)x and ionic Si shown in this work has the ability to target the expression of SOD1, the key antioxidant enzymes used by cells to reduce superoxide anion to water and oxygen.

*In-vivo* testing showed that the amorphous silicon oxynitride Si(ON)x overlay onto implant surfaces induced rapid regeneration of bone within rat

calvarial critical-sized fractures. The defect was nearly completely closed within 5 weeks (more than 50% of bone volume regenerated) whereas the control group showed no significant regeneration of bone over the same time period under exactly similar conditions. The empty defect showed no healing and confirmed that the defect was critical-sized defect and did require an external implant for healing. XANES data confirmed the presence of Ca coordinated with phosphates indicated by characteristic peaks for HA. It also illustrated that the newly formed bone matched the coordination chemistry of the surrounding bone. P L-ege (Figure 10b) and P K-edge (Figure 10c) both confirmed the presence of HA on the newly formed bone surface but interesting information was observed when compared with the surrounding bone. P L-edge spectra indicated that the shoulder after peak c (137.8 eV) was not as significant for newly formed bone when compared to the surrounding bone. This indicates reduced bone maturity whereas P K-edge showed fully mature bone for both the newly formed and the surrounding bone. This might be due to different energy ranges and the penetration depth for the two beams. P L-edge (low energy beam) takes into account only the top 40-50 nm whereas P K-edge (high energy beam) data corresponds to a 3-4 μm penetration depth. This suggests that the top few tens of nanometer layers were not as mature as the surrounding bone but bottom layers were found to be fully mature. Though XANES provided valuable information on the coordination chemistry, it doesn't quantify the species present on the surface. This is where the Raman was employed to study, quantify and compare the content of phosphates and other species. The spectra showed

interesting results on bone maturity with proportionally varying content of phosphates indicated by the $v_1PO_4^{3-}$ peak intensity. As mentioned above, the full width half maximum of $v_1PO_4^{3-}$ corresponds to c-axis length of crystal and hence relates to maturity of the crystal. Raman spectra revealed that the mineralized content ($v_1PO_4^{3-}$ peak intensity) was maximal at the interface of the surrounding bone and the newly grown bone and decreased as we moved towards the center of the defect. It also indicated the presence of collagen specific peaks, Amide III, Amide I formation and $CH_2$ deformation in the middle of the defect. Altogether, it validated the XANES data on the presence of phosphates and assessed the maturity of the newly grown bone by quantifying the mineralized content. It also illustrated the mechanism of bone regeneration for Si(ON)x surface where early formation of HA promotes the collagen synthesis followed by biomineralization to generate mature bone.

In the immediate application of these materials, we have shown the effectiveness of these materials to enhance bone-healing *in-vivo*. Previously, we established that these overlay materials were well-adherent to metal surfaces like titanium (Ti), which is the typically used material for permanent/semi-permanent fixtures in fracture healing.[24] Since ascorbic acid was used in the culture media and it is an antioxidant, so the role of Si is as a combinatorial antioxidant that works in tandem with other antioxidants to heal bone. The enhancement of the osteogenic pathway by ionic silicon via Si(ON)x coated metal implants can be used to hasten the healing phase of bone formation. This can improve the efficacy of these implants in long-term to remain as a permanent fixture because

the bone-SiOx-Ti/$TiO_2$ interface can remain as a composite interface. The mechanistic effect opens new roles into our understanding of cations and their impact on bone regeneration. This study shows the first evidence of the effect that cations have on linking osteogenic response to immune response. Although much evidence exists showing that amorphous silica and Si ions have a stimulatory effect on osteogenesis, this is the first evidence of showing how this takes place. Future work will expand upon this principle to determine what other aspects of healing can be utilized from this work.

## 4. Conclusions

In this study, we tested the hypothesis that ionic Si and PECVD amorphous silica-based biomaterials enhance osteogenesis via antioxidant expression. Ionic Si was tested with wild type and SOD1 knockdown osteoprogenitor cells (MC3T3). It showed enhanced expression of antioxidant and osteogenic markers in wild type cells but all markers were down-regulated in SOD1 knockdown cells. These results indicated the dependence of $Si^{+4}$ on SOD1 to enhance osteogenesis in osteoprogenitor cells during osteogenesis. We devised PECVD-based amorphous silica for $Si^{+4}$ release delivery and found similar results for these biomaterials using MC3T3 and human periosteum cells. The surface topographies of these test samples were patterned to influence the cellular behaviors. Favorable cell response to these surfaces gave an enhanced expression of osteogenic markers and a high density of cells attached to the surface as compared to control group. Maximal enhancement occurred at an amorphous silica surface with O/N ratio very close to unity. *In-vivo* evaluation of

these samples in rat critical size calvarial defect model showed that these biomaterials stimulated the bone regeneration and filled the interfacial gap within 5 weeks which didn't occur for control group. XANES and Raman spectroscopy showed that the newly grown bone chemistry exactly matched the surrounding bone and the mineralized content was maximum at the interface of newly formed and the surrounding bone. This study therefore supports the conclusion that Si plays a combinatorial antioxidant role in enhancing osteogenesis and PECVD-based amorphous silica can potentially be used as an overlay onto metal implants for rapid bone healing. This study opens new avenues in how we interpret cellular function and how cells respond to their surrounding extracellular matrix cation environment.

## 5. Experimental Section

### Study design

The first part of this study aimed to determine the effect of ionic Si on SOD1 and osteogenesis. Two treatment conditions (control, ionic Si) were prepared and tested with osteoblast progenitor cells (mouse calvarial 3T3, MC3T3). Control treatments were prepared by alpha-MEM supplemented with 10% FBS, 1% pen-strep and 50ppm ascorbic acid 2 phosphate whereas ionic Si treatment was prepared by adding 0.1 mM $Na_2SiO_3$ to the control treatment. Wild type and SOD1 knockdown cells (using siRNA) were tested with each treatment. The second part of this study aimed to devise and test an ionic Si delivery device for the up-regulation of SOD1 and osteogenesis. PECVD-based amorphous silicon oxynitride Si(ON)x overlays with varying levels of O/N ratios were

investigated for $Si^{+4}$ release and osteogenic gene expressions *in-vitro*. The last part of this study contained *in-vivo* evaluation of these biomaterials for their bone-regeneration capability in a rat critical size calvarial defect model using control samples (substrate only group and no implant group).

## 5.1. Effect of ionic Si on SOD1 and osteogenesis

### *5.1.1. Cell culture*

MC3T3 cells were cultured in 150 $cm^2$ flasks with alpha-minimum essential medium, α-MEM (Life Technologies Corp., Grand Island, NY, USA) containing 10% fetal bovine serum, FBS (VWR, Radnor, PA) and antibiotics (1% streptomycin/penicillin) in a humidified atmosphere of 95% air and 5% $CO_2$ at 37º C and expanded as needed to obtain the required cells for each experiment. Cells of passage number 18 to 22 were used in this study.

### *5.1.2. SOD1 siRNA Transfection*

The siRNA cocktails targeting the mouse gene SOD1 were purchased from Life Technologies - Thermo Fisher Scientific (Rochester, NY, USA). MC3T3-E1 cells were synchronized with αMEM, 1% FBS, and 1% pen-strep for 48 hours. Cells were then transfected by Lipofectamine (Invitrogen) using the transfection agent concentration of 6 nM for $10^5$ cells/well as per manufacturer's protocol. After 5-7 hours of transfection in a $CO_2$ incubator at 37° C containing growth media (without pen-strep), the cells were introduced to growth media for 24 hours followed by their respective treatments. Cells were lysed 72 hours after the treatments were introduced and analyzed for gene expression using

quantitative reverse transcriptase polymerase chain reaction (qRT-PCR). Histological analysis for collagen fiber bundle formation was performed 6 days after treatment.

*5.1.3. qRT-PCR Analysis for Osteogenic Gene Expression Studies*

For gene expression studies, cells were seeded at a density of 100,000 cells $cm^{-2}$ in 6-well plates. The cells were lysed using buffer RLT (guanidinium thiocyanate) as a lysis buffer (10 µl ß-Mercaptoethanol per 1 ml Buffer RLT). Then, the cells were sheared with rubber cell scrapper (1.8 cm blade) under moderate pressure to lyse the cells on the surface and purified to collect mRNA (RNeasy Mini Kit, Qiagen, Valencia, CA, USA), converted to cDNA using qRT-PCR method (Reverse Transcription System, Promega, Madison, WI, USA) according to the manufacture's protocol. Absorbance measurements of mRNA and cDNA samples were performed using a micro-volume UV-Vis spectrophotometer (Nano Drop 2000c, Thermo Fisher Scientific Inc., Waltham, MA, USA). Using glyseraldehyde-3-phosphate dehydrogenase (GAPDH) as internal reference gene, relative quantification of gene expression was evaluated by the comparative cycle threshold (CT) method and fold change calculated using $2^{-\Delta\Delta CT}$. Details regarding qRT-PCR were given in our previous work.[33] Genes assayed included SOD1, LOX, OSX, and COL(I)-α1.

*5.1.4. Histology*

Seeding of cells at 100,000/$cm^2$ was used for collagen matrix experiments. Cells were seeded onto autoclaved glass cover slips for 6 days and analyzed for collagen formation. Samples were fixed and stained using

picrosirius staining using the previously described method[33] and imaged using an optical microscope (Nikon Eclipse 80i) with a CCD camera and Image Pro software.

## 5.2. Fabrication of $Si^{+4}$ Release Device and its Effect on SOD1 and Osteogenesis

### *5.2.1. Preparation of Nanofabricated Si(ON)x samples*

The samples with amorphous silica based overlays were prepared using conventional photolithography followed by plasma enhanced chemical vapor deposition (PECVD) process. The fabrication process started with a single-side polished, p-type (100) orientation test grade silicon wafer (Nova Electronic Materials, Flower Mound, TX). Standard RCA cleaning was performed as explained previously.[24,34,35] After cleaning of the wafer, Microposit HMDS primer was spin coated at 3000 rpm for 30 sec and baked on hot plate at 150 °C for 90 seconds before spinning the photoresist. The primer was used as an adhesion promoter between the photoresist and the substrate surface. Then, the positive photoresist (Shipley S1813) was spin-coated at 4000 rpm for 30 sec to obtain a uniformly thick layer of photoresist (~1.35 μm). The wafer with primer and the photoresist was pre-baked on hot plate at 90 °C for 60 seconds and let it cool down for 1-2 minutes in ambient air before UV exposure. The wafer was then exposed to UV using EVG Aligner (I-line 365) at a dose of 139mJ/$cm^2$ in constant intensity mode and developed for 43 sec in MF-319 developer followed by hard bake (115 °C, 60 sec) to obtain the micrograting pattern on the surface of the wafer as shown in Figure 2.

After photolithography, the exposed Si surface was etched (200 nm etch depth) using deep reactive ion etching (DRIE) process in order to transfer the photoresist patterns into the underlying Si surface. TRION Deep Reactive Ion Etching System with $CF_4$ at 25 sccm gas flow rate, 25 mTorr pressure, 3000W ICP power and 100W RIE power etched Si at an etch rate of 862.5 Å/min. The photoresist was then removed completely by immersing the wafer in acetone and followed by piranha clean (3 $H_2SO_4$ : 1 $H_2O_2$) at 95 °C for 10 min. The wafer was rinsed in DI water and blow-dried under nitrogen.

The patterned wafer was used to deposit a uniform (non-uniformity < 1%) 100 nm thick oxide layer via PECVD process using TRION ORION II PECVD/LPCVD system. The oxidized wafer was then coated with 100 nm of amorphous silica oxynitride Si(ON)x overlay. All coatings were fabricated at a substrate temperature of 400 °C, chamber pressure of 900 mTorr, and ICP power of 30W with a 13.56 MHz excitation frequency applied. Source gases included silane ($SiH_4$) diluted in argon (Ar) (15%/85%), nitrous oxide ($N_2O$), nitrogen ($N_2$), and ammonia ($NH_3$). The refractive indices and the thickness of the wafer coatings were measured using ellipsometry at a wavelength of 632.8 nm (LS300, Gaertner Scientific Corporation, Skokie, IL, USA), and results were confirmed through the use of a reflectometer (Ocean Optics NC-UV-VIS TF Reflectometer) and a scanning electron microscope (SEM, S-3000N, Hitachi High-Tech, Tokyo, Japan). The wafer was cut into 12 × 12 $mm^2$ sections for post-process characterization and *in-vitro* testing.

### *5.2.2. $Si^{+4}$ Release Studies Using Inductively Coupled Plasma Optical Emission Spectra (ICP-OES) Characterization*

ICP-OES analysis was performed at the Shimadzu Center for Advanced Analytical Chemistry using the Shimadzu ICPE-9000 ICP-OES system. 12 mm x 12 mm wafer sections were placed in 4 mL of α-MEM at 37˚C and 5% $CO_2$ for 0, 6, 12, 24, 48, 96, and 192 hours. After soaking, 25x, 50x and 100x dilutions were used to investigate silicon content in the supernatant fluid. Aluminum was used as an internal standard, and the concentration measurements were taken from the α-MEM dissolution media in order to evaluate the surface degradation kinetics of the coatings. Single-element high purity ICP Al and Si standards (1000 µg/L) were purchased from Ultra Scientific. The variance in the ICP data for triplicate samples was used to determine the estimated thickness of the film dissolved in physiological conditions.

### *5.2.3. Cell Culture Studies for Si(ON)x samples*

Cells were seeded on the Si-wafer samples and glass cover slips (control surfaces) seated on the 6-well plate (BD, Franklin Lakes, NJ, USA). The glass cover slips and the test samples were sterilized (tissue culture treated) exactly in the same process. A dry heat was applied using standard bacti-cinerator inside the biosafety cabinet and allowed to cool down for 1-2 minutes before seeding the cells on the surface. Triplicate samples were seeded with cells at the number of 100,000/well and these cells were synchronized (α-MEM, 1% FBS, 1% streptomycin/penicillin) for an additional 48 hours. Medium was then exchanged for growth media (α-MEM, 10% FBS, 1% streptomycin/penicillin) with 50ppm

ascorbic acid-2-phosphate (AA2P, Sigma-Aldrich Corp., St. Louis, MO, USA) to induce differentiation. Cells were cultured for 6, 24, 48, and 72 hours before they were lysed for relative gene expression analysis.

The gene expressions of GAPDH, SOD1, OCN, RUNX2, Osterix (Sp7), and COL(Ⅰ)-α1 were studied. Data were normalized to GAPDH (internal reference gene) within each independent experiment and displayed as relative induction of control at corresponding time-point.

### 5.3. *In-vivo* Testing of Si(ON)x samples using Rat Calvarial Defect Model

#### *5.3.1. Surgical and Postoperative Protocol*

All procedures involving animals were performed in accordance with a protocol approved by the Institutional Animal Care and Use Committee at Baylor College of Dentistry, Texas A&M University. A critical size calvarial defect model was developed to assess the *in-vivo* bone healing efficiency of Si(ON)x coated materials as compared to control surfaces (substrate only group and no implant group) . A total of 9 rats (3 for each test group) were used in this study and one sample per animal was implanted to have triplicate samples for evaluation. Adult male rats (about 430 g each) were selected to study the osteoinductive properties of the proposed material in relatively slower bone-healing subjects. The rat was initially weighed and placed into an induction chamber for anesthesia. The rat was anesthetized with 5% isoflurane in oxygen for about 2-3 minutes, then its head was shaved and held onto a stereotaxic frame. Figure 6 shows the step-by-step surgical procedure. The surgery started with an incision (about 1.5 cm) made by a scalpel blade. The periosteum layer was scratched

down using the scalpel blade and the incision site was iteratively washed with sterile saline followed by the air blow to dry the exposed skull bone. A 3 × 5 $mm^2$ Si(ON)x test sample (sterilized by standard bacti-cinerator) was placed at exact location where we wanted to implant it and marked the boundary with a marker on dry skull. The defect site was chosen to have maximum flat surface with minimum sutures involved. Then, the dental bur (#1 or #2) with about 0.5 mm diameter tip was used to precisely cut the bone along the drawn boundary to create the critical sized calvarial defect without nicking the dura. After creating the bone defect, the defect site was thoroughly washed with sterile saline followed by the air blow to get it dry. A small amount (~1-2 µl) of gel glue was put on the bottom surface of the implant and placed upside down in the defect so that it is glued to the dura and doesn't move during healing (Figure 6e). Finally, monofilament taper point suture needle was used to suture the incision site making square knots and ensuring adequate space to allow skin healing. The incision site was cleaned thoroughly and a small volume (80-100 µl) of painkiller/sedative medicine (nalbuphine) was injected intramuscularly using 1 ml syringe. The rat was observed for behavioral study to record any signs of pain/distress for the next few days and then allowed 5 weeks for healing before analyzing the effect of Si(ON)x based material on bone regeneration.

*5.3.2. Micro-level computerized tomography (µCT) Scan*

The implants with the surrounding calvarial bone were extracted out after 5 weeks of recovery time and were analyzed using an X-ray microCT imaging system (µCT 35, Scanco Medical, Basserdorf, Switzerland). The unit consists of

an x-ray source directed towards a specimen holder that hosts bone-implant samples. Serial tomographic imaging at an energy level of 55 kV and intensity of 145 μA for the samples was performed. 3D micrographs were generated to evaluate different sample surfaces for the fracture healing after the same recover time. The lower and upper threshold values used for this analysis were 280 and 1000 respectively. The microCT data was further analyzed to determine the bone mineral density and the ratio of bone volume (BV) to total volume (TV) using the built-in function of microCT imaging system.

*5.3.3. X-ray Absorbance Near Edge Structure (XANES) Spectroscopy*

XANES spectroscopy was performed at the Canadian Light Source at the University of Saskatchewan in Saskatoon, Saskatchewan, Canada. XANES is a very sensitive and advanced technique to probe the presence of atomic species and characterize the local coordination of individual elements, by using the fine structural features at the absorption edge.[36] Since the bone mineral is mainly made of calcium phosphate apatite, calcium (Ca) and phosphorous (P) edges are mostly investigated for bone analysis to determine the nature and local coordination of Ca and P in bone.[28,37,38] The Ca and the P K-edge spectra were obtained over the energy range of 2140–2190 eV and 4000–4130 eV, respectively using soft X-ray beam-line for the micro-characterization of materials (SXRMB) beam-line. The step size for Ca and P K-edge spectra were 0.3 and 0.25 eV respectively. Plane Grating Monochromator (PGM) beam-line was used to acquire the P L-edge spectra in the region of 130-155 eV. PGM operates at the low energy range between 5-250 eV and a step size of 0.1 eV. The oxygen

(O) K-edge spectra was recorded for energy ranges between 525-560 eV using Spherical Grating Monochromator (SGM) beam-line that operates in the midrange energy of 250 – 2000 eV with a step size of 0.15 eV.

*5.3.4. Raman Spectroscopy*

Raman spectroscopy is a very convenient and valuable technique to analyze biological samples without need for staining, fixation or sample preparation but needs a relatively high-power laser beam to overcome the inherent low Raman scattering efficacy of biological molecules.[39,40] Microspot Raman spectroscopy (DXR, Thermo Scientific) with 780 nm laser source and 100 mW power was used to characterize the extracted bone sample. Different regions (A, B, C, D) on the extracted sample were analyzed to evaluate the newly grown bone chemistry in comparison to the surrounding bone. The phosphates, amides and other significant peak intensities were used to gauge the mineralized content and the maturity of the bone. Details of the Raman procedure are provided in our earlier work.[39]

*5.3.5. Scanning Electron Microscopy (SEM) of Extracted Bone Samples*

The extracted bone samples were completely dried and a thin layer of gold (50 nm) was coated on the surface to make it conductive for electron microscopy. Samples were imaged using a scanning electron microscopy (SEM, JOEL USA Inc., Peabody, MA, USA) with secondary electron mode at 5-15 kV energy to get the finest results.

*5.3.6. Statistical analysis*

Data were presented as the mean ± standard error. One-way analysis of variance (ANOVA) was used for parametric analyses and $p<0.05$ was used for statistical significance. Posthoc student T-test was used for between group comparisons and $p < 0.05$ was used to establish statistical significance.

Acknowledgments

The authors would like to thank Jonathan Havener and Rebecca Martinez for their help on cell culture studies. We are also thankful to Gerald Hill and Priscilla Hooks for their assistance with animal studies and Connie Tillberg for her help on histology. We also acknowledge the staff at Nanotechnology Research Center, University of Texas at Arlington for their assistance on device fabrication and characterization. XANES experiments were carried out at the Canadian Light Source, Saskatoon, Canada, which is supported by NSERC, NRC, CIHR, and the University of Saskatchewan. The work was supported by a grant from National Institutes of Health (1R03DE023872-01A1) to V. G. Varanasi and partially supported by Departmental startup (#304-128170, Varanasi, PI), Enhancement grant (#24444100005, Varanasi, PI), and CNMS grant (#2010-080, Varanasi, PI).

References:

[1] S. R. Pitts, R. W. Niska, J. Xu & C. W. Burt, *Natl Health Stat Report* **2008**, *7*, 1.

[2] S. Nukavarapu, J. Freeman & C. Laurencin. *Regenerative Engineering of Musculoskeletal Tissues and Interfaces*. (Woodhead Publishing, **2015**).

[3] I. Idris & O. Sugiura, *Japanese journal of applied physics* **1998**, *37*, 6562.

[4] S. Jebahi, H. Oudadesse, H. El Feki, T. Rebai, H. Keskes, P. Pellen & A. El Feki, *Journal of Applied Biomedicine* **2012**, *10*, 195.

[5] H. Nojiri, Y. Saita, D. Morikawa, K. Kobayashi, C. Tsuda, T. Miyazaki, M. Saito, K. Marumo, I. Yonezawa & K. Kaneko, *Journal of Bone and Mineral Research* **2011**, *26*, 2682.

[6] A. Sandukji, H. Al-Sawaf, A. Mohamadin, Y. Alrashidi & S. A. Sheweita, *Hum Exp Toxicol* **2011**, *30*, 435.

[7] A. Hannemann, N. Friedrich1, C. Spielhagen, R. Rettig, T. Ittermann, M. Nauck & H. Wallaschofski, *BMC Endocrine Disorders* **2013, :**, *13*, 11.

[8] J. M. Lean, J. T. Davies, K. Fuller, C. J. Jagger, B. Kirstein, G. A. Partington, Z. L. Urry & T. J. Chambers, *Journal of Clinical Investigation* **2003**, *112*, 915.

[9] F. Jakob, K. Becker, E. Paar, R. Ebert-Duemig & N. Schutze, *Methods Enzymol* **2002**, *347*, 168.

[10] H. Nojiri, Y. Saita, D. Morikawa, K. Kobayashi, C. Tsuda, T. Miyazaki, M. Saito, K. Marumo, I. Yonezawa, K. Kaneko, T. Shirasawa & T. Shimizu, *J Bone Miner Res* **2011**, *26*, 2682.

[11] S. A. E. Badr, E. A. E. Badr, G. E. Hammouda, M. Hadhoud, S. G. Soliman & D. Pandey, *Turk Geriatri Derg* **2008**, *11*, 174.

[12] E. Fabian, I. Gerstorfer, H. W. Thaler, H. Stundner, P. Biswas & I. Elmadfa, *Wien Klin Wochenschr* **2011**, *123*, 88.

[13] C. Y. Turk, M. Halici, A. Guney, H. Akgun, V. Sahin & S. Muhtaroglu, *J Int Med Res* **2004**, *32*, 507.

[14] M. Iwai-Yoshida, Y. Shibata, Wurihan, D. Suzuki, N. Fujisawa, Y. Tanimoto, R. Kamijo, K. Maki & T. Miyazaki, *J Mech Behav Biomed Mater* **2012**, *13*, 230.

[15] P. Valerio, M. M. Pereira, A. M. Goes & M. F. Leite, *Biomaterials* **2004**, *25*, 2941.

[16] V. G. Varanasi, K. K. Leong, L. M. Dominia, S. M. Jue, P. M. Loomer & G. W. Marshall, *Journal of Oral Implantology* **2012**, *38*, 325.

[17] S. Foppiano, S. J. Marshall, G. W. Marshall, E. Saiz & A. P. Tomsia, *Acta biomaterialia* **2007**, *3*, 765.

[18] N. S. Tousi, M. F. Velten, T. J. Bishop, K. K. Leong, N. S. Barkhordar, G. W. Marshall, P. M. Loomer, P. B. Aswath & V. G. Varanasi, *Materials Science and Engineering: C* **2013**, *33*, 2757.

[19] H. Jeon, C. G. Simon & G. Kim, *Journal of Biomedical Materials Research Part B: Applied Biomaterials* **2014**, *102*, 1580.

[20] K. Seunarine, A. S. Curtis, D. Meredith, C. D. Wilkinson, M. Riehle & N. Gadegaard, *NanoBioscience, IEEE Transactions on* **2009**, *8*, 219.

[21] W. Asghar, Y.-T. Kim, A. Ilyas, J. Sankaran, Y. Wan & S. M. Iqbal, *Nanotechnology* **2012**, *23*, 475601.

[22] T. Albrektsson & A. Wennerberg, *The International journal of prosthodontics* **2003**, *17*, 536.

[23] M. Ventre, C. F. Natale, C. Rianna & P. A. Netti, *Journal of The Royal Society Interface* **2014**, *11*, 20140687.

[24] A. Ilyas, N. V. Lavrik, H. K. Kim, P. B. Aswath & V. G. Varanasi, *ACS applied materials & interfaces* **2015**, *7*, 15368.

[25] J. S. Blum, M. A. Barry, A. G. Mikos & J. A. Jansen, *Human gene therapy* **2003**, *14*, 1689.

[26] P. P. Spicer, J. D. Kretlow, S. Young, J. A. Jansen, F. K. Kasper & A. G. Mikos, *Nature protocols* **2012**, *7*, 1918.

[27] J. P. SCHMITZ & J. O. Hollinger, *Clinical orthopaedics and related research* **1986**, *205*, 299.

[28] J. Rajendran, S. Gialanella & P. B. Aswath, *Materials Science and Engineering: C* **2013**, *33*, 3968.

[29] F. Fauteux, W. Rémus-Borel, J. G. Menzies & R. R. Bélanger, *FEMS Microbiology letters* **2005**, *249*, 1.

[30] E. A. Pilon-Smits, C. F. Quinn, W. Tapken, M. Malagoli & M. Schiavon, *Current opinion in plant biology* **2009**, *12*, 267.

[31] S. S. Lee, W. Song, M. Cho, H. L. Puppala, P. Nguyen, H. Zhu, L. Segatori & V. L. Colvin, *ACS nano* **2013**, *7*, 9693.

[32] S. Das, J. M. Dowding, K. E. Klump, J. F. McGinnis, W. Self & S. Seal, *Nanomedicine* **2013**, *8*, 1483.

[33] V. Varanasi, E. Saiz, P. Loomer, B. Ancheta, N. Uritani, S. Ho, A. Tomsia, S. Marshall & G. Marshall, *Acta biomaterialia* **2009**, *5*, 3536.

[34] A. Ilyas, W. Asghar, Y.-t. Kim & S. M. Iqbal, *Biosensors and Bioelectronics* **2014**, *62*, 343.

[35] A. Ilyas, W. Asghar, S. Ahmed, Y. Lotan, J.-T. Hsieh, Y.-t. Kim & S. M. Iqbal, *Analytical Methods* **2014**, *6*, 7166.

[36] H. Demirkiran, Y. Hu, L. Zuin, N. Appathurai & P. B. Aswath, *Materials Science and Engineering: C* **2011**, *31*, 134.

[37] O. O. Aruwajoye, H. K. Kim & P. B. Aswath, *Calcified tissue international* **2015**, *96*, 324.

[38] J. Kruse, P. Leinweber, K.-U. Eckhardt, F. Godlinski, Y. Hu & L. Zuin, *Journal of synchrotron radiation* **2009**, *16*, 247.

[39] M. Maginot, S. Lin, Y. Liu, B. Yuan, J. Q. Feng & P. B. Aswath, *Bone* **2015**, *81*, 602.

[40] G. Puppels, F. De Mul, C. Otto, J. Greve, M. Robert-Nicoud, D. Arndt-Jovin & T. Jovin, **1990**

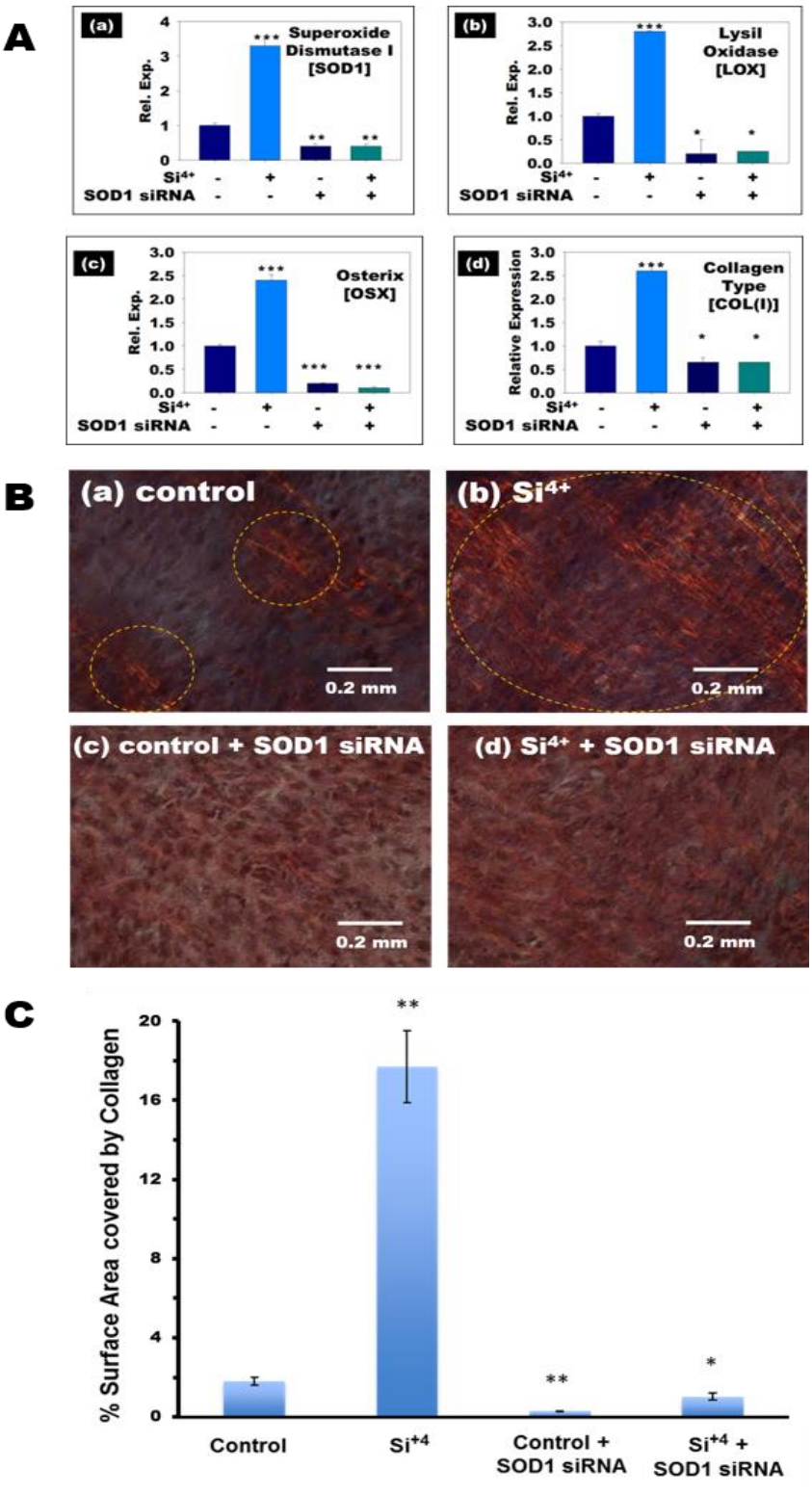
A
(a)
Superoxide Dismutase I [SOD1]
Rel. Exp.
(b)
Lysil Oxidase [LOX]
Rel. Exp.
(c)
Osterix [OSX]
Rel. Exp.
(d)
Collagen Type [COL(I)]
Relative Expression
Si4+
SOD1 siRNA
B
(a) control
(b) Si4+
(c) control + SOD1 siRNA
(d) Si4+ + SOD1 siRNA
0.2 mm
C
% Surface Area covered by Collagen
Control
Si+4
Control + SOD1 siRNA
Si+4 + SOD1 siRNA

Figure 2-11: PCR Analysis, Histology and quantitative analysis.

**Figure 11 (A).** Effect of $Si^{+4}$ on SOD1 and other osteogenic markers after 72 hours of treatment. $Si^{+4}$ enhanced **(a)** SOD1 and osteoblast differentiation markers **(b)** LOX **(c)** OSX and **(d)** Col(I) for wild-type MC3T3-E1 cells whereas SOD1 knockdown cells using (siRNA) inhibited this enhancement. (ANOVA, *p<0.05, **p<0.01, ***p<0.001). **(B)**. $Si^{+4}$ promotes collagen matrix formation (dense, Picrosirius red stained tissue with yellow-orange elongated collagen fibers) vs. control treated cells where SOD1 knockdown cells inhibited the matrix formation and ionic silicon couldn't enhance the matrix formation. **(C)** Quantitative analysis confirms one order of magnitude higher collagen formation for wild type cells in the presence of ionic silicon. It shows that enhancement of osteogenic markers and collagen matrix formation by $Si^{+4}$ depends upon SOD1 enhancement.

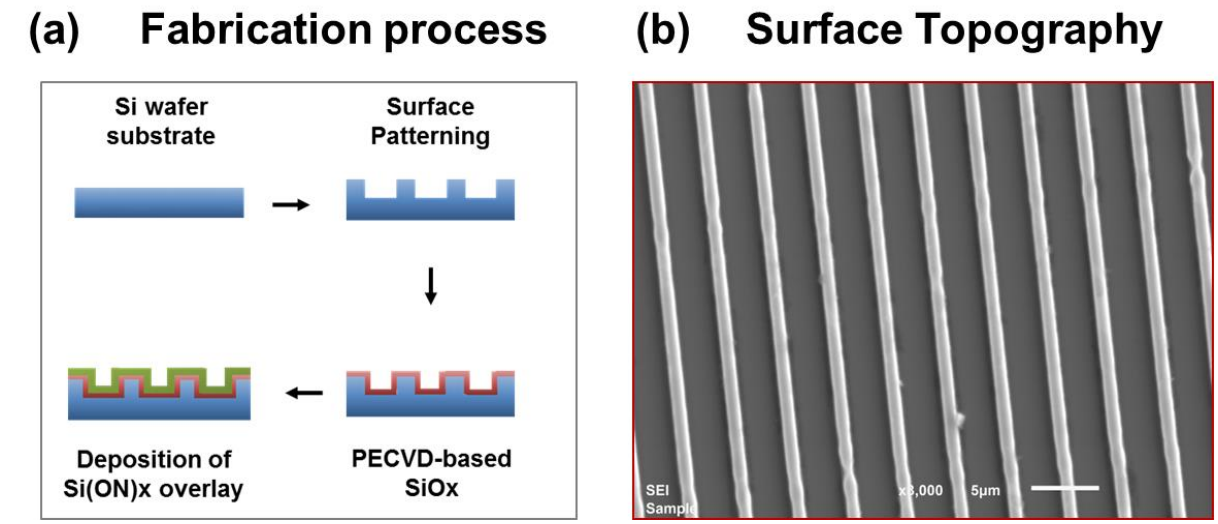


Figure 2-12 : Fabrication of Si(ON)x overlays

(a) A schematic diagram to illustrate the fabrication process for PECVD amorphous silicon oxynitride overlays with Si wafer substrate. (b) SEM micrograph shows the surface topography of a representative sample after photolithography, etching and PECVD deposition of amorphous silica (feature size 2 μm).

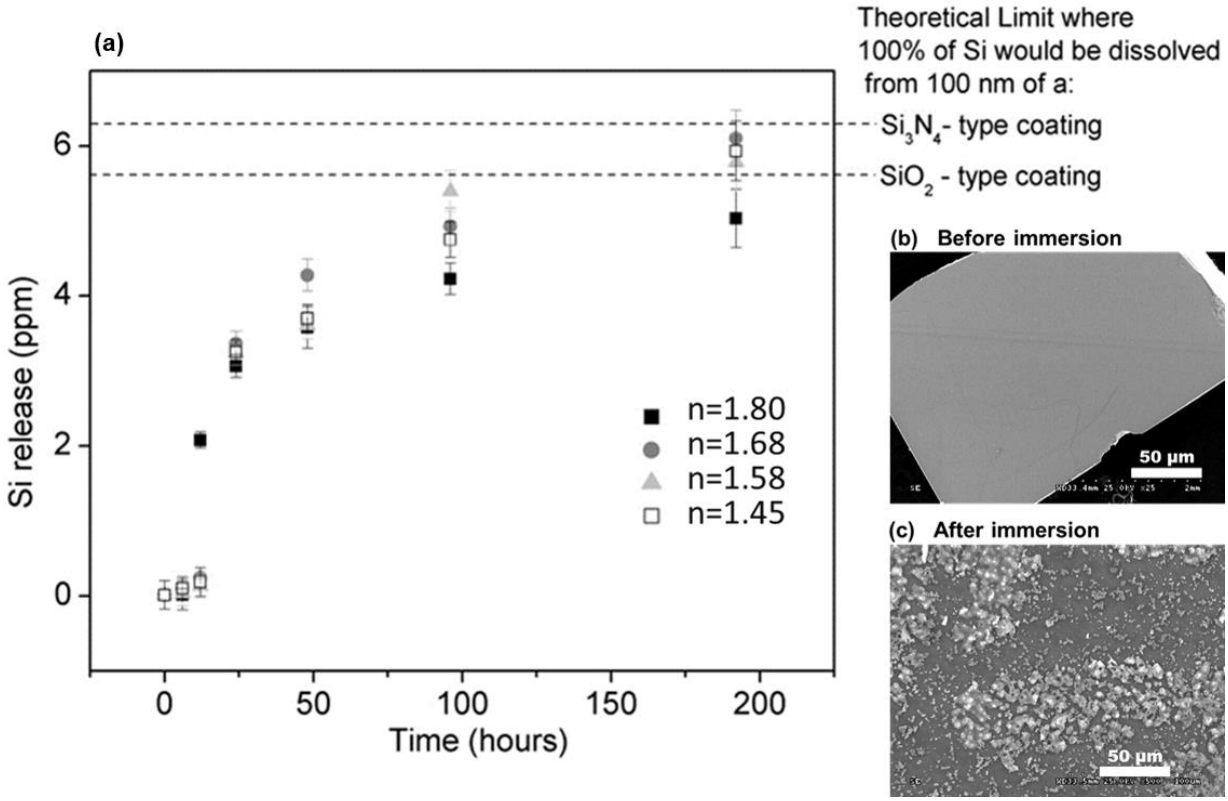


Figure 2-13: Silicon ion release and SEM micrographs of before and after immersion

(a) Silicon release from Si(ON)x sample chemistries immersed in αMEM as determined by ICP-OES analysis

shows sustained release of $Si^{+4}$ over a period of 8 days. Higher N content appears to slow down $Si^{+4}$ release after 24 hours of *in-vitro* immersion. SEM micrographs show surface topographies for Si(ON)x samples (b) before and (c) after *in-vitro* immersion.

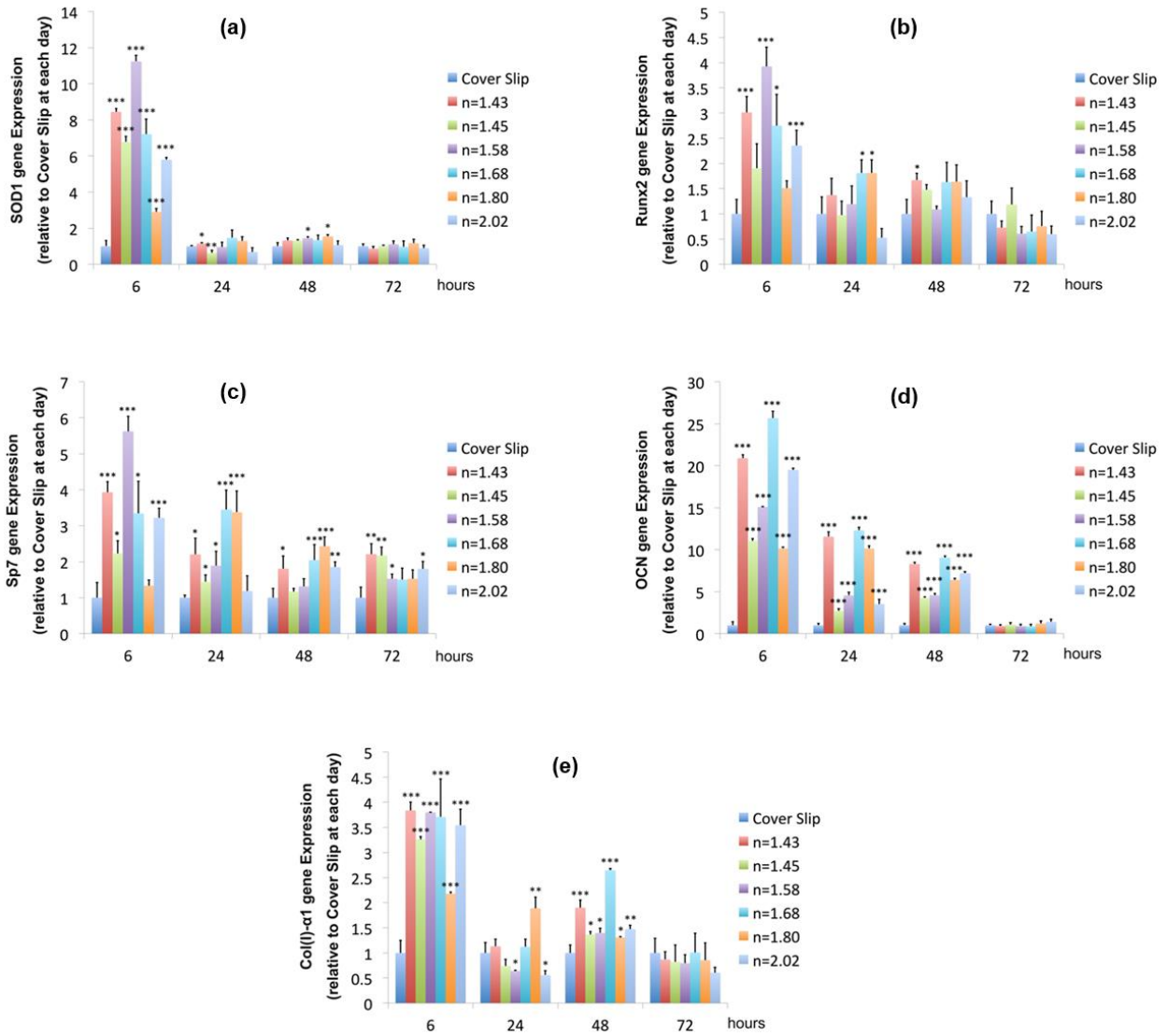


Figure 2-14: Gene expression studies on MC3T3 cells

Si(ON)x surfaces showed an enhanced expression of (a) SOD1 (b) Runx2 (c) Sp7 (d) OCN and (e) Col(Ⅰ)-α1 osteogenic markers for MC3T3 cells when compared to control surfaces. Maximal enhancement was observed for the surface with O/N ratio nearly equal to unity (n=1.58). Moreover, MC3T3 cells showed maximum enhancement to the Si(ON)x surface at the very initial time point (6h).

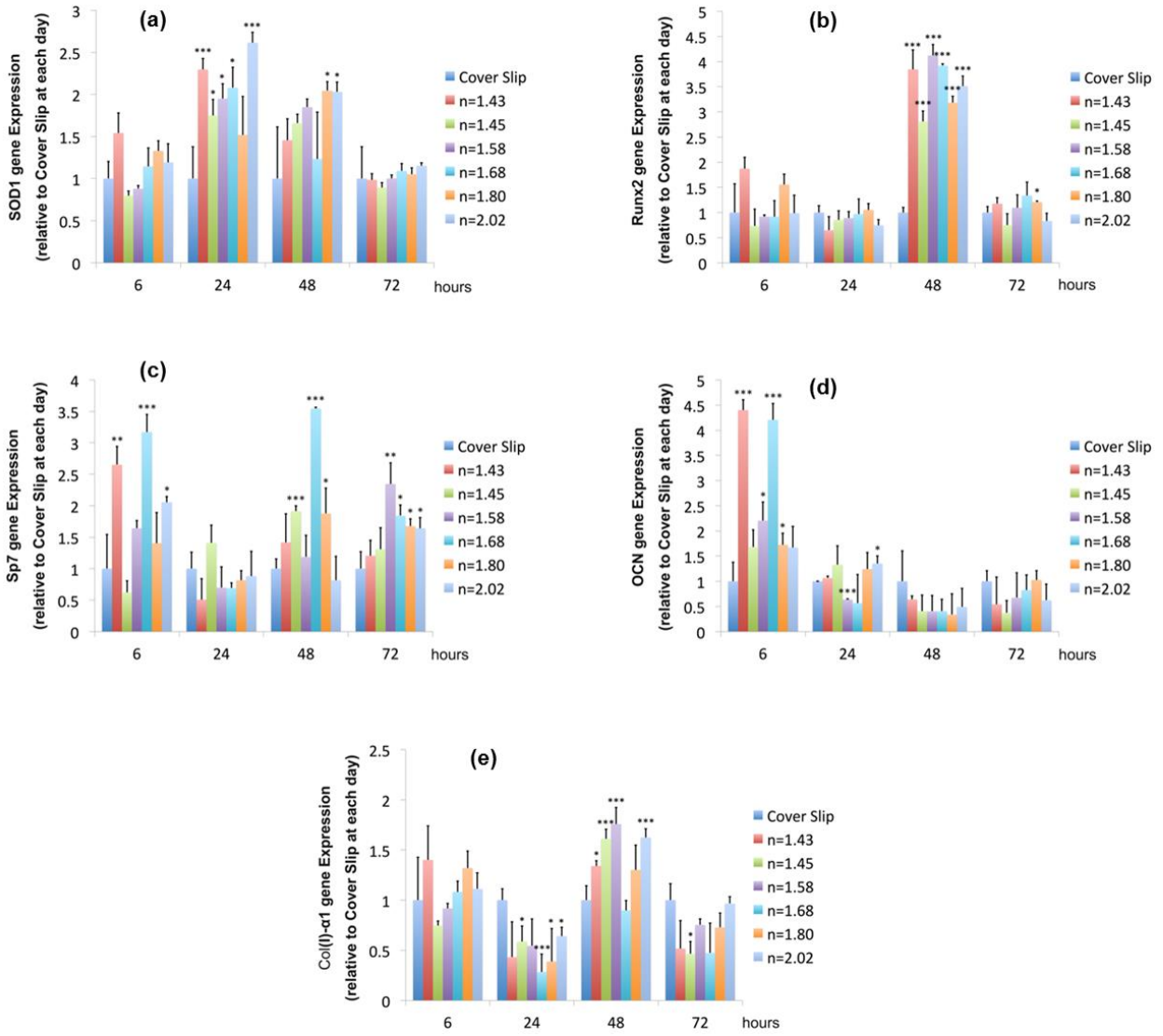


Figure 2-15: Gene expression studies on human periosteum cells

Human periosteum cells also showed up-regulated expression of (a) SOD1 which downstream enhanced the expression for other osteoblast differentiation markers including (b) Runx2 (c) Sp7 (d) OCN and (e) Col( Ⅰ )-α1 on Si(ON)x surfaces. Maximal enhancement for human periosteum cells was observed at 48 hours after induction of differentiation.

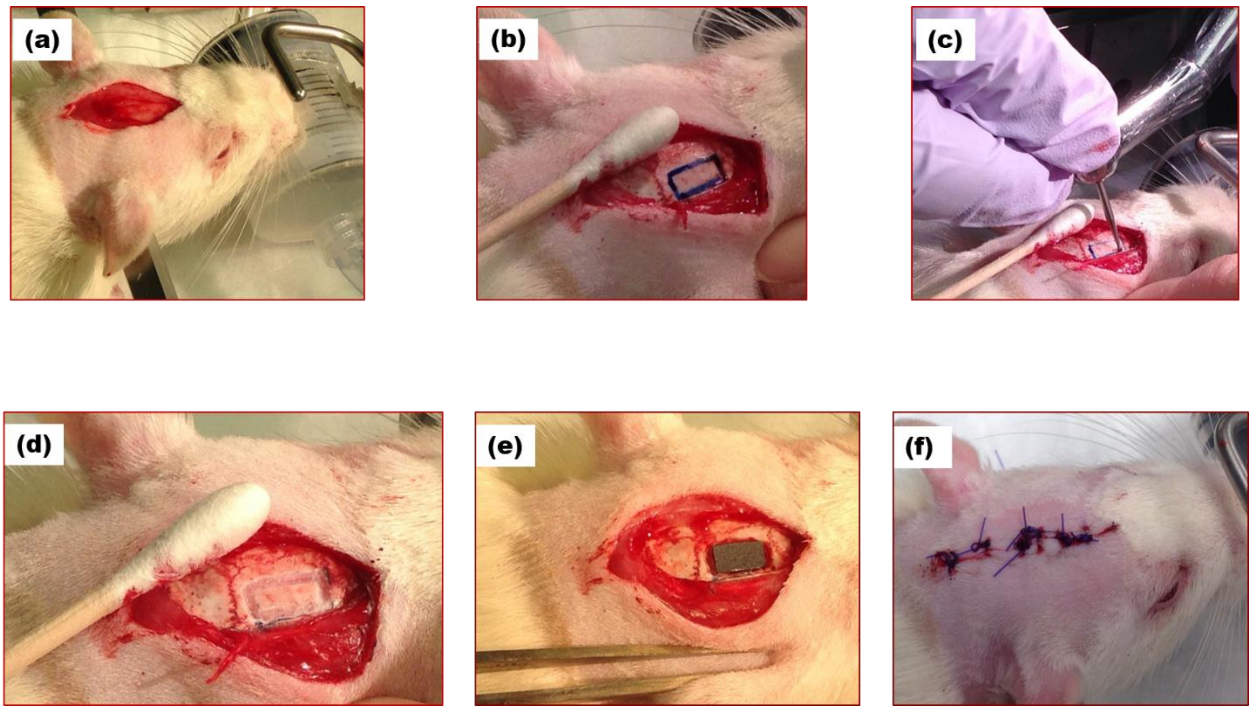


Figure 2-16:Operative procedure to implant the test sample in a rat critical sized calvarial defect model

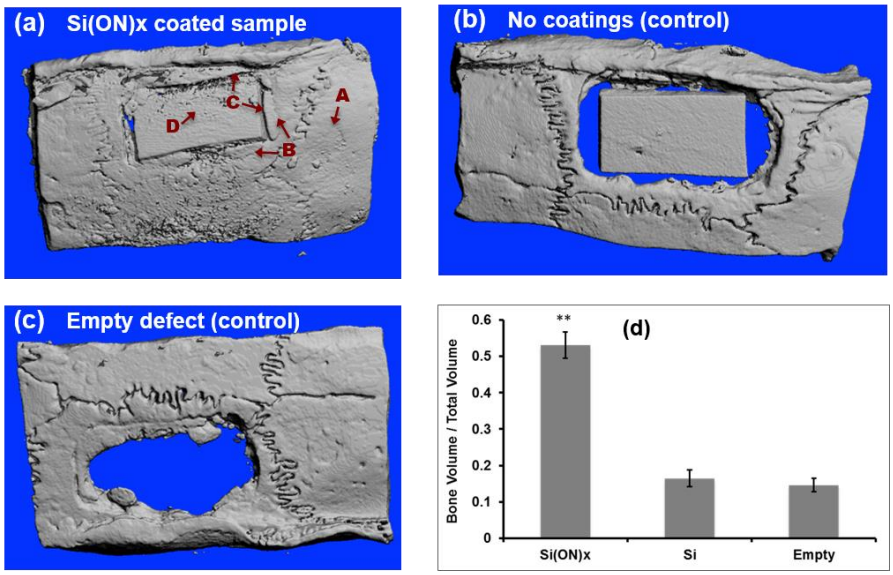


Figure 2-17: MicroCT micrographs

showed that (a) Si(ON)x samples triggered the rapid bone-regeneration process and filled the gap nearly completely within 5 weeks whereas the control samples (b) and (c) didn't show much bone to fill the interfacial gap over the same time period. (d) Quantitative analysis shows larger volume of mineralized bone regenerated for the Si(ON)x surfaces, indicated by higher bone to volume ratio (5 folds) when compared to control surfaces. The Arrows A, B, C and D in part (a) indicate four different regions as we move from surrounding bone toward the middle of the implant. Figure 9 (below) shows Raman analysis of these four different regions.

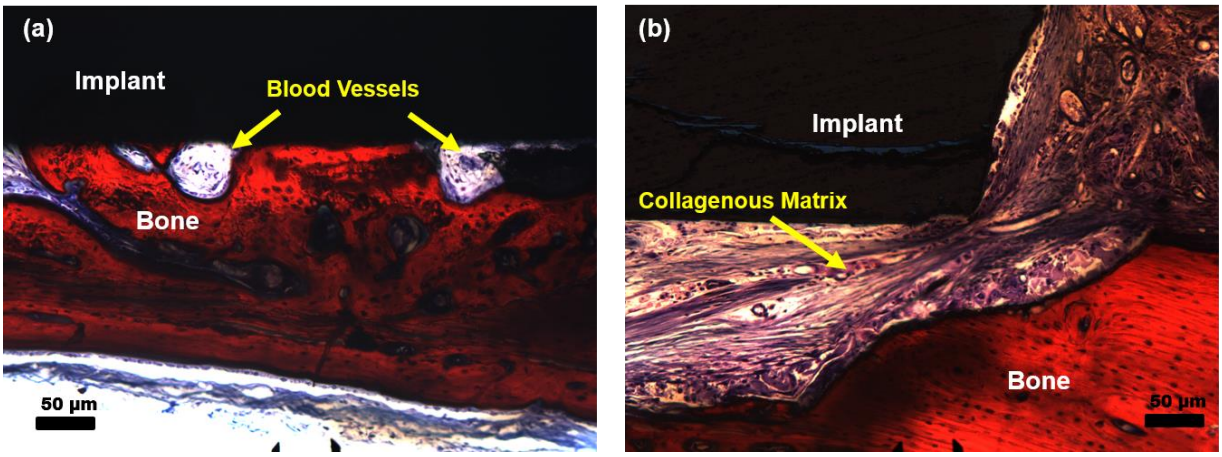


Figure 2-18;Histology of extracted samples after 5 weeks of recovery demonstrate that (a) Si(ON)x surfaces showed fully mineralized bone at the bone implant interface whereas (b) the control samples showed less mineral formation with mostly collagenous fiber filling the interfacial gap.

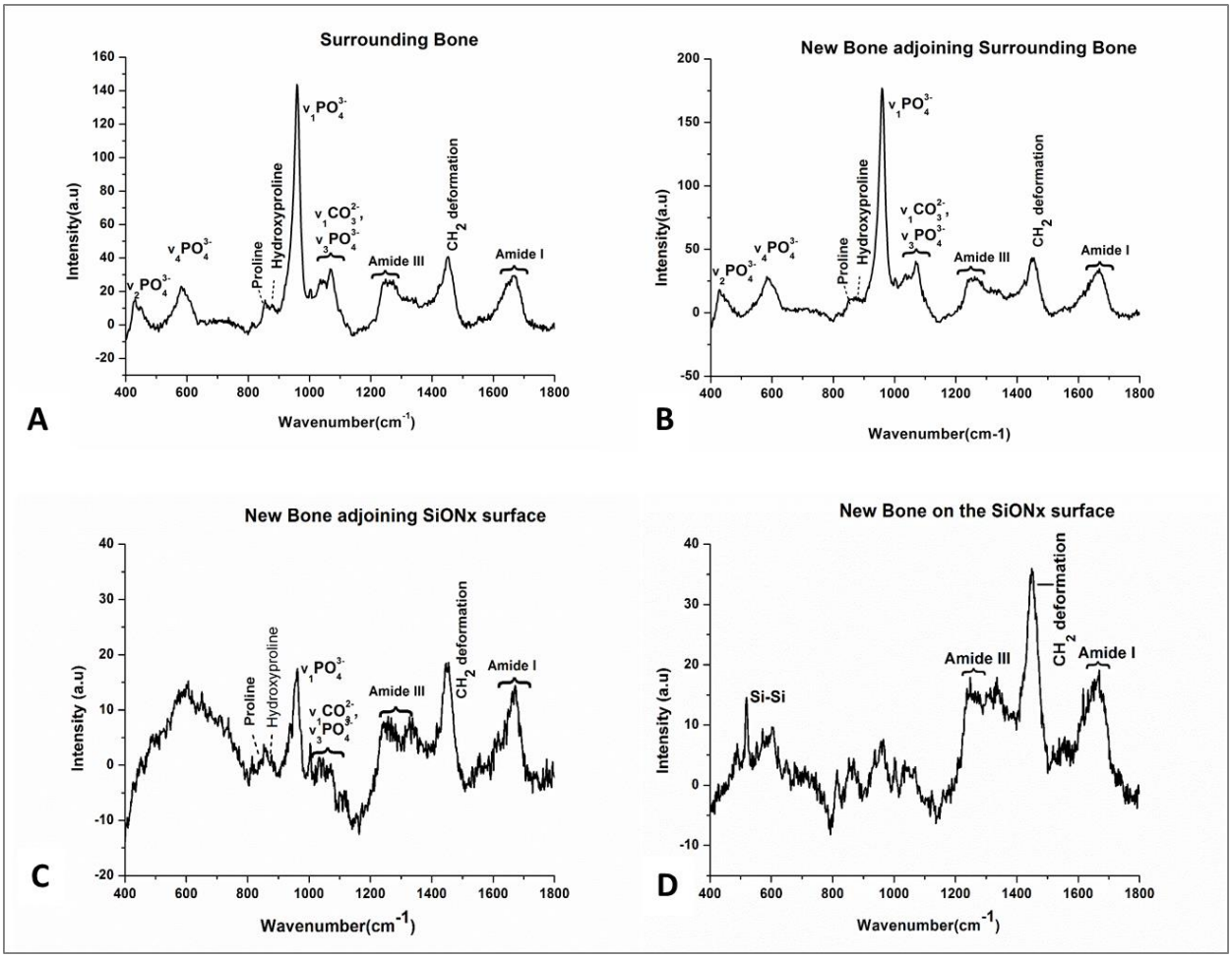


Figure 2-19:Comparison of mineralized content in newly formed bone in different regions (A) Surrounding bone representing the non-defected original bone shows all the peaks expected to be present in a mature rat bone. (B) High intensity of $v_1PO_4^{3-}$ peak indicates the complete mineralization of the newly formed bone at the interface of new/surrounding bone. (C) A drop in $v_1PO_4^{3-}$ peak intensity and presence of distinct peaks for collagen, Amide III , Amide I and $CH_2$ deformation demonstrate the presence of collagenous matrix and some immature mineralized content whereas (D) no mineralized content is present in the center of the defect but amide peaks show the presence of collagen. The regions A,B,C and D are marked in Figure 7.

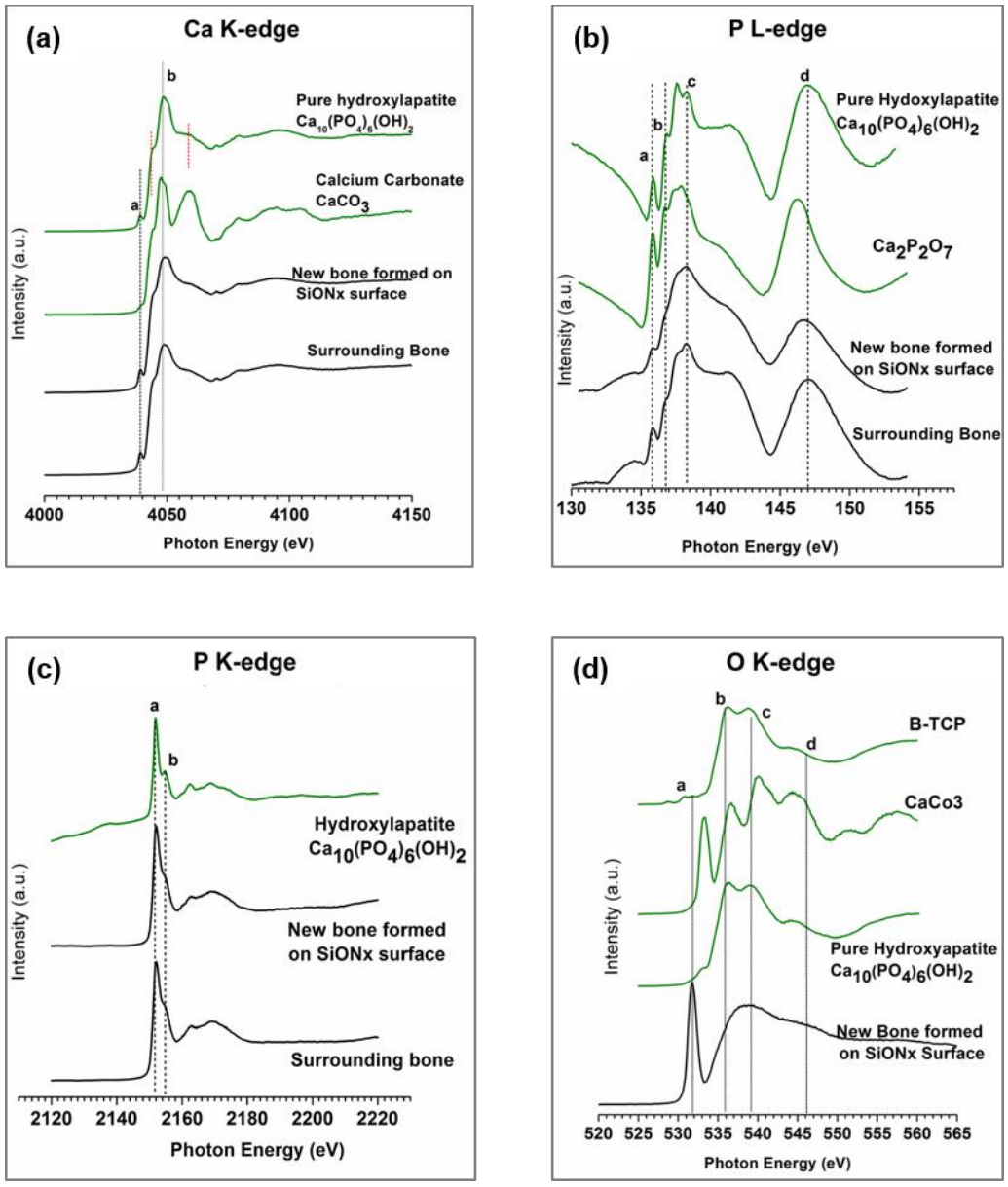


Figure 2-20: X-ray absorbance near edge structure (XANES) spectroscopy comparative data for newly formed bone and the surrounding bone with respect to HA model compounds. Bone-implant test samples were probed to examine the presence of calcium and phosphorus. The data analysis reveals the presence of abundant Ca

phosphates on the Si(ON)x coated implant surface. XANES also confirms that coordination chemistry for the newly grown bone exactly matches the surrounding bone.

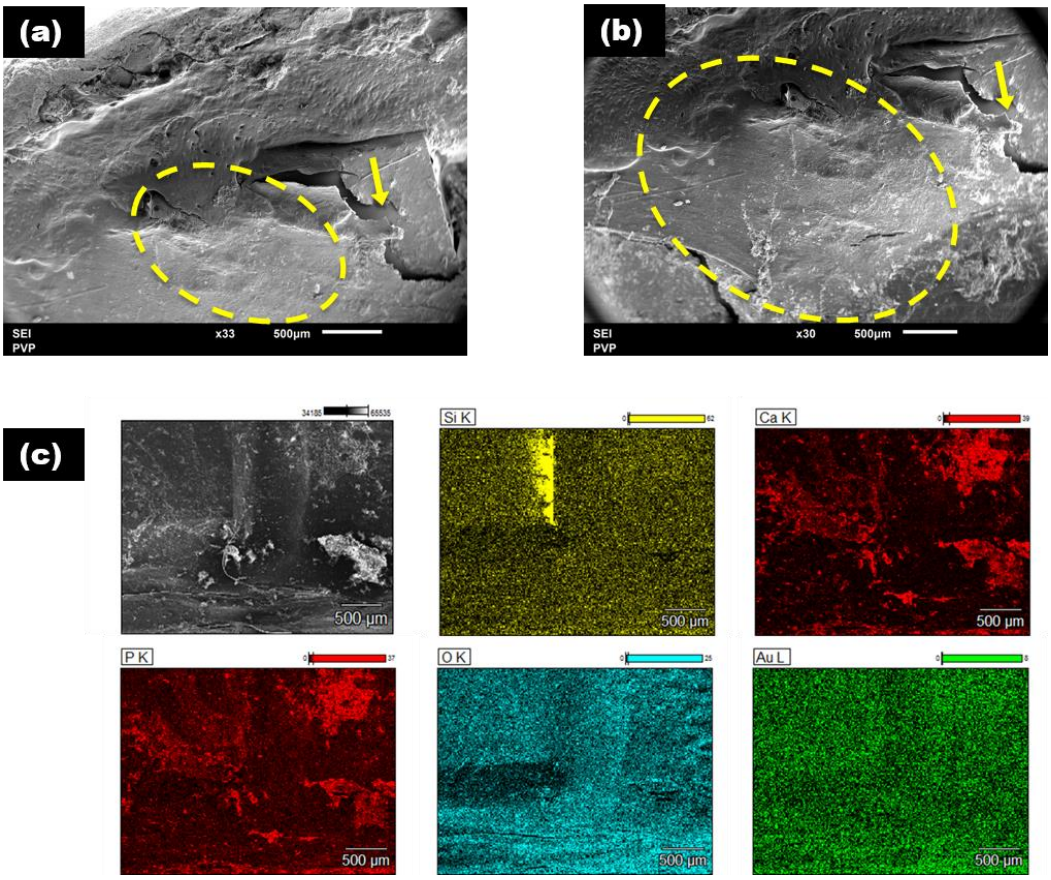


Figure 2-21:SEM micrographs and EDX maps of the samples used in-vivo

SEM micrographs (a) and (b) showed that the bone grows over the surface (indicated by the dotted circle) of the Si(ON)x test sample (pointed out by arrow) within 5 weeks of recovery time. (c) EDS analysis of extracted bone with Si(ON)x test sample shows that bone grows over the surface of the implant and mineralized content (Ca and P) is all over the surface. Excessive Si present at the implant surface that is exposed (not covered by newly generated bone yet) indicates that boney union is nearly complete. The sample was coated with gold so Au is uniform all over the surface.

# Chapter 3. Biomimicking silica formation based on Marine sponges using only synthetic monomers.

Authors: A. Shah, A. Motta, P.B Aswath, V.Varanasi

Abstract

The synthesis of well- defined nanometre silica structures at neutral pH and ambient conditions in TEOS precursor system using imidazole and glucose compounds is reported here. The products were characterised using SEM, EDX, FTIR, Raman and XRD. A design of experiments was created to study the functional contribution of reactants in silica structure formation. XPS and XANES techniques were used to study the products at Si $L_{2,3}$, N K and O K edges to look at the molecular structure and effects of varying parameters on them. XANES studies were also pursued on Tethya aurantia spicules, natural biosilica model that inspired the synthesis mechanism. It was found that the reaction system gave particles with same molecular structure as natural material. The function of reactants was not just as catalytic effect, but the imidazole functionality got incorporated into the structure as well, indicating more complex role of these compounds.

## 1. Introduction:

Synthesis and characterisation of materials at nanometre scales is of great interest for emerging technologies. These materials have tremendous potentials for applications in fields of materials science, optics, ceramics, tire and rubber technology. They also find ample use in catalysis, separations, paints,

magnetic fluids and paper coatings. Controlled and tuneable synthesized nanomaterials are attracting attention in biomedical field as biosensors, drug delivery and tissue engineering applications. [46–50]

Silicon is one the most abundant elements in the earth's crust as is oxygen, silica ($SiO_2$) is one such product. In sol gel methods silicon precursors undergoes hydrolysis to form a colloidal solution of silicic acids. These colloids undergo condensation to form siloxane linkages.[46,49] In this way the resulting particles grow in size either by linkage between larger particles or addition of smaller particle to larger particle. It has been shown that for tetraethyloxysilane (TEOS) the hydrolysis and condensation reactions obey first order kinetics with rate constant depending on reaction temperature and composition .[48] The sol gel synthesis of novel silica structure has been studied under severe pH and/ or temperature conditions. [46,51,52]

Intricate and highly repeatable biosilica structures are observed in marine organisms like sponges and diatoms. They synthesis such elaborate structures at ambient pressure and temperature conditions in neutral or near neutral pH conditions. This piqued the interest of researchers in the field in developing synthesis of silica at ambient conditions in neutral environment.

In the pursuit of achieving this aim, studies were conducted to understand the biomineralization process in the natural materials. It was discovered that proteins like silaffins and silicatein acted enzymatically in the formation of silica in diatoms and sponges respectively.[53] Silicateins were seen exhibit structure directing behaviour.[4] A site directed mutagenesis study of silicatein showed that

Ser-26 and His-165 moieties were active sites involved in hydrolysis of TEOS, used as a Si precursor in-vitro.[15] Model studies of silica formation in presence of poly-histidine have generated conflicting results with one study showing silica formation from tetramethyloxysilane (TMOS)[54] at neutral conditions in presence of poly-histidine, whereas in another study using TEOS as precursor, poly-histidine alone did not prove to be active.[55]

Although silicatein proteins have been used to generate a range of different materials including silica and titania (natural and recombinant silicatein)[1556–59], zirconia (recombinant silicatein)[57] and gallium oxide ( natural silicatein)[60], they are expensive to produce, and it would be more attractive to find cost effective alternatives that show activity in catalysing the mineral formation. Cha et al found that the hydroxyl bond from the Ser site initiates a nucleophilic attack on the Si ion in the precursor, causing hydrolysis of TEOS, leading to condensation of TEOS and formation of Si-O-Si bond.[15]

Based on study by Cha et al[15] poly-histidine alone in presence of TEOS wasn't active[4], due to necessity of presence of OH to initiate nucleophilic attack and catalyse the hydrolysis of TEOS. Whereas TMOS readily hydrolyses in presence of water, and histidine only functioned to allow directed condensation to from precipitates. In this study we propose the use of imidazole and glucose, structurally similar compounds, together to replace the functions of both active moieties serine and histidine, with TEOS precursor to form silica. Silica like structures were successfully precipitated within 10 min of reaction time in the solution and with by-product being just ethanol and water. These particles were

characterized using SEM, EDX, XRD, Raman and FTIR to observe for the basic morphology, chemical composition and structure. The variables investigated were chosen to study the specific functions of the reactants contributing to formation of silica structure. The variation in the product chemical structure was studied via XPS and XANES.

## 2. Results

### *2.1. Synthesis and characterisation of silica particles using the 3-compound reaction system.*

Imidazole and glucose are first allowed to react with the TEOS, to catalyse the hydrolysis reaction which is completed by later stage addition of water. This is followed by auto condensation reaction.

Precipitation is observed within 10 min of reaction time. This precipitate is formed in a solution of water and ethanol, which is released as by product of the above reactions. The ethanol is further added to stop the reaction. Solution is centrifuged, and supernatant is removed. Precipitate is washed thrice in DI water and centrifuged and collected to dry overnight.

#### 2.1.1.SEM/EDX

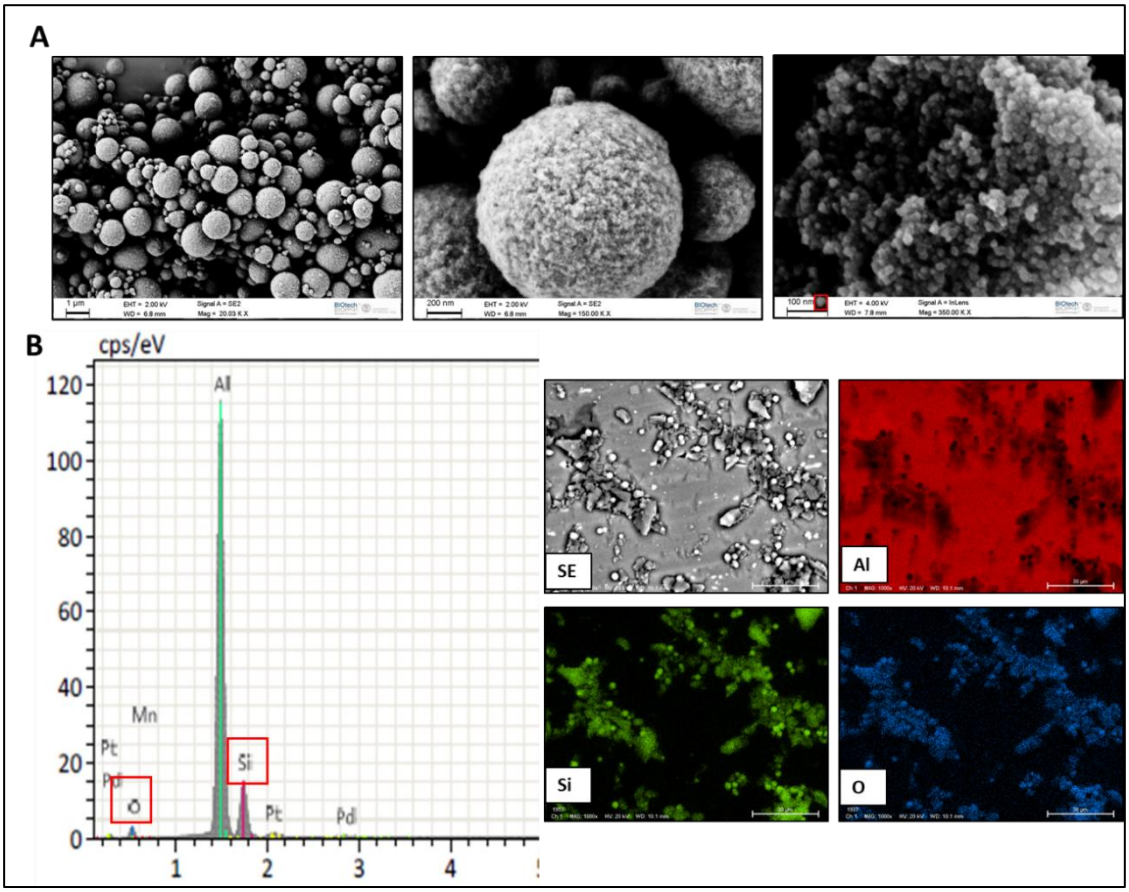


Figure 3-1: (A) SEM of the created particles Biosilica BS1 at 20x, 150x, and 350x.(B) EDX spectrum (left) and EDX maps (right) of Biosilica BS1. Al (red) Si (green) O (blue)

SEM and EDX analysis was performed on the precipitate to look at the

morphology and composition of particles. To prepare for the study, the particles were suspended in ethanol solution and sonicated using water bath sonicator for 15 minutes to deagglomerate the precipitates. After sonication the particles were dispersed in the solution using a touch mixer. Drop from this mixture was taken on an aluminium foil and allowed to dry. Quick drying of ethanol led to lesser agglomeration and allowed for better dispersed sample to be observed. The sample was coated with platinum/palladium coating before testing under SEM and EDX.

Spherical morphology of the particles is observed, and higher magnification studies show that the 200nm spherical particles are again agglomerates of smaller particles about 40-60nm in diameter. The agglomerate size is a varied distribution, but the spherical morphology is uniform throughout the spread. It can be seen from Figure 3-1 that particles are formation of Si and O and may not be stochiometric chemistry of SiO2.

2.1.2.Raman/FTIR

Raman and Infrared spectroscopy was performed to look at chemical composition of the particles.

Representative FTIR spectrum is shown in Figure 3-2_A. The peaks around 1035$cm^{-1}$ and 798$cm^{-1}$ are due to Si-O stretching in Si-O-Si and Si-O bending in Si-OH linkages. The incorporation of imidazole in the product can be seen by amine hydrogen bonding observed at 544$cm^{-1}$ and the out of plane NH2 bond at 655$cm^{-1}$. Peaks between 2950$cm^{-1}$ and 3650$cm^{-1}$ represent various CH and OH stretching modes. These results validate the silica like structure

formation. In addition, they also observe that imidazole was incorporated in the material.

Representative Raman spectrum shown in Figure 3-2_B compliments the data observed in IR spectrum. Si-Si peak is observed in 400-600cm$^{-1}$ region. Fingerprint peaks of imidazole are observed in 1100 cm$^{-1}$ to 1550 cm$^{-1}$ region with

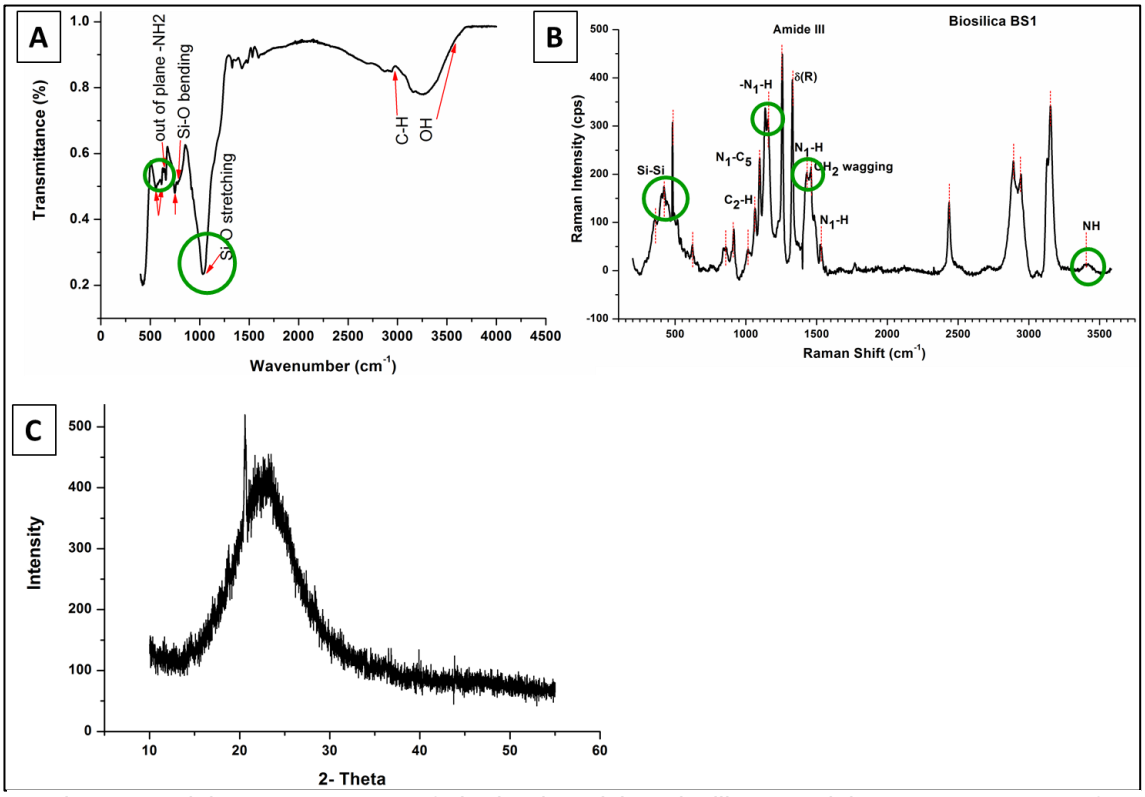


Figure 3-2: (A) FTIR Spectrum of obtained particles Biosilica BS1 (B) Raman spectrum of Biosilica BS1 (C) theta- 2theta XRD analysis of Biosilica BS1.

a slight shift to higher wavenumber, indicating its bonding affected due to incorporation with the silica structure. Characteristic NH peak is also observed at 3450cm$^{-1}$ indicating possible imidazolium like structure formation.

2.1.3.XRD

XRD was performed on Bruker D8 Advance X-Ray diffractometer. Theta 2-theta configuration was used to observe the crystallinity of the obtained material. The spectrum is seen in Figure 3-2. It can be seen from Figure 3-2_C that silica formed is amorphous and the peaks represent the captured imidazole.

2.1.4.XPS

X-Ray photoelectron spectroscopy is used to look at the nature of the chemical coordination of Si and N elements at their 2p and 1s edges respectively. These edges are examined at to help decipher how imidazole is involved in the final structure of biosilica obtained. N1s and Si2p peaks are observed in the survey spectrum which are further studied at high resolution to look at specific peak position and the nature of the peak. The deconvoluted peaks are studied to look at possible mixture of co-ordinations the elements are surrounded by. Si 2p deconvoluted peaks shows the characteristic peak of Si-N coordination from Si3N4 at 101.8. Si-N bond from SiON type of coordination is observed to centre around 102.8eV and Si-O bond is observed at 104. 2eV. N1s peak when deconvoluted shows supportive data Si-N type coordination observed at 397eV.

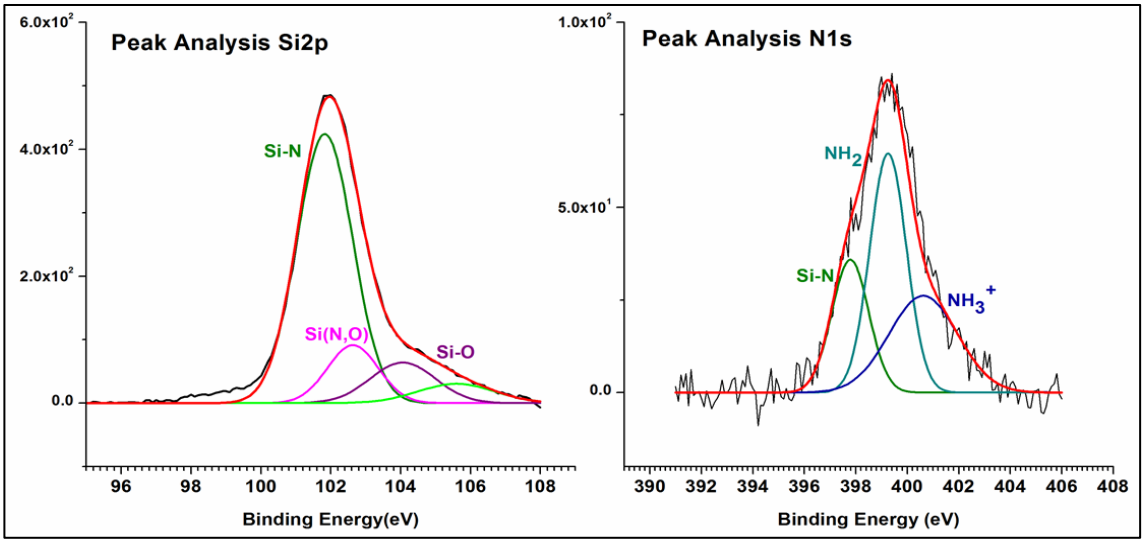


Figure 3-3: XPS analysis of Biosilica BS1 (left) Si 2p (right) N 1s

Thus, XPS gives that Si atom is in coordination with N and O both alike. Also, that imidazole is chemically incorporated in the biosilica structure and not just physically encapsulated forming SiON structure, as observed from the similar data studied by Gritsenko et.al [61]in their XPS study on Si 2p edge on various silicon oxynitride compositions.

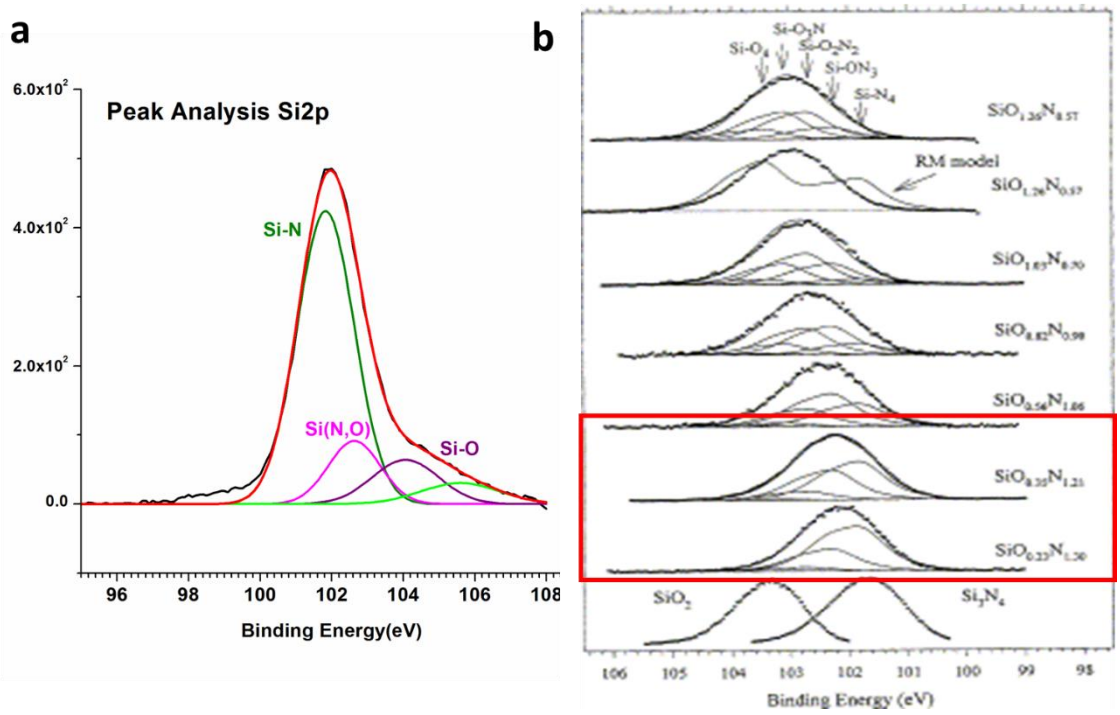


Figure 3-4: XPS Data Si 2p edge Biosilica compared with modelled data

a. Si 2p edge on biosilica particles. b. Si 2p XPS spectra of SiOxNy with different composi- tions. The experimental spectra are shown in dots and the simulated spectra are depicted in solid lines. Reprinted with permission from Elsevier: Journal of Non-Crystalline Solids, copyright (2002).[61]

up

2.1.5.XANES

X-Ray Absorption near edge spectroscopy helps look at the exact interactions involved in the Si and N atoms. The exact type of molecular co-ordinations can be predicted helping understand the exact structure of the biosilica. The biosilica is studied at Si L, NK and O K edge. It is compared with studied on natural siliceous spicules obtained from Tethya Aurantia sponge, whose natural Si formation system is replicated in this study. It is also compared with model compounds of Si3N4 and SiO2 to look at the known edges.

Si L2,3 edge shows presence of Si-N bond due to presence of peak e which is the characteristic edge identifying Si3N4 from SiO samples. The broad shape of these peaks and shifted energies indicate that the coordination isn't stoichiometric Si3N4 but SiON type of structure. Peak a and peak b represent the Si2p1/2 and 2p3/2 split orbitals. Main peak c observes the transition from Si 2p orbital to 3s/3d orbitals. The position of peak c can be used as a finger print to distinguish between $Si^{[4]}$ and $Si^{[6]}$. For [4]Si, the main peak is centred at 107.9 ± 0.2eV while in [6]Si an additional main edge peak is observed at 106.7 ± 0.2 eV. The shift of peak c to the left than observed Si3N4 peak c (tetrahedrally coordinated), we can indicate presence of Si[6] coordination as well.

N K edge shows the details in difference between Si3N4 coordination with that of Biosilica particles and Siliceous spicules. The representative peaks a at 402.6 eV and resonance peak c at 421 eV have shifted to higher energies in the samples than the model compound. Three pre-edge peaks are observed in the

samples. Peak at 398.6 eV are known to represent NH bonds. Remaining peaks could indicate CN bonds from imidazole.

O K edge shows standard peak a 535.2 eV, peak b at 537.8eV and main absorption peak c at 540eV. Peak a represents OH bond coordination,

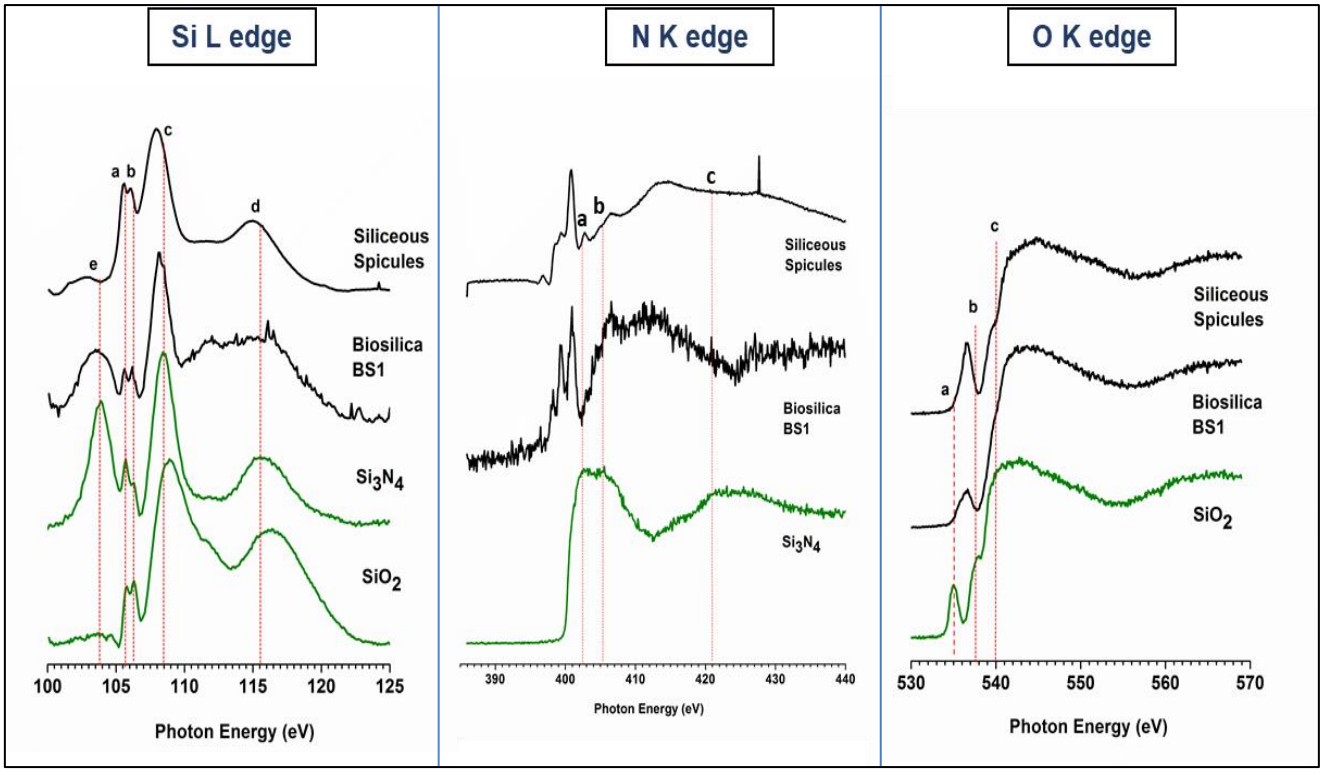


Figure 3-5: XANES analysis of Siliceous spicule (natural biosilica), Biosilica BS1 (created particles), Si3N4 (Model Compound), nanopowder SiO2(Model compound).

peak b represents Si-OH bond and peak c is fingerprint for Si-O bonding. All the peaks are shifted to higher energy in the samples suggesting distortion in SiO2 matrix due to N incorporation.

It is seen that the obtained particles have similar spectrum and hence exhibit same coordination as siliceous spicules at all three edges, indicating the hypothesized reaction helps obtain structurally same material as natural material.

*2.2. Synthesis Mechanism*

To understand the mechanism and the importance of presence OH bond for initiating catalyst action in the hydrolysis reaction, reaction containing only imidazole and TEOS was conducted. To observe whether OH bond remains tethered and that OH inducing catalyst has any templating effect, glucose was replaced with Fibroin (natural protein, polymer with dangling OH bonds free to react). Besides the reaction time of these processes being observed, the products of these reactions were studied for their structure, morphology and chemical composition. XANES and XPS were performed to study the nature of chemical coordination existing and how exactly was imidazole involved in these.

2.2.1.Process Observations

Biosilica BS0: Imidazole was added to 10 µl TEOS solution was in (2:1) mole proportions, and once imidazole dissolved, water was added in (2:1) mole proportions to TEOS to complete the hydrolysis reaction. Unlike imidazole glucose, no immediate precipitation was observed. The solution was left at room temperature for long term studies. Entire solution was precipitated into white silica like formation at the end of 48hours.

Biosilica BS2: 50µl of 9% w/v fibroin solution was mixed with 10µl TEOS solution. This mixture was allowed to react for 24h. This solution was visually pretty clear and well mixed. After 24h, 20µl ethanol was added to stop the

reaction any further. Immediate coagulation of some part of fibroin was observed. The solution was further left to dry, with the intention that it may need freeze drying. But instead in 3 days the sample instead became like a dry film, that could be removed as an entirety from its surface. And it was non-flexible due to its breaking when tried to remove from the vial whose neck was smaller than the film diameter. The film particles were anyway retrieved and studied under SEM and EDX.

Biosilica BS3: 50µl of 9% w/v fibroin solution was mixed with equal weight imidazole. After the mixing, 10µl TEOS solution was added and as soon as they were mixed, 20µl ethanol was added to stop the reaction. Immediate coagulation was observed but of TEOS as opposed to fibroin. The solution was further left to dry, with the intention that it may need freeze drying. But instead in 3 days the sample became like a dry transparent film, that could be removed as an entirety from its surface. The sample *was flexible* due to its folding observed when tried to remove from the vial whose neck was smaller than the film diameter and still achieving entire film. It was studied under SEM and EDX.

2.2.2.SEM/EDX

Biosilica BS0: SEM showed uniform distribution of agglomerates of spherical particles of about 100-200nm size range. These agglomerates observed were not as spherical as observations made for biosilica which could be due absence of glucose and hence its templating activity. The agglomerates are made of particles in the size range of 30-40nm.

Biosilica BS2: SEM showed that there was some agglomeration on the fibroin surface as compared to control fibroin. Also, the part that had coagulated

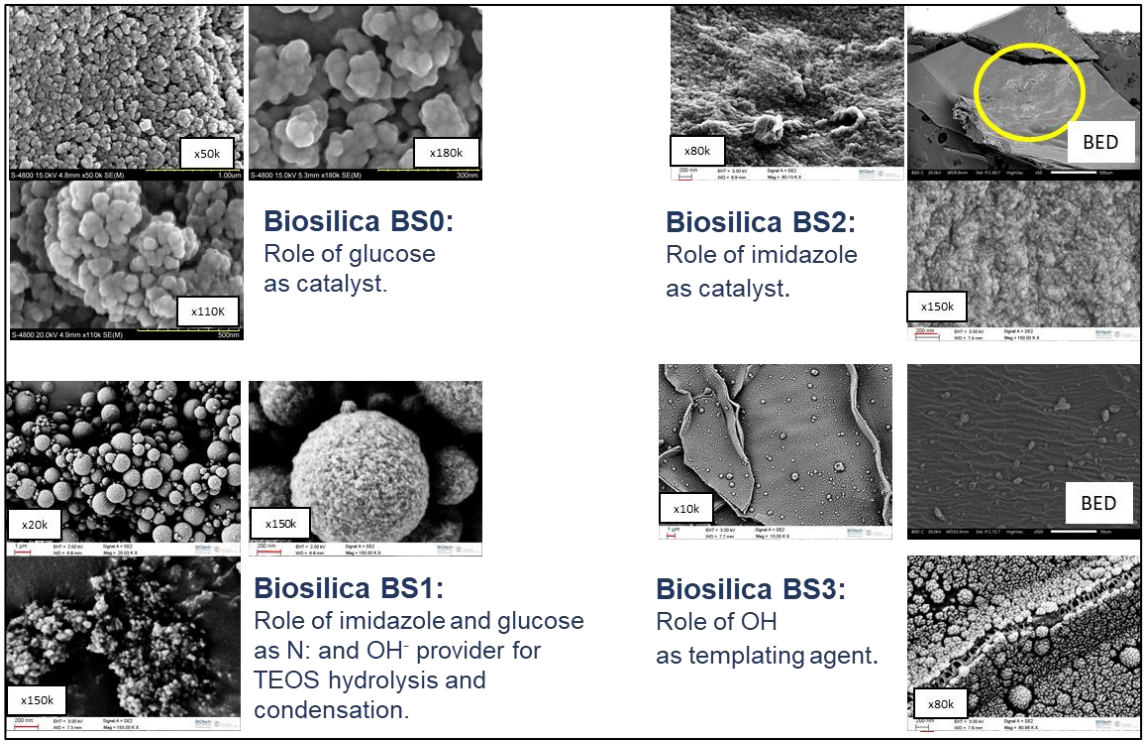


Figure 3-6: SEM images of Design of experiments to study the role of reactants

immediately upon addition of ethanol was unreacted fibroin as seen in second image. EDX showed a mix contribution of Si, N and O (data not shown). Also, according to BED, the compositional spread isn't uniform.

Biosilica BS3: SEM showed uniform distribution of particles and larger aggregates throughout the film surface. Higher Mag images show the entire film surface covered in aggregates. The EDX also showed higher Si presence in spot analysis and also in general on entire film (data not shown). BED also shows uniform film composition. EDX map shows patterned distribution of Si

complimented with distribution of O and N. It covered the entire fibroin film, giving a uniform formation of Si aggregates on a film-based substrate. Also, the EDX showed a considerable amount of Si:O:N ratio. (supplemental data 1)

2.2.3.FTIR

FTIR analysis on the films are seen in Figure 3-7. Figure 3-7**Error! R eference source not found.**_a represents spectrum for Biosilica BS3, all the characteristic peaks representing fibroin are seen. Amide I, II and III are observed in the range of 1250 to 1700$cm^{-1}$. Distinct secondary amine peak is observed at 3250$cm^{-1}$. Si-O stretching from the particle formation is observed in 1050-1100$cm^{-1}$ range. Similar peaks are observed for Biosilica BS2 (Figure 3-7_b) and Si-O stretching signal is distinctly weak. From the comparison though Figure 3-7_c and Figure 3-7_d, again the Biosilica BS1 particles exhibit same peaks as siliceous spicules. Role of imidazole is vital in homogeneous nucleation for SiO formation is seen when compared with Figure 3-7_b. Role of OH provider as a templating agent is seen from successful formation of Si-O particles as coating on these films as seen from SEM and FTIR studies combined.

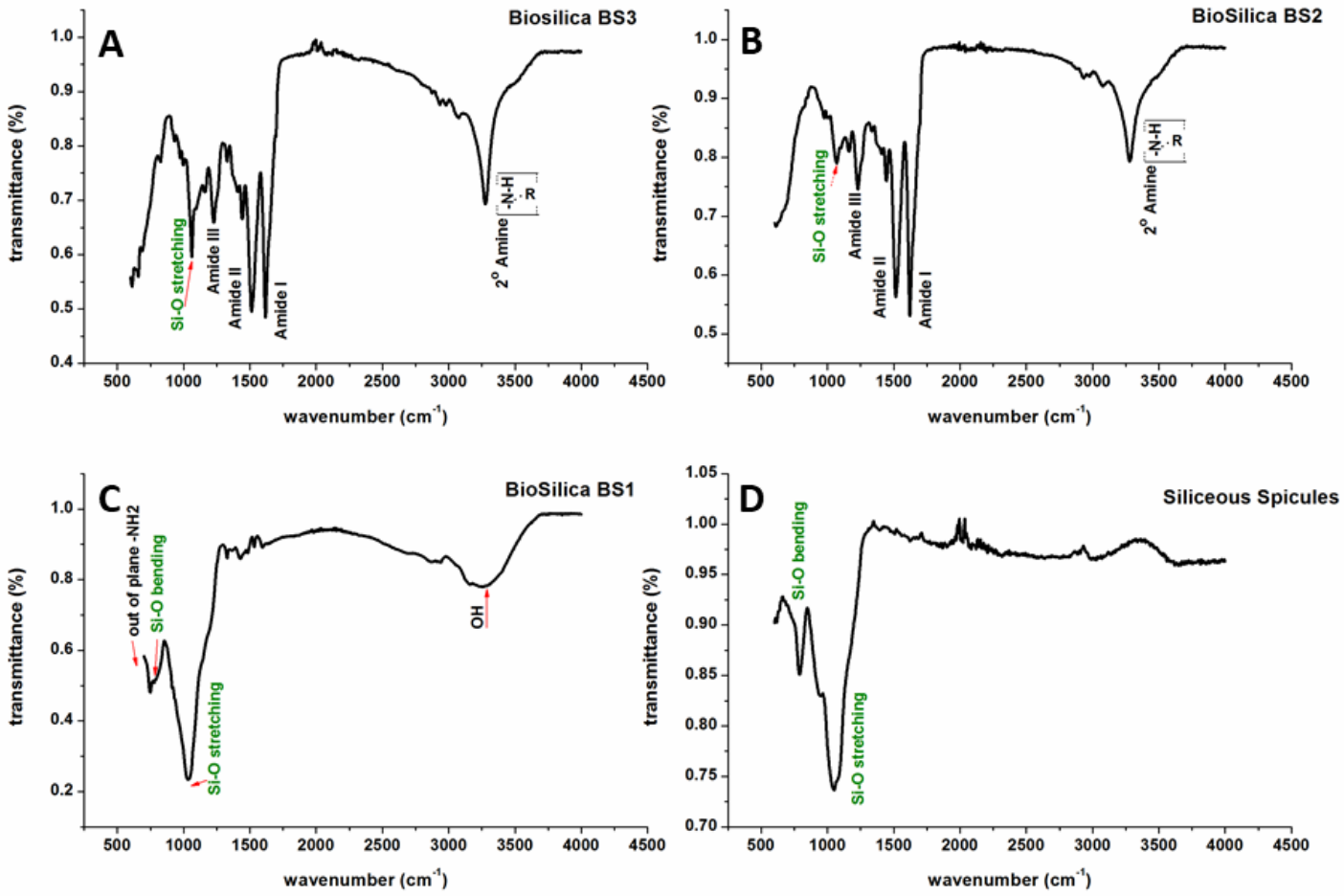


Figure 3-7: FTIR spectrums [A] Biosilica BS3 (Role of OH as templating agent) [B] Biosilica BS2 (Role of imidazole as catalyst) [C] Biosilica BS1 (original reaction) [D] Siliceous spicules (natural particle)

2.2.4.XANES

Near Edge spectroscopy is performed to look at the molecular changes contributed by the different reactants and establish their role in the reaction. Si L, N K and O K edges are studied to establish the molecular coordination of these elements.

*2.2.4.1. Role of $OH^-$ as catalyst:*

To understand the role of $OH^-$ as a catalyst, spectrums of Biosilica BS0 (formation without any OH provider) are compared with Biosilica BS1 (formation including both N: and $OH^-$ provider). These are then compared with model compounds of Si3N4 and SiO2 to be able to distinguish and identify peaks.( Figure 3-8)

Si L edge shows similar peaks for BS0 as BS1. Peak a and peak b represent the Si2p ½ and Si2p3/2 split orbital activity. Peak c position helps identify the Si[4] to Si[6] coordination and the ratio in which they are present. Identical positioning of peak c is observed in BS0 and BS1 indicating the co-ordinations are unaffected by the absence of OH provider. Peak d is resonant peak observed in region of 116 eV. Peak e at 103.8 eV is distinctive peak observed for Si-N coordination and absent in SiO2 model compound. Broad peaks observed in the same region for BS0 and BS1, representing some type of Si-N coordination involved in these structures.

N K edge is observed for BS0, BS1 and imidazole and Si3N4 as model compound. Peak a, b and c match the imidazole peaks. Peak at 398.6 eV is known to represent NH bond, thus peak b and peak c maybe representing C-N

and C=N transitions. Peak d at 406.5 represents the shifted Si-N peak observed in SI3N4 at 402.6 eV. Again, the distinctive peaks are observed in both BS0 and BS1 peaks, indicating absence of OH provider doesn't affect the molecular structure and its involvement as a true catalyst.

O K edge is observed for BS0, BS1 and Glucose and SiO2 model compounds. Peak a at 535 eV represents pure OH transitions. Peak b at 537.6 eV represent Si-OH transitions and peak c at 540 is characteristic peak of Si-O transition in Si-O-Si linkage. All these peaks are shifted to the right in BS0 and BS1. Absorption peak c in glucose represents C-O transition in C-O-C linkage and shifted to lower energy. Pure OH transitions aren't observed in the BS0 spectrum, they were also absent in spectrum for glass slide (data not shown), indicating these occur in nano powders due to their high reactivity, causing hydroxylation of native layers.

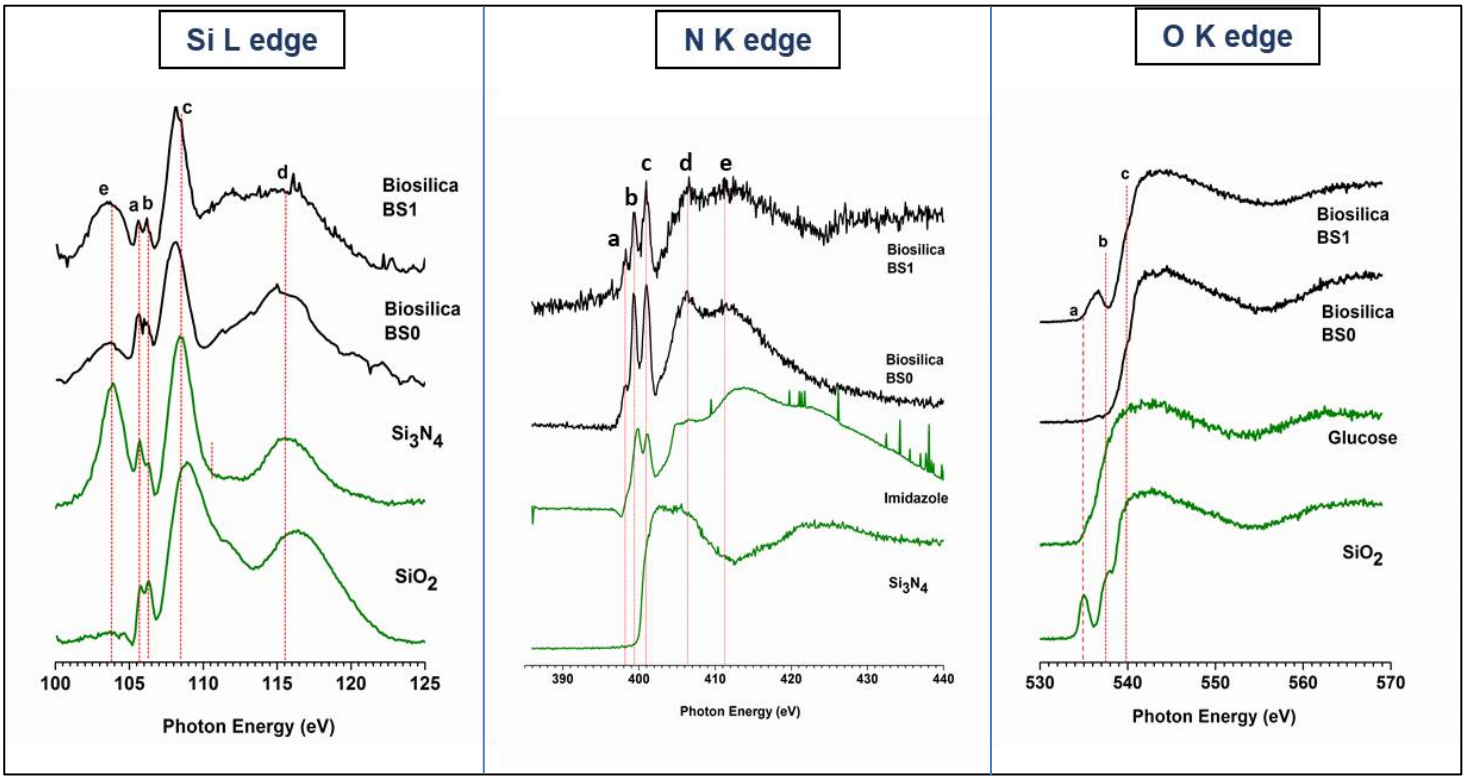


Figure 3-8: XANES Analysis; Biosilica BS0 (imidazole/TEOS formation) , Biosilica BS1 (Imidazole/Glucose/TEOS formation), Si3N4, nanopowder SiO2, Imidazole, Glucose (model compounds)

*2.2.4.2. Role of imidazole (N: provider) as an accelerant:*

To understand role of imidazole as accelerant, XANES analysis of BS1 is compared with BS2 (absence of N: in the reaction, replaced OH provider) and BS3 (presence of N: as well as fibroin as $OH^-$ provider). These are compared with imidazole, fibroin, Si3N4 and SiO2 as model compounds. Again, Si L, N K and O K edges are studied to have a complete understanding of the effects of molecular changes. (Figure 3-9)

Si L edge shows the distinctive peak e that represents Si-N coordination is absent in BS2 spectra. BS3 and BS1 spectra peaks are similar, thus showing imidazole is actively involved in reaction and affects the molecular structure of product, and not just a catalyst. All the remaining characteristic peaks representing SiO2 formations are observed in all the three spectra.

N K edge shows BS1 and BS3 with similar peaks as imidazole and shifted peaks as Si3N4. BS2 spectra doesn't show peak a and peak b, showing marked absence of molecular structural changes due to imidazole incorporation. It can be also seen peak b to peak c intensity ratio changed for BS3 as compared from BS1 and imidazole, which can be attributed to added signal from N activity present in Fibroin.

O K edge shows similar peaks for BS1, BS2 and BS3 with different intensity ratios. OH transitions, peak a, are observed in BS1 at the lowest level then in BS3 which is SiO particle coating fibroin base and BS2 which is mostly fibroin with scattered SiO formation. High intensity of OH activity signal in fibroin can be compared with peak observed in BS2. Peak a to peak c ratio can be used to

distinguish between Si-O formation and OH activity from fibroin only. BS1 has lowest peak a: peak c ratio, BS3 has higher than BS1, indicating peak a signal is mix from fibroin as SiO activity. Peak a: peak c ratio is inverted for BS2, but presence of peak c and shoulder near peak b which represents Si-OH activity, validates SEM results of weak formations of SiO on fibroin.

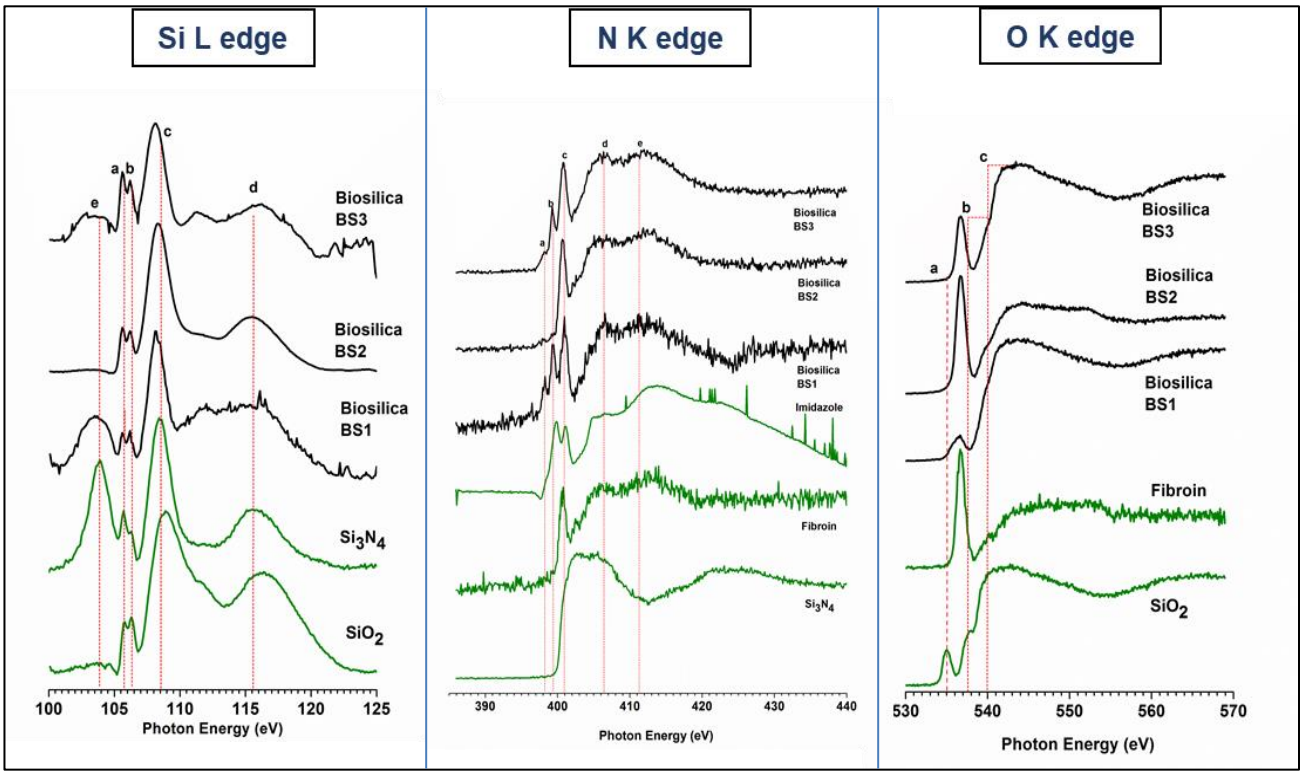


Figure 3-9: XANES Analysis; Biosilica BS3 (Imidazole/Fibroin/TEOS), Biosilica BS2 (Fibroin/TEOS), Biosilica BS1 (Imidazole/Glucose/TEOS), Si3N4, nanopowder SiO2, Fibroin, imidazole (model compounds)

2.2.5.RBM, RMM and Partial Charge Theory

The RMM calculations were based on the theory that the model is a simple mixture of $Si_3N_4$, Si-Si and $SiO_2$ phases. The Bruggeman approximation equation helps associate the refractive index to the volume fractions of the phases.[62],[63] It is given by;

$$vSiO_{2.} \cdot \frac{n_{SiO_2}^2 - < n >^2}{n_{SiO_2}^2 + 2 < n >^2} + vSi_3N_{4.} \cdot \frac{n_{Si_3N_4}^2 - < n >^2}{n_{Si_3N_4}^2 + 2 < n >^2} + vSi \cdot \frac{n_{Si}^2 - < n >^2}{n_{Si}^2 + 2 < n >^2} = 0 \quad (1)$$

where,$v_x$ is the volume fraction of that phase and $n_x$ is the refractive index of the phase and $n$ is refractive index of the film.

The Bruggeman effective medium approximation (EMA) method assumes that the grains of each phase in the composite are randomly mixed, and that their dimensions are much smaller than the wavelength of light but large enough for each grain to be characterized by its bulk optical response.[64] For our model we considered excess Si, $Si_3N_4$ and $SiO_2$ (i.e. Si-Si, Si-N and Si-O bonds) phases.

We assumed that all the oxygen and nitrogen were found in the form of bonded $Si_3N_4$ and $SiO_2$ states. Thus, using mass balance equations:

$$n[Si] + 2n[O] \rightarrow n[SiO_2]$$

$$3n[Si] + 4n[N] \rightarrow n[Si_3N_4]$$

One can derive,

$$\frac{[O]}{[O] + [N]} = \left[1 + \cdot 2 \cdot 1.3 \cdot \frac{v[Si_3N_4]}{v[SiO_2]}\right]^{-1} \quad (2)$$

The factor of 1.3 stems from the ratio of the atomic concentration of oxygen in $SiO_2$ ($4.64 \times 10^{22}$ cm $^{-3}$) and that of nitrogen in $Si_3N_4$ ($5.88 \times 10^{22}$ cm$^{-3}$).[63]

The volume fractions of all the phases should sum to one,

$$\sum v_f = 1 \qquad (3)$$

Using equations 1, 2 & 3 we modelled the expected phase mixture ratios of $SiO_2$, $Si_3N_4$ and Si-Si phases. This was denoted as the RMM fit and the results are shown in. Table 3-1: RMM/RBM and partial charge calculations for the nanoparticles

For the RBM, there are five distinct stoichiometric tetrahedrons possible: $Si_zO_xN_y$ where x+y=4. By convention, these tetrahedrons are referred to as $Si_z$ where z is equal to the number of silicon atoms in a given tetrahedron. A relation for the distribution of these $Si_z$ tetrahedrons as a function of oxygen (x) and nitrogen (y) contents has been developed by Phillips and is given in Equation 4.[64]

$$W_v(x,y) = \left(\frac{2x}{2x+3y}\right)^v \left(\frac{3y}{2x+3y}\right)^{4-v} \frac{4!}{v!(4-v)!} \qquad (4)$$

where, W(x,y) is the work function associated with the random bonding model. The ratios of O/Si (x) and N/Si (y) are used along with the coordination number (v) for finding the random distribution of the five potential tetrahedrons that represent the $SiO_vN_{4-v}$ models.

Partial charge calculations were conducted to observe the trend in the shift of the Si $2p_{3/2}$ peaks as compared to partial charge on Si. In addition, when

the net charge (summation of partial charges on Si, O and N) was considered equal to zero, the mathematical model used to find the different O and N stoichiometry in each film composition was completely satisfied.[61] The equations used for partial charge calculations were as follows:

$$P_j(v) = (S_{SiON} - S_j)/(2.08S_j^{1/2}), \qquad (5)$$

where $S_{SiON}=(S_{Si}{}^{k}S_O{}^{m}S_N{}^{n})^{1/(k+m+n)}$

$$P_{Si}(x,y) = \sum_{v=0}^{4}[P_{Si}(v)W(v,x,y]\Big/\sum_{v=0}^{4}[W(v,x,y)] \quad (6)$$

$$P_O(x,y) = \sum_{v=0}^{4}[P_O(v)W(v,x,y]\Big/\sum_{v=0}^{4}[W(v,x,y)] \quad (7)$$

$$P_N(x,y) = \sum_{v=0}^{4}[P_N(v)W(v,x,y]\Big/\sum_{v=0}^{4}[W(v,x,y)] \quad (8)$$

The calculations for RMM and RBM models are shown in Table 3-1, Figure 3-10 and Figure 3-11.

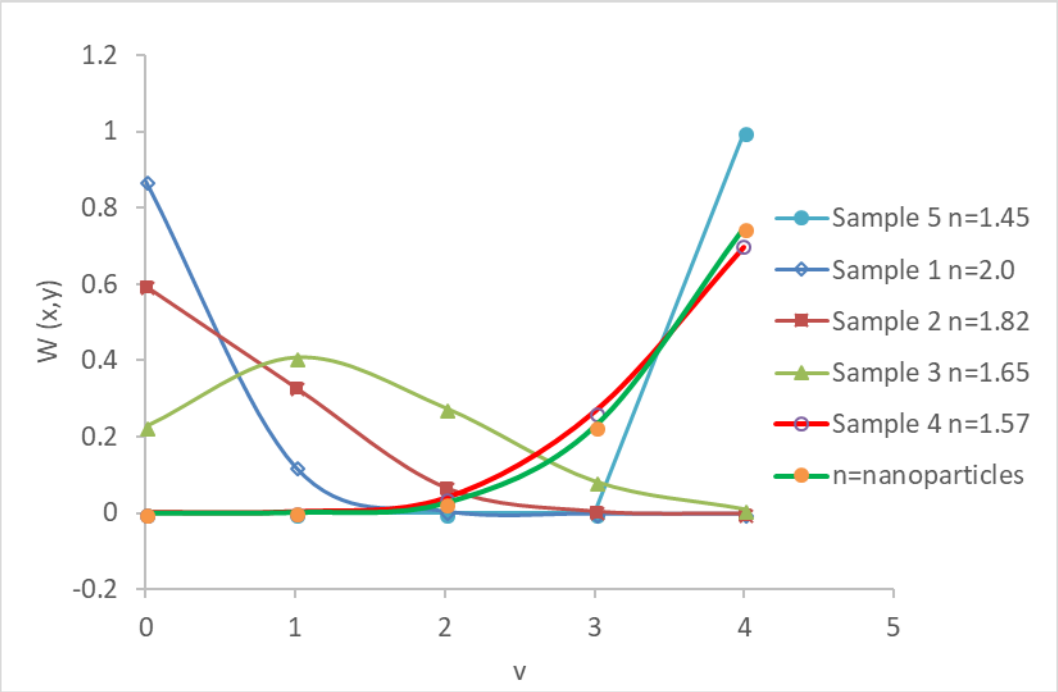


Figure 3-10: Work distribution function of various tetrahedral mix as present in the nanoparticles (green) as compared to the PECVD chemistries

[Matches sample 4 (red)]

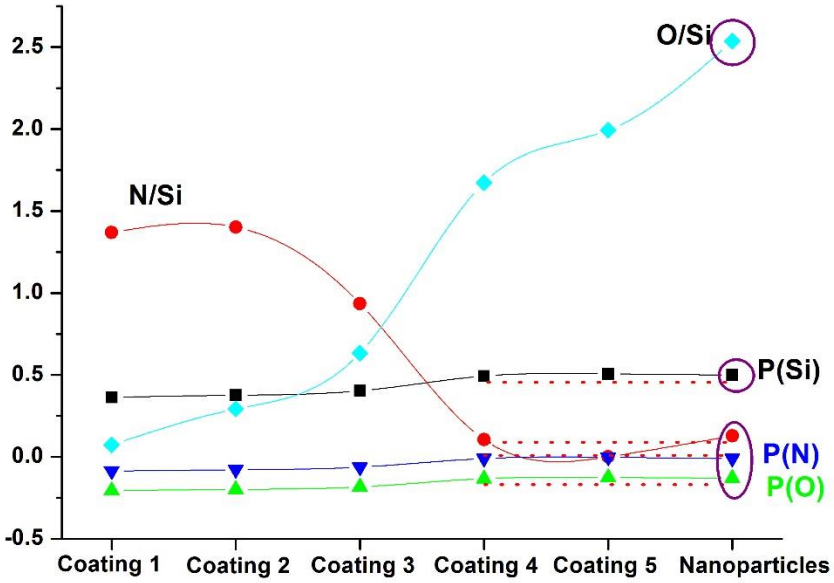


Figure 3-11: Partial charge distribution on element in nanopartyicles compared with SION chemistries

| Sample | RBS comp. /EDS comp (XPS comp for nanoparticles). | | | RMM | | | RBM | | | Partial Charge | | | Sum of Partial Charge |
|---|---|---|---|---|---|---|---|---|---|---|---|---|---|
| | Si | O | N | SiO2 | a-Si | Si3N4 | z | x | y | Si | O | N | |
| Si3N4 | 43.80 | 0.80 | 45.30 | 0.01 | 0.01 | 0.98 | 1.00 | 0.00 | 1.33 | 0.24 | 0.00 | -0.18 | 0.00 |
| 1 | 410.77 | 29.65 | 562.70 | 0.03 | 0.02 | 0.95 | 1.00 | 0.14 | 3.86 | 0.36 | -0.21 | -0.09 | 0.00 |
| 2 | 420.15 | 122.70 | 589.00 | 0.13 | -0.10 | 0.97 | 1.00 | 0.49 | 3.51 | 0.38 | -0.20 | -0.08 | 0.00 |
| 3 | 356.04 | 225.20 | 333.30 | 0.35 | -0.15 | 0.80 | 1.00 | 1.24 | 2.76 | 0.40 | -0.18 | -0.06 | 0.00 |
| **4** | **424.66** | **710.70** | **44.95** | **0.86** | **0.05** | **0.08** | **1.00** | **3.65** | **0.35** | **0.49** | **-0.13** | **-0.01** | **0.00** |
| 5 | 408.88 | 814.70 | 0.00 | 1.00 | 0.00 | 0.00 | 1.00 | 4.00 | 0.00 | 0.51 | -0.13 | 0.00 | 0.00 |
| SiO2 | 32.20 | 67.80 | 0.00 | 0.99 | 0.01 | 0.00 | 1.00 | 2.00 | 0.00 | 0.40 | -0.20 | 0.00 | 0.00 |
| **nanoparticles** | **0.2728** | **0.6922** | **0.0348** | **0.90** | **0.08** | **0.02** | **1.00** | **3.72** | **0.28** | **0.50** | **-0.13** | **-0.01** | **0.00** |

Table 3-1: RMM/RBM and partial charge calculations for the nanoparticles

They are overlayed on the previously obtained data to show comparative performance with distinctly modelled SiON chemistries fabricated via repeatable PECVD processes in work done by Ilyas et al [65]. XPS data is used to model the RBM fit of the nanoparticles. It can be seen that the W(distribution) for nanoparticle resembles the sample 4 from the PECVD chemistry whose reflective index is 1.57. Because of the close fit, the refractive index for the particles can be assumed to be approximately equal to 1.57 as well. The Figure 3-10 shows the calculated work function distribution of the nanoparticles based on RBM view of the structure using the XPS data to fit various types of silica tetrahedra. It is seen that nanoparticles like the high O chemistries, have higher mixture of tetrahedral coordination of the type $SiO_4$, as also seen in XANES. The partial charge calculations show that the partial charge of Si is shifted from pure $SiO_2$ and thus indicates incorporation of N in structure comparable to what is observed in the chemistry from the study done by Ilyas et al[65]

### 2.2.6.Phenomenological Model

Based on all the characterisation studies, a phenomenological model is developed to represent the cohesive understanding of the nanoparticle structure. XPS and XANES studies give the most important understanding of the different molecular bonds involved and the surrounding structure of each element helping build the basic structure. As seen from the Si L, N K edge and O K edges studies in XANES besides SiO and Si-OH bonding, Si-N bonds are also involved in the structure. The Si atom is mainly in tetrahedral coordination as seen from XANES studies as well as the model developed by RBM calculations which supports the fact that there is higher involvement of tetrahedral coordination in the structure. The products of design of experiments table followed to understand the roles of reactants, FTIR studies and XANES studies on the products combined show that the reactants act as templates and are thus incorporated into the structure. It can be assumed that OH provider reactant, forms a hydrogen interaction with the imidazole moiety which is interacting with SiON structure. This is seen when the Fibroin is replaced as OH donor and spherical particles are formed on the fibroin film as a layer, the XANES studies do not show any change in molecular structure, but the particles are bound to film, indicating that there could be some electrostatic interaction causing the particles to form as a coating on the fibroin. The spherical aggregation is attributed to condensation and precipitation activity catalysed by imidazole presence which keeps pH to little greater than 7 allowing for slightly charged particles to follow Ostwald ripening process and hence growth of the particle size. Thus the structure is consisted of the OH moiety in

electrostatic interactions with imidazole moiety that is incorporated in to particles as Si-O-N structure.

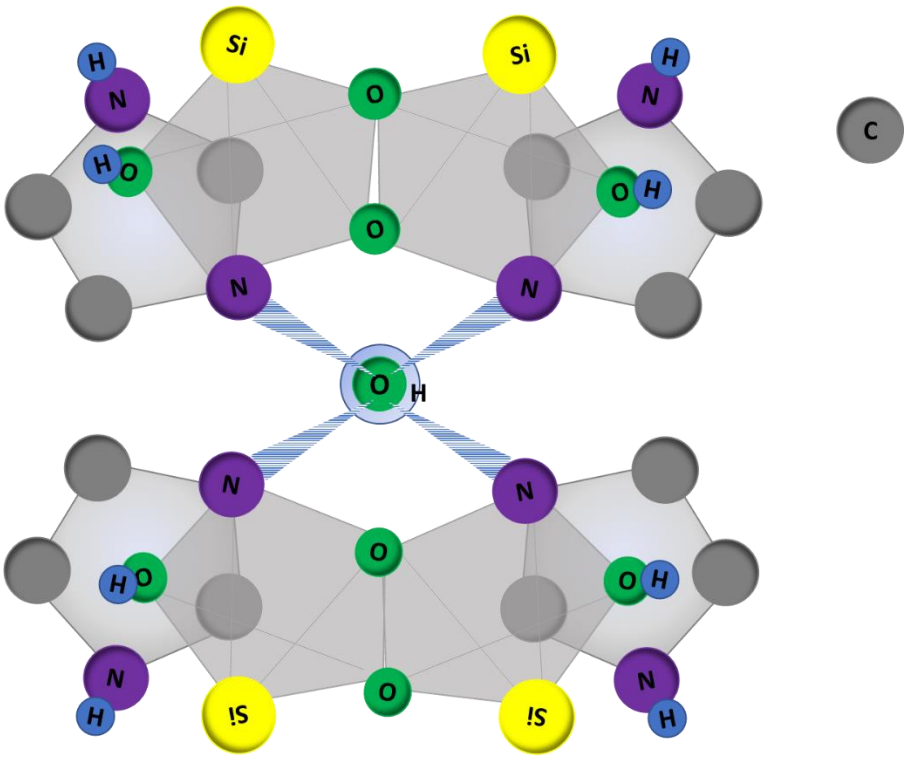


Figure 3-12: Phenomenological model of silicon oxynitride structure

## 3. Discussion

In this study we achieved the synthesis of biosilica nanoparticles from TEOS precursor system with definite nitrogen incorporation into the system, thus obtaining amorphous silicon oxynitride structure. The TEOS was successfully catalysed to precipitate the nanoparticles at near neutral pH and ambient conditions. The precipitation was obtained in the short time period of 10 minutes, with no hazardous by-products, just a mixture of ethanol and water. Cleaning process as well requires only the use of DI water and centrifuging process.

It is observed that the silicification process of TEOS is catalysed due to combinatorial presence of charged nitrogen presence and dangling OH bonds. The silicification process involves first hydrolysis of the precursor to form silicic acids and condensation reaction to form siloxane (Si-O-Si) linkages. The condensation/polymerisation process of silica sols is a three-step process, polymerisation of monomers to form particles, particle growth and particle linkage to form network forming aqueous silica gels. It is found from this study, to achieve successful synthesis of nanoparticles from the TEOS precursor system changes at two steps is required, catalysis during hydrolysis step of TEOS and condensation processes interrupted at step 2 to prevent particle linkage to form gels and instead precipitate out. The previous studies followed by other groups on TEOS failed to initiate this catalysis of the hydrolysis step, leading to their mis-conclusion of histidine (imidazole sidechain) being inactive in the role of TEOS silicification catalysis.

The specific role of each reactant was studied to understand it's functional contribution in the reaction and understand how it progressed. It is seen that imidazole moiety, forms a hydrogen bond from its N3 (pyridine like site) with OH dangling bond of glucose, rendering the O atom to initiate a nucleophilic attack on Si atom of TEOS. This is confirmed from the experimental results of SEM, EDX and XANES, when reactions are conducted in absence of each element and the above mentioned catalytic effect isn't observed. Further imidazole moiety also interacts with silicic acids to catalyse condensation process and forms interactions with particles to produce precipitates instead of gelation, possibly from its cationically charged basic site N3. This is also observed experimentally (SEM, EDX, XANES) when imidazole compound was introduced and removed from Fibroin/TEOS reactive system, and its effects on the product.

The particles precipitated are mainly amorphous in nature as observed from the XRD. SEM analysis shows spherical agglomerates of about 200nm in size which are further made up of 30-40 nm in diameter, individual particles. The spherical morphology can be attributed to the slightly higher than 7 pH conditions, contributed by the active basic site of imidazole leading to precipitation reaction following Ostwald ripening process and particle growth. The XPS and XANES results confirm the formation of silicon oxynitride structure with Si-O and Si-N bonds clearly noted in the peaks. The Si-N bonding could possibly be arising during the acceleration of condensation process and interruption in the network formation to give out precipitate instead of sol-gels. It

is also noted that FTIR analysis exhibits, imidazole fingerprint bonds as is in the silicon oxynitride structure indicating its function as templating agent as well. Thus, our particles have a silicon oxynitride structure that are templated over the imidazole and OH donating moieties. The RMM/RBM studies based on XPS data showed that these particles follow the random bonding model like the high O chemistries in the SiON wafer studies pursued by (cite). The partial charge on the atoms in these particles are similar to sample with refractive index equal to 1.57, while the total charge is zero. It is noted, in the SiON PECVD coating on Si wafer study that the N incorporation in Si-O-N structure is hindered by N-H bonds, thus leaving the only possible bonding site as N3 (pyridine site) that gets involved in Si-O-N structure.

This synthesis process was also successful with Silk Fibroin system , replacing glucose as OH donor moiety indicating the wide variety of applicability of the knowledge acquired from these systems, that can be further used to create these particles. The tethered formation of these particles on silk fibroin layer, also introduce the possibility of one-pot synthesis system, avoiding the necessity of repeated cleaning and centrifuging process to separately obtain the particles.

The reaction system can be extended to polymers with OH bonds free to react, and particles can be made tethered on to these polymers. The system can be recreated with any catalyst system having these bonds thus initiating nucleophilic attack and rendering catalysis of hydrolysis system as well as directing the condensation reaction to form precipitates. These are first experiments as of knowledge on TEOS precursor system to prove this without

use of natural proteins like silicatein or modulated silicatein. It is also scalable, as seen by from using scaled (~300x) amount of reactant and managed to produce the same product. Industrially, it would be greener method to adopt.

## 4. Conclusion

1.1. Spherical silica structures were successfully created from TEOS precursor system by using imidazole and glucose (dangling OH functionalities) and their structures and morphologies were studied. The created particles were compared with Tethya aurantia spicules and found to share the same chemical structure, exhibiting successful biomimicry achieved.

1.2. Design of experiments to study the reactant functional roles and XANES study combined show imidazole functionality catalyses precursor hydrolysis via hydrogen bonding with glucose, rendering nucleophilic attack on Si, accelerates silicic acid condensation by forming hydrogen bonds with silicic acid, while protonated imidazole groups increase silica precipitation activity via electrostatic interaction with oligomeric silicic acids, and gets incorporated into the structure. This has been experimentally observed for the first time.

1.3. It was demonstrated that not only natural enzymes, but synthetic functionally similar compounds can form silica structures from TEOS precursor system at almost neutral pH and ambient conditions.

# 5. Methods

## 5.1. Materials

TEOS, Imidazole, Glucose were obtained from Sigma Aldrich. Ethanol, DI water. Silk Fibroin (SF) was isolated from Bombyx mori silkworm cocoons (Co-operative Sociolario, Como, Italy).

Silk cocoons were treated twice in alkaline water baths at 98C for 1.5hours with 1.1g/l and 0.4g/l $Na_2CO_3$, respectively. Degummed silk was the washed several times in de-ionized (DI) water and dried at room temperature (RT). Fibroin was then dissolved in 9.3M LiBr solution (2g of fibroin in 10ml of LiBr solution) at 65C for 4h. The solution was dialyzed against DI water for 3 days at RT in Slide A Lyzer dialysis cassette (3.5K MWCO, pierce, Rockford, IL, USA) to remove LiBr salt. The fibroin concentration was measured by absorbance spectroscopy using a Nanodrop™ spectrophotometer (Thermo Fisher Scientific, Wilmington, DE, USA).

Before any further use, silk fibroin solution was filtered using a ceramic filter (porosity <5micron) to eliminate impurities.

## 5.2. Silica particle synthesis

Imidazole and glucose are measured and collected in Eppendorf tube. TEOS is added and mixed using touch mixer. The glucose/imidazole to TEOS ratio is 2:1 mole ratio. When the materials are completely dissolved, about 30 secs after the mixing, water is added. (2:1 moles with TEOS). And 10 min after they are allowed to react, 90% ethanol is added to stop the reaction. The solution is thoroughly mixed using touch mixer to allow complete mixing. After the mixing,

the solution is centrifuged for 5 min to settle the stable precipitate at the bottom. The precipitate is collected by removing the supernatant, washed 3 times with DI water. The precipitate is allowed to dry completely overnight. The schematic of the synthesis process is as shown in the Figure 3-13. The particles generated from this mechanism are termed as Biosilica BS1.

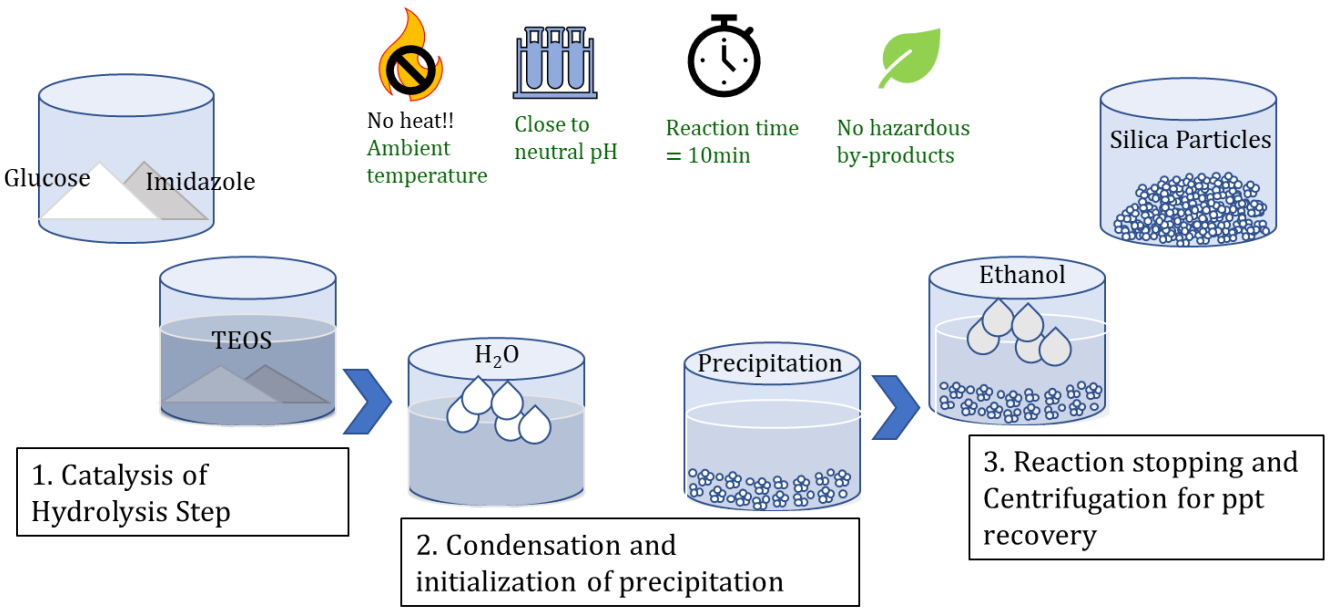


Figure 3-13: Synthesis mechanism of the particles

The reaction that may have proceeded is hypothesized as follows:

Imidazole and glucose, interact to form hydrogen bonding, which leads to nucleophilic attack on the Si atom in TEOS molecule, causing ethanol displacement and pentavalent coordination status of Si atom. This further in presence of water, is broken down to complete hydrolysis of the TEOS.

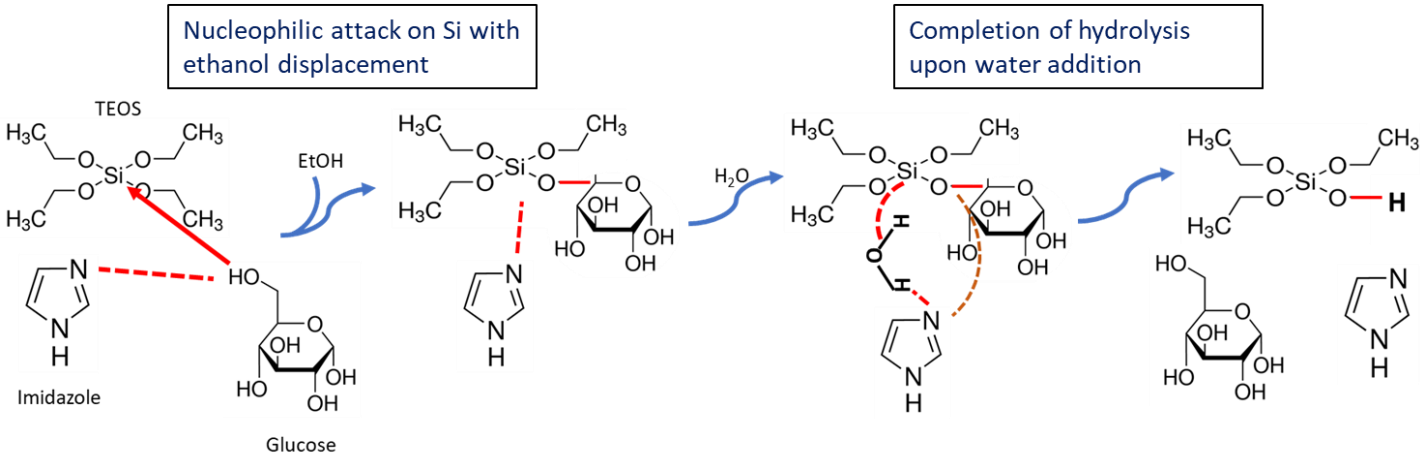


Figure 3-15: Catalysis of the hydrolysis of TEOS

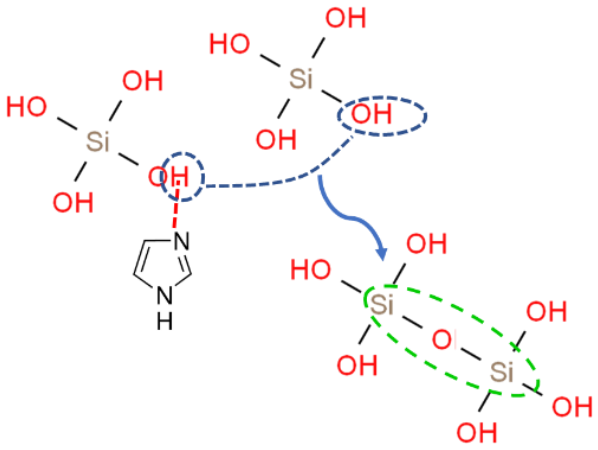

Figure 3-14: Catalysis of the condensation of silicic acids

Imidazole further forms hydrogen bonding with silicic acids to catalyse condensation process.

5.3. Silica particle with Fibroin

8% Silk fibroin solution is prepared from degummed silk by dissolving in LiBr solution, and dialysis against DI water. It is concentrated to 8% solution by dialysing against ‘10M” PEG solution. 50 µl of this solution was taken in glass vial. Equal amount of imidazole was added and let mix. 10 µl TEOS solution was added and 20 µl ethanol was added as soon as the mixing of the former had occurred to stop any further reaction. Immediate TEOS coagulation was observed 24hrs later, the solution had dried to form a film like structure.

5.4. Characterisation

The dried particles were mixed on ethanol solution and sonicated. Drop of this sonicated liquid was taken on aluminium foil to let dry and observe under SEM. The drop on the foil and the film were coated with Pt to observe the microstructure. Same preparation was used to observe the chemical makeup of the particles under EDX. Particles as is were used for remaining characterization to look at the chemical composition using Raman and FTIR. The structure of the particles was observed using XRD.

5.5. XANES/XPS

To understand the nature of chemical coordination existing between the elements, XANES and XPS was performed. X-ray Absorption Near Edge Structure (XANES), also known as Near edge X-ray Absorption Fine Structure (NEXAFS), is loosely defined as the analysis of the spectra obtained in X-ray absorption spectroscopy experiments. It is an element-specific and local bonding-sensitive spectroscopic analysis [66]. XANES work was performed at

Canadian Light Source synchrotron facility at Saskatoon Canada. This study was helpful in looking at the near bonding structure of silicon, oxygen and nitrogen elements, to establish a model of molecular structure of biosilica formed. The study was also performed on a number of other test samples specifically designed to study the role of reactants, glucose and imidazole or in other words the contributions of OH and N: moieties on the final molecular structure. The Silicon $L_{2,3}$ -edge data was collected at Variable Line Spacing Plane Grating Monochromator (VLSPGM) beam station. This beam line has a photon resolution of greater than 10,000 E/ΔE and the energy range from 5.5 eV to 250 eV. SGM (spherical grating monochromator) beamline was used to observe the N K edge and the O K edge data. Typical operating parameters for SGM are: energy-200-2000 eV; photon resolution->5000 E/ΔE; spot size-50 μm x 50 μm.

XPS analysis were performed with the Kratos Axis Ultra system using monochromatic Al Kα X-ray source. This spectroscopic technique reveals the presence of an element, its abundance on the sample surface (typical detection depth ~10 nm) and the chemical bonding state. For analysis, the particles were stuck on carbon tape in dense layer loaded on the sample holder. For data collection the machine setting was at 120W 12kV/10ma conditions. Si 2p and N1s high resolution data was obtained to study their deconvoluted features and the mix of coordination that the elements shared.

References


1. Rahman IA, Padavettan V. Synthesis of Silica Nanoparticles by Sol-Gel: Size-Dependent Properties, Surface Modification, and Applications in Silica-Polymer Nanocomposites—A Review. *J Nanomater*. 2012;2012:1-15. doi:10.1155/2012/132424.

2. Wong Po Foo C, Patwardhan S V., Belton DJ, et al. Novel nanocomposites from spider silk-silica fusion (chimeric) proteins. *Proc Natl Acad Sci*. 2006;103(25):9428-9433. doi:10.1073/pnas.0601096103.

3. World Markets for Precipitated Silica 2006. 2006. http://www.notchconsulting.com/pdf/Silica_Contents06.pdf. Accessed August 27, 2017.

4. Tacke. Milestones in the Biochemistry of Silicon: From Basic Research to Biotechnological Applications. *Angew Chem Int Ed Engl*. 1999;38(20):3015-3018. http://www.ncbi.nlm.nih.gov/pubmed/10540406. Accessed August 27, 2017.

5. Tréguer P, Nelson DM, Bennekom AJ Van, et al. The Silica Balance in the World Ocean: A Reestimate. *Source Sci*. 1995;268(21):375-379. http://www.jstor.org/stable/2886587. Accessed August 27, 2017.

6. Belton DJ, Deschaume O, Perry CC. An overview of the fundamentals of the chemistry of silica with relevance to biosilicification and technological advances. *FEBS J*. 2012;279(10):1710-1720. doi:10.1111/j.1742-4658.2012.08531.x.

7. Schloßmacher U, Wiens M, Schröder HC, Wang X, Jochum KP, Müller WEG. Silintaphin-1 - interaction with silicatein during structure-guiding bio-silica formation. *FEBS J*. 2011;278(7):1145-1155. doi:10.1111/j.1742-4658.2011.08040.x.

8. Patwardhan S V., Lee KB, Kim DJ, et al. Biomimetic and bioinspired silica: recent developments and applications. *Chem Commun*. 2011;47(27):7567. doi:10.1039/c0cc05648k.

9. Wang X, Schröder HC, Müller WEG. Enzyme-based biosilica and biocalcite: Biomaterials for the future in regenerative medicine. *Trends Biotechnol*. 2014;32(9):441-447. doi:10.1016/j.tibtech.2014.05.004.

10. Weaver JC, Pietrasanta LI, Hedin N, Chmelka BF, Hansma PK, Morse DE. Nanostructural features of demosponge biosilica. *J Struct Biol*. 2003;144(3):271-281. doi:10.1016/j.jsb.2003.09.031.

11. Polini A, Pagliara S, Camposeo A, et al. Optical properties of in-vitro biomineralised silica. *Sci Rep*. 2012;2:0-5. doi:10.1038/srep00607.

12. Imsiecke G, Steffen R, Custodio M, Borojevic R, G MiLLER WE. FORMATION OF SPICULES BY SCLEROCYTES FROM THE FRESHWATER SPONGE EPHYDATIA MUELLERI IN SHORT-TERM CULTURES IN VITRO. *Vitr Cell Dev Biol--Animal*. 1995;31:528-535. https://link.springer.com/content/pdf/10.1007/BF02634030.pdf. Accessed August 27, 2017.

13. Arakaki A, Shimizu K, Oda M, Sakamoto T, Nishimura T, Kato T. Biomineralization-inspired synthesis of functional organic/inorganic hybrid materials: Organic molecular control of self-organization of hybrids. *Org Biomol Chem*. 2015;13(4):974-989. doi:10.1039/C4OB01796J.

14. Murr MM, Morse DE. Fractal intermediates in the self-assembly of silicatein filaments. http://www.pnas.org/content/102/33/11657.full.pdf. Accessed August 27, 2017.

15. Cha JN, Shimizu K, Zhou Y, et al. Silicatein filaments and subunits from a marine sponge direct the polymerization of silica and silicones in vitro. *Proc Natl Acad Sci U S A*. 1999;96(2):361-365. doi:10.1073/PNAS.96.2.361.

16. Zhou Y, Shimizu K, Cha J, Stucky G. Efficient catalysis of polysiloxane synthesis by silicatein α requires specific hydroxy and imidazole functionalities. *Angew Chemie*. 1999. http://onlinelibrary.wiley.com/doi/10.1002/(SICI)1521-3773(19990315)38:6%3C779::AID-ANIE779%3E3.0.CO;2-%23/full. Accessed August 27, 2017.

17. Arakaki A, Shimizu K, Oda M, Sakamoto T, Nishimura T, Kato T. Biomineralization-inspired synthesis of functional organic/inorganic hybrid materials: organic molecular control of self-organization of hybrids. *Org Biomol Chem*. 2015;13(4):974-989. doi:10.1039/C4OB01796J.

18. Wang X, Schröder HC, Wang K, et al. Genetic, biological and structural hierarchies during sponge spicule formation: from soft sol–gels to solid 3D silica composite structures. *Soft Matter*. 2012;8(37):9501. doi:10.1039/c2sm25889g.

19. Müller WEG, Binder M, von Lintig J, et al. Interaction of the retinoic acid signaling pathway with spicule formation in the marine sponge Suberites domuncula through activation of bone morphogenetic protein-1. *Biochim Biophys Acta - Gen Subj*. 2011;1810(12):1178-1194. doi:10.1016/j.bbagen.2011.09.006.

20. Simpson TL. *The Cell Biology of Sponges*. New York, NY: Springer New York; 1984. doi:10.1007/978-1-4612-5214-6.

21. Müller WEG, Blumbach B, Wagner-Hülsmann C, Lessel U, 淳平林. Galectins in the Phylogenetically Oldest Metazoa, the Sponges (Porifera). *Trends Glycosci Glycotechnol*. 1997;9(45):123-130. doi:10.4052/tigg.9.123.

22. Schütze J, Krasko A, Diehl-Seifert B, Müller WEG. Cloning and expression of the putative aggregation factor from the marine sponge Geodia cydonium. *J Cell Sci*. 2001;114(17). http://jcs.biologists.org/content/114/17/3189.short. Accessed August 28, 2017.

23. Harrison F, Davis D. Morphological and cytochemical patterns during early stages of reduction body formation in Spongilla lacustris (Porifera: Spongillidae). *Trans Am Microsc Soc*. 1982. http://www.jstor.org/stable/3225749. Accessed August 28, 2017.

24. Müller W, Rothenberger M, Boreiko A. Formation of siliceous spicules in the marine demosponge Suberites domuncula. *Cell tissue*. 2005. http://link.springer.com/article/10.1007/s00441-005-1141-5. Accessed August 28, 2017.

25. Schröder HC, Boreiko A, Korzhev M, et al. Co-expression and Functional Interaction of Silicatein with Galectin. *J Biol Chem*. 2006;281(17):12001-12009. doi:10.1074/jbc.M512677200.

26. Müller WEG, Schloßmacher U, Wang X, et al. Poly(silicate)-metabolizing silicatein in siliceous spicules and silicasomes of demosponges comprises dual enzymatic activities (silica polymerase and silica esterase). *FEBS J*. 2008;275(2):362-370. doi:10.1111/j.1742-4658.2007.06206.x.

27. Silicase, an enzyme which degrades biogenous amorphous silica: contribution to the metabolism of silica deposition in the demosponge Suberites domuncula. *Prog Mol Subcell*. 2003. http://link.springer.com/content/pdf/10.1007/978-3-642-55486-5.pdf#page=252. Accessed August 28, 2017.

28. Bernard C. *Introduction à l'étude de La Médecine Expérimentale Par m. Claude Bernard*.; 1865. https://books.google.com/books?hl=en&lr=&id=iBdSKwntgUAC&oi=fnd&pg=PA5&dq=C+bernard+1865+introduction+a+l%27Etude&ots=xW586PKZEE&sig=amCMOH0qSlxoTYVZ4BALTOOGT84. Accessed August 28, 2017.

29. Wang X, Schröder H, Wiens M, Ushijima H. Bio-silica and bio-polyphosphate: applications in biomedicine (bone formation). *Curr Opin*. 2012. http://www.sciencedirect.com/science/article/pii/S095816691200033X. Accessed August 28, 2017.

30. Jugdaohsingh R. Silicon and bone health. *J Nutr Health Aging*. 2007. https://www.ncbi.nlm.nih.gov/pmc/articles/PMC2658806/. Accessed August 28, 2017.

31. Wiens M, Wang X, Schröder H, Kolb U. The role of biosilica in the osteoprotegerin/RANKL ratio in human osteoblast-like cells. *Biomaterials*. 2010.

http://www.sciencedirect.com/science/article/pii/S0142961210008434. Accessed August 28, 2017.

32. Schröder H, Wang X, Wiens M. Silicate modulates the cross-talk between osteoblasts (SaOS-2) and osteoclasts (RAW 264.7 cells): Inhibition of osteoclast growth and differentiation. *J Cell*. 2012. http://onlinelibrary.wiley.com/doi/10.1002/jcb.24196/full. Accessed August 28, 2017.

33. Jo BH, Kim CS, Jo YK, Cheong H, Cha HJ. Recent developments and applications of bioinspired silicification. *Korean J Chem Eng*. 2016;33(4):1125-1133. doi:10.1007/s11814-016-0003-z.

34. Boehm H. The chemistry of silica. Solubility, polymerization, colloid and surface properties, and biochemistry. Von RK Iler. John Wiley and Sons, Chichester 1979. XXIV, 886 S.,. *Angew Chemie*. 1980. http://onlinelibrary.wiley.com/doi/10.1002/ange.19800920433/full. Accessed August 28, 2017.

35. Patwardhan S V, Mukherjee N, Clarson SJ. Effect of process parameters on the polymer mediated synthesis of silica at neutral pH. *Silicon Chem*. 2002;1(1):47-54. doi:10.1023/A:1016026927401.

36. Global Precipitated Silica Market 2017-2021 | Market Research Reports - Industry Analysis Size & Trends - Technavio. Technavio. https://www.technavio.com/report/global-specialty-chemicals-global-precipitated-silica-market-2017-2021. Published 2017. Accessed August 27, 2017.

37. Specialty Silica Market - Global Industry Analysis, Size and Forecast, 2016 to 2026. Future Market Insights. doi:2016-05-24.

38. Odatsu T, Azimaie T, Velten MF, et al. Human periosteum cell osteogenic differentiation enhanced by ionic silicon release from porous amorphous silica fibrous scaffolds. *J Biomed Mater Res - Part A*. 2015;103(8):2797-2806. doi:10.1002/jbm.a.35412.

39. Ilyas A, Lavrik N V., Kim HKW, Aswath PB, Varanasi VG. Enhanced Interfacial Adhesion and Osteogenesis for Rapid “bone-like” Biomineralization by PECVD-Based Silicon Oxynitride Overlays. *ACS Appl Mater Interfaces*. 2015;7(28):15368-15379. doi:10.1021/acsami.5b03319.

40. Cicco SR, Vona D, De Giglio E, et al. Chemically Modified Diatoms Biosilica for Bone Cell Growth with Combined Drug-Delivery and Antioxidant Properties. *Chempluschem*. 2015;80(7):1104-1112. doi:10.1002/cplu.201402398.

41. Le TDH, Bonani W, Speranza G, et al. Processing and characterization of diatom

nanoparticles and microparticles as potential source of silicon for bone tissue engineering. *Mater Sci Eng C*. 2016;59:471-479. doi:10.1016/j.msec.2015.10.040.

42. Likhoshway Y V., Sorokovikova EG, Belykh OI, et al. Visualization of the silicon biomineralization in cyanobacteria, sponges and diatoms. *Biosph Orig Evol*. 2008;(Table 1):219-230. doi:10.1007/978-0-387-68656-1_16.

43. M??ller WEG, Wang X, Cui FZ, et al. Sponge spicules as blueprints for the biofabrication of inorganic-organic composites and biomaterials. *Appl Microbiol Biotechnol*. 2009;83(3):397-413. doi:10.1007/s00253-009-2014-8.

44. Müller WEG, Wang X, Belikov SI, et al. Formation of Siliceous Spicules in Demosponges: Example Suberites domuncula. *Handb Biomin Biol Asp Struct Form*. 2008;1:59-82. doi:10.1002/9783527619443.ch4.

45. Wang S, Wang X, Draenert FG, et al. Bioactive and biodegradable silica biomaterial for bone regeneration. *Bone*. 2014;67:292-304. doi:10.1016/j.bone.2014.07.025.

46. Iler RK. *The Chemistry of Silica : Solubility, Polymerization, Colloid and Surface Properties, and Biochemistry*. Wiley; 1979. https://www.wiley.com/en-us/The+Chemistry+of+Silica%3A+Solubility%2C+Polymerization%2C+Colloid+and+Surface+Properties+and+Biochemistry+of+Silica-p-9780471024040. Accessed May 6, 2018.

47. Healy TW. Stability of Aqueous Silica Sols. In: ; 1994:147-159. doi:10.1021/ba-1994-0234.ch007.

48. Chen* S-L, Peng Dong, Guang-Hua Yang and, Yang J-J. Kinetics of Formation of Monodisperse Colloidal Silica Particles through the Hydrolysis and Condensation of Tetraethylorthosilicate. 1996. doi:10.1021/IE9602217.

49. Coltrain BK, Kelts LW. The Chemistry of Hydrolysis and Condensation of Silica Sol—Gel Precursors. In: ; 1994:403-418. doi:10.1021/ba-1994-0234.ch019.

50. Patwardhan S V., Clarson SJ. Silicification and biosilicification. *Polym Bull*. 2002;48(4-5):367-371. doi:10.1007/s00289-002-0043-x.

51. Brinker CJ, Scherer GW. *Sol-Gel Science : The Physics and Chemistry of Sol-Gel Processing*. Academic Press; 1990.

52. Stöber W, Fink A, Bohn E. Controlled growth of monodisperse silica spheres in the micron size range. *J Colloid Interface Sci*. 1968;26(1):62-69. doi:10.1016/0021-9797(68)90272-5.

53. Kröger N, Deutzmann R, Sumper M. Polycationic peptides from diatom biosilica that direct silica nanosphere formation. *Science*. 1999;286(5442):1129-1132.

http://www.ncbi.nlm.nih.gov/pubmed/10550045. Accessed May 6, 2018.

54. Patwardhan S V, Clarson SJ. Silicifacation and biosilicification Part 6. Poly-L-histidine mediated synthesis of silica at neutral pH. *J Inorg Organomet Polym*. 2003;13(1):49-53. doi:10.1023/A:1022952931063.

55. Cha JN, Stucky GD, Morse DE, Deming TJ. Biomimetic synthesis of ordered silica structures mediated by block copolypeptides. *Nature*. 2000;403(6767):289-292. doi:10.1038/35002038.

56. Tahir MN, Théato P, Müller WEG, et al. Monitoring the formation of biosilica catalysed by histidine-tagged silicatein. *Chem Commun*. 2004;0(24):2848-2849. doi:10.1039/B410283E.

57. Tahir MN, Théato P, Müller WEG, et al. Formation of layered titania and zirconia catalysed by surface-bound silicatein. *Chem Commun*. 2005;0(44):5533. doi:10.1039/b510113a.

58. Tahir MN, Eberhardt M, Therese HA, et al. From Single Molecules to Nanoscopically Structured Functional Materials: Au Nanocrystal Growth on TiO2 Nanowires Controlled by Surface-Bound Silicatein. *Angew Chemie Int Ed*. 2006;45(29):4803-4809. doi:10.1002/anie.200503770.

59. Jan L. Sumerel, Wenjun Yang, David Kisailus, James C. Weaver, Joon Hwan Choi and, Morse* DE. Biocatalytically Templated Synthesis of Titanium Dioxide. 2003. doi:10.1021/CM030254U.

60. Kisailus D, Choi JH, Weaver JC, Yang W, Morse DE. Enzymatic Synthesis and Nanostructural Control of Gallium Oxide at Low Temperature. *Adv Mater*. 2005;17(3):314-318. doi:10.1002/adma.200400815.

61. Gritsenko VA, Kwok RWM, Wong H, Xu JB. Short-range order in non-stoichiometric amorphous silicon oxynitride and silicon-rich nitride. *J Non Cryst Solids*. 2002;297(1):96-101. doi:10.1016/S0022-3093(01)00910-3.

62. Bruggeman DAG, G. DA. Berechnung verschiedener physikalischer Konstanten von heterogenen Substanzen. I. Dielektrizitätskonstanten und Leitfähigkeiten der Mischkörper aus isotropen Substanzen. *Ann Phys*. 1935;416(7):636-664. doi:10.1002/andp.19354160705.

63. Kuiper AET. Deposition and composition of silicon oxynitride films. *J Vac Sci Technol B Microelectron Nanom Struct*. 1983;1(1):62. doi:10.1116/1.582543.

64. Snyder PG, Xiong Y-M, Woollam JA, et al. Graded refractive index silicon oxynitride thin film characterized by spectroscopic ellipsometry. 1992. http://digitalcommons.unl.edu/electricalengineeringfacpub. Accessed May 19, 2018.

65. Varanasi VG, Ilyas A, Velten MF, Shah A, Lanford WA, Aswath PB. Role of Hydrogen and Nitrogen on the Surface Chemical Structure of Bioactive Amorphous Silicon Oxynitride Films. *J Phys Chem B*. 2017;121(38):8991-9005. doi:10.1021/acs.jpcb.7b05885.

66. XANES: Theory - Chemistry LibreTexts. https://chem.libretexts.org/Core/Physical_and_Theoretical_Chemistry/Spectroscopy/X-ray_Spectroscopy/XANES%3A_Theory. Accessed May 5, 2018.

67. Wang S-F, Wang X-H, Gan L, Wiens M, Schröder HC, Müller WEG. Biosilica-glass formation using enzymes from sponges [silicatein]: Basic aspects and application in biomedicine [bone reconstitution material and osteoporosis]. *Front Mater Sci*. 2011;5(3):266-281. doi:10.1007/s11706-011-0145-1.

68. Kim S. *Marine Biomaterials Characterization, Isolation and Applications.* CRC Pr I Llc; 2017.

69. Silva TH, Alves A, Ferreira BM, et al. Materials of marine origin: a review on polymers and ceramics of biomedical interest. *Int Mater Rev*. 2012;57(5):276-306. doi:10.1179/1743280412Y.0000000002.

70. Sowjanya JA, Singh J, Mohita T, et al. Biocomposite scaffolds containing chitosan/alginate/nano-silica for bone tissue engineering. *Colloids Surfaces B Biointerfaces*. 2013;109:294-300. doi:10.1016/j.colsurfb.2013.04.006.

71. Ravichandran R, Sundaramurthi D, Gandhi S, Sethuraman S, Krishnan UM. Bioinspired hybrid mesoporous silica–gelatin sandwich construct for bone tissue engineering. *Microporous Mesoporous Mater*. 2014;187:53-62. doi:10.1016/J.MICROMESO.2013.12.018.

72. Wang X, Schröder HC, Grebenjuk V, et al. The marine sponge-derived inorganic polymers, biosilica and polyphosphate, as morphogenetically active matrices/scaffolds for the differentiation of human multipotent stromal cells: potential application in 3D printing and distraction osteogenesis. *Mar Drugs*. 2014;12(2):1131-1147. doi:10.3390/md12021131.

73. Wang X, Schröder HC, Wiens M, Ushijima H, Müller WE. Bio-silica and bio-polyphosphate: applications in biomedicine (bone formation). *Curr Opin Biotechnol*. 2012;23(4):570-578. doi:10.1016/j.copbio.2012.01.018.

74. Patwardhan S V, Mukherjee N, Steinitz-Kannan M, Clarson SJ. Bioinspired synthesis of new silica structures. doi:10.1039/b302056h.

75. Le TDH, Liaudanskaya V, Bonani W, Migliaresi C, Motta A. Enhancing bioactive properties of silk fibroin with diatom particles for bone tissue engineering applications. *J Tissue Eng Regen Med*. 2018;12(1):89-97. doi:10.1002/term.2373.

76. Rezwan K, Chen QZ, Blaker JJ, Boccaccini AR. Biodegradable and bioactive porous polymer/inorganic composite scaffolds for bone tissue engineering. *Biomaterials*. 2006;27:3413-3431. doi:10.1016/j.biomaterials.2006.01.039.

77. Wu X, Liu Y, Li X, et al. Preparation of aligned porous gelatin scaffolds by unidirectional freeze-drying method. *Acta Biomater*. 2010;6(3):1167-1177. doi:10.1016/j.actbio.2009.08.041.

78. Liu C, Xia Z, Czernuszka JT. Design and Development of Three-Dimensional Scaffolds for Tissue Engineering. *Chem Eng Res Des*. 2007;85(7):1051-1064. doi:10.1205/cherd06196.

79. Holzwarth JM, Ma PX. Biomimetic nanofibrous scaffolds for bone tissue engineering. *Biomaterials*. 2011;32(36):9622-9629. doi:10.1016/j.biomaterials.2011.09.009.

80. Guarino V, Causa F, Ambrosio L. Bioactive scaffolds for bone and ligament tissue. *Expert Rev Med Devices*. 2007;4(3):405-418. doi:10.1586/17434440.4.3.405.

81. Descamps M, Richart O, Hardouin P, Hornez JC, Leriche A. Synthesis of macroporous β-tricalcium phosphate with controlled porous architectural. *Ceram Int*. 2008;34(5):1131-1137. doi:10.1016/j.ceramint.2007.01.004.

82. Ko E, Cho S-W. Biomimetic Polymer Scaffolds to Promote Stem Cell-Mediated Osteogenesis. *Int J Stem Cells*. 2013;6(2):87-91. doi:10.15283/ijsc.2013.6.2.87.

83. Mieszawska AJ, Llamas JG, Vaiana CA, Kadakia MP, Naik RR, Kaplan DL. Clay enriched silk biomaterials for bone formation. *Acta Biomater*. 2011;7(8):3036-3041. doi:10.1016/j.actbio.2011.04.016.

84. Ilyas A, Odatsu T, Shah A, et al. Amorphous Silica: A New Antioxidant Role for Rapid Critical-Sized Bone Defect Healing. *Adv Healthc Mater*. 2016;5(17):2199-2213. doi:10.1002/adhm.201600203.

## Chapter 4. Processing and Characterisation of the synthesized silica particles for potential bone tissue engineering applications

Authors: A. Shah, A. Motta, P. B Aswath, V. Varanasi, S. Chiera, W. Bonani

Abstract

Many studies have been recently pursued to show the potential of natural biosilica in biomedical applications like bone tissue engineering. These have been divided in two areas, understanding the silicification process in the natural sources to recreate similar material. Using the natural material directly to explore its potentials as biomaterial. In this study we have tested biosilica BS1 particles created using a bio-mimicked process based of sponges and compared with siliceous spicules from Tethya Aurantia by loading them on silk fibroin films for their potential as biomaterial. The particles are tested for cytotoxicity, proliferation, metabolic activity as well as adhesion and morphology via confocal microscopy. The particles do not show any significant cytotoxic effects as compared to the controls. Moreover, they show enhanced metabolic activity as compared to bare silk fibroin control and comparable proliferation rate. The confocal microscopy also showed well adhered and well spread cellular morphology. The performance of Biosilica BS1 particles is equivalent to natural siliceous particles, thus promising potential as a biomaterial in biomedical application.

Key words: Biosilica, Tethya Aurantia spicules, silicon donor, bone tissue engineering .

## 1. Introduction

It is seen in literature that Si based materials have improved bone regeneration rate.[38,39,9] Silicon is involved in biomineralization process, though the exact pathway is unknown. Sponges and diatoms are one of the most commonly known organism forming biosilica.[40,41,42] The understanding of silicification process in these natural sources has been well documented.[42,44,43] Researchers have been inspired by this biomineralization process to develop novel materials with " nature as a model" towards biomedical applications. Recently, much development has been focused on to developing the biomaterials to cure the bone-related diseases.[67] Marine sponges and its biosilica have become popular in biomedical application such as tissue engineering and drug delivery. In recent years, significant development has been achieved in marine-derived biomaterials for tissue regeneration.[68,69] Silicon is seen to accumulate in mammal, in tissues adjoining bone forming regions.[2] Silica and its biocomposite are becoming familiar in making the artificial scaffold for bone tissue engineering.[70] Sowjanya et al. prepared the blends of chitosan and alginate with nanosilica composite scaffold for bone regeneration. The presence of nanosilica (nSiO2) in the composite increased the protein adsorption and controlled the swelling. The addition of nSiO2 in the composite scaffold significantly increases the mineral deposition on the composite scaffolds. The developed scaffold is biocompatible with osteo-lineage cells. In another study, Ravichandran et al. presented the fabrication procedure of gelatin with

mesoporous silica fibers for bone tissue regeneration. The bioactivity of the developed scaffolds initiates the viability of MG63 cells and also increases the alkaline phosphatase activity. The expression of important genes such as osteocalcin, osteopontin, bone sialoprotein, collagen I, and alkaline phosphatase are also increased.[71] Muller et al. found that biosilica positively affects the SaOS-2 cells growth and mineralization; further it significantly increases the osteoprotegerin (OPG) expression. Owing to this excellent property of biosilica, it is extensively used in the biomedical application, especially bone-related diseases.[43] Wang et al. reported that biosilica have shown morphogenetic effect and differentiation effect on osteoblast cells and stem cells. Biosilica have a capacity to induce the and also found to increase substantial gene expression such as bone morphogenetic protein-2 (BMP-2) and ALP in osteogenic cells. It was suggested that biosilica are morphogenetically active additives for several composites biomaterials.[72] Biosilica can be used for osteoporosis treatment, as mentioned earlier, its huge capacity to induce the BMP-2 directly and also inhibiting the function of osteoclast. So, it will be an excellent candidate to treat the bone-related diseases.[73]

Researchers have narrowed down the biomineralization process in the natural sources to catalytic involvement of enzymes like silicatein present in sponges and sillafins present in diatoms, that help generate $SiO_2$ at low temperature, pressure and neutral pH conditions. The use of biosilica based materials like diatoms have shown improved rate of bone regeneration.[40,41] Biotechnologists, have used this knowledge to further enhance its applicability as

biomaterial in bone regeneration applications. They have incorporated silicatein, as encapsulated nanomaterials loaded at the defect site, to improve regeneration by supplying the catalyst at the defect site and relying on Si ions from the natural system as a source to create silica.[45] It has been demonstrated that silicon, and biosilica prepared with silicatein as well, have shown upregulation of osteoblasts[31] and adverse effects on osteoclasts.[32] It was seen in SaOS-cell line that presence of biosilica displayed differential gene expression, with increasing steady state level of osteoprotegerin (OPG) transcripts without changing the transcript level of the osteoclasto-genic ligand, receptor activator of nuclear factor-kB (NF-kB) ligand (RANKL).[31] Thus making biosilica a potential replacement biomaterial for osteogenic applications. It is also considered for other biomedical applications like surface coatings, scaffolds and biomolecules delivery.[33]

Various researchers have created silica like structures based on these natural processes by replacing the natural enzymes with functionally similar materials and using TMOS as a precursor.[74] But these particles haven't been tested for their biocompatibility. In this study, the biocompatibility and bioactivity of such particles previously created by our group was studied. The particles were tested for cytotoxicity, adhesion and morphology on the surface. Their proliferation and metabolic activity was monitored for 1, 3 and 7 days. To efficiently test these particles, they were loaded on Silk Fibroin films, while simultaneously using unloaded bare silk fibroin film as a control. The

performance of these particles was also compared to siliceous spicules obtained from Tethya Aurantia sponge, the natural source of $Si^{+}$ ions.

## 2. Materials and Methods:

Biosilica particles are prepared using the imidazole-glucose-TEOS reaction method described in chapter 3. The particles are thoroughly washed with ethanol and rinsed thrice with DI water at the end of reaction to remove any unbound imidazole or glucose particles. The particles are left to dry overnight. The agglomerate size range was in 200nm and he actual particles were in size of 30-50nm as observed using Scanning Electron Microscopy.

Siliceous spicules obtained from Tethya aurantia sponge are cleaned in distilled water and allowed to dry overnight in chemical hood. These spicules are about 15-20 micron in diameter and 800-1000 micron in length and shaped like rods as observed in SEM.

Silk Fibroin (SF) was isolated from Bombyx mori silkworm cocoons (Co-operative Sociolario, Como, Italy).

### *2.1. Film Preparation:*

Film studies would provide for a wider range of cell tests to be run. It would allow for not only cytotoxicity but also proliferation, metabolism and morphological studies. Fibroin was selected as base material to load the particles or spicules in.

Design Table 1 indicates the samples and sample codes used for the further tests:

Table 4-1: Composition of Silk Fibroin and Silica particles

| CODE | TYPE |
|---|---|
| SS | 2% tethya aurantia spicules + 4% SF |
| BS-1 | 2% bio-inspired $SiO_2$ particles (deposited on) 4% SF |
| SF | 4% silk fibroin film |
| BS-P | 2% bio-inspired $SiO_2$ particles. |

*2.2. Fibroin formation:*

Silk cocoons were treated twice in alkaline water baths at 98C for 1.5hours with 1.1g/l and 0.4g/l $Na_2CO_3$, respectively. Degummed silk was the washed several times in de-ionized (DI) water and dried at room temperature (RT). Fibroin was then dissolved in 9.3M LiBr solution (2g of fibroin in 10ml of LiBr solution) at 65C for 4h. The solution was dialyzed against DI water for 3 days at RT in Slide A Lyzer dialysis cassette (3.5K MWCO, pierce, Rockford, IL, USA) to remove LiBr salt. This dissolved solution is let to dialyse in bd.$H_20$ for 3 days with minimum 3 water changes per day. The fibroin concentration was measured by absorbance spectroscopy using a Nanodrop™ spectrophotometer (Thermo Fisher Scientific, Wilmington , DE, USA) which is around 6% and the pH is around 6.0.Before any further use, silk fibroin solution was filtered using a ceramic filter(porosity <5micron) to eliminate impurities.

The Fibroin is freshly used to form the films since stored fibroin can start forming gel if left at room temperature.

The films are formed in petri dishes. The sample prep for different films is as follows,

- SS films are prepared by depositing the sponge spicules on the bottom surface of the petri dish with help of ethanol, let them dry and then layering it with silk fibroin solution and leaving them to dry.
- BS-1 films are prepared by mixing the particles in the additional water content required to dilute the fibroin to 4% concentration, sonicating them for approximately 45 min or more to break down the agglomerates, and using this water with particles to dilute the fibroin solution and then layering the diluted fibroin solution in the petri dish to form a film.
- BS-P samples are just the nano particles of $SiO_2$ used in BS-1 films, suspended in the medium to check for cytotoxicity.
- SF films are prepared by just casting 4% silk fibroin solution in the petri dish.

*2.3. Film Characterisation:*

A Field Emission Scanning Electron Microscope was used to observe the surface morphology of fabricated films. Prior analysis, sample were coated with Pt/Pd coating.

FTIR spectroscopy was used to observe any changes in bonding structure of the Fibroin.

*2.4. Cell Culture:*

NIH3T3 – normal murine embryo fibroblasts were used to assess the cytotoxicity effects of the material. Initially, a vial containing 1.5 million of cells were thawed and the cells were cultured in a T175 flask. When confluent, they were split and seeded into 96 well plates.

NIH 3T3 cells were expanded with standard NIH 3T3 medium:

Table 4-2: Cell culture medium for NIH 3T3 cells

| **NIH 3T3** medium composition | |
|---|---|
| ***product*** | *quantity* |
| **MEM** | 450 mL |
| **Fetal Calf Serum** | 50 mL |
| **L-glutamine** | 5 mL (2 mM) |
| **Sodium Piruvate** | 5 mL (1 mM) |
| **Antibiotic/Antimycotic** | 5 mL |

MG63- fibroblast human osteosarcoma were used for assessment of Morphology, Adhesion, Proliferation and Metabolic activity. Initially, a vial containing 1.5 million of cells were thawed and the cells were cultured in a T175 flask. These cells were split once after 96h before being seeded into 48 well plates.

MG63 cells were expanded with standard MG63 medium:

Table 4-3: Cell culture medium for MG63 cells

| MG63 medium composition | |
|---|---|
| *product* | ***Quantity*** |
| MEM Invitrogen [+4°C] | **450 mL** |
| Glucose (aready inside) | **1000mg/L** |
| Fetal Calf Serum [-80°C] | **50 mL** |
| L-glutamine 200mM [-20°C] | **5 mL [584mg/l]= (2 mM)** |
| Sodium Piruvate 100mM [+4°C] | **5 mL [110mg/lL]=(1 mM)** |
| Non-essential Amino acids [+4°C] | **5mL** |
| Antibiotic/Antimycotic [-20°C] | **5 mL** |

*2.5. Assessment of Cytotoxicity:*

Cytotoxic effects on the cells is measured using the LDH Assay (Sigma TOX kit) following the manufacturer's instructions. In brief, the NIH3T3 normal murine embryo fibroblasts were cultured for a week, split once before seeding them on the films. The seeded cells on the films were incubated in culture medium for 24h and 48h. At the end of the time points the culture medium was collected and centrifuged. 30µl of this medium is added to 60 µl of assay mixture and the reaction is run in dark for 30 min. Reaction is terminated using 1M HCl solution. The absorbance is measured at 490nm with a Safire microplate reader (Tecan, Männedorf, Switzerland)

*2.6. Assessment of Morphology, Adhesion, Proliferation and Metabolic activity:*

Cell morphology and proliferation, metabolic activity is further tested on films made with the same process as described earlier. MG63 cell line is used for these tests. The cells were again cultured and split once before they were seeded onto the films to initiate the tests.

2.6.1.Cell metabolic activity:

Alamar Blue Assay was used to quantify the metabolic activity of the cells as they were cultured through Day 1, Day 3 and Day 7. The test principle is based on resazurin being used as an oxidation-reduction (REDOX) indicator that undergoes colorimetric change in response to cellular metabolic reduction. The reduced form resorufin is pink and highly fluorescent, and the intensity of fluorescence produced is proportional to the number of living cells respiring. Through detecting the level of oxidation during respiration alamarBlue® acts as a

direct indicator to quantitatively measure cell viability and cytotoxicity. The test was conducted by adding the dye at the decided time point, waiting for the required time and then collecting the culture medium for further testing. This test is done in presence of live cells. And then medium is replaced with fresh medium to let the cells grow further.

2.6.2.Cell proliferation/ DNA quantification test:

PicoGreen® Assay was used to quantify the DNA and hence number of cells at timepoints of Day 1, Day 3 and Day 7. Test was performed following manufacture instructions. In brief, the cells were fixed on films and cultured in growth medium for the decided time. At the end of the time point the cells were fixed and permeabilized using Triton-X. The growth medium is collected and sonicated and further used for the assay. The dye included samples are measured against calibrated samples using microplate reader.

2.6.3.Adhesion and morphology:

This test helps stain the nuclei of the cells (DAPI) to help visualize the number of cells adhered to the surface and Phalloidin staining helps to stain the actin filament that helps observe the morphology of the cells, round morphology indicating the cells do not prefer the surface and well spread morphology would indicate the cells like to grow on the surface. We use confocal microscopy to observe the cells. The cells are allowed to grow for the decided period of time and then fixed on the surface using formaldehyde. They are then permeabilized and stained using the intended dyes to prepare for observation.

## 3. Results and Discussion:

### *3.1. SEM Characterisation:*

The SEM of films is shown in Figure 4-1

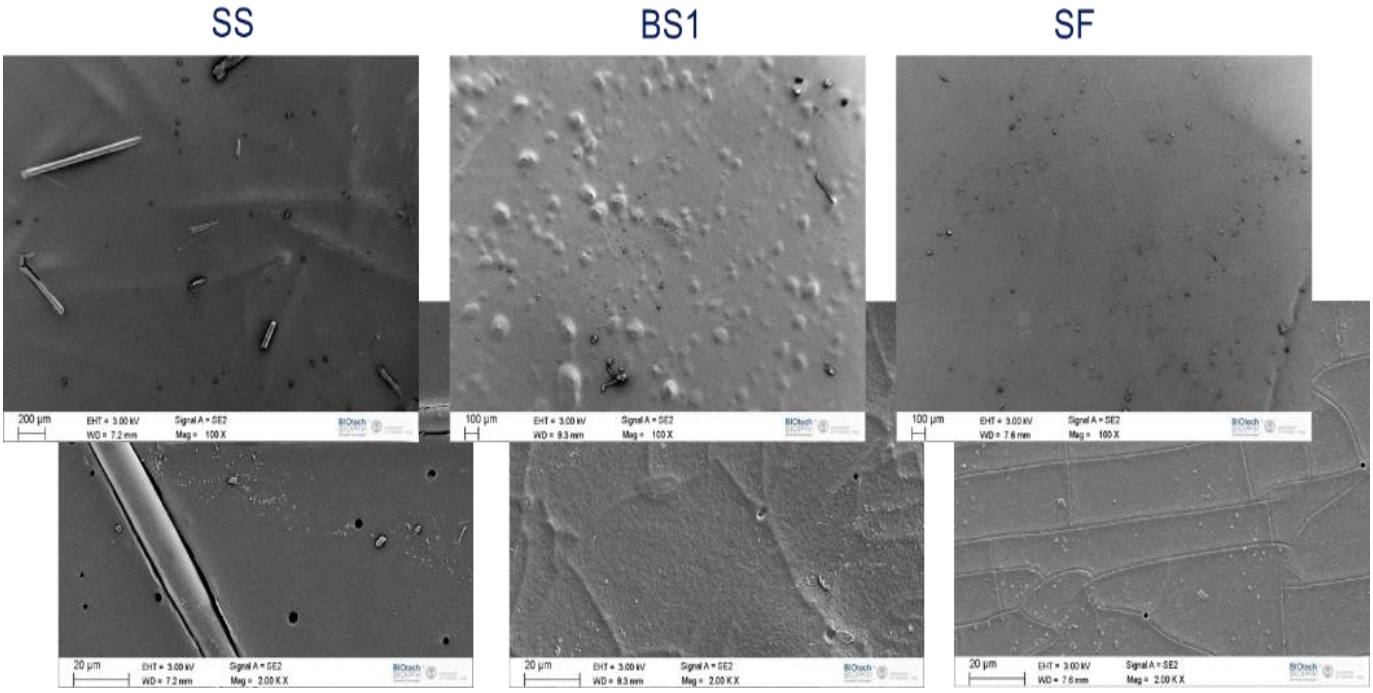


Figure 4-1: SEM images of the films used for biocompatibility testing. (L-R) SS - 2% Tethya aurantia spicules + 4% SF, BS1 - 2% bio-inspired SiO2 particles (deposited on) 4% SF, SF - 4% silk fibroin film.

The SEM shows that particles are uniformly distributed and giving the surface a texture pattern at micron level as compared to plain silk fibroin. Higher magnification images show that some silica spicules are exposed on the surface while some are embedded and covered in thin layer of fibroin. Biosilica BS1 film on the other hand shows all the agglomerates being submerged in thin fibroin coating.

*3.2. FTIR Analysis:*

The protein secondary confirmation and the effect of the silica particle addition on the samples conformation were evaluated by the infrared spectroscopy as seen in Figure 4-2. Pure fibroin film as well as composite films show adsorption bands around 1622 $cm^{-1}$ (amide I), 1518 $cm^{-1}$ (amide II), 1260 $cm^{-1}$ (amide III), and the shoulder at 1265 $cm^{-1}$ confirmed β- sheet as main

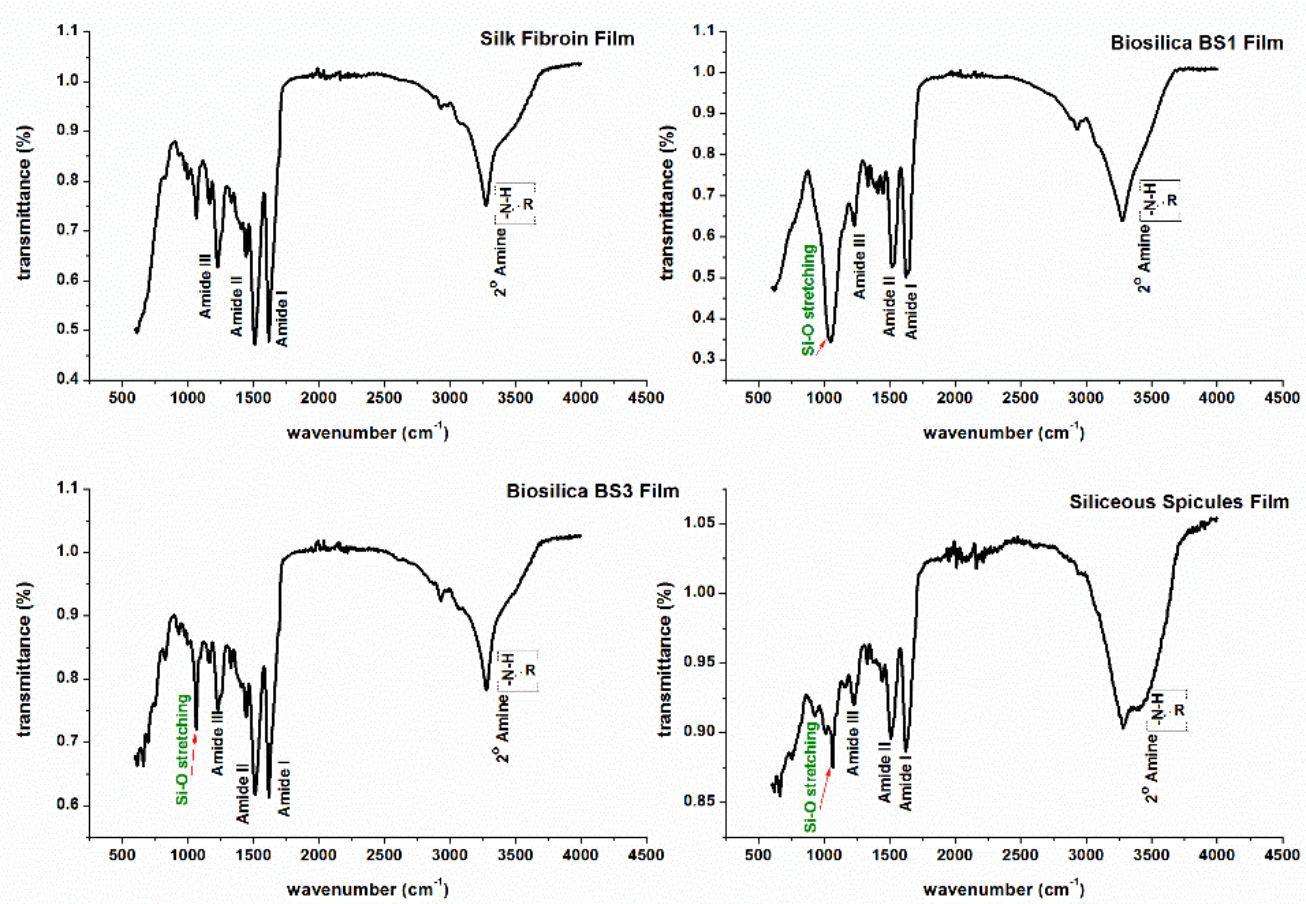


Figure 4-2: FTIR analysis of films. (clockwise) Bare silk fibroin film, Biosilica BS1 film, Siliceous spicules SS film, Biosilica BS1 particles

secondary conformation. Shoulder at 1690 $cm^{-1}$ suggests that this β form is of the anti-parallel type. The addition of the particles did not cause structural conformation modifications to SF. The feature peak related to Si-O stretching around 1030 $cm^{-1}$ is observed in the films at different intensities probably due to inhomogeneity in dispersion pattern at submicron levels, due to the size difference of siliceous spicules compared with particles. [75]

*3.3. Biocompatibility Results:*

3.3.1.Cytotoxicity Assessment:

The results are compared with the positive and negative controls. Positive control was, cell seeded in the tissue culture plate and grown in medium until the test point and lysate using Triton-X just before the testing. Negative control was

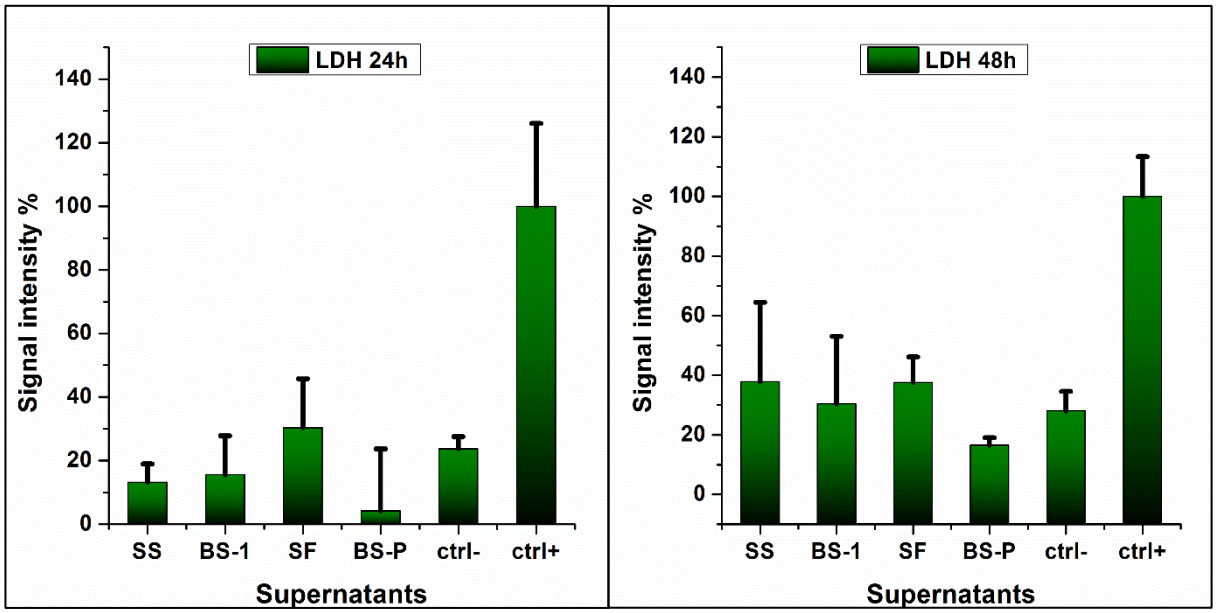


Figure 4-3: LDH Assay test results at 24h (left) and 48h (right). SS - 2% Tethya aurantia spicules + 4% SF, BS1 - 2% bio-inspired SiO2 particles (deposited on) 4% SF, SF - 4% silk fibroin film. BS-P - 2% bio-inspired SiO2 particles, ctrl- - NIH3T3 cells cultured on TCP, ctrl+ - NIH3T3 cells cultured and

just cells grown in TCP in growth medium for decided time point.

It is observed that on both time points 24h and 48h, all the samples have performed significantly better than the positive control. And their performance comparable with the negative control at both times. Also the addition of silica in either form, synthesized (BS1) or natural (SS), doesn't induce the cytotoxic effect when compared with only silk fibroin. Thus, all the samples prove to be safe for cells to grow in their environment.

3.3.2.Metabolic activity and Proliferation Assessment:

Resazurin is used as an oxidation-reduction (REDOX) indicator that undergoes colorimetric change in response to cellular metabolic reduction. The reduced form resorufin is pink and highly fluorescent, and the intensity of fluorescence produced is proportional to the number of living cells respiring. Through detecting the level of oxidation during respiration alamarBlue® acts as a direct indicator to quantitatively measure cell viability and cytotoxicity.The results of Alamar blue are represented by observing the fluorescence intensity measured using the plate reader (Figure 4-4-Right). Metabolic activity of cells is complex process of cell behaviour depending on variety of factors. Both SS (natural) and BS1 (synthetic) silica particle-based films show increased activity than bare silk fibroin on Day 1 and Day 7. The BS1 particle loaded film performs better than bare silk fibroin on Day 3 as well.

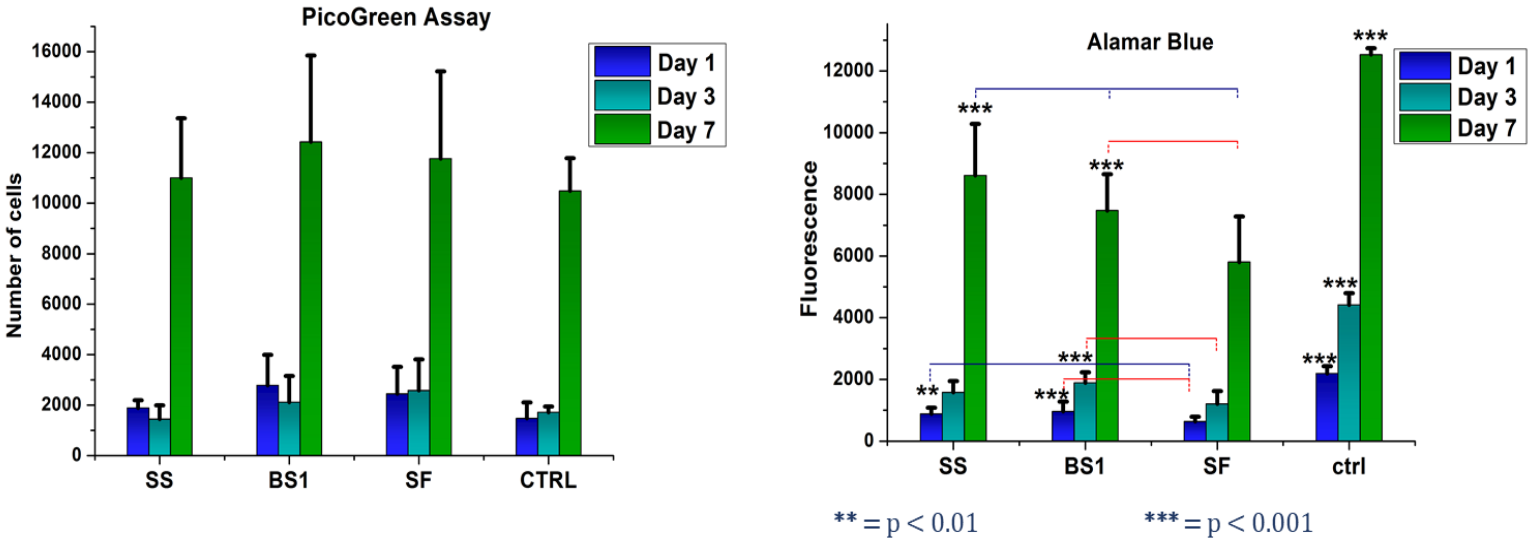


Figure 4-4 (Left) PicoGreen Assay- Number of cells in different groups at different time periods. (Right) Alamar Blue Assay- Fluorescence intensity of different test groups at different time periods. SS - 2% Tethya aurantia spicules + 4% SF, BS1 - 2% bio-inspired SiO2 particles (deposited on) 4% SF, SF - 4% silk fibroin film. BS-P - 2% bio-inspired SiO2 particles, ctrl- - NIH3T3 cells cultured on TCP, ctrl+ - NIH3T3 cells cultured and lysate with Triton. Day 1 (Dark Blue), Day 3 (Light Blue), Day 7 ( Green).

Picogreen Assay test helps estimate the proliferation rate or amount of live cells through quantification of dsDNA, which is stained using the PicoGreen reagent. The performance of all the groups is comparable with the control. There is significant increase on Day 7 from Day 3 and Day 1 in each group. This maybe due to good confluence of the cells achieved between day 3 and day 7. Since the number of cells are statistically similar, when used to normalize metabolic activity data for Day7, we can see the silica based groups have higher metabolic activity/cell.

In general from the metabolic activity and proliferation test, it seems the presence of silica sources in fibroin upregulate both mechanisms and in particular metabolic activity

3.3.3.Cell Adhesion and Morphology Assessment:

The cells nuclei and actin filament are stained helping locate and observe the number of cells adhered on the surface as well as its morphology.

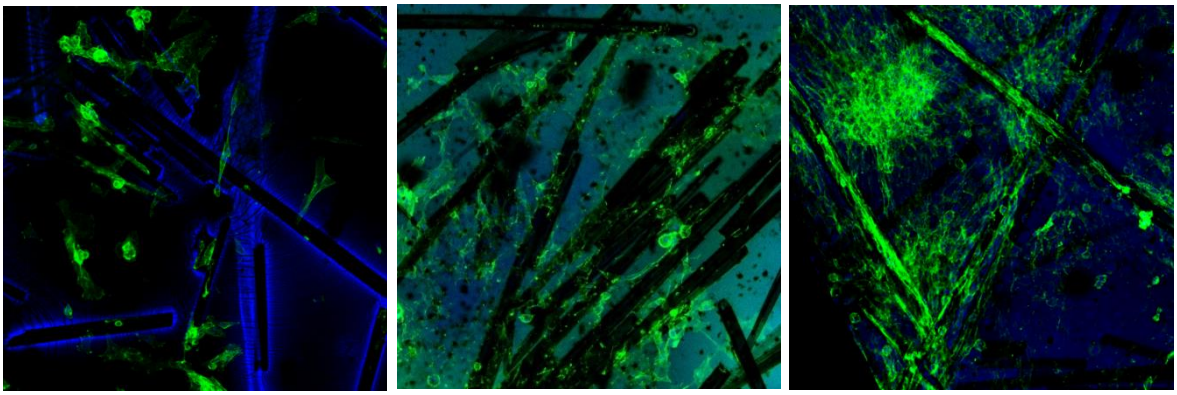

Figure 4-5: Silk fibroin film loaded with Siliceous Spicules. (L-R) Day 1, Day 3 and Day 7. Blue- nuclei , Green-Actin staining.

We can see that cells were able to adhere to the surfaces assuming a

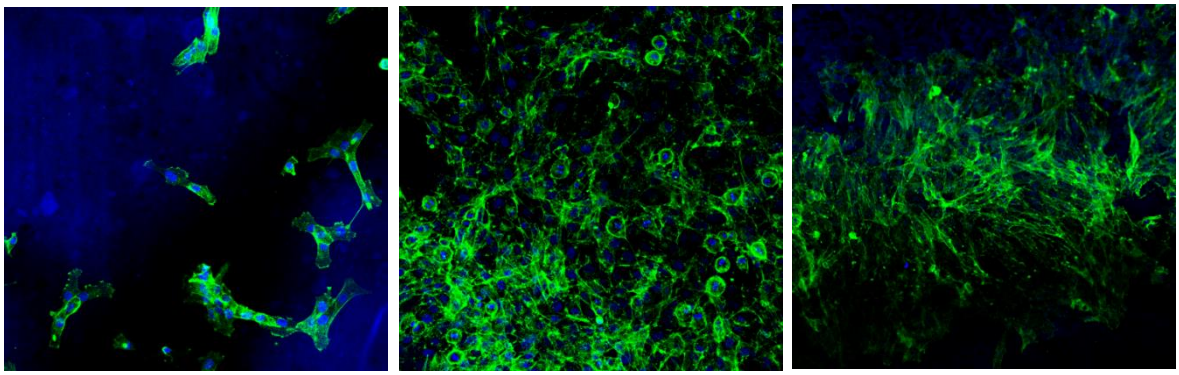

Figure 4-6: Silk fibroin film loaded with Bioinspired SiO2 particles (L-R) Day1, Day 3 and Day 7. Blue- nuclei, Green-Actin staining.

quite high degree of spreading. Also the increasing concentration as the time increases. We can also see that they prefer areas near the spicule, probably indicating preference of the Si ion concentrated region.

We can see that cells prefer to adhere and grow on the BS1 particles incorporated film surface as well, so confirming the impact of silicon ions on cell activity. The blue stained nuclei show the higher number of cells as the time point increases. The green dye shows the morphology of the actin filament, showing the well spread shape of the cells, indicating the cell surface interaction.

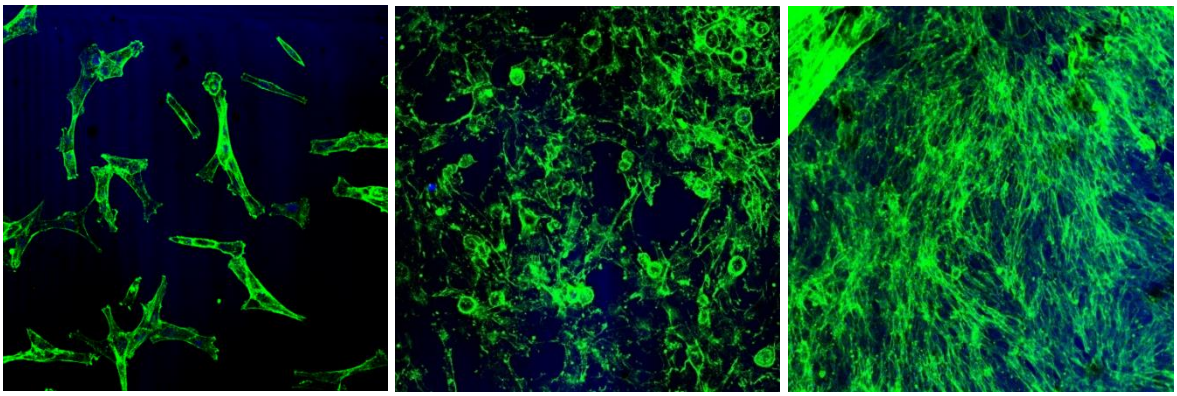

Figure 7:Silk fibroin film used as control against effect of SiO2(L-R) Day 1, Day 3 and Day 7. Blue-nuclei , Green-Actin staining.

Silk Fibroin was used as a system control for comparison of cell growth. We can see that the cells perform as good as fibroin, in the presence of the particles as well. Indicating the comparable performance of the new samples.

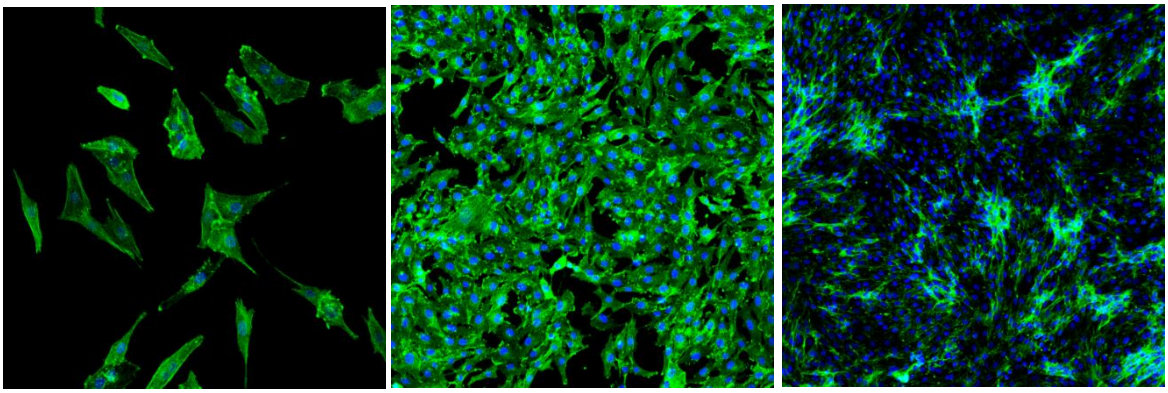

Figure 8: TCP used as control against any fabricated material effects(L-R) Day 1, Day 3 and Day 7. Blue- nuclei , Green-Actin staining.

Tissue culture plate is used as general control system to evaluate cell behaviour when seeded on all samples with different formulations. We can see that the fabricated materials have a comparable performance with TCP, indicating them as possible biocompatible materials, that can be explored further for their specific application.

## 4. Conclusion

Biosilica BS1 particles created by using imidazole and glucose to replace the natural enzymes, being structurally similar molecules, and TEOS as precursor were tested for their bioactivity. The activity of these particles was compared with the naturally created Siliceous spicules obtained from Tethya aurantia. Extensively studied silk fibroin is used as platform to embed these particles and study them for cellular activities like adhesion and morphology besides proliferation and metabolic activity. The studies showed that they are not just non-cytotoxic but also release $Si^{+}$ ions and improve the cellular adhesion and growth. Also normalized metabolic activity shows the Si based groups have

higher metabolic activity/ cell, inferring the cells to be at healthier levels than in bare silk fibroin test group. The performance of biosilica BS1 particles is equivalent to the natural siliceous spicules. In conclusion, we are reporting for the first time the silica particles created by the “nature as a model “method without the use of silicateins to be safe as well as bioactive in the vitro model considered, thus replacing the need to harvest the ecology for the benefits of natural material.

References:


1. Rahman IA, Padavettan V. Synthesis of Silica Nanoparticles by Sol-Gel: Size-Dependent Properties, Surface Modification, and Applications in Silica-Polymer Nanocomposites—A Review. *J Nanomater*. 2012;2012:1-15. doi:10.1155/2012/132424.

2. Wong Po Foo C, Patwardhan S V., Belton DJ, et al. Novel nanocomposites from spider silk-silica fusion (chimeric) proteins. *Proc Natl Acad Sci*. 2006;103(25):9428-9433. doi:10.1073/pnas.0601096103.

3. World Markets for Precipitated Silica 2006. 2006. http://www.notchconsulting.com/pdf/Silica_Contents06.pdf. Accessed August 27, 2017.

4. Tacke. Milestones in the Biochemistry of Silicon: From Basic Research to Biotechnological Applications. *Angew Chem Int Ed Engl*. 1999;38(20):3015-3018. http://www.ncbi.nlm.nih.gov/pubmed/10540406. Accessed August 27, 2017.

5. Tréguer P, Nelson DM, Bennekom AJ Van, et al. The Silica Balance in the World Ocean: A Reestimate. *Source Sci*. 1995;268(21):375-379. http://www.jstor.org/stable/2886587. Accessed August 27, 2017.

6. Belton DJ, Deschaume O, Perry CC. An overview of the fundamentals of the chemistry of silica with relevance to biosilicification and technological advances. *FEBS J*. 2012;279(10):1710-1720. doi:10.1111/j.1742-4658.2012.08531.x.

7. Schloßmacher U, Wiens M, Schröder HC, Wang X, Jochum KP, Müller WEG. Silintaphin-1 - interaction with silicatein during structure-guiding bio-silica formation. *FEBS J*. 2011;278(7):1145-1155. doi:10.1111/j.1742-4658.2011.08040.x.

8. Patwardhan S V., Lee KB, Kim DJ, et al. Biomimetic and bioinspired silica: recent developments and applications. *Chem Commun*. 2011;47(27):7567. doi:10.1039/c0cc05648k.

9. Wang X, Schröder HC, Müller WEG. Enzyme-based biosilica and biocalcite: Biomaterials for the future in regenerative medicine. *Trends Biotechnol*. 2014;32(9):441-447. doi:10.1016/j.tibtech.2014.05.004.

10. Weaver JC, Pietrasanta LI, Hedin N, Chmelka BF, Hansma PK, Morse DE. Nanostructural features of demosponge biosilica. *J Struct Biol*. 2003;144(3):271-281. doi:10.1016/j.jsb.2003.09.031.

11. Polini A, Pagliara S, Camposeo A, et al. Optical properties of in-vitro biomineralised silica. *Sci Rep*. 2012;2:0-5. doi:10.1038/srep00607.

12. Imsiecke G, Steffen R, Custodio M, Borojevic R, G MiLLER WE. FORMATION OF SPICULES BY SCLEROCYTES FROM THE FRESHWATER SPONGE EPHYDATIA MUELLERI IN SHORT-TERM CULTURES IN VITRO. *Vitr Cell Dev Biol--Animal*. 1995;31:528-535. https://link.springer.com/content/pdf/10.1007/BF02634030.pdf. Accessed August 27, 2017.

13. Arakaki A, Shimizu K, Oda M, Sakamoto T, Nishimura T, Kato T. Biomineralization-inspired synthesis of functional organic/inorganic hybrid materials: Organic molecular control of self-organization of hybrids. *Org Biomol Chem*. 2015;13(4):974-989. doi:10.1039/C4OB01796J.

14. Murr MM, Morse DE. Fractal intermediates in the self-assembly of silicatein filaments. http://www.pnas.org/content/102/33/11657.full.pdf. Accessed August 27, 2017.

15. Cha JN, Shimizu K, Zhou Y, et al. Silicatein filaments and subunits from a marine sponge direct the polymerization of silica and silicones in vitro. *Proc Natl Acad Sci U S A*. 1999;96(2):361-365. doi:10.1073/PNAS.96.2.361.

16. Zhou Y, Shimizu K, Cha J, Stucky G. Efficient catalysis of polysiloxane synthesis by silicatein α requires specific hydroxy and imidazole functionalities. *Angew Chemie*. 1999. http://onlinelibrary.wiley.com/doi/10.1002/(SICI)1521-3773(19990315)38:6%3C779::AID-ANIE779%3E3.0.CO;2-%23/full. Accessed August 27, 2017.

17. Arakaki A, Shimizu K, Oda M, Sakamoto T, Nishimura T, Kato T. Biomineralization-inspired synthesis of functional organic/inorganic hybrid materials: organic molecular control of self-organization of hybrids. *Org Biomol Chem*. 2015;13(4):974-989. doi:10.1039/C4OB01796J.

18. Wang X, Schröder HC, Wang K, et al. Genetic, biological and structural hierarchies during sponge spicule formation: from soft sol–gels to solid 3D silica composite structures. *Soft Matter*. 2012;8(37):9501. doi:10.1039/c2sm25889g.

19. Müller WEG, Binder M, von Lintig J, et al. Interaction of the retinoic acid signaling pathway with spicule formation in the marine sponge Suberites domuncula through activation of bone morphogenetic protein-1. *Biochim Biophys Acta - Gen Subj*. 2011;1810(12):1178-1194. doi:10.1016/j.bbagen.2011.09.006.

20. Simpson TL. *The Cell Biology of Sponges*. New York, NY: Springer New York; 1984. doi:10.1007/978-1-4612-5214-6.

21. Müller WEG, Blumbach B, Wagner-Hülsmann C, Lessel U, 淳平林. Galectins in the Phylogenetically Oldest Metazoa, the Sponges (Porifera). *Trends Glycosci Glycotechnol*. 1997;9(45):123-130. doi:10.4052/tigg.9.123.

22. Schütze J, Krasko A, Diehl-Seifert B, Müller WEG. Cloning and expression of the putative aggregation factor from the marine sponge Geodia cydonium. *J Cell Sci*. 2001;114(17). http://jcs.biologists.org/content/114/17/3189.short. Accessed August 28, 2017.

23. Harrison F, Davis D. Morphological and cytochemical patterns during early stages of reduction body formation in Spongilla lacustris (Porifera: Spongillidae). *Trans Am Microsc Soc*. 1982. http://www.jstor.org/stable/3225749. Accessed August 28, 2017.

24. Müller W, Rothenberger M, Boreiko A. Formation of siliceous spicules in the marine demosponge Suberites domuncula. *Cell tissue*. 2005. http://link.springer.com/article/10.1007/s00441-005-1141-5. Accessed August 28, 2017.

25. Schröder HC, Boreiko A, Korzhev M, et al. Co-expression and Functional Interaction of Silicatein with Galectin. *J Biol Chem*. 2006;281(17):12001-12009. doi:10.1074/jbc.M512677200.

26. Müller WEG, Schloßmacher U, Wang X, et al. Poly(silicate)-metabolizing silicatein in siliceous spicules and silicasomes of demosponges comprises dual enzymatic activities (silica polymerase and silica esterase). *FEBS J*. 2008;275(2):362-370. doi:10.1111/j.1742-4658.2007.06206.x.

27. Silicase, an enzyme which degrades biogenous amorphous silica: contribution to the metabolism of silica deposition in the demosponge Suberites domuncula. *Prog Mol Subcell*. 2003. http://link.springer.com/content/pdf/10.1007/978-3-642-55486-5.pdf#page=252. Accessed August 28, 2017.

28. Bernard C. *Introduction à l'étude de La Médecine Expérimentale Par m. Claude Bernard*.; 1865. https://books.google.com/books?hl=en&lr=&id=iBdSKwntgUAC&oi=fnd&pg=PA5&dq=C+bernard+1865+introduction+a+l%27Etude&ots=xW586PKZEE&sig=amCMOH0qSlxoTYVZ4BALTOOGT84. Accessed August 28, 2017.

29. Wang X, Schröder H, Wiens M, Ushijima H. Bio-silica and bio-polyphosphate: applications in biomedicine (bone formation). *Curr Opin*. 2012. http://www.sciencedirect.com/science/article/pii/S095816691200033X. Accessed August 28, 2017.

30. Jugdaohsingh R. Silicon and bone health. *J Nutr Health Aging*. 2007. https://www.ncbi.nlm.nih.gov/pmc/articles/PMC2658806/. Accessed August 28, 2017.

31. Wiens M, Wang X, Schröder H, Kolb U. The role of biosilica in the osteoprotegerin/RANKL ratio in human osteoblast-like cells. *Biomaterials*. 2010.

http://www.sciencedirect.com/science/article/pii/S0142961210008434. Accessed August 28, 2017.

32. Schröder H, Wang X, Wiens M. Silicate modulates the cross-talk between osteoblasts (SaOS-2) and osteoclasts (RAW 264.7 cells): Inhibition of osteoclast growth and differentiation. *J Cell*. 2012. http://onlinelibrary.wiley.com/doi/10.1002/jcb.24196/full. Accessed August 28, 2017.

33. Jo BH, Kim CS, Jo YK, Cheong H, Cha HJ. Recent developments and applications of bioinspired silicification. *Korean J Chem Eng*. 2016;33(4):1125-1133. doi:10.1007/s11814-016-0003-z.

34. Boehm H. The chemistry of silica. Solubility, polymerization, colloid and surface properties, and biochemistry. Von RK Iler. John Wiley and Sons, Chichester 1979. XXIV, 886 S.,. *Angew Chemie*. 1980. http://onlinelibrary.wiley.com/doi/10.1002/ange.19800920433/full. Accessed August 28, 2017.

35. Patwardhan S V, Mukherjee N, Clarson SJ. Effect of process parameters on the polymer mediated synthesis of silica at neutral pH. *Silicon Chem*. 2002;1(1):47-54. doi:10.1023/A:1016026927401.

36. Global Precipitated Silica Market 2017-2021 | Market Research Reports - Industry Analysis Size & Trends - Technavio. Technavio. https://www.technavio.com/report/global-specialty-chemicals-global-precipitated-silica-market-2017-2021. Published 2017. Accessed August 27, 2017.

37. Specialty Silica Market - Global Industry Analysis, Size and Forecast, 2016 to 2026. Future Market Insights. doi:2016-05-24.

38. Odatsu T, Azimaie T, Velten MF, et al. Human periosteum cell osteogenic differentiation enhanced by ionic silicon release from porous amorphous silica fibrous scaffolds. *J Biomed Mater Res - Part A*. 2015;103(8):2797-2806. doi:10.1002/jbm.a.35412.

39. Ilyas A, Lavrik N V., Kim HKW, Aswath PB, Varanasi VG. Enhanced Interfacial Adhesion and Osteogenesis for Rapid “bone-like” Biomineralization by PECVD-Based Silicon Oxynitride Overlays. *ACS Appl Mater Interfaces*. 2015;7(28):15368-15379. doi:10.1021/acsami.5b03319.

40. Cicco SR, Vona D, De Giglio E, et al. Chemically Modified Diatoms Biosilica for Bone Cell Growth with Combined Drug-Delivery and Antioxidant Properties. *Chempluschem*. 2015;80(7):1104-1112. doi:10.1002/cplu.201402398.

41. Le TDH, Bonani W, Speranza G, et al. Processing and characterization of diatom

nanoparticles and microparticles as potential source of silicon for bone tissue engineering. *Mater Sci Eng C*. 2016;59:471-479. doi:10.1016/j.msec.2015.10.040.

42. Likhoshway Y V., Sorokovikova EG, Belykh OI, et al. Visualization of the silicon biomineralization in cyanobacteria, sponges and diatoms. *Biosph Orig Evol*. 2008;(Table 1):219-230. doi:10.1007/978-0-387-68656-1_16.

43. M??ller WEG, Wang X, Cui FZ, et al. Sponge spicules as blueprints for the biofabrication of inorganic-organic composites and biomaterials. *Appl Microbiol Biotechnol*. 2009;83(3):397-413. doi:10.1007/s00253-009-2014-8.

44. Müller WEG, Wang X, Belikov SI, et al. Formation of Siliceous Spicules in Demosponges: Example Suberites domuncula. *Handb Biomin Biol Asp Struct Form*. 2008;1:59-82. doi:10.1002/9783527619443.ch4.

45. Wang S, Wang X, Draenert FG, et al. Bioactive and biodegradable silica biomaterial for bone regeneration. *Bone*. 2014;67:292-304. doi:10.1016/j.bone.2014.07.025.

46. Iler RK. *The Chemistry of Silica : Solubility, Polymerization, Colloid and Surface Properties, and Biochemistry*. Wiley; 1979. https://www.wiley.com/en-us/The+Chemistry+of+Silica%3A+Solubility%2C+Polymerization%2C+Colloid+and+Surface+Properties+and+Biochemistry+of+Silica-p-9780471024040. Accessed May 6, 2018.

47. Healy TW. Stability of Aqueous Silica Sols. In: ; 1994:147-159. doi:10.1021/ba-1994-0234.ch007.

48. Chen* S-L, Peng Dong, Guang-Hua Yang and, Yang J-J. Kinetics of Formation of Monodisperse Colloidal Silica Particles through the Hydrolysis and Condensation of Tetraethylorthosilicate. 1996. doi:10.1021/IE9602217.

49. Coltrain BK, Kelts LW. The Chemistry of Hydrolysis and Condensation of Silica Sol—Gel Precursors. In: ; 1994:403-418. doi:10.1021/ba-1994-0234.ch019.

50. Patwardhan S V., Clarson SJ. Silicification and biosilicification. *Polym Bull*. 2002;48(4-5):367-371. doi:10.1007/s00289-002-0043-x.

51. Brinker CJ, Scherer GW. *Sol-Gel Science : The Physics and Chemistry of Sol-Gel Processing*. Academic Press; 1990.

52. Stöber W, Fink A, Bohn E. Controlled growth of monodisperse silica spheres in the micron size range. *J Colloid Interface Sci*. 1968;26(1):62-69. doi:10.1016/0021-9797(68)90272-5.

53. Kröger N, Deutzmann R, Sumper M. Polycationic peptides from diatom biosilica that direct silica nanosphere formation. *Science*. 1999;286(5442):1129-1132.

http://www.ncbi.nlm.nih.gov/pubmed/10550045. Accessed May 6, 2018.

54. Patwardhan S V, Clarson SJ. Silicifacation and biosilicification Part 6. Poly-L-histidine mediated synthesis of silica at neutral pH. *J Inorg Organomet Polym*. 2003;13(1):49-53. doi:10.1023/A:1022952931063.

55. Cha JN, Stucky GD, Morse DE, Deming TJ. Biomimetic synthesis of ordered silica structures mediated by block copolypeptides. *Nature*. 2000;403(6767):289-292. doi:10.1038/35002038.

56. Tahir MN, Théato P, Müller WEG, et al. Monitoring the formation of biosilica catalysed by histidine-tagged silicatein. *Chem Commun*. 2004;0(24):2848-2849. doi:10.1039/B410283E.

57. Tahir MN, Théato P, Müller WEG, et al. Formation of layered titania and zirconia catalysed by surface-bound silicatein. *Chem Commun*. 2005;0(44):5533. doi:10.1039/b510113a.

58. Tahir MN, Eberhardt M, Therese HA, et al. From Single Molecules to Nanoscopically Structured Functional Materials: Au Nanocrystal Growth on TiO2 Nanowires Controlled by Surface-Bound Silicatein. *Angew Chemie Int Ed*. 2006;45(29):4803-4809. doi:10.1002/anie.200503770.

59. Jan L. Sumerel, Wenjun Yang, David Kisailus, James C. Weaver, Joon Hwan Choi and, Morse* DE. Biocatalytically Templated Synthesis of Titanium Dioxide. 2003. doi:10.1021/CM030254U.

60. Kisailus D, Choi JH, Weaver JC, Yang W, Morse DE. Enzymatic Synthesis and Nanostructural Control of Gallium Oxide at Low Temperature. *Adv Mater*. 2005;17(3):314-318. doi:10.1002/adma.200400815.

61. Gritsenko VA, Kwok RWM, Wong H, Xu JB. Short-range order in non-stoichiometric amorphous silicon oxynitride and silicon-rich nitride. *J Non Cryst Solids*. 2002;297(1):96-101. doi:10.1016/S0022-3093(01)00910-3.

62. Bruggeman DAG, G. DA. Berechnung verschiedener physikalischer Konstanten von heterogenen Substanzen. I. Dielektrizitätskonstanten und Leitfähigkeiten der Mischkörper aus isotropen Substanzen. *Ann Phys*. 1935;416(7):636-664. doi:10.1002/andp.19354160705.

63. Kuiper AET. Deposition and composition of silicon oxynitride films. *J Vac Sci Technol B Microelectron Nanom Struct*. 1983;1(1):62. doi:10.1116/1.582543.

64. Snyder PG, Xiong Y-M, Woollam JA, et al. Graded refractive index silicon oxynitride thin film characterized by spectroscopic ellipsometry. 1992. http://digitalcommons.unl.edu/electricalengineeringfacpub. Accessed May 19, 2018.

65. Varanasi VG, Ilyas A, Velten MF, Shah A, Lanford WA, Aswath PB. Role of Hydrogen and Nitrogen on the Surface Chemical Structure of Bioactive Amorphous Silicon Oxynitride Films. *J Phys Chem B*. 2017;121(38):8991-9005. doi:10.1021/acs.jpcb.7b05885.

66. XANES: Theory - Chemistry LibreTexts. https://chem.libretexts.org/Core/Physical_and_Theoretical_Chemistry/Spectroscopy/X-ray_Spectroscopy/XANES%3A_Theory. Accessed May 5, 2018.

67. Wang S-F, Wang X-H, Gan L, Wiens M, Schröder HC, Müller WEG. Biosilica-glass formation using enzymes from sponges [silicatein]: Basic aspects and application in biomedicine [bone reconstitution material and osteoporosis]. *Front Mater Sci*. 2011;5(3):266-281. doi:10.1007/s11706-011-0145-1.

68. Kim S. *Marine Biomaterials Characterization, Isolation and Applications.* CRC Pr I Llc; 2017.

69. Silva TH, Alves A, Ferreira BM, et al. Materials of marine origin: a review on polymers and ceramics of biomedical interest. *Int Mater Rev*. 2012;57(5):276-306. doi:10.1179/1743280412Y.0000000002.

70. Sowjanya JA, Singh J, Mohita T, et al. Biocomposite scaffolds containing chitosan/alginate/nano-silica for bone tissue engineering. *Colloids Surfaces B Biointerfaces*. 2013;109:294-300. doi:10.1016/j.colsurfb.2013.04.006.

71. Ravichandran R, Sundaramurthi D, Gandhi S, Sethuraman S, Krishnan UM. Bioinspired hybrid mesoporous silica–gelatin sandwich construct for bone tissue engineering. *Microporous Mesoporous Mater*. 2014;187:53-62. doi:10.1016/J.MICROMESO.2013.12.018.

72. Wang X, Schröder HC, Grebenjuk V, et al. The marine sponge-derived inorganic polymers, biosilica and polyphosphate, as morphogenetically active matrices/scaffolds for the differentiation of human multipotent stromal cells: potential application in 3D printing and distraction osteogenesis. *Mar Drugs*. 2014;12(2):1131-1147. doi:10.3390/md12021131.

73. Wang X, Schröder HC, Wiens M, Ushijima H, Müller WE. Bio-silica and bio-polyphosphate: applications in biomedicine (bone formation). *Curr Opin Biotechnol*. 2012;23(4):570-578. doi:10.1016/j.copbio.2012.01.018.

74. Patwardhan S V, Mukherjee N, Steinitz-Kannan M, Clarson SJ. Bioinspired synthesis of new silica structures. doi:10.1039/b302056h.

75. Le TDH, Liaudanskaya V, Bonani W, Migliaresi C, Motta A. Enhancing bioactive properties of silk fibroin with diatom particles for bone tissue engineering applications. *J Tissue Eng Regen Med*. 2018;12(1):89-97. doi:10.1002/term.2373.

76. Rezwan K, Chen QZ, Blaker JJ, Boccaccini AR. Biodegradable and bioactive porous polymer/inorganic composite scaffolds for bone tissue engineering. *Biomaterials*. 2006;27:3413-3431. doi:10.1016/j.biomaterials.2006.01.039.

77. Wu X, Liu Y, Li X, et al. Preparation of aligned porous gelatin scaffolds by unidirectional freeze-drying method. *Acta Biomater*. 2010;6(3):1167-1177. doi:10.1016/j.actbio.2009.08.041.

78. Liu C, Xia Z, Czernuszka JT. Design and Development of Three-Dimensional Scaffolds for Tissue Engineering. *Chem Eng Res Des*. 2007;85(7):1051-1064. doi:10.1205/cherd06196.

79. Holzwarth JM, Ma PX. Biomimetic nanofibrous scaffolds for bone tissue engineering. *Biomaterials*. 2011;32(36):9622-9629. doi:10.1016/j.biomaterials.2011.09.009.

80. Guarino V, Causa F, Ambrosio L. Bioactive scaffolds for bone and ligament tissue. *Expert Rev Med Devices*. 2007;4(3):405-418. doi:10.1586/17434440.4.3.405.

81. Descamps M, Richart O, Hardouin P, Hornez JC, Leriche A. Synthesis of macroporous β-tricalcium phosphate with controlled porous architectural. *Ceram Int*. 2008;34(5):1131-1137. doi:10.1016/j.ceramint.2007.01.004.

82. Ko E, Cho S-W. Biomimetic Polymer Scaffolds to Promote Stem Cell-Mediated Osteogenesis. *Int J Stem Cells*. 2013;6(2):87-91. doi:10.15283/ijsc.2013.6.2.87.

83. Mieszawska AJ, Llamas JG, Vaiana CA, Kadakia MP, Naik RR, Kaplan DL. Clay enriched silk biomaterials for bone formation. *Acta Biomater*. 2011;7(8):3036-3041. doi:10.1016/j.actbio.2011.04.016.

84. Ilyas A, Odatsu T, Shah A, et al. Amorphous Silica: A New Antioxidant Role for Rapid Critical-Sized Bone Defect Healing. *Adv Healthc Mater*. 2016;5(17):2199-2213. doi:10.1002/adhm.201600203.

# Chapter 5. Synthesis of 3D scaffolds as potential platforms to test biosilica bioactivity and its dissolution activity in in-vitro conditions.

Authors: A. Shah, A. Motta, P. B Aswath, V. Varanasi.

## Abstract

Many studies have been recently pursued to show the potential of natural biosilica in biomedical applications like bone tissue engineering. These have been divided in two areas, understanding the silicification process in the natural sources to recreate similar material. Using the natural material like sponges and diatoms directly to explore its potentials as biomaterial scaffolds. In this study we have fabricated silk fibroin and b-TCP based scaffolds incorporated with Biosilica BS1 (previously generated by group). These were also compared with the incorporation effects of the natural material, Tethya aurantia spicules. The scaffold were studied for their morphological properties required in tissue engineering applications via scanning electron microscopy, edx, ftir and porosity measurements. The scaffold were also studied for $Si^{4+}$ ions' dissolution kinetics to establish effects of different parameters like bonding nature, particle size and surface interactions and enable fine tuning of scaffold design in future studies for SOD1 enhancement via $Si^{4+}$ ions. Successful generation of biosilica incorporated scaffolds led to establishment of their potential as test platforms for complex in-vitro studies on biosilica.

Key words: Biosilica, silicon donor, bone tissue engineering, dissolution kinetics

## 1. Introduction

Bone tissue engineering involves using methods from materials engineering and from life sciences to create artificial constructs for the regeneration of new bone. One approach is to implant scaffolds for bone re-growth directly in vivo with the purpose of stimulating and directing bone formation. The advantage of this approach is the reduced number of operations needed which results in a shorter recovery time for the patient, compared to treatment with autograft.[76]

Tissue engineering is one of the important methods of constructing biological tissues or devices for reconstruction and repair of the organ structures in order to maintain and improve their function.[77] The production of scaffolds, which are used for framework and initial support for the cells to attach, proliferate and differentiate, and form an extracellular matrix, is one area of tissue engineering.[78] The aim of a scaffold is to provide a three-dimensional (3D) platform onto which cells can attach, proliferate, and differentiate. In particular, scaffolds for bone regeneration are designed as nanofibrous structure mimicking the natural 3D bone architecture. The engineered nanofibrous scaffolds have highly porous properties allowing ingrowth of cells, efficient transport of nutrients, oxygen, growth factors and also wastes, which facilitate bone cells to grow, differentiate, and eventually mineralize hydroxyapatite.[79] Morphogenetically active inorganic silica has been applied as a suitable material to scaffold fabrication of bone replacement. [33]

Besides the facilitation for cellular pathway, the 3D scaffolds also require appropriated properties that are able to maintain their structure for predictable times, even under load-bearing conditions.[80] The bioceramic scaffold is commonly used as a replacement of hard tissue through the 3D scaffold. The hydroxyapatite [HA], $Ca_{10}(PO_4)_6(OH)_2$, and β-tricalcium phosphate [β-TCP], $Ca_3(PO_4)_2$, are well-known bioceramics which are biocompatible and bioactive. These materials exhibit a close resemblance in chemical composition to the human bone, a high biocompatibility with the surrounding living tissue, and high osteoconduction characteristics.[81]

Among biological polymers, silk fibroin (SF) has been known for its excellent biocompatibility and controllable biodegradability, tunability of mechanical properties and shape/architecture, as sponge, fibre, thin film or injectable gel.[75] Loading SF with proper supplements or growth factors that support osteogenesis can significantly improve its osteoinductive properties. [82,83]

Amorphous silicon oxynitride (Si(ON)x) PECVD coatings study have been pursued to show that release of $Si^{4+}$ ions leads to enhanced osteogenesis.[84] It is theorized that in the event of traumatic fractures, structurally unstable sites are formed due to severe bone loss. These lead to high yield of reactive oxygen species (ROS) causing oxidative stress. This affects the osteoblast differentiation leading to longer healing times. Stimulations of antioxidants like superoxide dismutase (SOD1), can lead to reduction of ROS as well as stimulate osteogenesis and strengthen the collagen and mineral formations. The study showed that release of $Si^{4+}$ ions from the amorphous

silicon oxynitride films led to increase in SOD1 enabling rapid osteogenesis. The release of the $Si^{4+}$ ions was partially dependent on the chemistry of SiON varying with O/N ratio. Sustained release of the $Si^{4+}$ ions in the physiological environment is required to have continuous SOD1 enhancement. [84]

In this study, the goal was to incorporate the biosilica particles generated by the group previously, into the well-established 3D scaffold systems of silk fibroin and b-TCP with minimalistic fabrication changes. These scaffolds were studied for their architecture and surface morphology, besides the required porous properties of tissue engineered scaffolds. Successful generation of these scaffold will enable them to be potentially used as test platforms for complex in-vitro studies of cells in 3D environment. These scaffolds are also used as platform to study the effect of various parameters like bonding effect, particle size and surface area interaction on $Si^{4+}$ ions' dissolution kinetics.

## 2. Materials

Biosilica particles are prepared using the imidazole-glucose-TEOS reaction method described in chapter 3. The particles are thoroughly washed with ethanol and rinsed thrice with DI water at the end of reaction to remove any unbound imidazole or glucose particles. The particles are left to dry overnight. The agglomerate size range was in 200nm and he actual particles were in size of 30-50nm as observed using Scanning Electron Microscopy.

Siliceous spicules obtained from Tethya aurantia sponge are cleaned in distilled water and allowed to dry overnight in chemical hood. These spicules are

about 15-20 micron in diameter and 800-1000 micron in length and shaped like rods as observed in SEM.

Silk Fibroin (SF) was isolated from Bombyx mori silkworm cocoons (Co-operative Sociolario, Como, Italy).

Beta-tri calcium phosphate is obtained from Sigma Aldrich.

3. Scaffold Preparation:

3D scaffold studies would provide for a wider range of cell tests to be run. Following design table is used for the further tests:

Table 5-1: Sample codes for scaffold studies

| CODE | TYPE |
|---|---|
| FBS6 | 10 wt% $SiO_2$ particles (deposited on) salt leached silk fibroin |
| bBS-1 | 10 wt% bio-inspired $SiO_2$ particles (mixed with) beta TCP |
| bSS | 10 wt% silecous spicules (mixed with) beta-TCP |

*3.1. Scaffold fabrication*

3.1.1.Fibroin formation:

Silk cocoons were treated twice in alkaline water baths at 98C for 1.5hours with 1.1g/l and 0.4g/l $Na_2CO_3$, respectively. Degummed silk was the washed several times in de-ionized (DI) water and dried at room temperature (RT). Fibroin was then dissolved in 9.3M LiBr solution (2g of fibroin in 10ml of LiBr solution) at 65C for 4h. The solution was dialyzed against DI water for 3 days at RT in Slide A Lyzer dialysis cassette (3.5K MWCO, pierce, Rockford, IL, USA) to remove LiBr salt. This dissolved solution is let to dialyse in bd.$H_20$ for 3 days with minimum 3 water changes per day. The fibroin concentration was measured by absorbance spectroscopy using a Nanodrop$^{TM}$ sppectrophotometre

(Thermo Fisher Scientific, Wilmington , DE, USA) which is around 6% and the pH is around 6.0. It is further dialysed against 25 wt% PEG solution to concentrate to 8%. Before any further use, silk fibroin solution was filtered using a ceramic filter(porosity <5micron) to eliminate impurities.

The Fibroin is freshly used to form the scaffold since stored fibroin can start forming gel if left at room temperature. Salt leaching method is used to form the scaffold. NaCl particle size of 400-800 micron is used as porogen. The solution is poured over salt bed in 60mm petri dish and left overnight to form the scaffold. The salt is dissolved in DI water bath over the period of next 24h, after which the scaffolds are washed and ready for use.

Imidazole (50% of dry weight of scaffold) is deposited onto the scaffold via ethanol solution. Once the ethanol is evaporated, TEOS in molar ratio 1: 1.475 to imidazole is added onto the scaffold and water in 8:1 mole ratio to TEOS is added to complete the hydrolysis reaction. This scaffold is left for about 2 hrs in covered condition for the reaction to complete, after which it is left in open condition overnight to let the by-product ethanol evaporate out. Upon complete drying the weight of the scaffold is measured again and hence the weight of formed SiO2 particles is found. For further testing, they are cut to 3mm x 10mm height by diameter cylinders.

3.1.2.Beta-TCP scaffold Formation:

The cement was produced by the mixture β –TCP, 10 wt% silica particles (BS1/SS) and mixing with 2wt% gelatin(Sigma Aldrich, USA). Setting experiments of the liquid phase were also prepared by using deionized water.

Samples were prepared by mixing the powder with the required liquid volume with P/L=1/0.35 with a mortar and pestle for 2-3 minutes and shape and quench with Teflon moulds for 10mm diameter x 3 mm height. For uniform distribution of the Biosilica BS1 particles, the required quantity was taken in L phase calculated amount of 2wt% gelatin solution, sonicated for 4hrs to break down and thoroughly mix in the solution before being mixed with β -TCP. After setting for 30 minutes the cylinder sample will be removed from the moulds and left to dry. After drying overnight at room temperature, the samples were sintered at 700C for 1h with Thermolyne 6000 Muffle Furnace and cooled down over a period of another 24 hr.

*3.2. Scaffold Characterisation*

Field Emission Scanning Electron Microscopy was used to observe the surface morphology of the scaffolds created. The images were taken to look at microstructure of the scaffold surface to observe the particle distribution. Cross sections of the scaffold were observed to look at the particle distribution on z axis besides the radial distribution observed in the top. SEM images were also used to look at different pore size obtained in different scaffolds.

Energy Dispersive X-Ray spectroscopy and Mapping is performed to look at the uniformity in elemental distribution hence the compositional distribution within the scaffolds.

Fourier Transform InfraRed spectroscopy was analysed to look at the scaffolds and understand their chemical structure.

Water Contact Angle measurements were done using the sessile drop method to observe the hydrophilicity of the surfaces and any effect on the surface due to addition of Silica particles. 3 drops per scaffold were studied to take the measurement on the goniometer machine.

Porosity of the sponges were determined using ethanol displacement method. The dry weight of the scaffold was measured and noted as Ws. Weight of ethanol taken in the beaker at known volume is measured (W1). The scaffold is submerged in the ethanol and left for 30 seconds to completely get wet and the weight of scaffold plus ethanol mixture is measured. (W2). The sponge is removed and the weight of the remaining ethanol is measured (W3).

Pore volume of the scaffold is calculated as: $Vp = (W2 - W3 - Ws)/ \rho_{ethanol}$

Scaffold volume is calculated as: $Vs = (W1 - W2 + W3)/ \rho_{ethanol}$

Porosity $\Sigma = Vp / (Vp + Vs)$

*3.3. Dissolution study*

ICP-OES analysis is capable of detecting concentrations and changes in the concentrations of analyte elements on the order of parts per billion and is well known for its ability to quantify individual analyte elements in complex matrices with minimal interferences. Thus, it is a technique useful for both rapid dissolution and longer dissolution kinetic studies in a relatively complex environment meant to simulate a biological system of even greater complexity. ICP-OES analysis was performed at the Shimadzu Center for Advanced Analytical Chemistry using the Shimadzu ICPE-9000 ICP-OES system. Silicon concentration measurements were taken from the αMEM dissolution media in order to evaluate the surface

degradation kinetics of the scaffolds and the dissolution of Si ions out of scaffold and into the media. Single-element high purity ICP standards (1000 µg/L) were purchased from Ultra Scientific.

10mm Φ x 3mm height scaffold cylinders were placed in 3 mL of α-MEM at 37˚C for 0, 24, 48, 72, and 168 hours. After soaking, 25x, 50x and 100x dilutions were used to investigate salt content in the supernatant fluid.

## 4. Results and Discussion

The SiO2 formation on Fibroin scaffold was found to be at 55 wt% of the total scaffold ($SiO_2$: Fib = 1.22) (further labelled FBS6_10) and when the initial imidazole concentration was increased to 75 wt% of the dry scaffold, the $SiO_2$ formation was 60% of the total scaffold ( $SiO_2$ : Fib = 1.51)( further labelled FBS6_15).

### *4.1. SEM Results:*

The microstructure and the architecture of the composite silk fibroin scaffold/ BS6 , bTCP/BS1 and bTCP/BSS are seen in Figure 5-1 and Figure 5-2. We also have images for comparative study of FBS6_15, when the fibroin scaffold was created using imidazole as 75 wt% of fibroin instead of 50 wt% to look at effect of higher silica loading on microstructure.

It is seen that the basic architecture of Fibroin scaffolds at 20x magnifications remains the same for both FBS6_10 and FBS6_15. It is a porous structure with large, randomly distributed pores interconnected with micropores with no appreciable difference. Higher magnification imaging of the surface

reveals that the microstructure of the smooth fibroin film is converted to microsphere coated uniform surface. The size of these microspheres are significantly different in lower imidazole content as compared to higher. They are in the range of 50nm for the FBS6_10 whereas the FBS6_15 have microspheres in the range of 400-600nm. The surfaces are completely covered in these microsphere and their size distribution is highly narrow.

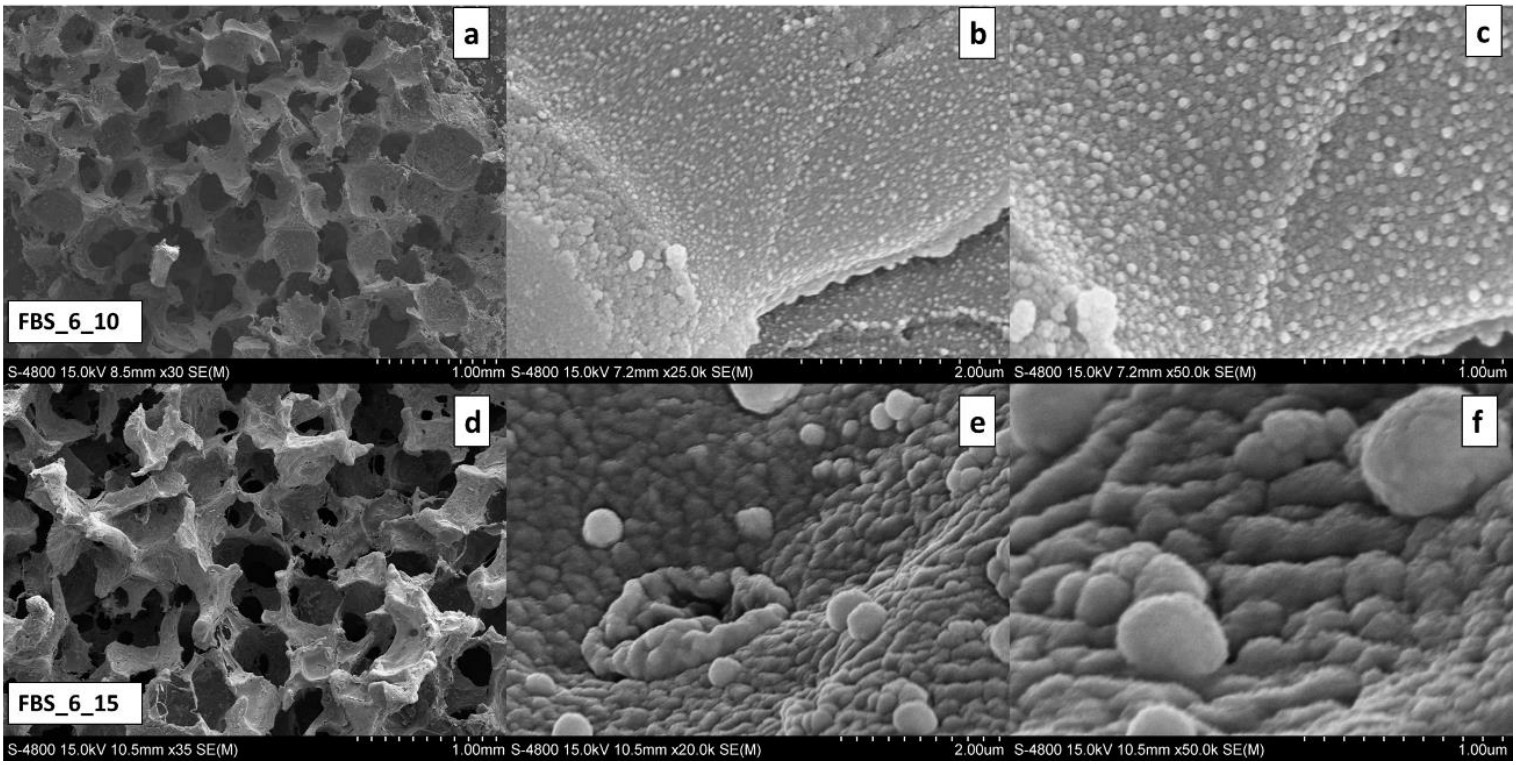


Figure 5-1: (a-c) FBS6_10: Biosilica particles generated by depositing 50 wt% imidazole on SF. (d-f) FBS6_15: Biosilica particles generated by depositing 75 wt% imidazole on SF.

The basic architecture of bTCP based scaffolds is very different than the Fibroin scaffolds. (

Figure 5-3) The randomly dispersed large pores are missing and the surface seems to have natural porosity achieved after moulding. The higher magnification images show the micron sized b-TCP particles being covered with nano BS1 particles. The distribution looks very uniform. In the bTCP-BSS scaffolds on the other hand due to macro size of the spicules, the distribution at micron level is more of concentrated type. Although in the architecture of the scaffold the spicules are seen to be uniformly distributed. (data not shown).

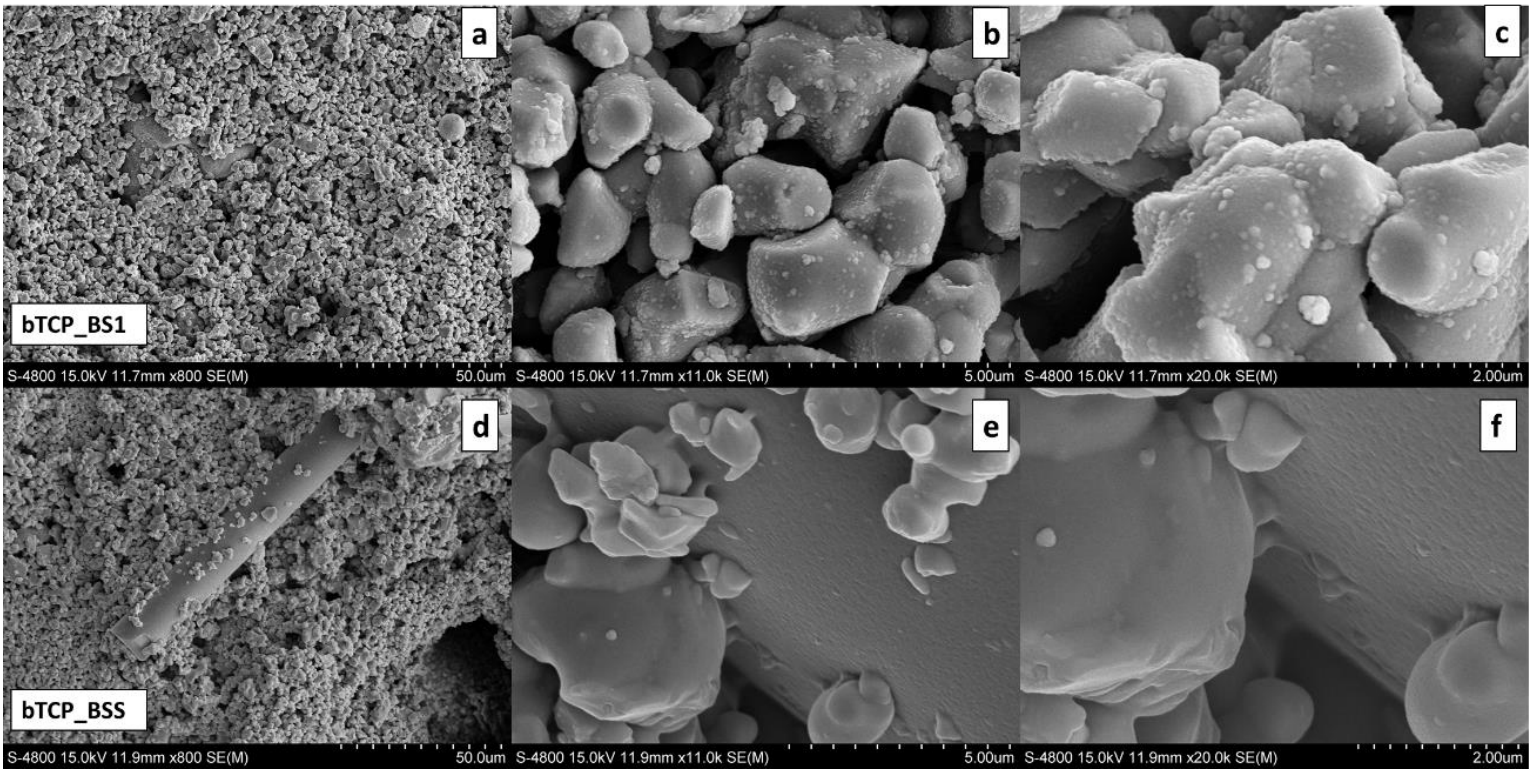


Figure 5-2: (a-c) bTCP_BS1: BTCP scaffolds incorporated with 10 w% Biosilica BS1. (d-f) bTCP_BSS: bTCP scaffold incorporated with 10 wt% SS particles.

*4.2. EDX Results*

To study the spread of silicon formation, the EDX maps are obtained for the FBS6_10 at the top as well as cross section regions. (

Figure 5-3) It is seen that silicon is very well spread throughout the surface of the fibroin. It can be seen from the complimentary data observed in the SE image of the scaffold. Also it can be seen in the cross section the that silicon formation has occurred uniformly showing no preference towards top or bottom , indicating that the imidazole distribution via ethanol had worked effectively.

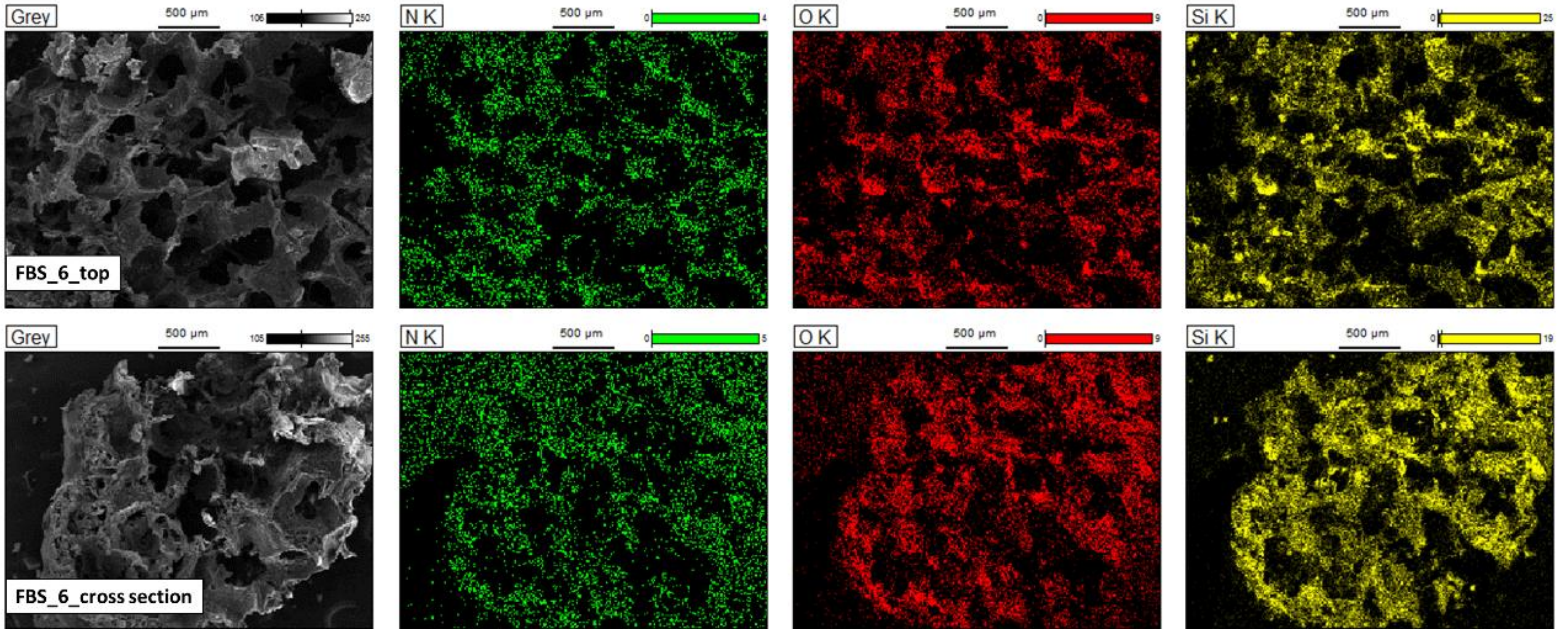


Figure 5-3: EDX maps (top) FBS6_top surface, (bottom) FBS6_cross section surface, N K (green), O K (red), Si K (yellow)

In the bTCP BS1 and bTCP BSS scaffolds the Si distribution is seen to correspond the particle distribution. (

Figure 5-4) Indicating no change occurs in the b-TCP original formulation due to mixing of the particles and that it acts merely as a platform to carry the particles. The presence of Si is also confirmed by the complimentary distribution of Ca and P elements in the maps. The weak signal intensities of Ca and P in the regions of Si presence in the bTCP-BS1 scaffold indicates that the Si particles are acting as a coating or covering for these particles. This may have occurred due to their addition via gelatin over direct mixing of the powders.

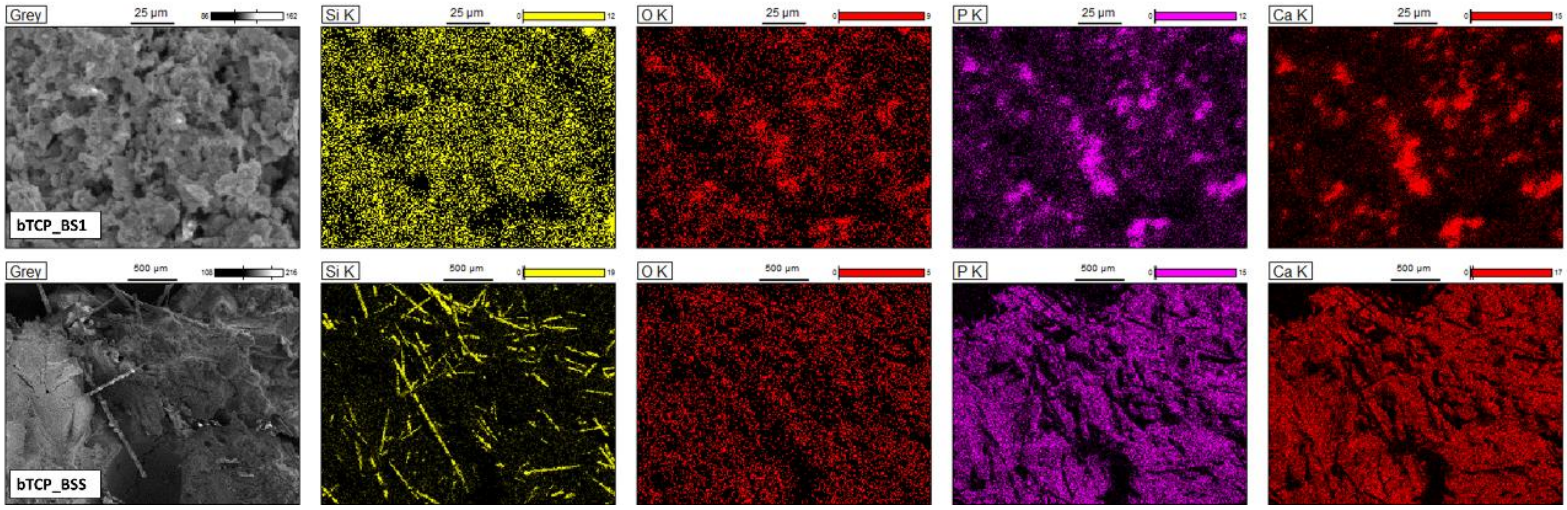


Figure 5-4: EDX maps (top) bTCP_BS1, (bottom) bTCP_BSS, Si K (yellow), O K (red), P K (purple), Ca K (red)

*4.3. FTIR*

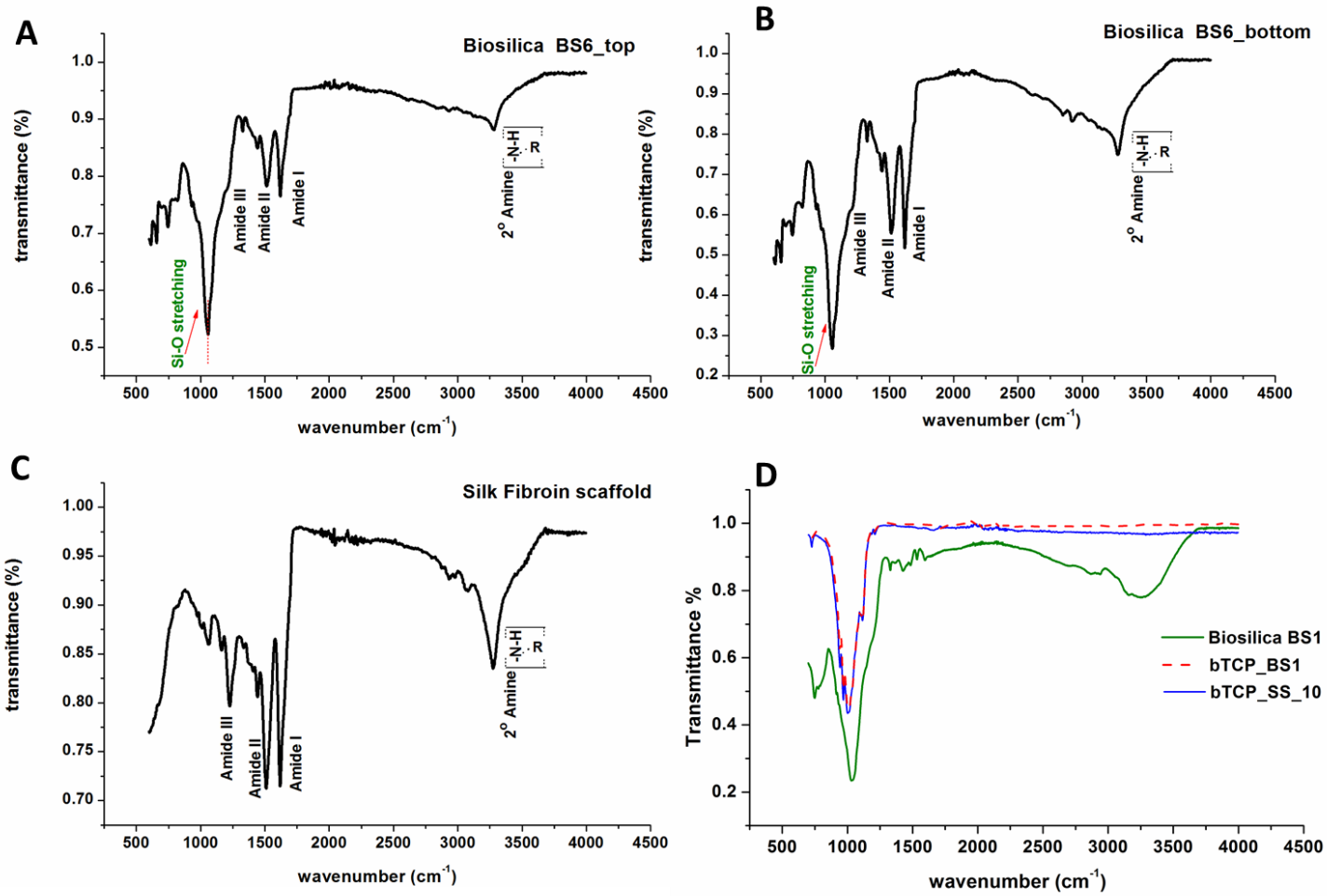


Figure 5-5: (A) FBS6_top (B) FBS6_bottom FTIR spectrums. (C): pure SF FTIR spectrum. (D) FTIR spectrums Biosilica BS1 (green), bTCP_BS1 (red dashed), bTCP_BSS (blue)

In the Figure 5-5 we observe the FTIR spectrums for FBS6 compared to bare silk fibroin, bTCP-BS1 and bTCP-BSS compared to biosilica BS1.

The protein secondary confirmation and the effect of the silica particle addition on the samples conformation were evaluated by the infrared spectroscopy as seen in Figure 4-2_a. Pure fibroin scaffold as well as composite scaffolds show adsorption bands around 1622 $cm^{-1}$ (amide I), 1518 $cm^{-1}$ (amide II), 1260 $cm^{-1}$ (amide III), and the shoulder at 1265 $cm^{-1}$ confirmed β- sheet as main secondary conformation. Shoulder at 1690 $cm^{-1}$ suggests that this β form is of the anti-parallel type. The addition of the particles did not cause structural conformation modifications to SF. The feature peak related to Si-O stretching around 1030 $cm^{-1}$ is observed in the films at different intensities probably due to inhomogeneity in dispersion pattern at submicron levels, due to the size difference of siliceous spicules compared with particles.

In the bTCP-BS1, and bTCP-SS FTIR analysis we see the peaks conform with the BS1 peaks with additional spikes in the main peaks. These arise from the phosphate peaks in the b-TCP that share a very close frequency with the Si-O stretching bond. Thus the peak observed is a convolution of the two intensity signals.

The analysis conforms the addition of silica particles without any changes to conformation of the base material thus establishing their potential use as inert platforms for the assessing the behaviour of the biosilica particles. It also suggests that the properties of the individual material is maintained and thus still enable us to exact their advantages as scaffold material. The addition of biosilica will give additive beneficial effects.

Water contact angle measurements were done using the sessile drop technique. All the groups were highly hydrophilic to be able to form stable drop and measure the difference in between the groups. Nevertheless, the high hydrophilicity is appreciated property for bioactivity of the scaffolds, thus ensuring their potential in the application.

*4.4. Pore Size*

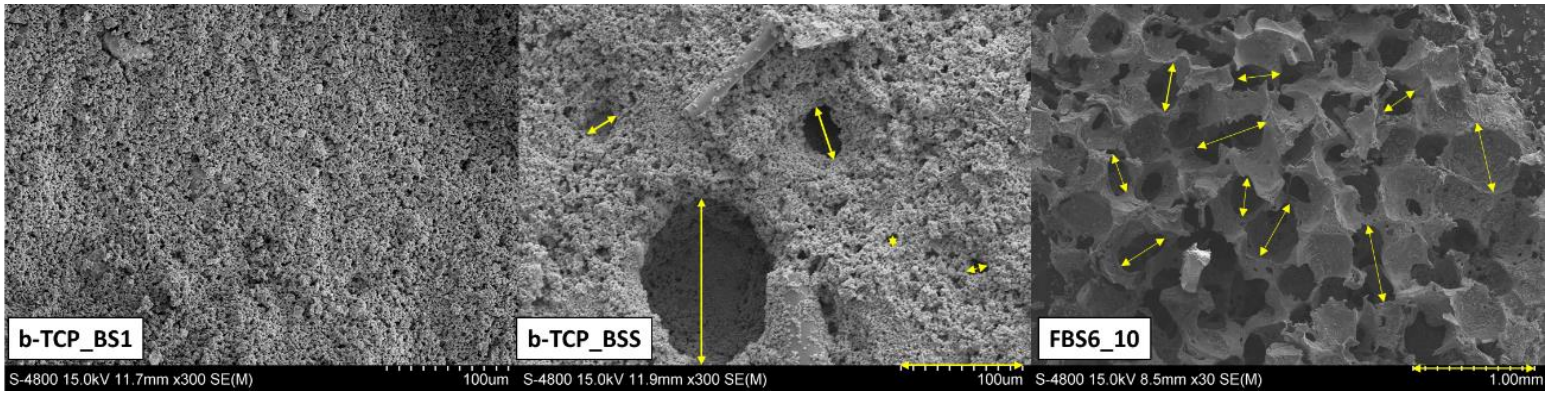


Figure 5-6: SEM images at 300x (l-r) bTCP_BS1, bTCP_SS, at 30x FBS6_10

We can see from

Figure 5-6 that bTCP_BS1 has no macro pores and its porosity is attributed only due to compaction of the slurry occurring from the moulding step. bTCP_BSS on the other hands exhibits macropores as well as micropores which may have occurred due to burning of the binder gelatin during sintering process. The fibroin scaffold on the other hand exhibits macro pores of the average size ranging of 450 microns, which is main contribution from the salt porogen of the same size distribution. Also these pores have more polygonal shape compared

to the very well defined circular shapes observed in bTCP_BSS scaffolds., confirming the higher possibility of the latter forming due to evaporation of liquid.

*4.5. Porosity*

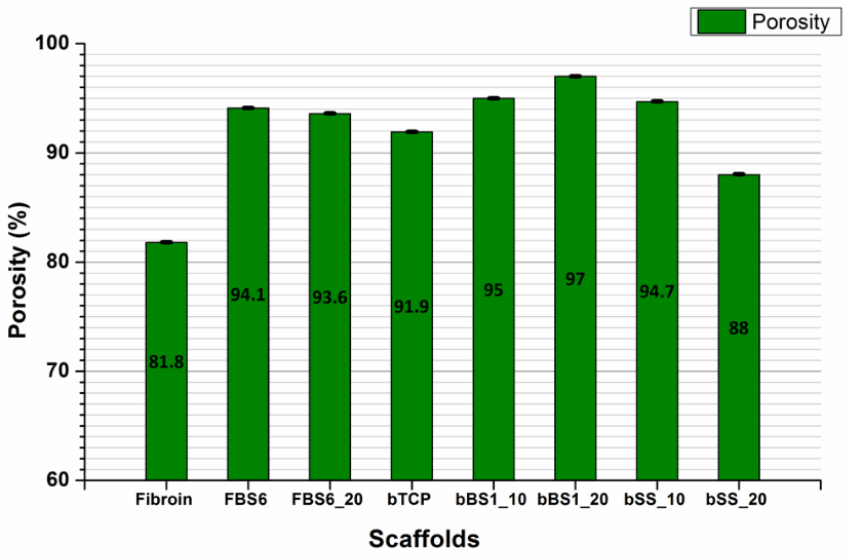


Figure 5-7: Porosity graph

The porosity of the scaffold was measured using ethanol displacement method. (Figure 5-7) The porosity for all the scaffold groups is in range of 91-95%. Except bare fibroin which is at 81% and bSS_20 which is at 88%.

This indicates the creation of biosilica particles on the bare fibroin leads to formation of micro pores, that lead to increasing of the porosity by almost 15%.

*4.6. Dissolution Study*

For enhanced osteogenesis effect sustained release of Si ion is required. Previous study showed partial dependence of Si release kinetics on the chemistry of coating and its thickness. In this study we tested different other parameters on same chemistry that could affect Si release kinetics that could help fine tune the Si ion carrier device designs. These studies were done for Day 1, 2, 3, 5 and 7. The samples were immersed in alpha MEM that contained little to no silica (< 0.01 ppm)

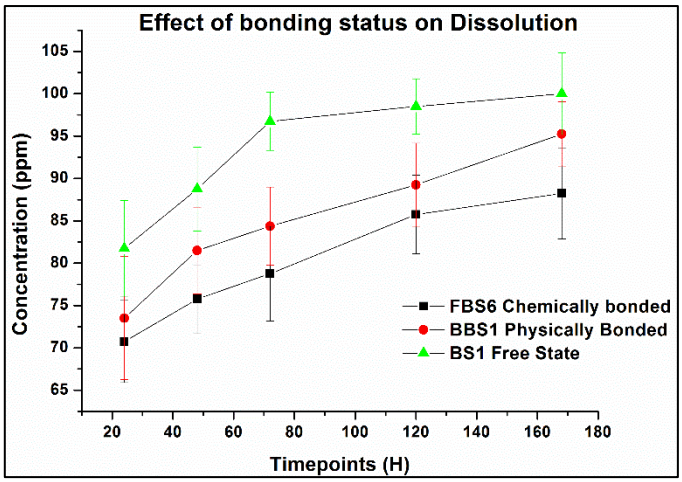


Figure 5-8: Effect of bonding status on dissolution rate

The effect of type of bonding of Si ion carrier on the release kinetics is studied. (Figure 5-8) The chemically bound FBS6 vs just physically captured TCP_BS1 vs just free particles in the solution. The free state particles naturally have the highest initial release. The release is fast and starts slowing down day 3 onwards.

Whereas the bonded particles (either way) have lower but a continuous release mechanism throughout the 7 days with almost a linear build up Day 1 onwards.

Other parameter that could affect the dissolution rate is particle size. With nano sized particles the total surface area interaction increases multiple times as compared to macro particles of the same mass. This can be seen from the Figure 5-9.

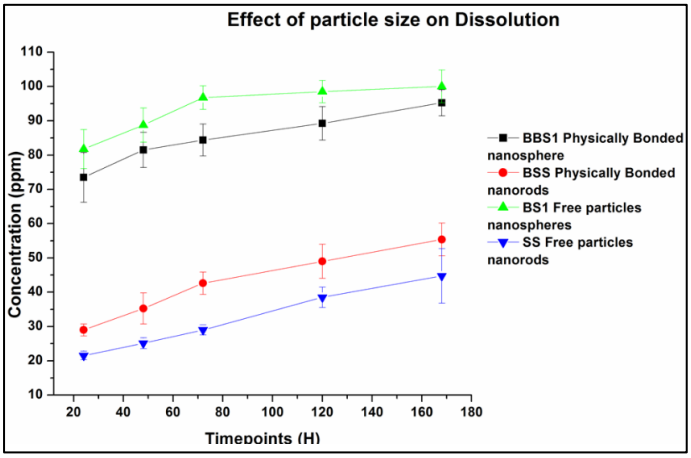


Figure 5-9: Effect of particle size on dissolution rate

Si release rates are higher for the nanoparticles and this can be useful study for drug release applications.

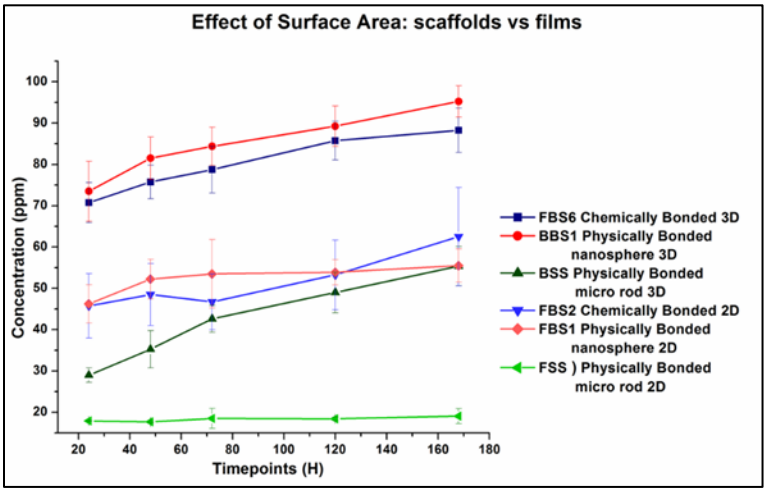


Figure 5-10: Effect of 3d surface vs 2D surface interaction on dissolution rate

Effect of 3D surface interaction vs 2D surface interaction was also seen by studying the dissolution kinetics from scaffolds vs same chemistries from films. It can be seen that the dissolution rate of films is pretty linear and almost flat, with very low release rate per day. (Figure 5-10)

As compared to the scaffolds that have higher release rate. None of the groups have reached theoretical maximum. Even if it is considered that alpha MEM saturation levels have been approached at Day 7 for the scaffolds, the film release is way lesser than that, thus confirming the flat release is effect of 2D vs 3D interaction.

## 5. Conclusion

The Biosilica BS1 particles were successfully incorporated in different model systems of 3D scaffolds with synergistic effects. The fabrication did not require excessively new or different steps and the changes were easily incorporated. Thus, showing the extensive adaptability of the material in various applications. The chemical bonds of the original systems remained unaffected thus their advantages as bioactive material will still be active. This study establishes the potential of these biosilica scaffolds to be studied as bioactive materials and the complex in-vitro activity of cells in 3D environment. The successful loading of the model systems with $SiO_2$ helped generate systems that would allow sustained release of $Si^{4+}$ ions, and thus make them potentially useful for bone healing applications. Effects of the various parameters is studied on the release rate, and depending on the application requirements, this study can be used to fine tune the scaffold design to achieve the similar dissolution kinetics.

References:


1. Rahman IA, Padavettan V. Synthesis of Silica Nanoparticles by Sol-Gel: Size-Dependent Properties, Surface Modification, and Applications in Silica-Polymer Nanocomposites—A Review. *J Nanomater*. 2012;2012:1-15. doi:10.1155/2012/132424.

2. Wong Po Foo C, Patwardhan S V., Belton DJ, et al. Novel nanocomposites from spider silk-silica fusion (chimeric) proteins. *Proc Natl Acad Sci*. 2006;103(25):9428-9433. doi:10.1073/pnas.0601096103.

3. World Markets for Precipitated Silica 2006. 2006. http://www.notchconsulting.com/pdf/Silica_Contents06.pdf. Accessed August 27, 2017.

4. Tacke. Milestones in the Biochemistry of Silicon: From Basic Research to Biotechnological Applications. *Angew Chem Int Ed Engl*. 1999;38(20):3015-3018. http://www.ncbi.nlm.nih.gov/pubmed/10540406. Accessed August 27, 2017.

5. Tréguer P, Nelson DM, Bennekom AJ Van, et al. The Silica Balance in the World Ocean: A Reestimate. *Source Sci*. 1995;268(21):375-379. http://www.jstor.org/stable/2886587. Accessed August 27, 2017.

6. Belton DJ, Deschaume O, Perry CC. An overview of the fundamentals of the chemistry of silica with relevance to biosilicification and technological advances. *FEBS J*. 2012;279(10):1710-1720. doi:10.1111/j.1742-4658.2012.08531.x.

7. Schloßmacher U, Wiens M, Schröder HC, Wang X, Jochum KP, Müller WEG. Silintaphin-1 - interaction with silicatein during structure-guiding bio-silica formation. *FEBS J*. 2011;278(7):1145-1155. doi:10.1111/j.1742-4658.2011.08040.x.

8. Patwardhan S V., Lee KB, Kim DJ, et al. Biomimetic and bioinspired silica: recent developments and applications. *Chem Commun*. 2011;47(27):7567. doi:10.1039/c0cc05648k.

9. Wang X, Schröder HC, Müller WEG. Enzyme-based biosilica and biocalcite: Biomaterials for the future in regenerative medicine. *Trends Biotechnol*. 2014;32(9):441-447. doi:10.1016/j.tibtech.2014.05.004.

10. Weaver JC, Pietrasanta LI, Hedin N, Chmelka BF, Hansma PK, Morse DE. Nanostructural features of demosponge biosilica. *J Struct Biol*. 2003;144(3):271-281. doi:10.1016/j.jsb.2003.09.031.

11. Polini A, Pagliara S, Camposeo A, et al. Optical properties of in-vitro

biomineralised silica. *Sci Rep*. 2012;2:0-5. doi:10.1038/srep00607.

12. Imsiecke G, Steffen R, Custodio M, Borojevic R, G MiLLER WE. FORMATION OF SPICULES BY SCLEROCYTES FROM THE FRESHWATER SPONGE EPHYDATIA MUELLERI IN SHORT-TERM CULTURES IN VITRO. *Vitr Cell Dev Biol--Animal*. 1995;31:528-535. https://link.springer.com/content/pdf/10.1007/BF02634030.pdf. Accessed August 27, 2017.

13. Arakaki A, Shimizu K, Oda M, Sakamoto T, Nishimura T, Kato T. Biomineralization-inspired synthesis of functional organic/inorganic hybrid materials: Organic molecular control of self-organization of hybrids. *Org Biomol Chem*. 2015;13(4):974-989. doi:10.1039/C4OB01796J.

14. Murr MM, Morse DE. Fractal intermediates in the self-assembly of silicatein filaments. http://www.pnas.org/content/102/33/11657.full.pdf. Accessed August 27, 2017.

15. Cha JN, Shimizu K, Zhou Y, et al. Silicatein filaments and subunits from a marine sponge direct the polymerization of silica and silicones in vitro. *Proc Natl Acad Sci U S A*. 1999;96(2):361-365. doi:10.1073/PNAS.96.2.361.

16. Zhou Y, Shimizu K, Cha J, Stucky G. Efficient catalysis of polysiloxane synthesis by silicatein α requires specific hydroxy and imidazole functionalities. *Angew Chemie*. 1999. http://onlinelibrary.wiley.com/doi/10.1002/(SICI)1521-3773(19990315)38:6%3C779::AID-ANIE779%3E3.0.CO;2-%23/full. Accessed August 27, 2017.

17. Arakaki A, Shimizu K, Oda M, Sakamoto T, Nishimura T, Kato T. Biomineralization-inspired synthesis of functional organic/inorganic hybrid materials: organic molecular control of self-organization of hybrids. *Org Biomol Chem*. 2015;13(4):974-989. doi:10.1039/C4OB01796J.

18. Wang X, Schröder HC, Wang K, et al. Genetic, biological and structural hierarchies during sponge spicule formation: from soft sol–gels to solid 3D silica composite structures. *Soft Matter*. 2012;8(37):9501. doi:10.1039/c2sm25889g.

19. Müller WEG, Binder M, von Lintig J, et al. Interaction of the retinoic acid signaling pathway with spicule formation in the marine sponge Suberites domuncula through activation of bone morphogenetic protein-1. *Biochim Biophys Acta - Gen Subj*. 2011;1810(12):1178-1194. doi:10.1016/j.bbagen.2011.09.006.

20. Simpson TL. *The Cell Biology of Sponges*. New York, NY: Springer New York; 1984. doi:10.1007/978-1-4612-5214-6.

21. Müller WEG, Blumbach B, Wagner-Hülsmann C, Lessel U, 淳平林. Galectins in

the Phylogenetically Oldest Metazoa, the Sponges (Porifera). *Trends Glycosci Glycotechnol*. 1997;9(45):123-130. doi:10.4052/tigg.9.123.

22. Schütze J, Krasko A, Diehl-Seifert B, Müller WEG. Cloning and expression of the putative aggregation factor from the marine sponge Geodia cydonium. *J Cell Sci*. 2001;114(17). http://jcs.biologists.org/content/114/17/3189.short. Accessed August 28, 2017.

23. Harrison F, Davis D. Morphological and cytochemical patterns during early stages of reduction body formation in Spongilla lacustris (Porifera: Spongillidae). *Trans Am Microsc Soc*. 1982. http://www.jstor.org/stable/3225749. Accessed August 28, 2017.

24. Müller W, Rothenberger M, Boreiko A. Formation of siliceous spicules in the marine demosponge Suberites domuncula. *Cell tissue*. 2005. http://link.springer.com/article/10.1007/s00441-005-1141-5. Accessed August 28, 2017.

25. Schröder HC, Boreiko A, Korzhev M, et al. Co-expression and Functional Interaction of Silicatein with Galectin. *J Biol Chem*. 2006;281(17):12001-12009. doi:10.1074/jbc.M512677200.

26. Müller WEG, Schloßmacher U, Wang X, et al. Poly(silicate)-metabolizing silicatein in siliceous spicules and silicasomes of demosponges comprises dual enzymatic activities (silica polymerase and silica esterase). *FEBS J*. 2008;275(2):362-370. doi:10.1111/j.1742-4658.2007.06206.x.

27. Silicase, an enzyme which degrades biogenous amorphous silica: contribution to the metabolism of silica deposition in the demosponge Suberites domuncula. *Prog Mol Subcell*. 2003. http://link.springer.com/content/pdf/10.1007/978-3-642-55486-5.pdf#page=252. Accessed August 28, 2017.

28. Bernard C. *Introduction à l'étude de La Médecine Expérimentale Par m. Claude Bernard*.; 1865. https://books.google.com/books?hl=en&lr=&id=iBdSKwntgUAC&oi=fnd&pg=PA5&dq=C+bernard+1865+introduction+a+l%27Etude&ots=xW586PKZEE&sig=amCMOH0qSlxoTYVZ4BALTOOGT84. Accessed August 28, 2017.

29. Wang X, Schröder H, Wiens M, Ushijima H. Bio-silica and bio-polyphosphate: applications in biomedicine (bone formation). *Curr Opin*. 2012. http://www.sciencedirect.com/science/article/pii/S095816691200033X. Accessed August 28, 2017.

30. Jugdaohsingh R. Silicon and bone health. *J Nutr Health Aging*. 2007. https://www.ncbi.nlm.nih.gov/pmc/articles/PMC2658806/. Accessed August 28, 2017.

31. Wiens M, Wang X, Schröder H, Kolb U. The role of biosilica in the osteoprotegerin/RANKL ratio in human osteoblast-like cells. *Biomaterials*. 2010. http://www.sciencedirect.com/science/article/pii/S0142961210008434. Accessed August 28, 2017.

32. Schröder H, Wang X, Wiens M. Silicate modulates the cross-talk between osteoblasts (SaOS-2) and osteoclasts (RAW 264.7 cells): Inhibition of osteoclast growth and differentiation. *J Cell*. 2012. http://onlinelibrary.wiley.com/doi/10.1002/jcb.24196/full. Accessed August 28, 2017.

33. Jo BH, Kim CS, Jo YK, Cheong H, Cha HJ. Recent developments and applications of bioinspired silicification. *Korean J Chem Eng*. 2016;33(4):1125-1133. doi:10.1007/s11814-016-0003-z.

34. Boehm H. The chemistry of silica. Solubility, polymerization, colloid and surface properties, and biochemistry. Von RK Iler. John Wiley and Sons, Chichester 1979. XXIV, 886 S.,. *Angew Chemie*. 1980. http://onlinelibrary.wiley.com/doi/10.1002/ange.19800920433/full. Accessed August 28, 2017.

35. Patwardhan S V, Mukherjee N, Clarson SJ. Effect of process parameters on the polymer mediated synthesis of silica at neutral pH. *Silicon Chem*. 2002;1(1):47-54. doi:10.1023/A:1016026927401.

36. Global Precipitated Silica Market 2017-2021 | Market Research Reports - Industry Analysis Size & Trends - Technavio. Technavio. https://www.technavio.com/report/global-specialty-chemicals-global-precipitated-silica-market-2017-2021. Published 2017. Accessed August 27, 2017.

37. Specialty Silica Market - Global Industry Analysis, Size and Forecast, 2016 to 2026. Future Market Insights. doi:2016-05-24.

38. Odatsu T, Azimaie T, Velten MF, et al. Human periosteum cell osteogenic differentiation enhanced by ionic silicon release from porous amorphous silica fibrous scaffolds. *J Biomed Mater Res - Part A*. 2015;103(8):2797-2806. doi:10.1002/jbm.a.35412.

39. Ilyas A, Lavrik N V., Kim HKW, Aswath PB, Varanasi VG. Enhanced Interfacial Adhesion and Osteogenesis for Rapid “bone-like” Biomineralization by PECVD-Based Silicon Oxynitride Overlays. *ACS Appl Mater Interfaces*. 2015;7(28):15368-15379. doi:10.1021/acsami.5b03319.

40. Cicco SR, Vona D, De Giglio E, et al. Chemically Modified Diatoms Biosilica for Bone Cell Growth with Combined Drug-Delivery and Antioxidant Properties. *Chempluschem*. 2015;80(7):1104-1112. doi:10.1002/cplu.201402398.

41. Le TDH, Bonani W, Speranza G, et al. Processing and characterization of diatom nanoparticles and microparticles as potential source of silicon for bone tissue engineering. *Mater Sci Eng C*. 2016;59:471-479. doi:10.1016/j.msec.2015.10.040.

42. Likhoshway Y V., Sorokovikova EG, Belykh OI, et al. Visualization of the silicon biomineralization in cyanobacteria, sponges and diatoms. *Biosph Orig Evol*. 2008;(Table 1):219-230. doi:10.1007/978-0-387-68656-1_16.

43. M??ller WEG, Wang X, Cui FZ, et al. Sponge spicules as blueprints for the biofabrication of inorganic-organic composites and biomaterials. *Appl Microbiol Biotechnol*. 2009;83(3):397-413. doi:10.1007/s00253-009-2014-8.

44. Müller WEG, Wang X, Belikov SI, et al. Formation of Siliceous Spicules in Demosponges: Example Suberites domuncula. *Handb Biomin Biol Asp Struct Form*. 2008;1:59-82. doi:10.1002/9783527619443.ch4.

45. Wang S, Wang X, Draenert FG, et al. Bioactive and biodegradable silica biomaterial for bone regeneration. *Bone*. 2014;67:292-304. doi:10.1016/j.bone.2014.07.025.

46. Iler RK. *The Chemistry of Silica : Solubility, Polymerization, Colloid and Surface Properties, and Biochemistry*. Wiley; 1979. https://www.wiley.com/en-us/The+Chemistry+of+Silica%3A+Solubility%2C+Polymerization%2C+Colloid+and+Surface+Properties+and+Biochemistry+of+Silica-p-9780471024040. Accessed May 6, 2018.

47. Healy TW. Stability of Aqueous Silica Sols. In: ; 1994:147-159. doi:10.1021/ba-1994-0234.ch007.

48. Chen* S-L, Peng Dong, Guang-Hua Yang and, Yang J-J. Kinetics of Formation of Monodisperse Colloidal Silica Particles through the Hydrolysis and Condensation of Tetraethylorthosilicate. 1996. doi:10.1021/IE9602217.

49. Coltrain BK, Kelts LW. The Chemistry of Hydrolysis and Condensation of Silica Sol—Gel Precursors. In: ; 1994:403-418. doi:10.1021/ba-1994-0234.ch019.

50. Patwardhan S V., Clarson SJ. Silicification and biosilicification. *Polym Bull*. 2002;48(4-5):367-371. doi:10.1007/s00289-002-0043-x.

51. Brinker CJ, Scherer GW. *Sol-Gel Science : The Physics and Chemistry of Sol-Gel Processing*. Academic Press; 1990.

52. Stöber W, Fink A, Bohn E. Controlled growth of monodisperse silica spheres in the micron size range. *J Colloid Interface Sci*. 1968;26(1):62-69. doi:10.1016/0021-9797(68)90272-5.

53. Kröger N, Deutzmann R, Sumper M. Polycationic peptides from diatom biosilica

that direct silica nanosphere formation. *Science*. 1999;286(5442):1129-1132. http://www.ncbi.nlm.nih.gov/pubmed/10550045. Accessed May 6, 2018.

54. Patwardhan S V, Clarson SJ. Silicifacation and biosilicification Part 6. Poly-L-histidine mediated synthesis of silica at neutral pH. *J Inorg Organomet Polym*. 2003;13(1):49-53. doi:10.1023/A:1022952931063.

55. Cha JN, Stucky GD, Morse DE, Deming TJ. Biomimetic synthesis of ordered silica structures mediated by block copolypeptides. *Nature*. 2000;403(6767):289-292. doi:10.1038/35002038.

56. Tahir MN, Théato P, Müller WEG, et al. Monitoring the formation of biosilica catalysed by histidine-tagged silicatein. *Chem Commun*. 2004;0(24):2848-2849. doi:10.1039/B410283E.

57. Tahir MN, Théato P, Müller WEG, et al. Formation of layered titania and zirconia catalysed by surface-bound silicatein. *Chem Commun*. 2005;0(44):5533. doi:10.1039/b510113a.

58. Tahir MN, Eberhardt M, Therese HA, et al. From Single Molecules to Nanoscopically Structured Functional Materials: Au Nanocrystal Growth on TiO2 Nanowires Controlled by Surface-Bound Silicatein. *Angew Chemie Int Ed*. 2006;45(29):4803-4809. doi:10.1002/anie.200503770.

59. Jan L. Sumerel, Wenjun Yang, David Kisailus, James C. Weaver, Joon Hwan Choi and, Morse* DE. Biocatalytically Templated Synthesis of Titanium Dioxide. 2003. doi:10.1021/CM030254U.

60. Kisailus D, Choi JH, Weaver JC, Yang W, Morse DE. Enzymatic Synthesis and Nanostructural Control of Gallium Oxide at Low Temperature. *Adv Mater*. 2005;17(3):314-318. doi:10.1002/adma.200400815.

61. Gritsenko VA, Kwok RWM, Wong H, Xu JB. Short-range order in non-stoichiometric amorphous silicon oxynitride and silicon-rich nitride. *J Non Cryst Solids*. 2002;297(1):96-101. doi:10.1016/S0022-3093(01)00910-3.

62. Bruggeman DAG, G. DA. Berechnung verschiedener physikalischer Konstanten von heterogenen Substanzen. I. Dielektrizitätskonstanten und Leitfähigkeiten der Mischkörper aus isotropen Substanzen. *Ann Phys*. 1935;416(7):636-664. doi:10.1002/andp.19354160705.

63. Kuiper AET. Deposition and composition of silicon oxynitride films. *J Vac Sci Technol B Microelectron Nanom Struct*. 1983;1(1):62. doi:10.1116/1.582543.

64. Snyder PG, Xiong Y-M, Woollam JA, et al. Graded refractive index silicon oxynitride thin film characterized by spectroscopic ellipsometry. 1992. http://digitalcommons.unl.edu/electricalengineeringfacpub. Accessed May 19,

2018.

65. Varanasi VG, Ilyas A, Velten MF, Shah A, Lanford WA, Aswath PB. Role of Hydrogen and Nitrogen on the Surface Chemical Structure of Bioactive Amorphous Silicon Oxynitride Films. *J Phys Chem B*. 2017;121(38):8991-9005. doi:10.1021/acs.jpcb.7b05885.

66. XANES: Theory - Chemistry LibreTexts. https://chem.libretexts.org/Core/Physical_and_Theoretical_Chemistry/Spectroscopy/X-ray_Spectroscopy/XANES%3A_Theory. Accessed May 5, 2018.

67. Wang S-F, Wang X-H, Gan L, Wiens M, Schröder HC, Müller WEG. Biosilica-glass formation using enzymes from sponges [silicatein]: Basic aspects and application in biomedicine [bone reconstitution material and osteoporosis]. *Front Mater Sci*. 2011;5(3):266-281. doi:10.1007/s11706-011-0145-1.

68. Kim S. *Marine Biomaterials Characterization, Isolation and Applications.* CRC Pr I Llc; 2017.

69. Silva TH, Alves A, Ferreira BM, et al. Materials of marine origin: a review on polymers and ceramics of biomedical interest. *Int Mater Rev*. 2012;57(5):276-306. doi:10.1179/1743280412Y.0000000002.

70. Sowjanya JA, Singh J, Mohita T, et al. Biocomposite scaffolds containing chitosan/alginate/nano-silica for bone tissue engineering. *Colloids Surfaces B Biointerfaces*. 2013;109:294-300. doi:10.1016/j.colsurfb.2013.04.006.

71. Ravichandran R, Sundaramurthi D, Gandhi S, Sethuraman S, Krishnan UM. Bioinspired hybrid mesoporous silica–gelatin sandwich construct for bone tissue engineering. *Microporous Mesoporous Mater*. 2014;187:53-62. doi:10.1016/J.MICROMESO.2013.12.018.

72. Wang X, Schröder HC, Grebenjuk V, et al. The marine sponge-derived inorganic polymers, biosilica and polyphosphate, as morphogenetically active matrices/scaffolds for the differentiation of human multipotent stromal cells: potential application in 3D printing and distraction osteogenesis. *Mar Drugs*. 2014;12(2):1131-1147. doi:10.3390/md12021131.

73. Wang X, Schröder HC, Wiens M, Ushijima H, Müller WE. Bio-silica and bio-polyphosphate: applications in biomedicine (bone formation). *Curr Opin Biotechnol*. 2012;23(4):570-578. doi:10.1016/j.copbio.2012.01.018.

74. Patwardhan S V, Mukherjee N, Steinitz-Kannan M, Clarson SJ. Bioinspired synthesis of new silica structures. doi:10.1039/b302056h.

75. Le TDH, Liaudanskaya V, Bonani W, Migliaresi C, Motta A. Enhancing bioactive properties of silk fibroin with diatom particles for bone tissue engineering

applications. *J Tissue Eng Regen Med*. 2018;12(1):89-97. doi:10.1002/term.2373.

76. Rezwan K, Chen QZ, Blaker JJ, Boccaccini AR. Biodegradable and bioactive porous polymer/inorganic composite scaffolds for bone tissue engineering. *Biomaterials*. 2006;27:3413-3431. doi:10.1016/j.biomaterials.2006.01.039.

77. Wu X, Liu Y, Li X, et al. Preparation of aligned porous gelatin scaffolds by unidirectional freeze-drying method. *Acta Biomater*. 2010;6(3):1167-1177. doi:10.1016/j.actbio.2009.08.041.

78. Liu C, Xia Z, Czernuszka JT. Design and Development of Three-Dimensional Scaffolds for Tissue Engineering. *Chem Eng Res Des*. 2007;85(7):1051-1064. doi:10.1205/cherd06196.

79. Holzwarth JM, Ma PX. Biomimetic nanofibrous scaffolds for bone tissue engineering. *Biomaterials*. 2011;32(36):9622-9629. doi:10.1016/j.biomaterials.2011.09.009.

80. Guarino V, Causa F, Ambrosio L. Bioactive scaffolds for bone and ligament tissue. *Expert Rev Med Devices*. 2007;4(3):405-418. doi:10.1586/17434440.4.3.405.

81. Descamps M, Richart O, Hardouin P, Hornez JC, Leriche A. Synthesis of macroporous β-tricalcium phosphate with controlled porous architectural. *Ceram Int*. 2008;34(5):1131-1137. doi:10.1016/j.ceramint.2007.01.004.

82. Ko E, Cho S-W. Biomimetic Polymer Scaffolds to Promote Stem Cell-Mediated Osteogenesis. *Int J Stem Cells*. 2013;6(2):87-91. doi:10.15283/ijsc.2013.6.2.87.

83. Mieszawska AJ, Llamas JG, Vaiana CA, Kadakia MP, Naik RR, Kaplan DL. Clay enriched silk biomaterials for bone formation. *Acta Biomater*. 2011;7(8):3036-3041. doi:10.1016/j.actbio.2011.04.016.

84. Ilyas A, Odatsu T, Shah A, et al. Amorphous Silica: A New Antioxidant Role for Rapid Critical-Sized Bone Defect Healing. *Adv Healthc Mater*. 2016;5(17):2199-2213. doi:10.1002/adhm.201600203.

# Chapter 6. General Conclusions:

Silicon is one of the most abundant elements found in the earth's crust in various forms silica being one of them . It finds applications in various industries ranging from paints to food and optics to biomedical devices. The industrial silica production capacity is $10^3$ tonnes per annum less than the production found in the nature. Moreover, the industrial methods are far high harsher conditions and less control than compared to what nature has already modelled and perfected over years of evolution. Developing controlled synthesis of nanometre sized material has tremendous demand in the emerging technologies. Thus, studying and mimicking the natural biosilica synthesis process seem the appropriate next step towards making the silica industry a step closer to being faster, smarter and green (ecologically).

In our research work we demonstrated that in the combined presence of imidazole and glucose compounds, TEOS silicification process can be accelerated to form silica like precipitates at near neutral pH and ambient conditions . The combined presence of imidazole functionality and dangling OH based compound is necessary to achieve the formation of nanostructured silica like particles at accelerated rates of 15 minutes or under.

The presence of imidazole functionality and dangling free OH bond, causes hydrogen bonding , leading to nucleophilic attack on the Si atom in the TEOS molecule, catalysing the hydrolysis step of the silicification process. And

this is observed by elongated times to form precipitation product when each of the reactant was absent from the reaction system.

The imidazole functionality, form hydrogen bonding with the silicic acids to accelerate the condensation process, and the active functionalities accelerate the silica precipitation possibly via electrostatic interaction with the oligomers. The imidazole functionality gets involved in the molecular structure as well, indicating its interaction isn't mere electrostatic type of activity, and to elucidate its complete role further study is needed.

The created particles exhibit biocompatibility and enhanced bioactivity when compared with silk fibroin. They are easily incorporated into the various known and established scaffold systems, without any antagonistic effects due to the addition. Sustained release of $Si^{4+}$ ions was observed in the dissolution kinetics study for the scaffold systems. Thus, synthesized biosilica like structures has definite potential in biomedical field of bone tissue engineering.

Overall study pursued establishes a new, green and quick synthesis method of nano silica like structures, with potential biomedical use, using the most commonly used TEOS precursor. The process is highly repeatable and easily scalable and hence industrially adaptable. The knowledge acquired from this study adds to (i) a new synthesis method for nano spherical silica like structure production (ii) understanding of silicification of TEOS precursor system, (iii) the role of active moieties in biosilicification process (iv) potential new bioactive material in bone tissue engineering applications (v) effects of various

parameters like bonding nature, particle size, number of surfaces for interaction on dissolution kinetics of $Si^{4+}$ ions.

## Biographical Information

Ami Shah was born in Pune, Maharashtra (India) and did her schooling from the same place. She pursued her undergrad from the University of Poona and got her degree in Mechanical Engineering. She joined the Tribology group with Dr. Aswath in September 2012. She has worked on various projects in Tribology in grease development and presented twice at the Annual STLE conference. She gained her master's degree in Material Science in 2012. She continued to pursue her Ph.D degree under able guidance of Dr. Pranesh Aswath with focusing her research in biomaterials. She spent a semester at University of Trento, Italy at the BioTech lab under guidance of Dr Motta. After her graduation in May 2018 she plans to move back to India and join her family's pharmaceutical company.